

TOWARDS NEAR-ZERO COEFFICIENTS OF THERMAL EXPANSION IN
 $A_2M_3O_{12}$ MATERIALS

by

Kimberly J. Miller

Submitted in partial fulfilment of the requirements
for the degree of Doctor of Philosophy

at

Dalhousie University
Halifax, Nova Scotia
December 2012

© Copyright by Kimberly J. Miller, 2012

DALHOUSIE UNIVERSITY
DEPARTMENT OF CHEMISTRY

The undersigned hereby certify that they have read and recommend to the Faculty of Graduate Studies for acceptance a thesis entitled “Towards Near-Zero Coefficients of Thermal Expansion in $A_2Mo_3O_{12}$ Materials” by Kimberly J. Miller in partial fulfilment of the requirements for the degree of Doctor of Philosophy.

Dated: December 6th, 2012

External Examiner: _____

Research Supervisor: _____

Examining Committee: _____

Departmental Representative: _____

DALHOUSIE UNIVERSITY

DATE: December 6th, 2012

AUTHOR: Kimberly J. Miller

TITLE: Towards Near-Zero Coefficients of Thermal Expansion in $A_2Mo_3O_{12}$
Materials

DEPARTMENT OR SCHOOL: Department of Chemistry

DEGREE: PhD CONVOCATION: May YEAR: 2013

Permission is herewith granted to Dalhousie University to circulate and to have copied for non-commercial purposes, at its discretion, the above title upon the request of individuals or institutions. I understand that my thesis will be electronically available to the public.

The author reserves other publication rights, and neither the thesis nor extensive extracts from it may be printed or otherwise reproduced without the author's written permission.

The author attests that permission has been obtained for the use of any copyrighted material appearing in the thesis (other than the brief excerpts requiring only proper acknowledgement in scholarly writing), and that all such use is clearly acknowledged.

Signature of Author



~ DEDICATIONS ~

Dedicated to Dorothy Miller (Nana), Peter Miller, and Dr. Robert Haines. You may no longer be here, but the impressions you all have left on my life will never fade. Thank you for never giving up on me and encouraging me to be the best I could be.

TABLE OF CONTENTS

LIST OF TABLES	xiv
LIST OF FIGURES	xvi
ABSTRACT.....	xxvi
LIST OF ABBREVIATIONS AND SYMBOLS USED.....	xxvii
ACKNOWLEDGEMENTS.....	xxxiii
CHAPTER 1 INTRODUCTION	1
1.1 NEGATIVE THERMAL EXPANSION (THERMOMIOTIC) MATERIALS.....	2
1.1.1 WHY THERMOMIOTIC MATERIALS ARE INTERESTING	2
1.1.2 THERMAL EXPANSION AND MECHANICAL PROPERTIES OF MATERIALS	3
1.2 MECHANISMS OF NEGATIVE THERMAL EXPANSION	7
1.2.1 LATTICE VIBRATIONS	8
1.2.2 RIGID UNIT MODES (RUMs)	10
1.2.3 MACROSCOPIC NEGATIVE THERMAL EXPANSION.....	12
1.2.4 OTHER NEGATIVE THERMAL EXPANSION MECHANISMS.....	13
1.3 NEGATIVE THERMAL EXPANSION AND ITS RELATIONSHIP TO OTHER PROPERTIES.....	13
1.3.1 HEAT CAPACITY AND RELATED PROPERTIES	14
1.3.2 THERMAL CONDUCTIVITY.....	17
1.3.3 MODE GRÜNEISEN PARAMETER	18
1.3.4 PHONON DISPERSION RELATIONS AND DENSITY OF STATES	18
1.3.5 PHASE TRANSITIONS	19
1.4 APPLICATIONS OF THERMOMIOTIC MATERIALS	20

1.4.1 CURRENT AND POTENTIAL APPLICATIONS	20
1.4.2 CRITERIA FOR APPLICATIONS.....	22
1.5 SYNTHESIS AND CHARACTERIZATION TOOLS	24
1.5.1 SYNTHESIS	24
1.5.1.1 Solid-State Synthesis at High Temperature	24
1.5.1.2 Soft Chemistry Approaches	26
1.5.1.2.1 Sol-Gel Synthesis.....	27
1.5.1.2.2 Co-Precipitation	31
1.5.1.2.3 Hydrothermal Synthesis.....	32
1.5.1.3 Laser Synthesis	33
1.5.2 MICROSTRUCTURE	33
1.5.2.1 Sintering, Porosity and Microcracking	33
1.5.2.2 Effects of Particle Morphology.....	35
1.5.2.3 Coatings, Surface Treatments and Binders.....	35
1.5.3 EXPERIMENTAL DETERMINATION OF THERMAL EXPANSION.....	36
1.5.3.1 Diffraction Techniques	37
1.5.3.2 Dilatometry	40
1.5.3.3 Discrepancies between Diffraction and Dilatometric Results	41
1.6 TYPES OF THERMOMIOTIC MATERIALS	42
1.6.1 METAL OXIDES AND RELATED STRUCTURES	42
1.6.1.1 AM_2O_8	42
1.6.1.2 AM_2O_7	45
1.6.1.3 $A_2M_3O_{12}$	46

1.6.1.4 AMO_5	49
1.6.1.5 AO_3 and Related Structures.....	50
1.6.1.6 Other Oxides	52
1.6.1.6.1 Lithium aluminum silicates (LAS)	52
1.6.1.6.2 M_2O	52
1.6.1.6.3 Zeolites and Aluminophosphates.....	53
1.6.1.6.4 Perovskites and Anti-Perovskites	54
1.6.2 METAL CYANIDES.....	54
1.6.2.1 $M(CN)_2$	54
1.6.2.2 $A_x[M(CN)_6]$ ($x = 1, 1.5, 3$).....	55
1.6.2.3 $M CN$	56
1.6.2.4 Clathrates	56
1.6.3 OTHER STRUCTURES	57
1.6.3.1 Metal-Organic Framework (MOF) Materials.....	57
1.6.3.2 NaSICON.....	58
1.6.3.3 Nanomaterials	58
1.6.3.4 Other Structures	59
1.7 COMPOSITE MATERIALS.....	59
1.8 SOLID SOLUTIONS.....	61
1.9 RESEARCH GOALS	62
CHAPTER 2 SAMPLE PREPARATION	64
2.1 SYNTHETIC METHODS	64
2.1.1 SOLID-STATE REACTION METHOD.....	66

2.1.2 MECHANICAL ACTIVATION	67
2.1.3 SIMPLIFIED SOL-GEL SYNTHESIS	68
2.2 SAMPLE PREPARATION AND SINTERING METHODOLOGIES	69
2.2.1 SAMPLE PREPARATION.....	70
2.2.2 HYGROSCOPIC SAMPLE PREPARATION	70
CHAPTER 3 CHARACTERIZATION	74
3.1 SCANNING ELECTRON MICROSCOPY (SEM).....	74
3.2 TRANSMISSION ELECTRON MICROSCOPY (TEM).....	75
3.3 THERMOGRAVIMETRIC ANALYSIS	75
3.4 DIFFERENTIAL SCANNING CALORIMETRY (DSC)	77
3.5 DILATOMETRY	78
3.6 X-RAY POWDER DIFFRACTION.....	79
3.6.1 INSTRUMENTS	79
3.6.1.1 Siemens D-5000 Diffractometer.....	79
3.6.1.2 Siemens D-500 Powder Diffractometer.....	80
3.6.1.3 PANalytical X'Pert Pro Bragg-Brentano Diffractometer	81
3.6.2 REFINEMENT METHODS	82
3.6.2.1 Rietveld Method Using Rietica.....	82
3.6.2.2 Le Bail Fitting.....	85
3.7 HEAT CAPACITY	86
3.7.1 PPMS INSTRUMENT OVERVIEW	86
3.7.2 HEAT CAPACITY ANALYSIS MODELS	88
3.7.3 HEAT CAPACITY ACCURACY CRITERIA.....	90

3.8 THERMAL CONDUCTIVITY	91
3.8.1 PPMS INSTRUMENT OVERVIEW	92
3.8.1.1 Steady-State Measurement.....	93
3.8.1.2 Continuous-Measurement Mode.....	95
CHAPTER 4 SIMPLIFIED RAPID SYNTHESIS OF $\text{Al}_2\text{Mo}_3\text{O}_{12}$	98
4.1 MOTIVATIONS FOR DEVELOPMENT	98
4.2 METHODS	100
4.3 RESULTS AND DISCUSSION.....	100
4.4 CONCLUSIONS.....	106
CHAPTER 5 LOW-TEMPERATURE INVESTIGATION OF $\text{Y}_2\text{Mo}_3\text{O}_{12}$	107
5.1 INTRODUCTION	107
Table 5.1: Phase transition temperatures of select $A_2M_3O_{12}$ materials	108
5.2 METHODS	109
5.3 PHASE PURITY OF $\text{Y}_2\text{Mo}_3\text{O}_{12}$	110
5.4 HEAT CAPACITY AND DSC OF $\text{Y}_2\text{Mo}_3\text{O}_{12}$	111
5.4.1 DIFFERENTIAL SCANNING CALORIMETRY	111
5.4.2 HEAT CAPACITY	111
5.5 DETERMINATION OF THE INTRINSIC CTE AND POLYHEDRAL DISTORTION.....	113
5.5.1 COEFFICIENT OF THERMAL EXPANSION	113
5.6 $\text{Y}_2\text{Mo}_3\text{O}_{12}$ IN THE LOW-TEMPERATURE RANGE.....	114
5.7 CONCLUSIONS.....	118
CHAPTER 6 LOW-TEMPERATURE INVESTIGATIONS OF THE OPEN- FRAMEWORK MATERIAL $\text{HfMgMo}_3\text{O}_{12}$	119

6.1 INTRODUCTION	119
6.2 METHODS	120
6.3 RESULTS AND DISCUSSION	121
6.3.1 SAMPLE CHARACTERIZATION AND PHASE TRANSITION	121
6.3.2 HEAT CAPACITY	126
6.4 CONCLUSIONS.....	127
CHAPTER 7 PHASE TRANSITION INVESTIGATION OF $\text{In}_2\text{Mo}_3\text{O}_{12}$	128
7.1 MOTIVATIONS.....	128
7.2 METHODS	129
7.3 RESULTS AND DISCUSSION	129
7.3.1 SAMPLE CHARACTERIZATION AND PHASE TRANSITION	129
7.3.2 HEAT CAPACITY	133
7.4 CONCLUSIONS.....	134
CHAPTER 8 NEAR-ZERO THERMAL EXPANSION IN $\text{In}(\text{HfMg})_{0.5}\text{Mo}_3\text{O}_{12}$ AND $\text{In}_{1.5}(\text{HfMg})_{0.25}\text{Mo}_3\text{O}_{12}$	135
8.1 MOTIVATIONS.....	135
8.2 METHODS	136
8.3 RESULTS AND DISCUSSION.....	137
8.3.1 SAMPLE CHARACTERIZATION	137
8.3.2 PHASE TRANSITIONS	141
8.3.3 THERMAL EXPANSION COEFFICIENTS	144
8.3.3.1 Dilatometry	144
8.3.3.1.1 Dilatometry of $\text{In}(\text{HfMg})_{0.5}\text{Mo}_3\text{O}_{12}$	144
8.3.3.1.2 Dilatometry of $\text{In}_{1.5}(\text{HfMg})_{0.25}\text{Mo}_3\text{O}_{12}$	146

8.3.3.2 Temperature-Dependent XPRD.....	147
8.3.3.2.1 Determination of Room-Temperature Parameters.....	147
8.3.3.2.2 Determination of the CTEs by XRPD	149
8.4 CONCLUSIONS.....	154
CHAPTER 9 HEAT CAPACITY AND THERMAL CONDUCTIVITY OF THE $A_2\text{Mo}_3\text{O}_{12}$ FAMILY	156
9.1 MOTIVATIONS.....	156
9.2 METHODS	157
9.3 HEAT CAPACITY RESULTS.....	157
9.3.1 HEAT CAPACITY RESULTS FOR $\text{HfMgMo}_3\text{O}_{12}$, $\text{In}_2\text{Mo}_3\text{O}_{12}$, AND $\text{Y}_2\text{Mo}_3\text{O}_{12}$	157
9.3.2 HEAT CAPACITY OF $\text{In}(\text{HfMg})_{0.5}\text{Mo}_3\text{O}_{12}$	159
9.3.3 HEAT CAPACITY OF $\text{In}_{1.5}(\text{HfMg})_{0.25}\text{Mo}_3\text{O}_{12}$	160
9.4 ESTIMATING THE HEAT CAPACITY OF $A_2\text{Mo}_3\text{O}_{12}$ MATERIALS	162
9.4.1 CONSTITUENT ADDITIVITY MODEL.....	162
9.4.2 HEAT CAPACITY BY THE RULE OF MIXTURES	166
9.5 ANOMALOUS LOW-FREQUENCY MODES.....	168
9.6 DEBYE TEMPERATURE	172
9.7 THERMAL CONDUCTIVITY	175
9.8 EFFECTIVE PHONON MEAN FREE PATH.....	182
9.9 CONCLUSIONS.....	187
CHAPTER 10 CONCLUSIONS AND FUTURE WORK.....	188
APPENDIX A – Supplementary Data for Heat Capacity Measurements	192
A1 $\text{Y}_2\text{Mo}_3\text{O}_{12}$	192
A2 $\text{HfMgMo}_3\text{O}_{12}$	194

A3 $\text{In}_2\text{Mo}_3\text{O}_{12}$	196
A4 $\text{In}(\text{HfMg})_{0.5}\text{Mo}_3\text{O}_{12}$	198
A5 $\text{In}_{1.5}(\text{HfMg})_{0.25}\text{Mo}_3\text{O}_{12}$	200
APPENDIX B - Heat Capacity Data	202
B1 $\text{Y}_2\text{Mo}_3\text{O}_{12}$	202
B2 $\text{HfMgMo}_3\text{O}_{12}$	205
B3 $\text{In}_2\text{Mo}_3\text{O}_{12}$	207
B4 $\text{In}(\text{HfMg})_{0.5}\text{Mo}_3\text{O}_{12}$	211
B5 $\text{In}_{1.5}(\text{HfMg})_{0.25}\text{Mo}_3\text{O}_{12}$	214
APPENDIX C - Thermal Conductivity Data.....	217
C1 $\text{HfMgMo}_3\text{O}_{12}$	217
C2 $\text{In}(\text{HfMg})_{0.5}\text{Mo}_3\text{O}_{12}$	225
C3 $\text{In}_{1.5}(\text{HfMg})_{0.25}\text{Mo}_3\text{O}_{12}$	229
C4 $\text{In}_2\text{Mo}_3\text{O}_{12}$	232
C5 $\text{Y}_2\text{Mo}_3\text{O}_{12}$	235
APPENDIX D - DSC	238
APPENDIX E – X-Ray Powder Diffraction.....	239
E1 $\text{In}(\text{HfMg})_{0.5}\text{Mo}_3\text{O}_{12}$	239
E2 $\text{In}_{1.5}(\text{HfMg})_{0.5}\text{Mo}_3\text{O}_{12}$	241
APPENDIX F – Copyright Agreement Letters	243
PERMISSION FOR FIGURE 1.5 IN CHAPTER 1	243
PERMISSION FOR FIGURE 1.6 IN CHAPTER 1	244
PERMISSION FOR FIGURE 1.7 IN CHAPTER 1	245

PERMISSION FOR FIGURE 1.8 IN CHAPTER 1	246
PERMISSIONS FOR FIGURES 4.1, 4.2, 4.3, AND 4.4 IN CHAPTER 4.....	247
PERMISSIONS FOR FIGURES 5.1, 5.2, 5.4, AND 5.5 IN CHAPTER 5 AND FIGURE 9.3 IN CHAPTER 9.....	248
PERMISSIONS FOR FIGURES 6.1, 6.2, 6.3, 6.4, 6.5, AND 6.6 IN CHAPTER 6 AND FIGURES 9.1, 9.7, AND 9.18 IN CHAPTER 9.	249
REFERENCES	250

LIST OF TABLES

Table 1.1: Average linear coefficients of thermal expansion (α_l) for selected materials given at either a single temperature or over a temperature range.	4
Table 1.2: The Debye (or effective Debye) temperature for selected solids and the corresponding CTE.	16
Table 1.3: Average linear coefficients of thermal expansion (α_l) of select $A_2M_3O_{12}$ materials determined from X-ray powder diffraction, over a given temperature range.	48
Table 2.1: Members of the $A_2Mo_3O_{12}$ family synthesized by three reaction methods: solid-state reaction (SSR), mechanical activation (MA), and a simplified sol-gel approach.	65
Table 2.2: Suppliers and purities of reagents used for the three synthetic routes.	66
Table 3.1: Selected properties for Apiezon [®] greases.	90
Table 5.1: Phase transition temperatures of select $A_2M_3O_{12}$ materials.	108
Table 6.1: Lattice constants and space groups for HfMgMo ₃ O ₁₂ at 180 K and 120 K.	125
Table 7.1: Lattice constants and space groups for In ₂ Mo ₃ O ₁₂ at 298 K and 838 K compared to the literature values at 373 K and 773 K determined by Marinkovic <i>et al.</i> ¹⁹⁷	131
Table 8.1: Approximate experimental composition of In(HfMg) _{0.5} Mo ₃ O ₁₂ as determined by qualitative EDS analysis. All results are given in atomic %.	140
Table 8.2: Approximate experimental composition of In _{1.5} (HfMg) _{0.25} Mo ₃ O ₁₂ as determined by qualitative EDS analysis. All results are given in atomic %.	140
Table 8.3: Enthalpy and entropy changes for the monoclinic to orthorhombic phase transition with transition onset temperatures on heating, in helium atmosphere, at a heating rate of 10 K min ⁻¹ in aluminum pans for HfMgMo ₃ O ₁₂ and In ₂ Mo ₃ O ₁₂ and in stainless steel pans for In(HfMg) _{0.5} Mo ₃ O ₁₂ and In _{1.5} (HfMg) _{0.25} Mo ₃ O ₁₂	143
Table 8.4: Size and density of the 5 mm diameter pellets used for dilatometry measurements.	144

Table 8.5: Lattice parameters for the room-temperature Le Bail fit, with the $P2_1/a$ space group, of $\text{In}(\text{HfMg})_{0.5}\text{Mo}_3\text{O}_{12}$ and $\text{In}_{1.5}(\text{HfMg})_{0.25}\text{Mo}_3\text{O}_{12}$	148
Table 8.6: Intrinsic thermal expansion coefficients (α) for $\text{In}(\text{HfMg})_{0.5}\text{Mo}_3\text{O}_{12}$ and $\text{In}_{1.5}(\text{HfMg})_{0.25}\text{Mo}_3\text{O}_{12}$ as obtained from powder X-ray diffraction experiments and literature values for $\text{In}_2\text{Mo}_3\text{O}_{12}$ ¹⁹⁷ and $\text{HfMgMo}_3\text{O}_{12}$ ²⁰⁰ (note that $\text{In}_2\text{Mo}_3\text{O}_{12}$ was reported in space group $Pnma$, but the entries in this table are with respect to the $Pnca$ setting to allow direct comparison). Here α_ℓ represents the spatially averaged linear thermal expansion coefficient, and $\Delta\alpha_{max}$, the thermal expansion anisotropy, is the maximum difference in the axial thermal expansion coefficients.....	151
Table 9.1: Peak temperature of the low-temperature anomalous heat capacity and the average linear thermal expansion coefficients for the orthorhombic phases of $A_2\text{Mo}_3\text{O}_{12}$ materials.	171
Table 9.2: Young's moduli and the effective speeds of sound for members of the $A_2\text{Mo}_3\text{O}_{12}$ family calculated from θ_D^e	174
Table 9.3: Size and density of the 2.8 mm diameter pellets used to measure thermal conductivity.....	175

LIST OF FIGURES

Figure 1.1: A graphical depiction of the relationship between structure, processing, properties, and performance in materials science.	1
Figure 1.2: Potential energy (U) as a function of intermolecular separation (r) for a harmonic system (potential given by - - and average positions at different temperatures, $\langle r \rangle$, given by \circ) and an anharmonic system (potential given by — and $\langle r \rangle$ given by \bullet).	5
Figure 1.3: Longitudinal vibrations could lead to compression or expansion of the $M-O-M$ linkage while transverse vibrations would lead to compression. Adapted from Evans.	8
Figure 1.4: Librational vibrations show that the perceived distance of the $M-O$ bond decreases as the magnitude of the vibration increases. Styled after reference 6.	9
Figure 1.5: The room-temperature $P2_13$ crystal structure of ZrW_2O_8 with ZrO_6 octahedra shown in white and WO_3 tetrahedra shown in grey. Reprinted with permission from Evans, J. S. O.; Mary, T. A.; Vogt, T.; Subramanian, M. A.; Sleight, A. W. <i>Chem. Mater.</i> 1996 , 8, 2809–2823. Copyright 1996 American Chemical Society.	43
Figure 1.6 The ideal $Pa-3$ crystal structure of AM_2O_7 showing the corner-sharing AO_6 octahedra and MO_4 tetrahedra. Reprinted with permission from Korthuis, V.; Khosrovani, N.; Sleight, A. W.; Roberts, N.; Dupree, R.; Warren, W. W., Jr. <i>Chem. Mater.</i> 1995 , 7, 412–417. Copyright 1995 American Chemical Society.	45
Figure 1.7: Crystal structure of $Y_2Mo_3O_{12}$ in the $Pbcn$ phase with YO_6 octahedra in light grey and the MoO_3 tetrahedra shown in dark grey. Reprinted with permission from Gates, S. D.; Lind, C. J. <i>Solid State Chem.</i> 2007 , 180, 3510–3514. Copyright 2007 Elsevier.	46
Figure 1.8: A partial structure of MOF-5, showing that the ZnO_4 tetrahedra and the phenyl rings serve as the rigid units (I and II, respectively in the figure), while the carboxyl groups serve as a bridging unit. Negative thermal expansion in this material arises from the large amplitude transverse vibrations of the bridging carboxyl groups. From reference 251, with permission. Copyright 2008 the American Physical Society.	57
Figure 2.1: Approximately 50 mg of hydrated sample was loaded into a pellet press and heated prior to compression.	71

Figure 2.2: Between 5 mg and 20 mg of sample was loaded into the die assembly and 1 GPa of pressure is applied.....	72
Figure 3.1: Aluminum sample holder for heating and transporting hygroscopic samples.....	76
Figure 3.2: Schematic diagrams outlining the sample and platform setup and photo of the heat capacity puck.....	87
Figure 3.3: The temperature response to an applied power during the heat capacity measurement showing the two-tau™ method to model temperature decay. ³⁰⁵	88
Figure 3.4: Determination of the thermal conductivity of a sample with a cross-sectional area, A_c , by applying power, \dot{q} , to the right side of the sample, and creating a temperature gradient.....	92
Figure 3.5: Sample mounted on leads in a 2-probe configuration (left) and loaded onto the measurement platform and connected to a heater, heat sink, and thermometers (right).	93
Figure 3.6: An idealized temperature response to the heater power, in the steady-state measurement mode, showing the (a) heater power, (b) the time-based response of the hot and cold thermometers during measurement.....	94
Figure 3.7: The idealized temperature response to a heat pulse, in continuous measurement mode, showing the (a) heater power, (b) the time based response of the hot and cold thermometers during measurement, and (c) the temperature differentials, ΔT , across a sample, the estimated time constants, τ_1 and τ_2 , and the asymptotic differential, ΔT_∞	95
Figure 4.1: TGA and derivative TGA curves for $\text{Al}_2\text{Mo}_3\text{O}_{12}$ samples with 1:2 (dashed line) and 1:8 (solid line) metal to PVA ratios prepared using the assisted sol-gel method. Reprinted with permission from Ari, M.; Miller, K. J.; Marinkovic, B. A.; Jardim, P. M.; de Avillez, R.; Rizzo F.; White M. A. <i>J. Sol-Gel Sci. Technol.</i> 2011 , 58, 121–125. Copyright 2010 Springer.....	101
Figure 4.2: Experimental X-ray powder diffraction pattern (black), Rietveld fit (red) and residual (blue) for $\text{Al}_2\text{Mo}_3\text{O}_{12}$ prepared using PVA assisted sol-gel with 1:8 metal to PVA ratio after calcination at 600 °C for 20 min. The poor fit between 10° and 13°, in 2θ , indicates the presence of unreacted MoO_3 . Reprinted with permission from Ari, M.; Miller, K. J.; Marinkovic, B. A.; Jardim, P. M.; de Avillez, R.; Rizzo F.; White M. A. <i>J. Sol-Gel Sci. Technol.</i> 2011 , 58, 121–125. Copyright 2010 Springer.....	103

Figure 4.3: Micrographs of $\text{Al}_2\text{Mo}_3\text{O}_{12}$ prepared using the PVA-assisted sol-gel method and calcination at 600 °C for 20 min. (a) SEM in back scattering mode, (b) SEM in secondary electron mode (c) TEM, (d) secondary electron mode for the sample prepared by solid-state reaction with mechanical-activation. Reprinted with permission from Ari, M.; Miller, K. J.; Marinkovic, B. A.; Jardim, P. M.; de Avillez, R.; Rizzo F.; White M. A. <i>J. Sol-Gel Sci. Technol.</i> 2011 , 58, 121–125. Copyright 2010 Springer.....	104
Figure 4.4: SEM micrographs of the monophasic $\text{Al}_2\text{Mo}_3\text{O}_{12}$ powder prepared through PVA-assisted sol-gel method and calcined at 700 °C for 15 min using (a) 1:2 and (b) 1:8 metal to PVA ratio. Reprinted with permission from Ari, M.; Miller, K. J.; Marinkovic, B. A.; Jardim, P. M.; de Avillez, R.; Rizzo F.; White M. A. <i>J. Sol-Gel Sci. Technol.</i> 2011 , 58, 121–125. Copyright 2010 Springer.	105
Figure 5.1: High-resolution XRPD pattern for $\text{Y}_2\text{Mo}_3\text{O}_{12}$ at $T = 300$ K. Experimental profile (black points), calculated (red full lines) and difference profiles (blue full lines). Reprinted with permission from Marinkovic, B. A.; Ari, M.; de Avillez, R.; Rizzo F.; Ferreira, F.F.; Miller, K. J.; Johnson, M.B.; White M. A. <i>Chem. Mater.</i> 2009 , 21, 2886-2894. Copyright 2009 American Chemical Society.....	110
Figure 5.2: DSC results for 4.826 mg of anhydrous $\text{Y}_2\text{Mo}_3\text{O}_{12}$ measured in a helium atmosphere from 103 K to 673 K with a heating rate of 10 K min^{-1} . The arrows indicate the direction of the scan, starting at room temperature. Reprinted with permission from Marinkovic, B. A.; Ari, M.; de Avillez, R.; Rizzo F.; Ferreira, F.F.; Miller, K. J.; Johnson, M.B.; White M. A. <i>Chem. Mater.</i> 2009 , 21, 2886-2894. Copyright 2009 American Chemical Society.....	111
Figure 5.3: TGA of a sample of $\text{Y}_2\text{Mo}_3\text{O}_{12}$ heated under argon to 400 K in order to determine the dehydrated mass of the sample.	112
Figure 5.4: Heat capacity data for $\text{Y}_2\text{Mo}_3\text{O}_{12}$ samples ranging in size from 4.9491 mg to 13.9403 mg from 2 K to 390 K Lower temperature samples were measured using Apiezon [®] T grease, ○, and higher temperature samples were measured using Apiezon [®] H grease, +. Samples required heating to 340 K prior to measurements to ensure sample dehydration, as explained in Section 5.4.2, therefore, the low-temperature Apiezon [®] N grease was unsuitable for measurements with this system. Reprinted with permission from Marinkovic, B. A.; Ari, M.; de Avillez, R.; Rizzo F.; Ferreira, F.F.; Miller, K. J.; Johnson, M.B.; White M. A. <i>Chem. Mater.</i> 2009 , 21, 2886-2894. Copyright 2009 American Chemical Society.	113

Figure 5.5: Lattice parameters of $Y_2Mo_3O_{12}$ vs. temperature. Standard uncertainties are included but are too small to be visible in the graphs. Reprinted with permission from Marinkovic, B. A.; Ari, M.; de Avillez, R.; Rizzo F.; Ferreira, F.F.; Miller, K. J.; Johnson, M.B.; White M. A. <i>Chem. Mater.</i> 2009 , <i>21</i> , 2886-2894. Copyright 2009 American Chemical Society.....	114
Figure 5.6: Temperature of the orthorhombic to monoclinic phase transitions in $A_2Mo_3O_{12}$ and $A_2W_3O_{12}$ as a function of the electronegativity of A^{3+} ions (Li-Xue scale). ³¹⁷ A dashed line is included at 1.340 on the Li-Xue scale, indicating the electronegativity of Y^{3+} . ³¹⁷	115
Figure 6.1: SEM image of $HfMgMo_3O_{12}$ showing the homogeneous particle morphology and excellent sintering between the grains. Reprinted with permission from Miller, K. J.; Johnson, M. B.; White, M. A.; Marinkovic, B. A. <i>Solid State Commun.</i> 2012 , <i>152</i> , 1748-1752. Copyright 2012 Elsevier.	121
Figure 6.2: The DSC scan for $HfMgMo_3O_{12}$ at a heating rate of 10 K min^{-1} (exotherm up) shows the phase transition with an enthalpy change of 0.27 kJ mol^{-1} at an onset temperature of 173 K. Reprinted with permission from Miller, K. J.; Johnson, M. B.; White, M. A.; Marinkovic, B. A. <i>Solid State Commun.</i> 2012 , <i>152</i> , 1748-1752. Copyright 2012 Elsevier.	122
Figure 6.3: XRPD patterns for $HfMgMo_3O_{12}$ showing the measured pattern in black, the fitted pattern in red, and the difference plot in green. Peaks from the sample holder are marked with an x, and * marks correspond to the regions of the new peaks associated with the low -temperature phase for $T = 180\text{ K}$ showing an excellent fit to the orthorhombic $Pnma$ space group. The inset shows the quality of fit at low angles. Adapted from Miller, K. J.; Johnson, M. B.; White, M. A.; Marinkovic, B. A. <i>Solid State Commun.</i> 2012 , <i>152</i> , 1748-1752. Copyright 2012 Elsevier.	123
Figure 6.4: XRPD patterns for $HfMgMo_3O_{12}$ showing the measured pattern in black. Peaks from the sample holder are marked with an x, and * marks correspond to the regions of the new peaks associated with the low-temperature phase for $T = 160\text{ K}$ which could not be fit as a single phase material and showed both $Pnma$ and $P2_1/a$ character. Tick marks correspond to the orthorhombic $Pnma$ peak positions. Adapted from Miller, K. J.; Johnson, M. B.; White, M. A.; Marinkovic, B. A. <i>Solid State Commun.</i> 2012 , <i>152</i> , 1748-1752. Copyright 2012 Elsevier.	124

- Figure 6.5: XRPD patterns for $\text{HfMgMo}_3\text{O}_{12}$ showing the measured pattern in black, the fitted pattern in red, and the difference plot in green. Peaks from the sample holder are marked with an x, and * marks correspond to the regions of the new peaks associated with the low-temperature phase for $T = 80$ K showing an excellent fit for the monoclinic $P2_1/a$ space group. The inset shows the quality of fit at low angles. Adapted from Miller, K. J.; Johnson, M. B.; White, M. A.; Marinkovic, B. A. *Solid State Commun.* **2012**, *152*, 1748-1752. Copyright 2012 Elsevier. 124
- Figure 6.6: Experimental heat capacity data for $\text{HfMgMo}_3\text{O}_{12}$ for two samples (Δ , 13.26 mg; \circ , 14.69 mg) showing an anomaly at $T \sim 175$ K. Reprinted with permission from Miller, K. J.; Johnson, M. B.; White, M. A.; Marinkovic, B. A. *Solid State Commun.* **2012**, *152*, 1748-1752. Copyright 2012 Elsevier. 126
- Figure 7.1: XRPD pattern for $\text{In}_2\text{Mo}_3\text{O}_{12}$ illustrating a Le Bail fit to (a) the monoclinic $P2_1/a$ space group at 298 K and (b) the orthorhombic $Pnca$ space group at 838 K; the measured pattern is in black, the fitted pattern is red, and the difference plot is green. The highlighted regions ($38^\circ < 2\theta < 42^\circ$ and $44^\circ < 2\theta < 48^\circ$) were excluded from refinement due to contributions from the platinum stage and the inset regions show the quality of the fitted patterns. 130
- Figure 7.2: The DSC scan for 12.54 mg $\text{In}_2\text{Mo}_3\text{O}_{12}$, during heating (—) and cooling (---), at a heating rate of 10 K min^{-1} (exotherm up) shows the phase transition with an enthalpy change of 3.2 kJ mol^{-1} at an onset temperature of 615 K. 132
- Figure 7.3: Experimental heat capacity data for $\text{In}_2\text{Mo}_3\text{O}_{12}$ for four samples (\circ , 9.94 mg; \diamond , 18.62 mg; Δ , 20.64 mg; \square , 24.26 mg) showing no thermal anomalies from 2 K to 300 K. 134
- Figure 8.1: XRPD pattern of $\text{In}(\text{HfMg})_{0.5}\text{Mo}_3\text{O}_{12}$ at $T = 298$ K, illustrating an excellent Le Bail fit to the monoclinic $P2_1/a$ space group; the measured pattern is in blue, the fitted pattern is red, and the difference plot is grey. The inset shows the quality of fit at high angles. 138
- Figure 8.2: XRPD pattern of $\text{In}_{1.5}(\text{HfMg})_{0.25}\text{Mo}_3\text{O}_{12}$ at $T = 298$ K, illustrating an excellent Le Bail fit to the monoclinic $P2_1/a$ space group; the measured pattern is in blue, the fitted pattern is red, and the difference plot is grey. The inset shows the quality of fit at high angles. 138
- Figure 8.3: FE-SEM secondary electron images showing homogeneous particle morphology and excellent sintering between the grains of (a) $\text{In}(\text{HfMg})_{0.5}\text{Mo}_3\text{O}_{12}$ and (b) $\text{In}_{1.5}(\text{HfMg})_{0.25}\text{Mo}_3\text{O}_{12}$ 139

Figure 8.4: Qualitative EDS spectra of (a) $\text{In}(\text{HfMg})_{0.5}\text{Mo}_3\text{O}_{12}$ and (b) $\text{In}_{1.5}(\text{HfMg})_{0.25}\text{Mo}_3\text{O}_{12}$ identifying the elemental compositions of the samples.	141
Figure 8.5: DSC thermograms for (a) $\text{In}(\text{HfMg})_{0.5}\text{Mo}_3\text{O}_{12}$ and (b) $\text{In}_{1.5}(\text{HfMg})_{0.25}\text{Mo}_3\text{O}_{12}$ during heating (—) and cooling (---), both at 10 K min^{-1} (exotherm up), showing phase transitions with enthalpy changes of 0.89 kJ mol^{-1} and 1.3 kJ mol^{-1} at onset temperatures of 425 K and 520 K respectively.	142
Figure 8.6: The T_{trs} for $\text{In}_2\text{Mo}_3\text{O}_{12}$, $\text{In}_{1.5}(\text{HfMg})_{0.25}\text{Mo}_3\text{O}_{12}$, $\text{In}(\text{HfMg})_{0.5}\text{Mo}_3\text{O}_{12}$, and $\text{HfMgMo}_3\text{O}_{12}$ in relation to the percentage of $\text{In}_2\text{Mo}_3\text{O}_{12}$ in the solid solutions.	143
Figure 8.7: Dilatometry results for $\text{In}(\text{HfMg})_{0.5}\text{Mo}_3\text{O}_{12}$ over two heating and cooling cycles showing the change in length with respect to the original length as a function of temperature for: —, the first heating cycle; ---, first cooling cycle; -•-, the second heating cycle; and --, the second cooling cycle.....	145
Figure 8.8: Dilatometry results for $\text{In}_{1.5}(\text{HfMg})_{0.25}\text{Mo}_3\text{O}_{12}$ over a heating and cooling cycles showing the change in length with respect to the original length as a function of temperature for: —, heating cycle; ---, cooling cycle.	146
Figure 8.9: Le Bail fit for the room-temperature powder X-ray diffractogram of $\text{In}(\text{HfMg})_{0.5}\text{Mo}_3\text{O}_{12}$. Inset (a) emphasizes the low-angle region and inset (b) illustrates the fit quality for the high-angle regions. Black crosses = experimental data, red line = fit, blue line = difference, black markers = Bragg positions. $\chi^2 = 2.27$	148
Figure 8.10: Powder X-ray diffraction contour plot covering $18^\circ \leq 2\theta \leq 21.5^\circ$ for $\text{In}(\text{HfMg})_{0.5}\text{Mo}_3\text{O}_{12}$. The dashed line indicates the monoclinic ($P2_1/a$) to orthorhombic ($Pnca$) phase transition temperature at 436 K. The Miller indices at the top of the figure refer to the orthorhombic phase (space group: $Pnca$). Intensities are indicated as contours in constant increments from blue (lowest intensity) to red (highest intensity).	149
Figure 8.11: Le Bail fit for $\text{In}(\text{HfMg})_{0.5}\text{Mo}_3\text{O}_{12}$ for 973 K powder X-ray diffractogram during heating. Black crosses = experimental data, red line = fit, blue line = difference, black markers = Bragg positions. $\chi^2 = 2.48$	150

- Figure 8.12: Formula unit volume (V/Z) evolution in (a) $\text{In}(\text{HfMg})_{0.5}\text{Mo}_3\text{O}_{12}$ and (b) $\text{In}_{1.5}(\text{HfMg})_{0.25}\text{Mo}_3\text{O}_{12}$. \bullet, \circ = heating, \bullet, \circ = cooling, \circ, \circ = monoclinic phase ($P2_1/a$), \bullet, \bullet = orthorhombic ($Pnca$) phase. The data show the large positive unit cell expansion for the monoclinic phases and almost zero expansion for the orthorhombic phases, with the structural phase transition between 423 K and 448 K and 505 K and 525 K, respectively. The inset in (a) shows the linear fits to the heating (red) and cooling (blue) for the orthorhombic phase over the temperature range from 498 K to 923 K. Note that V/Z for heating and cooling are the same within the uncertainty. 152
- Figure 8.13: The average intrinsic linear thermal expansion coefficients of the orthorhombic phases of $\text{HfMgMo}_3\text{O}_{12}$,¹⁹⁹ $\text{In}_2\text{Mo}_3\text{O}_{12}$ (643 K to 1033 K),¹⁹⁶ $\text{In}(\text{HfMg})_{0.5}\text{Mo}_3\text{O}_{12}$ (498 K to 923 K), and $\text{In}(\text{HfMg})_{0.5}\text{Mo}_3\text{O}_{12}$ (573 K to 973 K) in relation to the composition of $\text{In}_2\text{Mo}_3\text{O}_{12}$, where the dashed line indicates the rule of mixtures prediction. 154
- Figure 9.1: Experimental heat capacity data for $\text{HfMgMo}_3\text{O}_{12}$ for two samples (Δ , 13.26 mg; \circ , 14.69 mg) showing an anomaly at $T \sim 175$ K (from Chapter 6, Section 6.3.2). Reprinted with permission from Miller, K. J.; Johnson, M. B.; White, M. A.; Marinkovic, B. A. *Solid State Commun.* **2012**, *152*, 1748-1752. Copyright 2012 Elsevier. 158
- Figure 9.2: Experimental heat capacity data for $\text{In}_2\text{Mo}_3\text{O}_{12}$ for four samples (\circ , 9.94 mg; \diamond , 18.62 mg; Δ , 20.64 mg; \square , 24.26 mg) showing no thermal anomalies from 2 K to 300 K (from Chapter 7, Section 7.3.2). 158
- Figure 9.3: Heat capacity data for $\text{Y}_2\text{Mo}_3\text{O}_{12}$ samples ranging in size from 4.9491 mg to 13.9403 mg from 2 K to 390 K. Lower temperature samples were measured using Apiezon[®] T grease, \circ , and higher temperature samples were measured using Apiezon[®] H grease, +. Samples required heating to 340 K prior to measurements to ensure sample dehydration, as explained in Section 5.4.2, therefore, the low-temperature Apiezon[®] N grease was unsuitable for measurements with this system (From Chapter 5, Section 5.4.2). Reprinted with permission from Marinkovic, B. A.; Ari, M.; de Avillez, R.; Rizzo F.; Ferreira, F.F.; Miller, K. J.; Johnson, M.B.; White M. A. *Chem. Mater.* **2009**, *21*, 2886-2894. Copyright 2009 American Chemical Society. 159
- Figure 9.4: Experimental heat capacities for three samples of $\text{In}(\text{HfMg})_{0.5}\text{Mo}_3\text{O}_{12}$ (Δ , 16.10 mg; \circ , 9.34 mg; \square , 6.05 mg) showing no thermal anomalies from 2 K to 300 K. 160
- Figure 9.5: Experimental heat capacities for three samples of $\text{In}_{1.5}(\text{HfMg})_{0.25}\text{Mo}_3\text{O}_{12}$ (Δ , 7.33 mg; \diamond , 15.01 mg; \square , 15.89 mg) showing no thermal anomalies from 2 K to 400 K. 162

- Figure 9.6: Experimental heat capacities for $Y_2Mo_3O_{12}$ (\circ) and —, the constituent additivity heat capacity of $Y_2Mo_3O_{12}$ calculated from the weighted sums of - - -, $C_P(Y_2O_3)^{326}$ and - - $C_P(MoO_3)^{327}$ 163
- Figure 9.7: The constituent additivity heat capacities, —, calculated from the weighted heat capacities of; - • • -, $C_P(In_2O_3)^{328}$ - • -, $C_P(HfO_2)^{330}$ ••••, $C_P(MgO)^{329}$ and - - -, $C_P(MoO_3)^{327}$ compared to the experimental heat capacities for $HfMgMo_3O_{12}$ (\circ) (Chapter 6). Reprinted with permission from Miller, K. J.; Johnson, M. B.; White, M. A.; Marinkovic, B. A. *Solid State Commun.* **2012**, *152*, 1748-1752. Copyright 2012 Elsevier. 164
- Figure 9.8: The constituent additivity heat capacities, —, calculated from the weighted heat capacities of; - • • -, $C_P(In_2O_3)^{328}$ - • -, $C_P(HfO_2)^{330}$ ••••, $C_P(MgO)^{329}$ and - - -, $C_P(MoO_3)^{327}$ compared to the experimental heat capacities for $In_2Mo_3O_{12}$ (\circ) (Chapter 7). 165
- Figure 9.9: The constituent additivity heat capacities, —, calculated from the weighted heat capacities of; - • • -, $C_P(In_2O_3)^{328}$ - • -, $C_P(HfO_2)^{330}$ ••••, $C_P(MgO)^{329}$ and - - -, $C_P(MoO_3)^{327}$ compared to the experimental heat capacities for $In(HfMg)_{0.5}Mo_3O_{12}$ 165
- Figure 9.10: The constituent additivity heat capacities, —, calculated from the weighted heat capacities of; - • • -, $C_P(In_2O_3)^{328}$ - • -, $C_P(HfO_2)^{330}$ ••••, $C_P(MgO)^{329}$ and - - -, $C_P(MoO_3)^{327}$ compared to the experimental heat capacities for $In_{1.5}(HfMg)_{0.25}Mo_3O_{12}$ (\circ). 166
- Figure 9.11: The rule of mixtures heat capacity, —, calculated from the averaged heat capacities of - - -, $HfMgMo_3O_{12}$ and - - -, $In_2Mo_3O_{12}$ compared to the experimental heat capacities of $In(HfMg)_{0.5}Mo_3O_{12}$ for (a) $5\text{ K} < T < 265\text{ K}$ and (b) $5\text{ K} < T < 50\text{ K}$ 167
- Figure 9.12: The rule of mixtures heat capacity, —, calculated from the averaged heat capacities of, - - -, $HfMgMo_3O_{12}$ and - - -, $In_2Mo_3O_{12}$ compared to the experimental heat capacities of $In_{1.5}(HfMg)_{0.25}Mo_3O_{12}$ for (a) $15\text{ K} < T < 265\text{ K}$ and (b) $15\text{ K} < T < 50\text{ K}$ 168
- Figure 9.13: $C_P T^{-3}$ vs. $\log(T/K)$ for, Δ , $HfMgMo_3O_{12}$,¹⁹⁹ +, $In(HfMg)_{0.5}Mo_3O_{12}$; \diamond , $In_{1.5}(HfMg)_{0.25}Mo_3O_{12}$; \circ , $In_2Mo_3O_{12}$; \square , $Y_2Mo_3O_{12}$,³⁵ - - -, $Sc_2Mo_3O_{12}$ (Monoclinic at $T < 178\text{ K}$);⁷⁴ —, and sapphire.⁶⁸ 170
- Figure 9.14: Correlation of peak temperature of the low-temperature anomalous heat capacity with the average linear thermal expansion coefficients for the orthorhombic phases of $A_2Mo_3O_{12}$ materials (Table 9.1). Error bars for $\log(\text{Peak Position} / K)$ are too small to be visible. 172

Figure 9.15: The low temperature heat capacity of $\text{Y}_2\text{Mo}_3\text{O}_{12}$ (\circ) (Chapter 5) plotted as $C_p T^{-3}$ against T^2 to determine θ_D^e from the linear fit.....	173
Figure 9.16: The low temperature heat capacities of (a) $\text{HfMgMo}_3\text{O}_{12}$ (\circ) (Chapter 6), (b) $\text{In}_2\text{Mo}_3\text{O}_{12}$ (\circ) (Chapter 7), (c) $\text{In}(\text{HfMg})_{0.5}\text{Mo}_3\text{O}_{12}$ (\circ), and (d) $\text{In}_{1.5}(\text{HfMg})_{0.25}\text{Mo}_3\text{O}_{12}$ (\circ) plotted as $C_p T^{-3}$ against T^2 to determine θ_D^e from the linear fits.	173
Figure 9.17: Temperature dependence of the experimental thermal conductivity data for $\text{HfMgMo}_3\text{O}_{12}$ (\circ , A1; \diamond , A2; \square , A3; where samples are described in Table 9.3). Open symbols represent the experimental data and closed circles represent the corresponding fully densified data calculated using the Klemen's model. ³³¹ ...	176
Figure 9.18: Temperature dependence of the fully dense thermal conductivity of $\text{HfMgMo}_3\text{O}_{12}$ (\circ , A1; \diamond , A2; \square , A3; where samples are described in Table 9.3); - - - denotes the theoretical minimum thermal conductivity. Reprinted with permission from Miller, K. J.; Johnson, M. B.; White, M. A.; Marinkovic, B. A. <i>Solid State Commun.</i> 2012 , 152, 1748-1752. Copyright 2012 Elsevier.	177
Figure 9.19: Temperature dependence of the fully dense thermal conductivity $\text{In}(\text{HfMg})_{0.5}\text{Mo}_3\text{O}_{12}$ (\circ , B1; \diamond , B2; \square , B3; where samples are described in Table 9.3); - - - denotes the theoretical minimum thermal conductivity.	178
Figure 9.20: Temperature dependence of the fully dense thermal conductivity $\text{In}_{1.5}(\text{HfMg})_{0.25}\text{Mo}_3\text{O}_{12}$ (\circ , C1; \diamond , C2; \square , C3; where samples are described in Table 9.3); - - - denotes the theoretical minimum thermal conductivity.	178
Figure 9.21: Temperature dependence of the fully dense thermal conductivity $\text{In}_2\text{Mo}_3\text{O}_{12}$ (\circ , D1; \diamond , D2; \square , D3; where samples are described in Table 9.3); - - - denotes the theoretical minimum thermal conductivity.	179
Figure 9.22: Temperature dependence of the fully dense thermal conductivity of $\text{Y}_2\text{Mo}_3\text{O}_{12}$ (\circ , E1; \diamond , E2; \square , E3; where samples are described in Table 9.3); - - - denotes the theoretical minimum thermal conductivity.	179
Figure 9.23: Temperature dependence of the fully dense thermal conductivities of: Δ (A1, from Table 9.3), $\text{HfMgMo}_3\text{O}_{12}$; \circ (B2, from Table 9.3), $\text{In}(\text{HfMg})_{0.5}\text{Mo}_3\text{O}_{12}$; \diamond (C2, from Table 9.3), $\text{In}_{1.5}(\text{HfMg})_{0.25}\text{Mo}_3\text{O}_{12}$; and \square (D2, from Table 9.3), $\text{In}_2\text{Mo}_3\text{O}_{12}$, <i>i.e.</i> the highest thermal conductivity for each compound, scaled up to fully densified values.	181
Figure 9.24: Temperature dependence of the effective phonon mean free path of $\text{Y}_2\text{Mo}_3\text{O}_{12}$ from the average fully densified thermal conductivity data, \circ , and the minimum phonon mean free path κ_{min} , - - -	183

Figure 9.25: Temperature dependence of the effective phonon mean free path of $\text{HfMgMo}_3\text{O}_{12}$ calculated from the average fully densified thermal conductivity data, \circ , and the minimum phonon mean free path κ_{\min} , - - -. Reprinted with permission from Miller, K. J.; Johnson, M. B.; White, M. A.; Marinkovic, B. A. *Solid State Commun.* **2012**, *152*, 1748-1752. Copyright 2012 Elsevier. 184

Figure 9.26: Temperature dependence of the effective phonon mean free path of $\text{In}(\text{HfMg})_{0.5}\text{Mo}_3\text{O}_{12}$ calculated from the average fully densified thermal conductivity data, \circ , and the minimum phonon mean free path κ_{\min} , - - -. 184

Figure 9.27: Temperature dependence of the effective phonon mean free path of $\text{In}_{1.5}(\text{HfMg})_{0.25}\text{Mo}_3\text{O}_{12}$ calculated from the average fully densified thermal conductivity data, \circ , and the minimum phonon mean free path κ_{\min} , - - -. 185

Figure 9.28: Temperature dependence of the effective phonon mean free path of $\text{In}_2\text{Mo}_3\text{O}_{12}$ calculated from the average fully densified thermal conductivity data, \circ , and the minimum phonon mean free path κ_{\min} , - - -. 185

Figure 9.29: Temperature dependence of the effective phonon mean free path of: Δ , $\text{HfMgMo}_3\text{O}_{12}$; \circ , $\text{In}(\text{HfMg})_{0.5}\text{Mo}_3\text{O}_{12}$; \diamond , $\text{In}_{1.5}(\text{HfMg})_{0.25}\text{Mo}_3\text{O}_{12}$; and \square , $\text{In}_2\text{Mo}_3\text{O}_{12}$, and $+$, $\text{Y}_2\text{Mo}_3\text{O}_{12}$ calculated from the maximum fully densified thermal conductivity data for each sample. 186

ABSTRACT

The $A_2\text{Mo}_3\text{O}_{12}$ family, where A^{3+} is a large trivalent cation, can show interesting thermal properties such as negative thermal expansion, also known as thermomiotic behavior, where the overall volume of the material contracts with increasing temperature. A selection of compounds in this family, namely $\text{HfMgMo}_3\text{O}_{12}$, $\text{In}_2\text{Mo}_3\text{O}_{12}$, $\text{Y}_2\text{Mo}_3\text{O}_{12}$, $\text{Al}_2\text{Mo}_3\text{O}_{12}$, $\text{In}(\text{HfMg})_{0.5}\text{Mo}_3\text{O}_{12}$, and $\text{In}_{1.5}(\text{HfMg})_{0.25}\text{Mo}_3\text{O}_{12}$, have been synthesized using solid-state and mechanical activation techniques as well as a simplified sol-gel approach ($\text{Al}_2\text{Mo}_3\text{O}_{12}$). Coefficients of thermal expansion were found to range from large-negative to low-positive in the orthorhombic phase, including near-zero in $\text{In}(\text{HfMg})_{0.5}\text{Mo}_3\text{O}_{12}$ and $\text{In}_{1.5}(\text{HfMg})_{0.25}\text{Mo}_3\text{O}_{12}$. This set of materials provided insight into the role of low-frequency phonon modes in open-framework materials. Low-temperature heat capacity and thermal conductivity measurements confirmed that low-frequency modes were active in thermomiotic materials, and also present to some extent in all members of the open-framework $A_2\text{Mo}_3\text{O}_{12}$ family examined. A clear correlation exists between the magnitude and sign of the coefficient of thermal expansion in the orthorhombic phase and the contribution of low-energy modes to the low-temperature heat capacity, with negative thermal expansion materials having a larger contribution. The low-frequency phonon modes result in low thermal conductivity and reduced phonon mean free paths when compared to conventional ceramics and indicate that these low values are characteristic of open-framework materials in NTE families even if the materials in the families are not thermomiotic themselves.

LIST OF ABBREVIATIONS AND SYMBOLS USED

PTE	positive thermal expansion
NTE	negative thermal expansion
CTE	coefficient of thermal expansion
α_ℓ	(linear) coefficient of thermal expansion along direction ℓ
α_V	volume coefficient of thermal expansion
T	temperature (in K)
V	volume
U	interatomic potential
r	interatomic distance
F	interatomic force
S	entropy
χ_T	isothermal compressibility
P	pressure
B	bulk modulus
E	Young's modulus
ν	Poisson's ratio
R_s	thermal shock resistance
κ	thermal conductivity
σ	material strength
γ	(bulk) Grüneisen parameter
γ_i	Grüneisen parameter of the i^{th} mode
ω_i	frequency of the i^{th} mode
V_m	molar volume
C_V	heat capacity at constant volume
RUM	rigid-unit mode
C	heat capacity
C_P	heat capacity at constant pressure

ν_E	Einstein frequency
ν_D	Debye (cut-off) frequency
N	number of atoms in a unit cell
R	molar gas constant
θ_D^{eff}	effective Debye temperature
θ_D	Debye temperature
h	Planck's constant
k_B	Boltzmann's constant
v_s	speed of sound
ρ	density
λ	phonon mean free path
DOS	density of states
IR	infrared
T_{trs}	transition temperature
LAS	lithium aluminum silicate
MEMS	microelectromechanical systems
D	coefficient of diffusion
EDTA	ethylene diamine tetraacetic acid
PVA	polyvinyl alcohol
Q	scattering vectors
TSPDF	total-scattering pair-distribution function
ΔL	change in sample length
L_0	original sample length
LVDT	linear variable differential transformer
MFI	mordenite framework inverted
ZSM5	$\text{Na}_n\text{Al}_n\text{Si}_{96-n}\text{O}_{192} \cdot 16\text{H}_2\text{O}$ ($0 < n < 27$)
AIPO	aluminophosphate
INS	inelastic neutron scattering
NaSICON	sodium super-ionic conductor

MOF	metal-organic framework
NZP	$\text{NaZr}_2(\text{PO}_4)_3$
T_N	Néel temperature
SSR	solid-state reaction
MA	mechanical activation
XRPD	X-ray powder diffraction
TGA	thermogravimetric analysis
SEM	scanning electron microscopy
FE-SEM	cold-field emission scanning electron microscopy
EDS	energy-dispersive spectrometer
TEM	transmission electron microscopy
SDT	simultaneous DSC-TGA
DSC	differential scanning calorimetry
LNCS	liquid nitrogen cooling system
FACS	forced air cooling system
χ^2	goodness of fit
LHPM	Lucas Heights Research Laboratories
y_{ib}	background intensity
B_m	background parameters ($m = 1$ to 6)
I_k	intensity of the k^{th} Bragg diffraction
y_{ic}	net intensity at point i
G_{ik}	peak profile function
k_1 and k_2	reflections
p	phases in the sample
S_f	scalar factor
M_k	multiplicity
L_k	Lorentz-polarization
P_k	effects of preferred orientation
A_k	correction of absorption

E_k	correction for extinction
F_k	structure factor
γ_m	mixing parameter
H_k	full-width at half maximum of the k^{th} Bragg reflection
FWHM	full-width at half maximum
U_b	broadening parameter due to strain
V_b and W_b	broadening parameters
R -factors	reliability factors
R_{wp}	weighted R -factor
y_{io}	observed net intensity
δy_{io}	the uncertainty in y_{io}
R_p	profile R -factor
R_{exp}	expected R -factor
P_a	number of adjusted parameters
R_B	Bragg R -factor
I_o	observed intensity
I_c	calculated intensity
w_c	weight of the net intensity
$A_1(obs)$	observed intensity
$A_2(obs)$	observed intensity
$obs(i)$ - $back(i)$	the observed peak contributions
PPMS	physical property measurement system
q	heat
\dot{q}	power
t	time
T_0	temperature of thermal bath
T_p	platform temperature
T_b	puck frame temperature
K_w	thermal conductance of supporting wires

$\dot{q}(t)$	heater power
$C_{platform}$	heat capacity of the platform
C_{sample}	heat capacity of the sample
K_g	thermal conductance due to grease
T_s	sample temperature
A_c	cross-sectional area
L	length
ΔT_∞	steady-state temperature differential
K	thermal conductance
TTO	thermal transport option
T_{hot}	temperature at the hot thermometer
T_{cold}	temperature at the cold thermometer
ΔT_{OFF}	temperature difference in the off state
ΔT_{ON}	temperature difference in the on state
τ_1 and τ_2	estimated time constants
ΔT_m	modeled temperature rise
$\Delta T_{m, heating}$	modeled T response during the heating cycle
$\Delta T_{m, cooling}$	modeled T response during the cooling cycle
K_{tot}	total thermal conductance
P_{rad}	radiative heat loss
S_A	total surface area
σ_T	Stefan–Boltzmann constant
$T_{hot/cold}$	average temperatures of the hot and cold thermometers
ε	emissivity
K_{sample}	thermal conductance of the sample
K_{shoes}	thermal conductance of the leads and the shoe assembly
PLZT	lanthanum modified lead zirconate titanate
TG/DTG	thermogramvmetric / differential thermogravimetric analysis
LNLS	Brazilian Synchrotron Light Laboratory

HRXRPD	high-resolution X-ray powder diffraction
$\Delta_{\text{trs}}H$	enthalpy of transition
$\Delta_{\text{trs}}S$	entropy of transition
$\Delta\alpha_{\text{max}}$	thermal expansion anisotropy
ZTE	zero thermal expansion
v^{eff}	average effective speed of sound
κ_{min}	minimum thermal conductivity
n	number density
v_{m}	mean speed of sound
κ_m	scaled up thermal conductivity
f	volume fraction

ACKNOWLEDGEMENTS

I would like to extend sincere gratitude to my supervisor, Dr. Mary Anne White, for her guidance and support during the course of my PhD. A supervisor undoubtedly finds that they must wear many hats, those of a friend, teacher, advisor, and critic. Finding a balance between those aspects cannot be easy, and I credit Dr. Mary Anne White with shaping the best aspects of my abilities as a researcher. My gratitude also extends to Dr. Jeff Dahn, Dr. Bojan Marinkovic, Dr. Mario Bieringer, and Andy George for their assistance and training with regards to X-ray diffraction. I would also like to thank the members of my committee, Dr. Jeff Dahn, Dr. Peng Zhang and Dr. Josef Zwanziger, for their guidance and to my external examiner, Dr. Cora Lind-Kovacs, as well as the members of the Dr. Mary Anne White research group, past and present, Dr. Andrew Ritchie, Dr. Michael Jakubinek, Jan Pöhls, Alex Bourque, Louis Desgrosseilliers, Paul Allred, Adam Bent, John Niven, Philippe Tremblay, Patrick Murray, Herman Stubeda, Eileen Burns, Craig Bryan, Dr. Ran Chen, Alex Safatli, Lauren Bilinsky, Patrick Murray, and Hong Tang. In addition I would also like to thank Michel Johnson, Carl Romao, Dr. Cathy Kennedy, Mike Boutilier, Richard Conrad, Patricia Scallion, Kevin Borgel, John Noodin, Todd Carter, Dr. Ulrike Werner-Zwanziger, Dr. Heather Andreas, and Dr. Mark Obrovac for advice and instrumental and technical support as well as Cheryl Coolen, Giselle Andrews, Sean Hartwell, Cheryl Stanton, and Deanna Wentzell for administrative support.

A special thank you is extended to Dr. Bojan Marinkovic, Prof. Fernando Rizzo, Dr. Monic Ari, and Luciana Prisco in Brazil. Not only were they exceptional collaborators, but they made my research trips to Brazil a pleasure and went beyond what could ever be expected as hosts. My gratitude is also extended to my other collaborators, Dr. Paula Jardim, Dr. Roberto de Avillez, Dr. Fabio Ferreira.

I would also like to thank my parents, Douglas and Barbara Miller; my sister, Jennifer Miller; and Andrea Pemberton for their unwavering support during my most trying times. Eric Lowther, Gavin Heverly-Coulson, Anthony Cerqueira, Matt Hume, Jack Tsao, Joel Slade, Sarah Rose (Skipper), Derek Rose and Cassandra Armsworthy are also thanked for their friendship and support. Without my family and friends to stand beside me I would not have made it this far.

CHAPTER 1 INTRODUCTION

Materials research is a broad field of study drawing together many disciplines in order to develop an understanding of interconnected relationships between structure, processing, performance, and properties (Figure 1.1). These components are inherently mingled and it is important for material design and development to understand their relationships. This work is primarily focused on the relationship between the structure and properties of materials with low or negative thermal expansion in order to develop a more complete understanding of the mechanisms that give rise to thermomiotic behavior (also known as negative thermal expansion) and its role in other properties of materials.

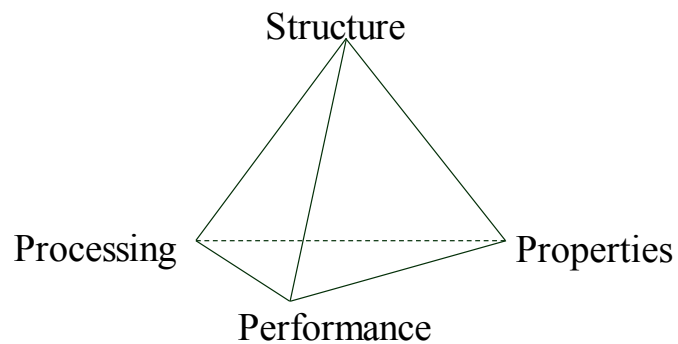


Figure 1.1: A graphical depiction of the relationship between structure, processing, properties, and performance in materials science.

1.1 NEGATIVE THERMAL EXPANSION (THERMOMIOTIC) MATERIALS*

1.1.1 WHY THERMOMIOTIC MATERIALS ARE INTERESTING

Most materials change their dimensions when the temperature changes. Usually, the dimensions increase with increasing temperature, and this property is referred to as positive thermal expansion (PTE). The thermally induced change in dimension of a material in a confined environment can lead to significant stress. If the stress exceeds the strength of the material when a thermal gradient is applied, the material will shatter, quite possibly with disastrous consequences.

On the other hand, some materials shrink with increasing temperature, giving rise to negative thermal expansion (NTE). Here the term *thermomiotic* (from the Greek, "thermo" for "heat" and "mio" for "contract") is introduced to describe such materials. The excitement about thermomiotic materials is that, in principle, they could compensate for positive thermal expansion, presenting materials that would not experience thermal stress fracture.

Some materials exhibit thermomiotic behavior only in certain directions, making the overall thermal expansion positive or negative. However, the most interesting materials exhibit NTE in all directions. In some cases this is an intrinsic property associated with the composition and the particular structure. Exposure of the relationship between structure and NTE is the main purpose of this chapter.

* Sections 1.1 to 1.8 were adapted from: Romao, C.P.; Miller, K. J.; Whitman, C.A.; Marinkovic, B. A.; White M. A. White, M. A. *Negative Thermal Expansion (Thermomiotic) Materials*, in press in *Concepts In Inorganic Chemistry*; Elsevier, **2012**. K. J. Miller's contributions to the work in this chapter were: drafting the chapter outline and writing sections labeled here as: 1.1, 1.3, 1.5.2.1 and 1.8; modifying Sections 1.6.1.7, 1.6.2 and 1.6.3; and collaborating on the other sections and general editing. The review chapter has been edited and adapted from the original version to fit the context of this thesis.

Here, the general principles and mechanisms for thermal expansion will be introduced, first for PTE materials, and then for NTE materials. This is followed by a presentation of the relationship between NTE and other properties as well as an overview of the current uses of thermomiotic materials and criteria for their further applications. The current methods to synthesize thermomiotic materials and the methods used to examine their NTE and related properties are summarized. The chapter is concluded with categories of thermomiotic materials according to their structure (pure materials, solid solutions and composites), and a look at future research directions and the goals of this thesis. While an effort has been made to include all relevant background information and areas of research to this work, further information, which may be of interest to the readers, can be found in reviews of negative thermal expansion materials,^{1,2,3,4,5,6,7,8} including patents.⁹

1.1.2 THERMAL EXPANSION AND MECHANICAL PROPERTIES OF MATERIALS

The coefficient of thermal expansion, generally abbreviated as α and also called CTE, can be defined in a particular direction, ℓ , as:¹⁰

$$\alpha_{\ell} = \frac{1}{\ell} \left(\frac{\partial \ell}{\partial T} \right)_P, \quad (1.1)$$

where, for example, ℓ , could be one of the principal crystallographic directions (a , b or c , giving α_a , α_b and α_c , respectively), and T is temperature. The volumetric coefficient of thermal expansion, α_V , is:

$$\alpha_V = \frac{1}{V} \left(\frac{\partial V}{\partial T} \right)_P, \quad (1.2)$$

where V is the volume. Note that both α_ℓ and α_V are intrinsic to a given material at a given temperature, and independent of the material's size. Both α_V and the directional values of α have units of K^{-1} , but it is important to distinguish the type of CTE. If the material is cubic, $\alpha_V = 3\alpha_a$, but for less symmetric structures the relationship is not so simple. Indeed, the α values in different directions could have different signs making α_V close to zero.

By far the majority of materials, regardless of phase, have positive coefficients of thermal expansion; examples are presented in Table 1.1.

Table 1.1: Average linear coefficients of thermal expansion (α_ℓ) for selected materials given at either a single temperature or over a temperature range.

Material	T / K	$\alpha_\ell / \text{K}^{-1}$
Silicon ¹¹	239.15	2.5×10^{-6}
Mercury ¹²	295	18×10^{-6}
Gold ¹³	283 – 338	13×10^{-6}
Silver ¹³	283 – 338	19×10^{-6}
Diamond ¹⁴	194 – 273	0.58×10^{-6}
Diamond ¹⁴	273 – 296	0.97×10^{-6}
Copper ¹⁵	295	17×10^{-6}
Copper ¹⁵	120	12×10^{-6}
Rock salt ¹⁵	300	40×10^{-6}
Rock salt ¹⁵	85	23×10^{-6}
Ice ¹⁶	45	-5×10^{-6}
Ice ¹⁷	73	0.8×10^{-6}
Ice ¹⁷	273.15	53×10^{-6}

In the case of solids, the primary focus of this study, the increase in volume can be most readily understood in terms of the potential energy diagram and the interatomic forces.

A typical diagram for an interatomic potential (U as a function of interatomic distance, r ; see Figure 1.2) is well-represented by a harmonic potential at low energy (near the bottom of the well), but deviates significantly from harmonicity when there is sufficient thermal energy. The average interatomic distance, $\langle r \rangle$, depends on the temperature and, for a true anharmonic potential, it increases with increasing thermal energy (*i.e.*, with height above the well minimum), as shown in Figure 1.2. This contrasts with the harmonic potential which shows $\langle r \rangle$ to be independent of temperature, giving $\alpha = 0 \text{ K}^{-1}$. Therefore, in general terms, the deviation of the CTE from zero is a measure of the anharmonic interactions in the interatomic potential.¹⁸

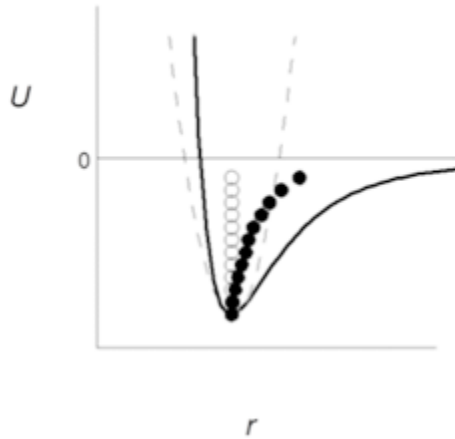


Figure 1.2: Potential energy (U) as a function of intermolecular separation (r) for a harmonic system (potential given by - - and average positions at different temperatures, $\langle r \rangle$, given by \circ) and an anharmonic system (potential given by — and $\langle r \rangle$ given by \bullet).

A few consequences based on Figure 1.2 are worth highlighting. One is that as $T \rightarrow 0$ K, the true potential approaches the harmonic potential and $\alpha \rightarrow 0$ K⁻¹. This is true for virtually all materials.

Another consequence concerns the relationship between the interatomic force, F , and the interatomic potential, U , given in general by:

$$F = - \left(\frac{\partial U}{\partial r} \right). \quad (1.3)$$

Since stronger interatomic forces lead to steeper potentials, stiffer materials tend to have smaller CTEs. Conversely, if the interatomic potential is weak then there will be a larger CTE. Our focus here is on inorganic materials, and generally their CTEs are smaller at a given temperature than those of organic materials or polymers.

Equation (1.2) can be re-written using a Maxwell relation, as:⁴

$$\alpha_V = \chi_T \left(\frac{\partial S}{\partial V} \right)_T, \quad (1.4)$$

where S is the entropy and χ_T is the isothermal compressibility ($= -V^{-1} (\partial V / \partial P)_T$, where P is pressure). Normally, entropy decreases with compression, but for most NTE materials, entropy increases when the volume drops.⁴ This point is taken up later in subsequent discussion.

The CTE of a material can have far reaching implications for applications since it is intrinsically tied to the other elastic properties of material, such as the bulk modulus,

$B (= \chi_T^{-1})$:¹⁹

$$B = \frac{E}{3(1-2\nu)}, \quad (1.5)$$

where E is the Young's modulus (also known as elastic modulus), a measure of a material's stiffness, and ν is Poisson's ratio, the negative of the ratio of lateral to

longitudinal strain in a material when a uniaxial tensile stress is applied. While the CTE quantifies the change in dimension with temperature, the Young's modulus and Poisson's ratio quantify the resistance to change of shape in extension or compression, and the bulk modulus represents a material's ability to resist changes in volume.

The elastic properties can be related to the CTE as a measure of a material's thermal shock resistance coefficient (R_s) which for a homogenous isotropic material can be expressed as:¹⁸

$$R_s = \frac{\kappa\sigma}{|\alpha_v|E}, \quad (1.6)$$

where κ is the thermal conductivity and σ is the material strength. The R_s value is useful to evaluate how a material will perform under thermomechanical stress.²⁰ From equation (1.6) it can be easily visualized that if the CTE of a material approaches zero, the ability of that material to withstand thermal shock will be increased.

1.2 MECHANISMS OF NEGATIVE THERMAL EXPANSION

Several different structural and dynamical thermomechanical mechanisms have been elucidated, although not all of the different mechanisms for negative expansion are fully understood for all of the systems in which NTE occurs. This section describes many of these mechanisms, starting with a description of lattice vibrations.

1.2.1 LATTICE VIBRATIONS

A phonon is a quantized lattice vibration in a crystal. The lattice waves can be along the propagation direction (longitudinal phonons) or across it (transverse phonons). A simple three-atom view of a metal-oxygen-metal ($M-O-M$) linkage is shown in Figure 1.3. With increasing temperature, the length of the $M-O$ bond increases due to normal (positive) thermal expansion. However, the average $M-M$ distance can decrease due to transverse vibrations as the bridging oxygen in the $M-O-M$ unit vibrates with increasing amplitude.

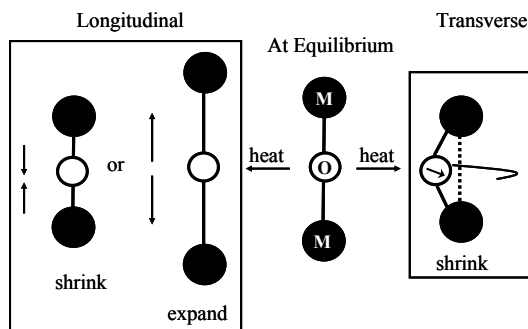


Figure 1.3: Longitudinal vibrations could lead to compression or expansion of the $M-O-M$ linkage while transverse vibrations would lead to compression. Adapted from Evans.²¹

In a three-dimensional solid with oxygen-connected rigid polyhedra, the transverse vibration of the $M-O-M$ unit will result in coupled rocking motion of the polyhedra. If the polyhedra must rotate in a cooperative manner without much distortion of the polyhedral units, NTE can result. This is an example of $(\partial S/\partial V)_T < 0$ as discussed in Section 1.1.2.

Librational (*i.e.*, rocking) vibrations in rigid bonds can lead to a decrease in the perceived atomic bond length from diffraction studies relative to true bond length.⁶

Figure 1.4 shows a schematic of the effect of libration on a $M-O$ bond. Strong librational

modes can accompany transverse vibrations and contraction in bonds. The decrease in perceived bond length of Si-O in zeolites as temperature is increased can result in very negative apparent thermal expansion coefficients.⁶

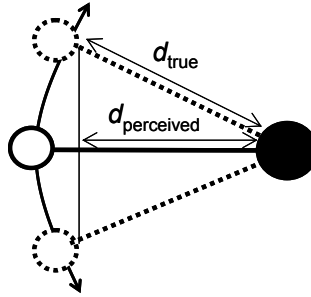


Figure 1.4: Librational vibrations show that the perceived distance of the M - O bond decreases as the magnitude of the vibration increases. Styled after reference 6.

Recall that positive thermal expansion is a result of the anharmonic nature of bonds (Section 1.1.2). Quantification of the anharmonicity in a solid can be achieved with the Grüneisen parameter, γ .

The mode-dependent Grüneisen parameter can be defined for a phonon mode i in terms of the frequency of that mode ω_i :²²

$$\gamma_i = -\left(\frac{\partial \ln \omega_i}{\partial \ln V}\right), \quad (1.7)$$

and it can be determined directly by high-pressure spectroscopic measurements. For a harmonic solid, ω_i is independent of volume so $\gamma_i = 0$ for all modes. Any deviation from zero in the Grüneisen parameter will therefore be an indication of the anharmonic interactions in the solid: the larger the magnitude, the larger the degree of anharmonicity. At low temperatures, as a consequence of increased harmonicity, $\gamma_i \rightarrow 0$ as $T \rightarrow 0$ K.

The bulk Grüneisen parameter, γ , is defined as the weighted averages of γ_i ,

$$\gamma = \frac{\sum_i \gamma_i C_{V,i}}{\sum_i C_{V,i}}, \quad (1.8)$$

where $C_{V,i}$ are the partial vibrational mode contributions to the heat capacity. The bulk Grüneisen parameter is related to other thermodynamic parameters as a function of temperature through:²²

$$\gamma = \frac{\beta_T V_m \alpha_V}{C_V}, \quad (1.9)$$

where B_T is the isothermal bulk modulus, V_m is the molar volume and C_V is the constant volume heat capacity. Equation (1.9) yields an averaged γ for all of the modes at the temperature being probed. Since C_V and V_m have positive values, and B_T is usually positive (although there are exceptions^{23,24}), usually the signs of the Grüneisen parameter and the CTE are the same (*i.e.*, both negative for NTE).

1.2.2 RIGID UNIT MODES (RUMs)

The rigid-unit mode (RUM) model states that when the temperature of a framework solid increases, linked rigid polyhedra will rock without being distorted and thus give rise to transverse vibrations perpendicular to the $M-O-M$ linkage axis.^{25,26} Generally, the associated potential is shallow and the vibrations can be excited even at low temperatures. $M-O-M$ linkage distortion requires less energy than distortion of the rigid polyhedra, so the framework shrinkage overrides the positive thermal expansion within the polyhedra and gives rise to thermomiotic behavior.

The RUM model was originally developed to describe the behavior of a large class of materials with the motif of vertex-linked polyhedra.²⁶ The applications of this model include interpretation of the nature of high-temperature phases²⁶ and linking the magnitude of the transition temperature to the polyhedral stiffness.^{27,28,29} The RUM model also has been used to provide insight into the stability and physical properties of framework silicates.^{29,30} In 1998, researchers used the RUM model to explain NTE in β -quartz³¹ and the extensive NTE (average $\alpha_a = -9 \times 10^{-6} \text{ K}^{-1}$ from 0.3 K to 1050 K)³² in ZrW_2O_8 .^{25,33} In certain systems, the polyhedral rotations give rise to small distortions in the polyhedra. These are said to be quasi-RUMs, and occur, for example, in the AM_2O_7 ³⁴ and $A_2M_3O_{12}$ ³⁵ families.

A detailed investigation by Tao and Sleight considered the correlation between RUMs and thermomiotic behavior for a series of framework oxides.³⁶ They used a computer program developed by Hammonds *et al.*,³⁷ to determine whether RUMs exist in the dynamical structure of oxides, and found that some oxides show RUMs but NTE is not observed. For example, in ReO_3 , RUMs exist for all wave vectors corresponding to rocking motion, but ReO_3 might have small, positive thermal expansion (see Section 1.6.1.5). It also was shown that strong NTE exists without RUMs. A large family of thermomiotic materials is the tungstates and molybdates of the general formula $A_2M_3O_{12}$ where the A and M cations are coordinated by oxygen octahedrally and tetrahedrally, respectively.³⁸ Orthorhombic $\text{Sc}_2\text{W}_3\text{O}_{12}$, $\text{Lu}_2\text{W}_3\text{O}_{12}$ and $\text{Y}_2\text{W}_3\text{O}_{12}$ are members of this family of oxides and all exhibit strong, anisotropic NTE over a large temperature range. However, these compounds do not have RUMs. The NTE in this family can still be understood in terms of the transverse vibrations and tilting of the essentially rigid

polyhedra.³⁸ Tao and Sleight's study concluded that although in some oxides the presence of RUMs is accompanied by NTE, there is no simple and/or direct correlation between the presence or absence of RUMs and the thermal expansion properties. In general, having one does not predict the other.

$\text{Zn}(\text{CN})_2$ has a negative CTE that is almost twice the magnitude of ZrW_2O_8 .³⁹ This material (and other similar materials) has linear metal–cyanide–metal ($M\text{--C--N--}M$) linkages which allow for a larger number of low-energy rigid-unit phonon modes, more than for $M\text{--O--}M$ linkages. This is attributed to the additional atoms in the linkages, allowing each rigid unit to rotate independently, and therefore the structure possesses RUMs at a wide range of wave vectors.³⁹

1.2.3 MACROSCOPIC NEGATIVE THERMAL EXPANSION

Thermomiotic behavior is inherently a structural phenomenon as is illustrated by the creation of macroscopic objects which possess NTE in two^{40,41,42,43} or three⁴⁴ dimensions, despite being made entirely of PTE materials. These constructs are composed of components (typically rods), arranged in a geometry which leads to NTE. These geometries generally involve expansion that causes the structure to bend into empty space, reducing the volume.^{40,41,42,44} Again, $(\partial S/\partial V)_T < 0$. The principles used in the development of these macrostructures can inform the design of micro- or nanostructures which enhance NTE, or even the development of new thermomiotic chemistries. For example, a 3D thermomiotic macrostructure could potentially be replicated chemically by replacing rods of different materials with organic linkages of different bond harmonicity.⁴⁴

1.2.4 OTHER NEGATIVE THERMAL EXPANSION MECHANISMS

The mechanisms already described show that NTE can arise due to unusual vibrations in the lattice. Unusual thermal expansion effects also can arise due to non-vibrational effects.

For example, Invar is an alloy ($\text{Fe}_{65}\text{Ni}_{35}$) that is considered to have zero thermal expansion at room temperature. Its low thermal expansion behavior arises due to magnetostriction.²¹

Perovskite materials can be thermomiotic and this property has been attributed to spontaneous polarization displacement of cations,⁴⁵ intermetallic or intersite charge transfer.^{46,47} Anti-perovskite manganese nitrides exhibit NTE due to a large magnetovolume transition over a broad temperature range.^{48,49}

Recently the NTE in the layered planes of crystalline TlGaSe_2 was attributed to negative area compressibility.⁵⁰ Further, thermomiotic behavior in TlGaSe_2 can be altered by illumination, external electric field and thermal annealing.⁵⁰

Negative or near-zero thermal expansion over a smaller temperature range also can arise from phase transitions; examples include $\text{Ca}_2\text{Ru}_{1-x}\text{Cr}_x\text{O}_4$,^{51,52} and BiNiO_3 .⁴⁶

1.3 NEGATIVE THERMAL EXPANSION AND ITS RELATIONSHIP TO OTHER PROPERTIES

The mechanisms that give rise to thermomiotic behavior can lead to interesting features and anomalies in other properties of materials, particularly in areas where the vibrational modes that give rise to NTE play an important role.

In insulating solids, which includes most thermomiotic materials, heat is carried primarily by acoustic phonons, and a direct relationship between thermal properties and NTE can be expected, as will be explored further in the following sections.

1.3.1 HEAT CAPACITY AND RELATED PROPERTIES

The heat capacity of a material, C , can be expressed under either constant volume, C_V , or constant pressure, C_P . The theoretical value is usually C_V whereas the experimental value is usually C_P .⁵³ If the system is isotropic, then C_V and C_P are related as:¹⁸

$$C_P - C_V = \frac{\alpha_V^2 TV}{\chi_T}. \quad (1.10)$$

For anisotropic systems it is necessary to consider the thermal expansion tensors and the elastic constants of the material.^{19,54}

Theoretical models of heat capacity can be useful to gain atomic-level insight. The two most important models are attributed to Einstein and Debye. The Einstein model considers each atom to be vibrating as an independent harmonic oscillator; if monatomic, they all have the same frequency, ν_E , the Einstein frequency. The Debye model considers a distribution of frequencies up to a maximum (cut-off) frequency, ν_D , the Debye frequency, which is more representative of the true lattice dynamics for monatomics. In more complex solids, with N atoms per unit cell, there are 3 acoustic modes which can be well represented by the Debye model, and the remaining $(3N-3)$ optic modes can be represented by the Einstein model.^{18,55} At very high temperatures, all modes are fully excited and C_V approaches the Dulong-Petit limit of $3NR$, where R is the molar gas constant.⁵⁶ However, as T drops, insights can be gained concerning lattice dynamics.

One common approximation, which does not apply if the optic modes are in the range of the acoustic modes, is to assume the entire lattice to be Debye-like and use low-temperature heat capacity data to quantify the lattice stiffness *via* an effective Debye temperature, θ_D^{eff} . (This is "effective" because the true Debye temperature [= $h\nu_D/k_B$ where h is Planck's constant, and k_B is Boltzmann's constant] would require accounting for the optic mode contribution by the Einstein model.) The value of θ_D^{eff} can be determined from:

$$\lim_{T \rightarrow 0} C_V = \frac{12}{5} \pi^2 N k_B \left(\frac{T}{\theta_D^{\text{eff}}} \right)^3 + O(T^5) + \dots, \quad (1.11)$$

where the higher-order terms are negligible at very low temperature. Values of θ_D^{eff} (or θ_D in the case of monatomics) and CTE values for selected materials are given in Table 1.2. The (true or effective) Debye temperature for NTE materials generally is lower than for PTE materials. This is due to the flexibility in the framework structures that give rise to NTE. The speed of sound of a material, v_s , is directly proportional to θ_D and v_s is related to the Young's modulus by:¹⁸

$$v_s = \sqrt{\frac{E}{\rho}}, \quad (1.12)$$

where ρ is the density of the material. Therefore, Young's moduli, speeds of sound and Debye temperatures for NTE materials are all characteristically lower than more conventional materials.

Table 1.2: The Debye (or effective Debye) temperature for selected solids and the corresponding CTE.

Material	θ_D / K	α_t / K^{-1}
ZrW ₂ O ₈	88 ⁵⁷	-8.7×10^{-6} (0.3 K to 693 K) ⁵⁸
ZrO ₂	590 ⁵⁹	10×10^{-6} (298.15 K to 1673.15 K) ⁶⁰
Diamond	2230 ⁶¹	1.1×10^{-6} (300 K) ⁶²
Gold	165 ⁶³	14×10^{-6} (300 K) ⁶³
Copper	343 ⁶³	17×10^{-6} (300 K) ⁶³

The temperature-dependence of the heat capacity can reveal information concerning unusual lattice dynamics in a material. Often, heat capacity of a material can be accurately predicted to within a few percent by the stoichiometric addition of the heat capacities of its solid elements, or from its constituent oxides. For instance the heat capacity of sodalite, Na₈Al₆Si₆O₂₄Cl₂, can be represented within a few per cent between $T = 100 \text{ K}$ and 1000 K by the heat capacity sum $3 C_P(\text{Na}_2\text{O}) + 3 C_P(\text{Al}_2\text{O}_3) + 6 C_P(\text{SiO}_2) + 2 C_P(\text{NaCl})$.⁶⁴ Fundamentally, this is because the atomic mass is the primary determinant of the lattice dynamics. However, for NTE materials, such a constituent additivity model can significantly underestimate the heat capacity, due in part to the open framework lattice and also because of low-frequency modes that give rise to NTE.^{65,66} The latter can be seen more explicitly in a plot of $C_P T^{-3}$ as a function of T (Figure 1.5). Equation (1.11) indicates that a normal lattice should have a small T^2 dependence in this region, but thermomiotic materials show an anomalous contribution due to additional low-frequency modes.

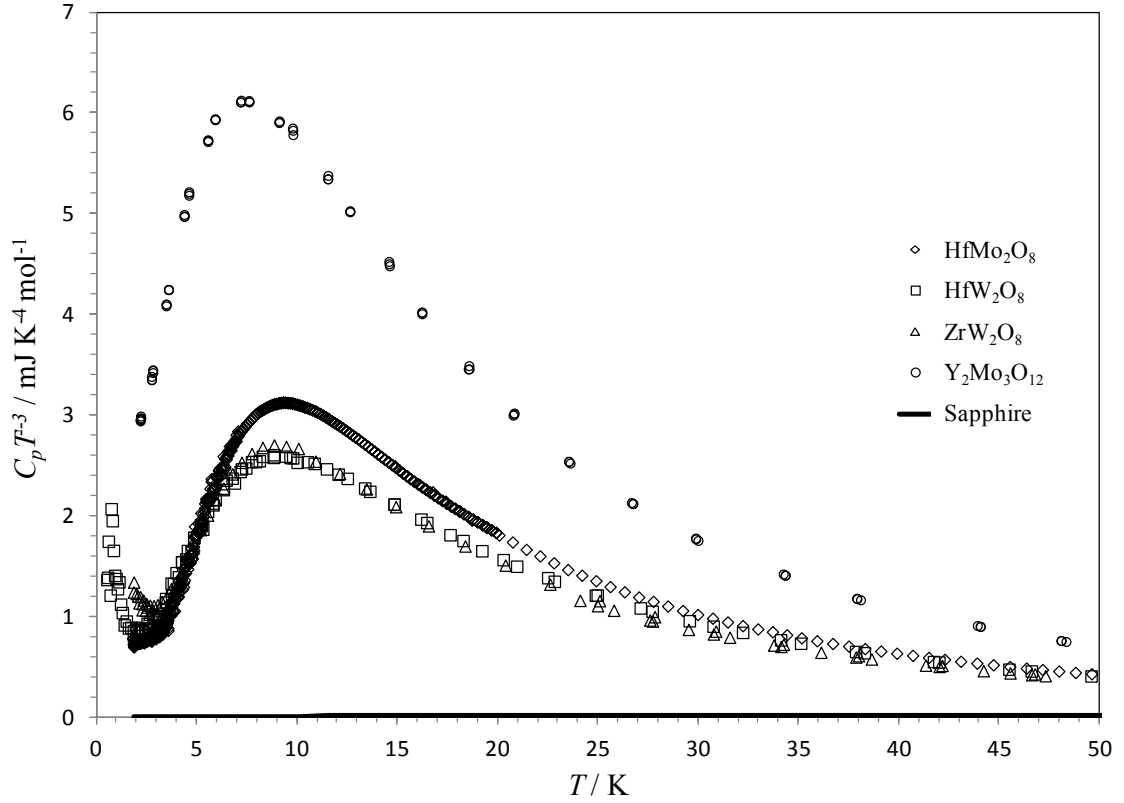


Figure 1.5: Anomalous heat capacity of open framework materials in families displaying thermomiotic behavior: HfMo_2O_8 ,⁶⁶ HfW_2O_8 ,⁶⁷ ZrW_2O_8 ,⁶⁵ $\text{Y}_2\text{Mo}_3\text{O}_{12}$,³⁵ and, as an example of a normal material, sapphire.⁶⁸

1.3.2 THERMAL CONDUCTIVITY

The thermal conductivity of an insulating solid can be related to the heat capacity, speed of sound (mean phonon speed) and phonon mean free path, λ , using the Debye model:¹⁸

$$\kappa = \frac{C_V v_s \lambda}{3} \quad (1.13)$$

It has been shown that the large number of low-frequency optic phonons in thermomiotic materials and materials with NTE-conductive structures interfere with the heat-carrying acoustic phonons, reducing the phonon mean free path compared with less flexible materials, leading to very low values for thermal conductivity⁶⁹ in ZrW_2O_8 ,⁵⁷

HfMo₂O₈,⁶⁶ and probably other thermomiotic materials. If the reduced thermal conductivity is a general phenomenon, then development of near-zero CTE materials is even more imperative to have high thermal fracture resistance (see equation (1.6)).

1.3.3 MODE GRÜNEISEN PARAMETER

Low-frequency modes, non-zero CTE and low thermal conductivity of thermomiotic materials are all manifestations of anharmonic interatomic interactions. These can be quantized further *via* deviations from zero of either the mode-dependent or the bulk Grüneisen parameter (equations (1.7) and (1.9)). Large negative values of γ have been observed for thermomiotic materials at low temperatures and these deviations from zero also scale with the magnitude of NTE.^{57,70,71}

1.3.4 PHONON DISPERSION RELATIONS AND DENSITY OF STATES

Since NTE in open framework structures can be largely attributed to the lattice vibrations, it can be informative to probe the phononic density of states (DOS) using IR and Raman spectroscopy and inelastic neutron scattering.

Thermomiotic materials often have two common characteristics: strongly bonded atoms and an open-framework structure. Together, these two features lead to environments that favor the mechanisms responsible for thermomiotic behavior: rigid polyhedra, connected by flexible bridging atoms, and the space to allow for cooperative polyhedral rotation. The low-energy translational and librational phonon modes typically have energies below 10 meV ($\sim 80 \text{ cm}^{-1}$) and can be used as an indicator of potential thermomiotic materials.^{72,73,74}

The phonon density of states played a significant role in delineating the origins of NTE in ZrW_2O_8 .⁷² Similarly, analysis of the phonon density of states from the Raman spectrum for HfMo_2O_8 identified an abundance of low-frequency optic modes and a band gap between 400 and 700 cm^{-1} ,⁶⁶ as seen with other $AM_2\text{O}_8$ materials (where A is a tetravalent cation and M is W^{6+} or Mo^{6+}).⁷⁵ Similar characteristics of the phonon DOS were observed by Yamamura *et al.*⁷⁴ for the $A_2M_3\text{O}_{12}$ family with compositions $\text{Sc}_2\text{W}_3\text{O}_{12}$ and $\text{Sc}_2\text{Mo}_3\text{O}_{12}$.

1.3.5 PHASE TRANSITIONS

Some thermomiotic materials exhibit polymorphism but only have NTE in one phase. This symmetry dependence of CTE has been studied for a variety of systems including ZrW_2O_8 ⁷⁵, $\text{Sc}_2\text{Mo}_3\text{O}_{12}$ ⁷⁶ and ZrV_2O_7 .⁷⁷ For instance, in $\text{Sc}_2\text{Mo}_3\text{O}_{12}$ the CTE is negative for the high-temperature orthorhombic phase while it is positive for the low-temperature monoclinic phase. There has been some work correlating the orthorhombic to monoclinic phase transitions of the $A_2M_3\text{O}_{12}$ family of materials with the electronegativities of the A atoms,^{38,78} but this correlation only holds within the molybdate or tungstate subsets and fails when the two sets are considered together.

It is generally accepted that polyhedral rigidity in thermomiotic systems plays a key role in the phase transitions. The modes responsible for NTE are highly temperature dependent and can soften (frequency goes to zero) as T approaches the transition temperature, T_{trs} .⁷⁹ The phase transition from an NTE structure to a PTE structure can be either first- or second-order. Most are the former: discontinuous and accompanied by a step-wise decrease in the unit cell volume (going from NTE at high T to a PTE phase at

low T). However, there are some materials which undergo a second-order NTE-PTE phase transition, such as ferrierite,⁸⁰ which changes symmetry from $Pm\bar{m}n$ to $Im\bar{m}m$, and $\text{HfMgW}_3\text{O}_{12}$,⁸¹ which changes symmetry from $Pnma$ to $P2_1/a$. Second-order phase transitions undergo a gradual change in unit cell volume which could be advantageous for NTE-based composites where volume discontinuities could lead to cracking and composite deterioration.⁸¹

In the case of ZrW_2O_8 , the crystalline phases all exhibit thermomiotic behavior. The cubic (α , $P2_13$) phase has the greatest NTE and is stable under ambient conditions, but at temperatures greater than 431 K it transforms into β - ZrW_2O_8 (space group of $Pa-3$) and at pressures greater than 0.2 GPa there is another transition to orthorhombic γ - ZrW_2O_8 ; ZrW_2O_8 becomes amorphous at even higher pressures.^{82,83} When preparing these materials for sample measurement or for applications it is essential to consider the environments that the materials will be used in and the stresses that will be applied, internally and externally.

1.4 APPLICATIONS OF THERMOMIOTIC MATERIALS

1.4.1 CURRENT AND POTENTIAL APPLICATIONS

Thermomiotic materials have prospective uses in many scientific and engineering fields where thermal expansion must be controlled. The lithium aluminum silicate (LAS) glass ceramic system, in which thermomiotic crystallites are formed in a PTE glass matrix, was the first widely commercialized composite material to achieve near-zero

thermal expansion over a wide range of temperatures.⁸⁴ These glass ceramics, such as those containing β -eucryptite, have excellent thermal shock resistance due to their low CTEs (and the small difference in CTE between the two components), and they are used as stovetops.⁸⁵ LAS glass ceramics are also important optical materials; they can be used to create lenses and mirrors with temperature-independent optical properties.⁸⁵

The wide variety of thermomiotic materials discovered since 1996 generally have not yet found commercial applications. However, the large number of recent patents regarding thermomiotic materials testifies to their potential use.⁹ Thermomiotic materials have been proposed for use in tires⁸⁶ and industrial equipment⁸⁷ to improve their ability to withstand high temperature. Several porous thermomiotic ceramics exhibit high strength and chemical durability at high temperatures for use in catalytic converters.⁸⁸

Several potential applications for thermomiotic materials in the field of optics have been identified. They can be used as substrates for fiber diffraction gratings, an application which is extremely sensitive to length changes,^{89,90,91} and lasers.⁹²

In the electronics industry, thermomiotic materials could be used in thermally sealed sockets,⁹³ or as substrates for high-frequency circuits.⁹⁴ They can also be used in packaging to remove thermal stress from CTE mismatch.⁹⁵ Thermal actuators combining NTE and PTE components can have enhanced sensitivity to temperature changes,^{96,97} which can be used to improve the efficiency of microelectromechanical systems (MEMS).⁹⁷

Thermal excursions of dental fillings during their curing⁹⁸ or the consumption of hot and cold beverages⁹⁹ can cause damage due to mismatched CTEs, which can be reduced by using a thermomiotic component in the filling.¹⁰⁰

1.4.2 CRITERIA FOR APPLICATIONS

The thermal stability of thermomiotic materials is of utmost importance as it determines their useful operational range. The metal oxide thermomiotic materials (*e.g.* ZrW_2O_8) have an advantage in this area, as they can be stable at temperatures of over 1000 K.¹⁰¹ Metal cyanide thermomiotic materials also can be stable at over 1000 K in inert atmosphere¹⁰² but can decompose at lower temperatures in air.¹⁰³ Many metal oxide thermomiotic materials are known to be metastable at ambient conditions;¹⁰⁴ they begin to decompose into their component oxides above room temperature.¹⁰¹

Phase transitions in thermomiotic materials have been introduced in Section 1.3.5. Temperature-induced solid-solid phase transitions can increase¹⁰¹ or decrease^{81,105} the CTE of a thermomiotic material. These phase transitions can change the lattice system of the unit cell,¹⁰⁵ cause structural disorder,¹⁰¹ or remove a superstructure.¹⁰⁶ If the volume of the unit cell changes during the phase transition the material can be damaged.¹⁰⁷ The temperature at which a phase transition occurs can be modified by the introduction of impurities.¹⁰⁸

Some thermomiotic materials undergo pressure-induced phase transitions and/or amorphization at relatively low pressures.^{82,109,110} These transitions lower the volume of the unit cell and usually increase the CTE. A general relationship between NTE and propensity to pressure induced amorphization due to steric hindrance has been proposed.¹¹¹ Thermal stress in PTE-NTE composites has been suspected to be sufficient to cause pressure-induced phase transitions.^{70,112} Increased temperature usually increases the pressure required to cause these phase transitions, and can reverse them.^{111,113}

Some metal oxide thermomiotic materials are hygroscopic;^{114,115} this is not surprising given the large amount of free space in their crystal structures. Molybdates are generally more likely to be hygroscopic than tungstates; for example ZrMo_2O_8 is hygroscopic while bulk ZrW_2O_8 is not.⁶⁵ The introduction of water into a thermomiotic material can significantly influence the CTE.^{114,115}

The bulk and/or Young's moduli of various thermomiotic materials have been reported^{116,117,118,119,120} and generally have been found to be lower than would be expected from the strengths of their chemical bonds.¹²¹ This has a deleterious effect on use of these materials in combination with PTE materials. There are several theoretical models for the bulk CTE of a mixture of materials; generally they include an average of the component CTEs weighted by their bulk moduli. Stiffer components have a greater impact on the bulk CTE because they are able to deform the other components more than they are themselves deformed during expansion and contraction. Consequently, larger quantities of NTE material are required to compensate for PTE of metals and ceramics than would be expected from the rule of mixtures (weighting of properties by composition). The problem can be avoided somewhat by using a thermomiotic material in conjunction with a ductile material such as a polymer,¹²² but large amounts of thermomiotic material are still required due to the polymer's characteristically large PTE.¹²³

1.5 SYNTHESIS AND CHARACTERIZATION TOOLS

1.5.1 SYNTHESIS

Advanced ceramic powders are a \$1 billion industry annually just in the United States.¹²⁴ Generally, it is convenient to classify ceramic synthesis techniques in two groups: (a) high-energy synthesis, such as solid-state reactions and mechanical methods; and (b) soft (wet) chemistry techniques, such as sol-gel or hydrothermal synthesis routes.

Three of the most investigated ceramic thermomiotic families, AM_2O_8 , $A_2M_3O_{12}$ and zeolites, were first obtained through different methods:^{125,126,127} solid-state reactions for ZrW_2O_8 ¹²⁵ and $Sc_2W_3O_{12}$ ¹²⁶, and hydrothermal for zeolites.¹²⁷ However, research progress, aligned with discovery of NTE in other ceramic families, has led to a significant increase in the number of synthetic routes to thermomiotic powders. Some of the most commonly used and the most promising methods for synthesis of thermomiotic ceramics are described here.

1.5.1.1 Solid-State Synthesis at High Temperature

The solid-state reaction method, or ceramic method, is a well-known processing route for obtaining thermodynamically stable phases at high temperatures through solid-state diffusion.

To obtain, for example, $Al_2Mo_3O_{12}$ from binary oxides, it is necessary to have a local 1:3 stoichiometry of Al_2O_3 to MoO_3 . Mixing these oxides in a ball mill, for times as long as 10 h,¹²⁸ can ensure a homogeneous distribution and a high contact area. (Initial kinetics of solid-state reactions strongly depends on the contact area between reacting

oxides.) Ball milling also assists mechanical activation of the precursor powder, *e.g.* due to high stresses and temperatures at the impact zone, generating defects that are planar (surfaces), linear (dislocations) and/or non-equilibrium (Schottky and Frenkel defects). Ball milling increases the surface area of the precursor powders by breaking initial crystallites, especially those with starting sizes higher than 100 nm.^{129,130} Precursor powders with crystal sizes ~ 10 nm seem to be hardly affected during ball milling.¹³¹ The increasing concentrations of defects during ball milling accelerates self-diffusion and therefore solid-state reactions. Therefore, a mechanically activated powder would have a higher coefficient of self-diffusion in comparison to the non-activated one. (A quantitative example of this is the coefficient of diffusion (D) of Ca^{2+} in mechanically activated CaO which is much higher than in non-activated CaO.¹²⁹) However, when a new phase, in this case $\text{Al}_2\text{Mo}_3\text{O}_{12}$, starts to nucleate and grow at the contacts between Al_2O_3 and MoO_3 particles, the rate of reaction starts to be controlled by the coefficients of diffusion of Al^{3+} or Mo^{6+} in $\text{Al}_2\text{Mo}_3\text{O}_{12}$, and it will depend if the reaction takes place on the $\text{MoO}_3/\text{Al}_2\text{Mo}_3\text{O}_{12}$ or on the $\text{Al}_2\text{O}_3/\text{Al}_2\text{Mo}_3\text{O}_{12}$ interfaces. Since the overall kinetics are slow, solid-state synthesis is rather time consuming.

To avoid incomplete reactions, it is necessary to expose previously mixed precursor powders to high temperatures during long time periods. Therefore, the final product often will consist of a thermodynamically stable phase showing large and dimensionally non-uniform crystallites. During the solid-state reaction the better mixed regions will react more rapidly, so to react the entire precursor powder, including the poorly mixed regions, it is common to have prolonged thermal treatment, as long as 240 h.¹²⁶ Crystallites of the new phases that were nucleated in the well-mixed regions will

have time to grow larger, while the crystallites nucleated in other regions will have smaller crystallites. Generally, micron size and non-uniform crystallites are obtained as in the case of $\text{Al}_2\text{Mo}_3\text{O}_{12}$.¹³²

Due to the formation of thermodynamically stable phases this synthesis method is widely adopted for evaluation of phase diagrams.

Disadvantages inherent to this method include the low surface area of the products, and sometimes incomplete reactions. Another important factor, for example with WO_3 and MoO_3 , is high vapor pressures at the reaction temperatures which could prevent control of the stoichiometry. More details concerning drawbacks of this method for synthesis of NTE materials are presented for $\text{Er}_{2-x}\text{Ce}_x\text{W}_3\text{O}_{12}$ ¹³³ and $\text{Ln}_{2-x}\text{Cr}_x\text{Mo}_3\text{O}_{12}$ ^{134,135} and through a comparison of the solid-state reaction procedure with a sol-gel method for synthesis of $\text{Al}_2\text{Mo}_3\text{O}_{12}$.¹³²

1.5.1.2 Soft Chemistry Approaches

The general idea of soft chemistry approaches is to make mass transport faster, allowing for lower reaction temperatures and/or more control of the crystallite size of the product. The faster mass transport could occur through reduced diffusion paths in solid precursors, such as in sol-gel or co-precipitation methods, or by use of a fluid state, as in hydrothermal synthesis.

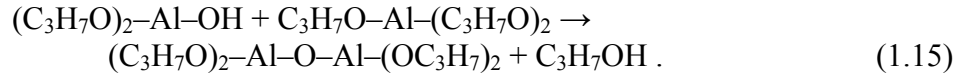
1.5.1.2.1 Sol-Gel Synthesis

The principal advantage of the sol-gel method over the solid-state reaction route is the ability to attain an atomically homogeneous mixture of ions in the precursor gel, resulting in a favorable local stoichiometry and short diffusion paths (atomic distances rather than in micron or sub-micron). The truly homogeneous mixture permits easier formation of stable, chemically homogeneous, ternary, quaternary or higher-order oxides and even thermodynamically metastable phases since reaction times can be very short. Also, the homogeneity of the precursor gel allows synthesis of solid solutions with precise cation ratios, which can assist finely tuning coefficients of thermal expansion within thermomiotic families, *i.e.* the $A_2M_3O_{12}$ family where different A^{3+} cations could result in materials with markedly different CTEs.¹²⁸ Homogeneity at the atomic level also facilitates formation of uniform nanocrystallites. A further advantage is that the sol-gel method is more energy efficient than high-temperature solid-state synthesis. The sol-gel approach has become a powerful bottom-up method to obtain nanostructures.

There are many varieties of the sol-gel process. The common feature for all is formation of a suspension (a sol) starting from different precursors, such as alkoxides or salts, followed by its transformation to a viscous gel. There are different ways to form a gel. In the classical sol-gel route, a gel is formed through hydrolysis and condensation reactions. Hydrolysis occurs when a metal-alkoxide, such as for example aluminum-propoxide, is dissolved in ethanol in a presence of water. The reaction between the alkoxide and water, such as:



results in formation of hydroxy metal alkoxide, which reacts further with metal alkoxide inducing gelation through a condensation reaction such as:



Propoxide groups from the condensation product could be hydrolyzed further, permitting formation of a 3D network of well-distributed, metal and oxygen atoms. The as-prepared gel is an assemblage of amorphous solid, containing organics, and liquid filled pores (alcohol or water). Therefore, before firing it is necessary to remove liquid from the pores through drying. A firing step removes organic matter and crystallizes the desired oxide. Firing is comparable to calcination in a solid-state reaction but can be completed at lower temperatures and especially over much shorter time intervals, as short as 15 min to 20 min,¹³² giving a chemically homogeneous and single phase product with small and uniform crystals.

There is a considerable literature reporting sol-gel synthesis of thermomiotic materials. Because cubic ZrW_2O_8 and related phases are thermodynamically stable only at high temperatures^{125,136} and decompose to binary oxides if cooled slowly, for solid-state synthesis it is necessary to quench the samples obtained at high temperatures ($T > 1370$ K) to retain their (meta)stability. Therefore, obtaining homogeneous cubic ZrW_2O_8 with controlled morphology, within conditions where it is metastable, is best achieved through a soft-chemistry approach. The first sol-gel synthesis of thermomiotic materials was reported for ZrW_2O_8 family.^{137,138}

ZrW_2O_8 , HfW_2O_8 and $\text{ZrW}_{2-x}\text{Mo}_x\text{O}_8$ (up to $x = 0.15$) powders, with average crystallite size of $\sim 1 \mu\text{m}$, have been produced from Zr, W or Mo salts with addition of HCl through a long gelation stage (at least one week), followed by firing at temperatures

not higher than 873 K for 10 h.¹³⁸ Concurrently, others started to explore a non-hydrolytic sol-gel method for synthesis of ZrW_2O_8 and $ZrMo_2O_8$.^{137,139} Subsequently, the non-hydrolytic sol-gel method was extended to the $A_2M_3O_{12}$ family, e.g., $Ga_2Mo_3O_{12}$ ¹⁴⁰ and $Y_2Mo_3O_{12}$,¹⁴¹ and as well as to the newly discovered $A^{4+}B^{2+}M_3O_{12}$ family, where $HfMgW_3O_{12}$ and $ZrMgW_3O_{12}$ were obtained through this method.¹⁴² In general, the non-hydrolytic sol-gel method is based on the reaction between metal chlorides and diisopropyl ether. First, metal chloride is dissolved in a solvent, such as chloroform or acetonitrile, followed by addition of ether. This mixture is confined to an ampoule which is cooled in liquid nitrogen, sealed under vacuum, then heated to ~ 370 K for periods as long as a week. The resultant tar is converted to a powder by heating to ~ 570 K for several hours. To remove organics and crystallize thermomiotic oxides, the powder is fired at 873 K for 3 h for $Ga_2Mo_3O_{12}$ ¹⁴⁰ or 1323 K for 0.5 h for $HfMgW_3O_{12}$ and $ZrMgW_3O_{12}$.¹⁴² Although small quantities of binary oxides such as MoO_3 , HfO_2 or ZrO_2 are present in the as-prepared samples, a major success of the non-hydrolytic sol-gel method was the first synthesis of metastable monoclinic $Ga_2Mo_3O_{12}$.¹⁴⁰

The citrate-gel method is another sol-gel route already employed for obtaining thermomiotic phases.^{143,144,145} To obtain a ZrW_2O_8 phase De Buysser *et al.*¹⁴³ started from a solution of Zr^{4+} and W^{6+} salts, gelled for 24 h at 333 K through addition of citric acid as the chelating agent. They showed that the metal ions/chelating agent ratio is an important parameter to complete gelation of the starting mixture; for ZrW_2O_8 only ratios as high as 1:6 induced complete gelation. When the as-prepared gel was fired at high temperatures (973 K to 1073 K) for 12 h to remove organics, the product was a porous mixture of monoclinic ZrO_2 and WO_3 phases, rather than ZrW_2O_8 . Therefore, a solid-state reaction

was carried out at 1453 K for 2 h and 15 h, followed by a quenching step to obtain cubic ZrW_2O_8 . Although cubic ZrW_2O_8 was ultimately obtained through a solid-state reaction, the time was shorter than usual.¹⁴³ Georgi and Kern¹⁴⁵ applied a similar citrate-gel method and succeeded to obtain tetragonal ZrW_2O_8 at 1010 K, which was converted to cubic ZrW_2O_8 at 1398 K in less than 1 min.

Ethylene diamine tetraacetic acid (EDTA) was another chelating agent applied for preparation of cubic ZrW_2O_8 .¹⁴⁶ Zr-EDTA and W-EDTA solutions were prepared separately. The Zr-EDTA solution precipitated overnight and colorless crystals were filtered off, thoroughly rinsed with water and then added to the W-EDTA solution. The solution transformed to a gel after 12 h at 333 K. Cubic ZrW_2O_8 was obtained after calcination for 2 h within the thermodynamic stability range followed by quenching.

The stearic acid sol-gel method is a very promising way to prepare nanometric NTE powders.¹⁴⁷ Xu *et al.* used this simple method to prepare $Al_2W_2MoO_{12}$.¹⁴⁷ Salts of W and Mo were added to melted stearic acid and thoroughly mixed. Afterwards an Al salt was added and the mixture was stirred for several hours. When cooled to room temperature a gel was formed. The precursor gel was ignited in air and then fired at 973 K for 6 h, resulting in a nanometric single phase powder.

The polyvinyl alcohol (PVA) assisted sol-gel method was recently employed to obtain $Al_2Mo_3O_{12}$.¹³² PVA was dissolved in water and then solutions of Al and Mo salts were added. PVA acts as chelating agent, by wrapping and covering metal ions avoiding their precipitation, forming a precursor gel. During the gelation process, -OH groups from the PVA chains interact with cations forming a cocoon-like local arrangement inhibiting precipitation. Drying for several hours at 373 K results in a xerogel, and when

fired at 873 K to 973 K for times as short as 15 min, a single phase powder with submicron crystallite sizes is formed. The metal to PVA ratio is an important parameter for tailoring crystallite sizes.

1.5.1.2.2 Co-Precipitation

Co-precipitation is especially well suited for preparation of nanomaterials. Solid precursors with a truly homogeneous mixture of cations are formed. These solid precursors could be solid solutions or intimate mixtures of two (or more) salts. For ternary and higher-order ceramics the procedure is generally based on the simultaneous precipitation of more than one cation from a supersaturated liquid solution. Solubility of a cation is generally decreased in mixed solutions of several cations, but temperature or pH can induce supersaturation. When precipitation occurs, homogeneous nucleation of insoluble phases, such as hydroxides or oxalates, takes place all over the solution. The as-formed nuclei tend to grow uniformly resulting, commonly, in homogeneous nanocrystallite powders. The as-prepared insoluble phases of mixed cations can be further heated for decomposition and transformation to the desired mixed oxides.

Despite its simplicity and encouraging results for preparation of homogeneous nanopowders there are few articles reporting the use of co-precipitation to obtain NTE powders.^{148,149} For example, Zhecheva *et al.* reported a successful synthesis of nanocrystalline $\text{Al}_2\text{W}_3\text{O}_{12}$,¹⁴⁸ by co-precipitation from aqueous $\text{Al}(\text{NO}_3)_3$ and Na_2WO_4 solutions at room temperature. The precipitate was filtered and dried at 353 K for several

hours, and used as precursor that gave fully crystallized nanometric powder after firing at 1073 K for 5 h.

1.5.1.2.3 Hydrothermal Synthesis

The major characteristic of this route is self-generated pressure in a sealed reactor. Crystallization takes place through rapid diffusion in the low-viscosity supercritical fluid, or through increased solubility due to the high temperature. Zeolites and related molecular sieves are commonly synthesized through hydrothermal methods. A detailed history of the development of this technique for zeolites and related structures is available elsewhere.¹²⁷

Cubic $\text{ZrW}_{2-x}\text{Mo}_x\text{O}_8$ ^{150,151,152,153} and $\text{ZrW}_{1.8}\text{V}_{0.2}\text{O}_{7.9}$ (a new solid solution with the cubic ZrW_2O_8 structure)¹⁵⁴ are among the thermomiotic materials produced through the hydrothermal route. Cubic $\text{ZrW}_{2-x}\text{Mo}_x\text{O}_8$ was obtained through a rapid calcination of $\text{ZrWMoO}_7(\text{OH})_2(\text{H}_2\text{O})_2$, an intermediate phase formed in the hydrothermal stage, at temperatures higher than 773 K. Different additives, such as acids (HCl , HNO_3 , H_2SO_4 etc.) and surfactant (*e.g.*, sodium dodecyl benzene sulfonate), were used in the hydrothermal process to control the morphology of intermediate phases, since it is observed that the shape of the $\text{ZrW}_{2-x}\text{Mo}_x\text{O}_8$ crystals strongly depends on the morphology of their precursor.¹⁵⁰

1.5.1.3 Laser Synthesis

This technique recently has been reported by Liang *et al.*, in a several papers considering preparation of thermomiotic phases such as cubic ZrW_2O_8 or HfW_2O_8 ^{155,156,157} and $A_2Mo_3O_{12}$ molybdates.¹⁵⁸ It uses a high-power continuous-wave CO_2 laser, and it is a rapid technique with several tens of grams of product produced in a matter of seconds. In the course of the synthesis, the laser beam is directed on the pellet made from a stoichiometric mixture of binary oxides (such as ZrO_2 and WO_3), previously thoroughly homogenized. The beam moves along the sample causing immediate melting of the exposed regions. When the laser beam moves to an adjacent region, the previously melted region solidifies rapidly, forming ternary oxides such as ZrW_2O_8 , HfW_2O_8 , $Y_2Mo_3O_{12}$ or $La_2Mo_3O_{12}$. The temperatures reached during interaction of the laser beam with the pellets are extremely high ($T > 2570$ K). Although, for example, MoO_3 is expected to be volatile at 2573 K, loss of MoO_3 is negligible¹⁵⁸ during the short synthesis period.

1.5.2 MICROSTRUCTURE

1.5.2.1 Sintering, Porosity and Microcracking

Heating (sintering) powders to temperatures below their melting point allows atomic diffusion to fuse the particles and produce a solid body of low porosity. Sintering works best for materials that have high melting points or that would decompose before reaching the melting point. Sintering can led to controlled grain sizes and porosity, while maintaining high purity.

Typical sintering methods for ceramics usually include mixing a powder precursor with water, binder, or deflocculent to form a slurry, which is then spray dried. The material is then placed into a mold to form a green body which is then heat treated in two steps. The first heating step serves to remove the binder and the second step sinters the material into the final product.

The sintering process used can be varied to accommodate the materials being used. Some of the most common processing methods that involve sintering are: (a) hot (isostatic) pressing, which can be used to produce complex shapes; (b) sintering without pressure which gives a more uniform density than hot pressing; (c) chemical vapor deposition in which gas precursors are converted to a solid by continuously depositing atomic layers of the material onto a heated substrate; (d) reaction bonding which uses a chemical reaction to bind ceramic powders into a solid form after which the binder is removed using heat treatments; the resulting preform is then impregnated with liquid reagents and heated to temperatures above the ceramic melting temperature to create the final product; (e) suspension plasma spraying in which nanometric powders are suspended in water or alcohol and injected into a plasma jet to evaporate the solvent; dense zones can form from fine solid particles;¹⁵⁹ (f) spark plasma sintering in which a high-temperature spark is generated between powder grains *via* an electrical discharge, giving dense materials with fine grain sizes.

Usually, thermomiotic ceramics do not sinter well. The resulting bulk material tends to have very low mechanical strength due to poor densification. Anisotropic CTE can lead to increased stress in the material, and the formation of microcracks upon cooling.

Microcracks can be reduced by employing low-temperature sintering techniques. A glassy bonding agent and spark plasma sintering has produced low CTE composites in which the thermomiotic phase would otherwise be mechanically unstable.¹⁶⁰ The choice of bonding agent is important.^{160, 161}

1.5.2.2 Effects of Particle Morphology

The formation of particles of thermomiotic materials of various sizes and shapes has been reported in the literature.^{153,162,163,164,165} Examples include rods,^{153,163} brushes,¹⁶³ cuboids,¹⁶³ spheroids,¹⁵³ ultra-thin fibers,¹⁶⁴ thin films,¹⁶⁵ and aerogels.¹⁶⁵ Particle size and morphology can be controlled by modification of the synthetic conditions (see 1.5.1), or, to some extent, by treatment after synthesis (*i.e.* grinding). It is desirable for many applications to have small particles with high surface area, as this leads to greater miscibility and matrix-filler bonding in a composite,¹⁶³ improving fracture resistance, and densification. Changes in the particle morphology have been shown to influence the extrinsic CTE of ZrW_2O_8 , sometimes leading to more pronounced NTE.^{153,165}

1.5.2.3 Coatings, Surface Treatments and Binders

The properties of particulate thermomiotic materials can be adjusted by physical (coating) or chemical (surface treatment) modification of the particle surfaces, or by a combination of the two methods. Surface treatments are generally used to improve a material's affinity to another material, *e.g.* to improve matrix-filler adhesion,^{122,160,166} or in preparation for coating.¹⁶⁷ Coating of thermomiotic particles with copper can be performed to improve the thermal conductivity of the material, *e.g.* for electronics

packaging applications.^{167,168} Copper coating was found to reduce the onset temperature and increase the temperature range over which the α - β transition in ZrW_2O_8 occurs.¹⁶⁸ If surface treatments or coatings change the residual stress distribution at the particle interface, the CTE of the bulk material will be affected.¹⁶⁹

Binders are often added to green ceramic bodies to increase their strength and flexibility prior to sintering. These include solvents, polymers, or both.¹⁷⁰ The binder vaporizes and/or undergoes oxidative decomposition during sintering.¹⁷⁰ Densification with binders can be improved by using minimal amounts, increasing the green body density, and by controlling the temperature profile to prevent the formation of bubbles from the binder vapor.¹⁷⁰

1.5.3 EXPERIMENTAL DETERMINATION OF THERMAL EXPANSION

Thermal expansion, one of the most fundamental material properties, can be measured through different experimental techniques, each offering different types of data, with corresponding advantages and limitations.

Diffraction techniques (using X-rays or neutrons) can be used to probe average or local crystal structures and to measure thermal evolution of lattice parameters, to calculate the intrinsic coefficient of thermal expansion. In the open framework ceramic structures, vibrational contributions are the principal intrinsic causes of the lattice parameter variations with temperature. The common feature of all intrinsic effects, non-vibrational (*e.g.* magnetic, electronic, residual stress) and vibrational, is their atomic scale origin and their impact on lattice parameters.

On the other hand, dilatometry (thermo-mechanical analysis) determines the thermal evolution of the length of a bulk specimen, giving primarily the extrinsic (macroscopic) coefficient of thermal expansion. In addition to intrinsic thermal expansion, dilatometry measures changes at the microstructural level, such as the elimination of microcracks and pores, which strongly influence specimen length. The extrinsic CTE also depends on the generation of new lattice sites due to increased numbers of point defects (vacancies and Schottky pairs) with temperature. Although this last effect is rigorously an atomic-scale event it can be classified as macroscopic since it is seen only in dilatometric measurements.

1.5.3.1 Diffraction Techniques

Lattice parameters and their variations with temperature are now routinely determined at very high accuracy¹⁷¹ and precision using X-ray or neutron diffraction, especially with the aid of high-resolution equipment at synchrotron sources, providing standard uncertainties as low as 10^{-6} Å.¹⁷² As long as the temperature at the sample also is determined accurately, diffraction can provide reliable CTEs, often to 2 or 3 significant figures, less if the CTE is very small.

In addition to the lattice parameters, diffraction can reveal atomic coordinates of the average crystal structure for single crystal or polycrystalline specimens. For both X-ray and neutron powder diffraction, Rietveld refinement of the average crystal structure provides the best accuracy.¹⁷³ X-rays diffract from electrons and neutrons scatter from nuclei, so the best accuracy is achieved by combining both sets of data (X-ray for heavy elements and neutrons for light elements such as oxygen). Accurate average atomic

coordinates (standard uncertainty $\approx 10^{-5}$ Å) provide deeper insight concerning the crystal structure building blocks (*e.g.* polyhedra) by knowledge of the intrapolyhedral (bond lengths and bond angles) and interpolyhedral (second neighbor non-bonding distances and angles) parameters. Also, bond valences of ions¹⁷⁴ and distortions of coordination polyhedra¹⁷⁵ can be calculated from atomic coordinates. Atomic displacement factors, which can be dynamic, static or both, can be calculated isotropically or anisotropically from diffraction experiments. These structure parameters are very useful for understanding the thermomiotic phenomenon, although one should be aware that lattice parameters can be measured to far greater absolute accuracy than the intrapolyhedral and interpolyhedral dimensions. An additional difficulty in obtaining meaningful bond lengths from diffraction is when the instantaneous atomic positions between neighboring atoms are correlated, and diffraction experiments give apparent (not actual) distances between the average positions. This is especially the case in the open framework thermomiotic materials where cation-anion position relationships are strongly correlated (see Figure 1.4) and apparent bond lengths can have unphysical variation with temperature. It also can be difficult to obtain reliable atomic displacement factors; higher scattering vectors (Q [Å⁻¹]) should always be probed by high-energy radiation, ideally from a neutron source, since atomic neutron scattering factors are constant with respect to the scattering vector. Thermal ellipsoids, constructed from the anisotropic atomic displacement factors, are a tool for examination of vibrational contributions to thermal expansion; *e.g.*, a flat ellipsoid of a two-fold coordinated atom could be an indication of its strong transverse vibrations. The temperature dependence of the thermal ellipsoids can be particularly revealing: non-zero atomic displacement factors near 0 K arise from static

(not dynamic) disorder. The static disorder can be associated with polyhedral distortion and enhanced by the nanometric nature of a material.¹⁷⁶

Local, or short-range, structure probing is possible through total scattering of high-energy X-rays (from synchrotron or even conventional Ag, $\lambda = 0.556 \text{ \AA}$, or Mo, $\lambda = 0.7107 \text{ \AA}$ sources) or neutrons, followed by pair-distribution analysis. The total-scattering pair-distribution function (TSPDF) gives information about the mean distances between atoms in condensed matter. The first peak in a TSPDF corresponds to the nearest-neighbor distance (first coordination polyhedron). One of the significant advantages of the TSPDF is that actual bond lengths can be determined even for correlated atomic pairs, such as Si-O¹⁷⁷ or any other correlated cation-anion pair,^{178,179} a common local feature in thermomiotic materials. Therefore, the CTE of any chemical bond can be directly estimated from experimental data. The capability of TSPDFs to reveal real temperature variations of the first-, second- or higher-order interatomic distances provides unbiased information concerning the role of bridging atoms in transverse vibration modes. A TSPDF can be used to evaluate the extent of atomic ordering in any solid (or liquid), and can clearly distinguish crystalline from nanocrystalline or amorphous solids.¹⁸⁰ Pressure-induced amorphization, an NTE-related phenomenon, can be conveniently investigated by TSPDF.¹⁸¹ The degree of static disorder of the local structure, another useful parameter, can be evaluated from TSPDF; broader TSPDF peaks are signatures of higher local disorder, such as more distorted polyhedra.

1.5.3.2 Dilatometry

Dilatometry is the most suitable technique for the determination of CTE in bulk specimens; it can also be used to determine phase transition temperatures, and vacancy information (concentration and formation enthalpy). In this technique, the linear change of sample length is recorded as a function of temperature, generally by a push-rod. The recorded pattern is plotted as $\Delta L/L_0$ versus temperature, where ΔL and L_0 are the change and the original sample length, respectively.

The main parts of a push-rod dilatometer are the linear variable differential transformer (LVDT), rod, furnace and a thermocouple. The rod is connected to the ferromagnetic core of the LVDT, and pushes against the sample so that change in length is recorded by the LVDT as a voltage due to the movement of the ferromagnetic core. The rod and its surrounding tube are made from a low thermal expansion material with a high melting temperature, *e.g.* fused silica or alumina.

Sample preparation is important for accurate dilatometry, and it is essential that the samples be well consolidated and have flat and parallel ends. Dilatometry can be carried out with lab-built instruments or commercial instruments. Current push-rod dilatometers can have $\Delta L/L_0$ accuracy better than $\pm 1\%$.¹⁸² Note that this does not necessarily convert to a fixed % uncertainty in CTE; CTEs closer to zero are the most uncertain.

1.5.3.3 Discrepancies between Diffraction and Dilatometric Results

One of the particularly important issues in optimizing thermal expansion coefficients can be the common discrepancy between intrinsic (diffraction-derived) and extrinsic (dilatometric) CTEs in the anisotropic thermomiotic ceramics that comprise the majority of available materials with unusual thermal expansion. This discrepancy is a major problem for the application of thermomiotic ceramics in bulk forms and coatings, since the ceramic forms can show negative thermal expansion even when their intrinsic CTE is low positive, as reported for $\text{Al}_2\text{W}_3\text{O}_{12}$.³⁸ Such discrepancies make it difficult to ascertain how the CTEs of such materials will behave in applications.

One common reason for the appearance of additional extrinsic thermal expansion in ceramic bodies is pore infilling during heating, especially near sintering temperatures, due to densification where previously insufficiently sintered. This effect can be reduced by sintering to near the full theoretical density prior to dilatometric measurements.

Since the CTEs of cubic thermomiotic materials, *i.e.*, for members of the AM_2O_8 family, are practically independent of the technique, diffraction or dilatometry,⁵⁸ microcrack formation due to anisotropy is invoked to understand further discrepancies observed for non-cubic phases.¹⁸³ The polycrystalline nature of bulk ceramics results in boundaries between grains of anisotropic materials with different crystallographic orientations and consequently different CTEs. High stress around grain boundaries would give rise to microcracks. Microcracks could be formed on cooling after the sintering step, and some microcrack healing would be expected on heating, appearing in dilatometric results as an extrinsic thermal expansion effect, not seen in corresponding diffraction results. Microcracks form for ceramic bodies with grains above a certain critical size.¹⁸⁴

Thus, an approach to reduce or even eliminate the discrepancy in CTEs for anisotropic NTE materials would be through microstructural manipulation: production of ceramics containing small, uniform grains.

Another way to tailor ceramics with well-controlled CTE, for which dilatometric and diffraction methods give the same results, is through making the material more isotropic, as reported for $\text{Al}_{1.6}\text{In}_{0.4}\text{W}_3\text{O}_{12}$.³⁸

1.6 TYPES OF THERMOMIOTIC MATERIALS

The principal mechanism causing NTE over a large temperature range is low-frequency vibrational modes. These modes, however, can significantly affect thermal properties only if certain crystallochemical conditions are satisfied. The most common crystallographic situation is an open framework structure that can allow transverse vibrations of two-coordinate atoms. This implies that the polyhedra are connected through vertices, interstitial sites are empty and phase transitions to denser and lower symmetry polymorphs are suppressed. Here the major families of thermomiotic materials are presented.

1.6.1 METAL OXIDES AND RELATED STRUCTURES

1.6.1.1 AM_2O_8

The crystal structure of ZrW_2O_8 was determined in 1996 by Evans *et al.* (Figure 1.5).⁵⁸ Several compounds adopt the same structure, and the general formula AM_2O_8

describes this structure family, where A is a cation capable to assume 6-fold coordination, and M is W^{6+} or Mo^{6+} and, as shown recently, V^{5+} .¹⁸⁵

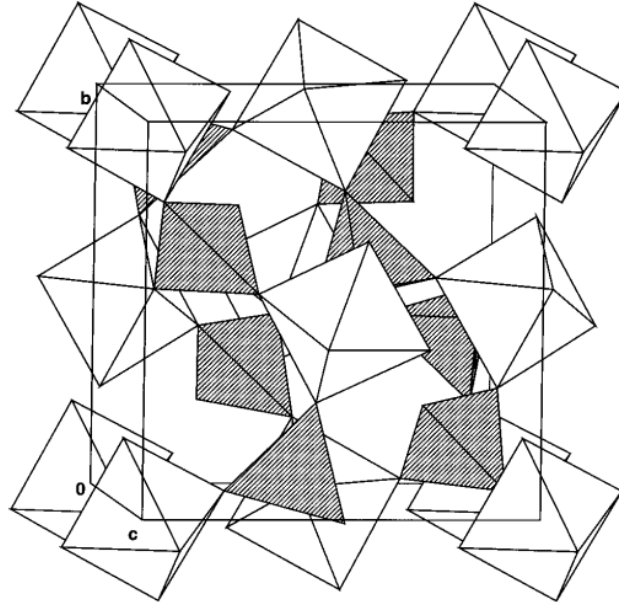


Figure 1.5: The room-temperature $P2_13$ crystal structure of ZrW_2O_8 with ZrO_6 octahedra shown in white and WO_3 tetrahedra shown in grey. Reprinted with permission from Evans, J. S. O.; Mary, T. A.; Vogt, T.; Subramanian, M. A.; Sleight, A. W. *Chem. Mater.* **1996**, 8, 2809–2823. Copyright 1996 American Chemical Society.

There are two main framework crystal structures that ZrW_2O_8 and related phases adopt over the temperature range of the solid. Both are cubic, leading to isotropic NTE. The phase transition between the two structures occurs at temperatures above room temperature as a consequence of unusual disordering of the MO_4 tetrahedra. Both low-temperature ($P2_13$) and high-temperature ($Pa-3$) structures are composed of corner-sharing AO_6 octahedra and MO_4 tetrahedra. However, a peculiarity of both structures, when compared to other framework structures composed of corner-sharing octahedra and tetrahedra, is that the MO_4 tetrahedron shares only three vertices with adjacent octahedra, while one vertex remains unlinked. On the other hand, the AO_6 octahedra assume more conventional local architecture in which each vertex is connected to adjacent MO_4

tetrahedra. As a result of such unusual local architecture there is always one terminal oxygen per tetrahedron, bonded only to M^{6+} and with a shorter bond ($\sim 1.7 \text{ \AA}$ for W-O) than for the oxygen in a two-fold arrangement ($\sim 1.8 \text{ \AA}$ for W-O). Terminal O- M^{6+} bonds have 3-fold symmetry, with the axis directed through the body diagonal. The existence of a terminal oxygen atom in a WO_4 group is a very rare structural feature and causes very high ionic conductivity in the high-temperature phase, comparable to the ionic conductivity of cubic stabilized ZrO_2 .⁵⁸

It is possible to detect the phase transition from $P2_13$ to the $Pa-3$ high-temperature space group (β -phase) due to the disappearance of the $hk0$ diffraction lines ($h \neq 2n$), *e.g.* for $T > 430 \text{ K}$ for ZrW_2O_8 . Dilatometry and diffraction (X-ray and neutron) results show a very small volume change, suggesting a second-order transition, while the CTE changes from $\alpha_a = -9.1 \times 10^{-6} \text{ K}^{-1}$ in the α -phase to $-5.4 \times 10^{-6} \text{ K}^{-1}$ in the β -phase.¹⁸⁶ The disordering of the WO_4 tetrahedra that provokes the phase transition can be understood as superposition of two different orientations of WO_4 , each one with 50 % occupation.

Another important structural feature of the ZrW_2O_8 -like phases which makes a major contribution to NTE is the rigidity of their polyhedra, *i.e.*, absence of internal distortions. (More flexible polyhedra could themselves exhibit positive thermal expansion that could mask the framework NTE.) Thus, the octahedra (AO_6) and tetrahedra (MO_4) can be treated as essentially rigid units. Also, it is important to note that a transition to a denser and lower symmetry polymorph is kinetically frustrated in ZrW_2O_8 , leading this material to have the unusual property of isotropic thermomiotic behavior over a very broad temperature range.

1.6.1.2 AM_2O_7

The pyrophosphate family, AM_2O_7 , embraces a large number of compounds since A can be any tetravalent cation that can adopt octahedral coordination, while M includes mainly V, P or As. This crystal family has an open framework structure, built from corner-shared AO_6 octahedra and MO_4 tetrahedra, adopting the cubic $Pa-3$ space group in its high-temperature thermomiotic structure (Figure 1.6).¹⁰⁶ The low-temperature form, which always presents normal positive thermal expansion, adopts a complex $3\times 3\times 3$ cubic superlattice although recently an orthorhombic structure¹⁸⁷ for ZrP_2O_7 or even triclinic in the case of CeP_2O_7 has been suggested.¹⁸⁸

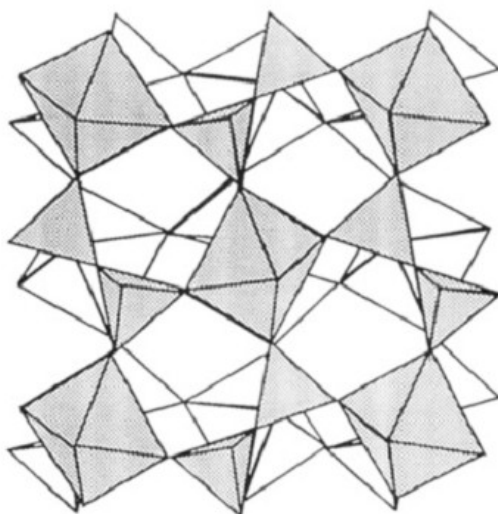


Figure 1.6 The ideal $Pa-3$ crystal structure of AM_2O_7 showing the corner-sharing AO_6 octahedra and MO_4 tetrahedra. Reprinted with permission from Korthuis, V.; Khosrovani, N.; Sleight, A. W.; Roberts, N.; Dupree, R.; Warren, W. W., Jr. *Chem. Mater.* **1995**, 7, 412–417. Copyright 1995 American Chemical Society.

The crystal structures of the cubic high-temperature forms in the AM_2O_7 and AM_2O_8 families are closely related. The AO_6 octahedra are linked through each vertex to adjacent MO_4 tetrahedra, the same as in the AM_2O_8 family. However, the connectivity of MO_4 tetrahedra in AM_2O_7 is different from the AM_2O_8 family: terminal oxygen atoms are

absent in AM_2O_7 . The MO_4 tetrahedra share three vertices with neighboring AO_6 octahedra, and the fourth is shared with another MO_4 tetrahedron.

1.6.1.3 $A_2M_3O_{12}$

Several different crystal structures exist for compounds with the $A_2M_3O_{12}$ formula. However, only the phases where A is a small rare earth (Ho to Lu, ionic radius 0.90 to 0.87 Å) or other trivalent metal (In to Al, ionic radius 0.80 to 0.54 Å) assume framework structures in the orthorhombic $Pbcn$ (Figure 1.7) or in the monoclinic $P2_1/a$ space groups. The connectivity in both framework structures is the same: AO_6 connect through vertices to six MO_4 which share all their vertices with adjacent AO_6 .

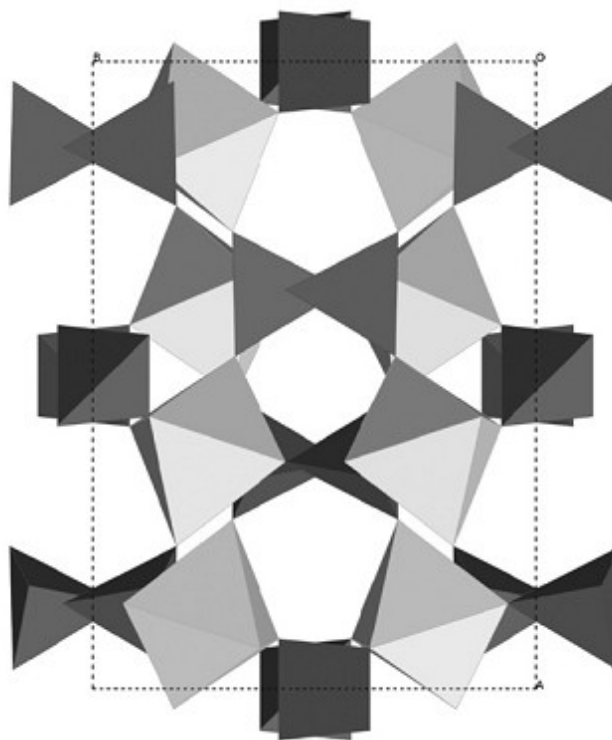


Figure 1.7: Crystal structure of $Y_2Mo_3O_{12}$ in the $Pbcn$ phase with YO_6 octahedra in light grey and the MoO_3 tetrahedra shown in dark grey. Reprinted with permission from Gates, S. D.; Lind, C. J. *Solid State Chem.* **2007**, *180*, 3510–3514. Copyright 2007 Elsevier.

Both structures descend from the denser garnet structure, which has three different fully occupied cation environments: octahedral, tetrahedral and 8-fold coordinate. The orthorhombic and monoclinic $A_2M_3O_{12}$ framework structures are similar. Whereas garnet has full occupation of the 8-fold sites, they are totally empty in the framework structures, creating microchannels. This can be a hindrance ($Y_2Mo_3O_{12}$,^{189,190,191} $Y_2W_3O_{12}$ ¹¹⁴ and rare-earth compounds¹³⁵ are highly hydroscopic taking water in the microchannels) or advantageous (fast ionic conduction through the insertion of small cations such as Li^+ inside the framework structure).¹⁹²

The phases which adopt the orthorhombic structure generally transform to monoclinic at lower temperatures, although in some cases such as $Sc_2W_3O_{12}$, $Y_2W_3O_{12}$ or $Y_2Mo_3O_{12}$ this phase transformation does not appear even at the lowest temperatures examined. The monoclinic phases are denser than the orthorhombic, and the former therefore demonstrate only positive thermal expansion while the latter can exhibit thermomiotic behavior (Table 1.3). The orthorhombic to monoclinic phase transformation is displacive with a very small enthalpy of transition, 2 kJ mol^{-1} or less.¹⁹³ Higher-temperature phase transitions are seen for Fe and Cr-based tungstates and molybdates in comparison to compounds with trivalent cations with lower electronegativity. Generally the $A_2Mo_3O_{12}$ orthorhombic phases transform to monoclinic counterparts at temperatures higher than for $A_2W_3O_{12}$.^{76, 194, 195, 196}

Table 1.3: Average linear coefficients of thermal expansion (α_ℓ) of select $A_2M_3O_{12}$ materials determined from X-ray powder diffraction, over a given temperature range.

Material	<i>Monoclinic Phase</i>		<i>Orthorhombic Phase</i>	
	<i>T / K</i>	$\alpha_\ell / \times 10^{-6} \text{ K}^{-1}$	<i>T / K</i>	$\alpha_\ell / \times 10^{-6} \text{ K}^{-1}$
$\text{Y}_2\text{Mo}_3\text{O}_{12}$ ³⁵	-	-	20-450	-9.02
$\text{Y}_2\text{Mo}_3\text{O}_{12}$ ¹⁸⁹	-	-	403-1073	-12.6
$\text{Y}_2\text{W}_3\text{O}_{12}$ ¹⁹⁷	-	-	15-1373	-7.0
$\text{In}_2\text{Mo}_3\text{O}_{12}$ ¹⁹⁶	373-593	12.4	643-1033	-1.85
$\text{In}_2\text{W}_3\text{O}_{12}$ ¹⁹⁸	-	-	250-600	3.1
$\text{HfMgMo}_3\text{O}_{12}$ ¹⁹⁹	-	-	298-1013	1.02
$\text{HfMgW}_3\text{O}_{12}$ ⁸¹	-	-	400-800	-1.2
$\text{Al}_2\text{W}_3\text{O}_{12}$ ³⁸	-	-	Not Reported	2.2
$\text{Al}_2\text{Mo}_3\text{O}_{12}$	150-450	9.51 ²⁰⁰	523-923	2.39 ²⁰¹
$\text{Sc}_2\text{Mo}_3\text{O}_{12}$ ⁷⁶	4-170	7.3	180-300	-2.1
$\text{Sc}_2\text{W}_3\text{O}_{12}$ ¹⁹⁵	-	-	10-1073	-2.2
$\text{Cr}_2\text{Mo}_3\text{O}_{12}$ ²⁰¹	-	-	693-1023	0.67
$\text{Yb}_2\text{Mo}_3\text{O}_{12}$ ²⁰²	-	-	473-1073	-6.103
$\text{Fe}_2\text{Mo}_3\text{O}_{12}$ ²⁰¹	-	-	823-1023	1.72

Another peculiarity of $A_2M_3O_{12}$ phases is lack of complete rigidity of their polyhedra. While ZrO_6 octahedra in ZrW_2O_8 ³⁵ are known to be highly distorted ($\approx 20\%$ as calculated through the Makovicky and Balic-Zunic approach¹⁷⁵), this distortion is independent of temperature (0.3 K to 1050 K). The polyhedra in $A_2M_3O_{12}$ are also distorted, but at a much lower level ($< 1\%$) and this distortion increases with increasing temperature. A correlation has been established between the degree of distortion of AO_6 and the coefficient of thermal expansion, suggesting that less rigid octahedra lead to more

negative CTEs within the $A_2M_3O_{12}$ family.³⁵ Liang *et al.*¹⁹⁰ used Raman spectroscopy to show that in $A_2M_3O_{12}$ high-energy optical phonon modes, due to distortion of MO_4 , together with the low-energy transverse thermal vibrations as commonly observed for the AM_2O_8 crystal family, are responsible for thermomiotic behavior.

In an attempt to synthesize $A_2M_3O_{12}$ compounds with a controllable coefficient of thermal expansion, Suzuki and Omote²⁰³ substituted the A^{3+} cation with Hf^{4+} and Mg^{2+} in a 1:1 ratio. Instead of $HfMgW_3O_{12}$ in an orthorhombic $Pbcn$ structure, they obtained an orthorhombic $Pnma$ phase at room temperature. However, Gindhart *et al.* reported a monoclinic $P2_1/a$ structure for $HfMgW_3O_{12}$ at room temperature, showing a transition to the orthorhombic $Pnma$ space group between 400 K and 473K.⁸¹ The orthorhombic phase demonstrates NTE. The reversibility of this phase transition suggests that the connectivity in $Pnma$ would be similar to the one established for the $Pbcn$ and $P2_1/a$ space groups. Other phases, such as $HfMgMo_3O_{12}$ ¹⁹⁹ and $ZrMgW_3O_{12}$ ¹⁴² adopt an orthorhombic $Pnma$ phase at ambient and higher temperatures. The full crystal structures of this class of ceramics are yet to be resolved.

1.6.1.4 AMO_5

The AMO_5 family includes at least four different framework structures, two of them tetragonal ($P4/n$ and $P4/nmm$), one monoclinic ($P2_1/c$) and one orthorhombic ($Pnma$). Tetragonal $NbOPO_4$ ($P4/n$) transforms to $P4/nmm$ at ~ 470 K,²⁰⁴ while monoclinic $NbOPO_4$ transforms to orthorhombic at ~ 570 K.²⁰⁵ All four structures are built from AO_6 octahedra and MO_4 tetrahedra and present the same type of corner connectivity, *i.e.*, the octahedra (AO_6) are connected through vertices to four MO_4

tetrahedra and two AO_6 , while MO_4 tetrahedra share their vertices only with AO_6 octahedra. However, only the orthorhombic phase has NTE along all three axes, resulting in overall NTE, while the tetragonal $P4/nmm$ and monoclinic phases present NTE only along the a -axis.^{204,205}

1.6.1.5 AO_3 and Related Structures

The crystal structure of the AO_3 ceramic family can be rationalized as a perovskite ABO_3 structure with completely vacant A sites, resulting in a simple framework structure formed exclusively from corner-shared octahedra with a lot of free space. This simple, primitive cubic structure is the archetypal polyhedral arrangement for the underlying NTE phenomenon in framework ceramic structures, since it best illustrates the transverse thermal motions of the two-fold atoms, considered as the basic mechanism responsible for NTE in framework structures.

However, the best known representative of this family, ReO_3 , unexpectedly demonstrates very complex, rarely negative, thermal expansion.^{172,206,207} Chatterji *et al.*,²⁰⁷ for example, reported a small negative CTE ($\approx -10^{-6} \text{ K}^{-1}$) for some temperature ranges, such as 2 K to 220 K and 600 K to 680 K, while between 220 K and 600 K and above 680 K they observed a positive CTE. On the other hand, Taylor²⁰⁸ reported a small positive CTE ($\approx 2 \times 10^{-6} \text{ K}$) between 123 K and 486 K. Based on a thorough neutron powder diffraction study, Rodriguez *et al.*²⁰⁹ proposed that the thermal expansion properties of ReO_3 are highly dependent on the crystal structure defects within the structure, more precisely on the static disorder of oxygen ions in the direction perpendicular (transverse) to the Re-O-Re linkages. The ReO_3 samples with more

pronounced oxygen static disorder³⁶ demonstrated NTE over a smaller temperature interval in comparison to the more ordered ReO_3 crystals. Static disorder of two-fold oxygens would impact lattice dynamics and diminish the contribution of low-energy modes responsible for NTE.

The isostructural compounds, TaO_2F and NbO_2F , corroborate only partially the rationalization of Rodriguez *et al.*²⁰⁹ on the static disorder effect over lattice dynamics of this structure, since only TaO_2F shows a complex, very low negative or positive coefficient of thermal expansion ($\approx \pm 10^{-7} \text{ K}^{-1}$) over the temperature range between 20 K and 773 K,²¹⁰ and static disorder of O/F ions in transverse directions is well documented for TaO_2F .³⁶ However, NbO_2F , shows high positive coefficient of thermal expansion ($\approx 10 \times 10^{-6} \text{ K}^{-1}$) in the range from 20 K to 300 K;²¹⁰ data on disorder of O/F and Nb might help sort this out.

Many metal trifluorides have a ReO_3 -type structure, however only ScF_3 crystallizes in the primitive cubic structure. Others adopt a rhombohedral structure in which octahedra unfold on heating leading to high positive CTE. ScF_3 is the only known example of a ReO_3 -type phase with a highly negative CTE, from 10 K to 1100 K.²¹¹ Recent inelastic neutron scattering results²¹² indicate that thermomiotic behavior is related to thermal stiffening of modes at low frequencies. The ScF_6 octahedra are more flexible than their oxide counterparts, and NTE is related to the anharmonic motion of F transverse to the bond direction, pulling the two Sc closer together.²¹²

1.6.1.6 Other Oxides

1.6.1.6.1 Lithium aluminum silicates (LAS)

Lithium aluminum silicates (LAS) and their unusual thermal expansion properties have been known for almost sixty years and for several decades have been the basic materials of the shock-resistant cookware industry.²¹³ Both β -spodumene and β -eucryptite, derived from the quartz crystal structure, form a denser structure with the negatively charged aluminosilicate framework balanced with Li^+ in the channels formed from Si,Al-O tetrahedra. The anomalous thermal expansion in the LAS family involves relief of strain in the tetrahedra-based rings (β -spodumene) and temperature-dependent disorder process of lithium cations moving from tetrahedra to six-fold coordination (β -eucryptite).²¹⁴

1.6.1.6.2 M_2O

Two members of the M_2O family, Cu_2O and Ag_2O , crystallize in a rare cubic crystal structure, known as cuprite, comprised of a framework built from corner-shared OM_4 tetrahedra with cations (Cu or Ag) in the two-fold coordination instead of oxygen. While Ag_2O shows NTE over its temperature stability range, Cu_2O has a change from NTE to PTE.^{215,216,217} The enhanced flexibility of OCu_4 tetrahedra at low temperature leads to a decrease in the vertex-vertex $M\bullet\bullet\bullet M'$ distance, and NTE, but when the $M\bullet\bullet\bullet M'$ distance is sufficiently low, at temperatures higher than 200 K, cuprophilic interactions dominate and lead to PTE.¹⁷⁹

1.6.1.6.3 Zeolites and Aluminophosphates

Zeolites are microporous aluminosilicate materials with open framework structures and can exhibit negative thermal expansion, although the magnitude and temperature range vary greatly. The framework structures can be described as alternating, corner-sharing SiO_4 and AlO_4 tetrahedra for aluminosilicate zeolites, or AlO_4 and PO_4 tetrahedra for aluminophosphates (AIPOs). NTE in zeolites and AIPOs was actually predicted from calculations before experiments were performed.^{218,219} Negative thermal expansion has been measured in many microporous zeolite-type solids,^{80,220,221,222,223,224,225,226,227,228,229,230,231} and it has been suggested that NTE in zeolite-type solids is the norm rather than the exception.²²³ The mechanisms for NTE in these materials are not completely understood, nor are they necessarily the same for all thermomiotic zeolites. For instance, siliceous faujasite, which has a cubic structure and $\alpha_V = -1.3 \times 10^{-5} \text{ K}^{-1}$ over the range 25 K to 573 K,²²⁶ has thermomiotic behaviour attributed to transverse vibrations of the bridging oxygen atoms while ferrierite, an anisotropic aluminosilicate zeolite shows NTE ($\alpha_V = -2.4 \times 10^{-5} \text{ K}^{-1}$ from 420 K to 560 K).⁸⁰ due to transverse vibrations of the bridging oxygen atoms leading to cooperative rotations of the SiO_4 or AlO_4 tetrahedra, which cause a partial collapse of the walls of the porous channels.⁸⁰ The negative thermal expansion in Na-zeolite X²¹⁸ and zeolite A²²² are also believed to be due to a partial structure collapse.²²¹ AIPO-17, an aluminophosphate that consists of alternating, corner-sharing AlO_4 and PO_4 tetrahedra, exhibits strong NTE ($\alpha_V = -3.5 \times 10^{-5} \text{ K}^{-1}$) from 18 K to 300 K²³² as do siliceous zeolites with the MFI structure.²²⁰

1.6.1.6.4 Perovskites and Anti-Perovskites

PbTiO₃-based compounds are ferroelectric perovskite materials that exhibit NTE. By substituting the Pb and Ti cations in these compounds, the thermal expansion characteristics can be tailored, from large NTE to near-zero NTE.^{45,233,234,235}

Mechanisms responsible for thermomiotic behavior in these systems include spontaneous polarization displacement,⁴⁵ phase transitions associated with intermetallic charge transfer,⁴⁶ intersite charge transfer, and magnetovolume transitions.⁴⁸

1.6.2 METAL CYANIDES

1.6.2.1 $M(\text{CN})_2$

Compounds of the form Zn_{1-x}Cd_x(CN)₂ ($0 \leq x \leq 1$) have been reported^{39,236} to have large isotropic NTE ($\alpha_\ell = -17$ to $-20 \times 10^{-6} \text{ K}^{-1}$) between 150 K and 375 K. Substitution of Zn by Cd leads to a more negative CTE.³⁹ Their polymeric network structure is formed by cyanide bridging ligands tetrahedrally coordinated to the metals, and the cubic unit cell contains two interpenetrating β -cristobalite-like tetrahedral networks.^{39,236} The apparent Zn–C/N bond length measured by diffraction decreases with increasing temperature due to the out-of-plane motion of the CN units.¹⁷⁸ Ni(CN)₂ is a 2D framework compound; the cyanide units bind to the nickel atoms in a square planar geometry, creating a structure consisting of layered sheets with NTE in the plane of the sheets, but a large PTE perpendicular to the sheets resulting in a positive α_γ .²³⁷

1.6.2.2 $A_x[M(CN)_6]$ ($x = 1, 1.5, 3$)

Many metal cyanides with the formula unit $A_x[M(CN)_6]$ form network structures that have been shown to display thermomiotic behavior.

The Prussian Blue analogs have $x = 1$, M is Pt^{4+} and A is a metal in the +2 oxidation state, usually a first-row transition metal.²³⁸ Their CTEs vary with the choice of A , with larger metals giving rise to larger NTE due to the weaker $A-N$ bonds.²³⁸ The subsequent increase in the flexibility of the structures increases the number of easily excited low-frequency phonon modes.²³⁸

Replacement of Pt^{4+} by Fe^{3+} Co^{3+} leads to related compounds with the formula unit $A_3[M(CN)_6]_2$, forming a perovskite-like structure.²³⁹ Compounds containing Co^{3+} have been found to consistently exhibit large thermomiotic behavior.²³⁹ while Fe^{3+} compounds were found to have a much broader range of CTEs, from largely positive to largely negative CTE.²³⁹ Hydration has been found to increase the NTE by enhancing the framework flexibility *via* replacement of the cyanide units.^{239,240}

$Ag_3[Co(CN)_6]$, the first “colossal” PTE and NTE material, (defined as $|\alpha_\ell| \geq 100 \times 10^{-6} K^{-1}$) has a trigonal framework structure in which octahedrally coordinated Co atoms are linked through Co–CN–Ag–NC–Co chains²⁴¹ Upon heating the layered structure expands (isomorphic to the Prussian Blue analogs), while the CTE in the direction perpendicular to the layers is extremely negative.²⁴¹ Subsequently, α_ν is large and positive.

1.6.2.3 MCN

MCN compounds ($M = \text{Cu}, \text{Ag}, \text{Au}$) exist as infinite $M\text{-CN-}M$ chains.²⁴² The thermal expansion along the chains is negative, but the volumetric CTEs are positive.^{242,243} In $\text{Au}(\text{CN})$, both transverse and rotational movements of cyanide units lead to thermomiotic behavior²⁴³ while NTE in $\text{Ag}(\text{CN})$ is mainly due to transverse motions: local vibrations of the CN bridges and non-local wave-like motions involving transverse displacement of the Ag atoms.²⁴³ The basic structure of $M\text{-CN}$ chains can be modified by using a mixture of metal atoms (Ag and Cu) and the introduction of a large cation such as Cs, producing novel structures such as helical Cu–CN chains linked by Ag–CN bridges and other 2D and 3D networks of linked Cu–CN chains.²⁴⁴ Unfortunately, the CTEs of these materials have yet to be reported.

1.6.2.4 Clathrates

Metal cyanide thermomiotic materials have a large amount of free space in their lattices. Two examples are $\text{Zn}[\text{Pt}(\text{CN})_6]$ and $\text{Cd}[\text{Pt}(\text{CN})_6]$ which have nanopores between their octahedral rigid units.²⁴⁵ Water molecules occupying the interstitial space and can increase the CTE of the material by dampening transverse vibrations of cyanide bridges, as observed for $\text{Zn}[\text{Pt}(\text{CN})_6]$.²⁴⁵ However, the increased volume of the interstitial spaces in $\text{Cd}[\text{Pt}(\text{CN})_6]$ prevents the water molecules from strongly interacting with the cyanide bridges and affecting the CTE.²⁴⁵

Clathrates such as $\text{Cd}(\text{CN})_2$ can undergo self-assembly from aqueous solution^{246,247} forming a $\text{Cd}(\text{CN})_2 \cdot \text{CCl}_4$ clathrate with tailorable CTE controllable by removal of the guest molecules.²⁴⁸ $\text{N}(\text{CH}_3)_4\text{CuZn}(\text{CN})_4$ is a nearly zero CTE clathrate

material (average $\alpha_\ell = 0.67 \times 10^{-6} \text{ K}^{-1}$ between 200 K and 400 K) where exactly half the interstitial pores are filled with positively charged $\text{N}(\text{CH}_3)_4^+$ guests.²⁴⁹

1.6.3 OTHER STRUCTURES

1.6.3.1 Metal-Organic Framework (MOF) Materials

Metal-organic framework materials are a class of porous materials that consist of metal-oxygen clusters connected by rigid (or semi-rigid) organic linkers. The interest in these materials is mainly for applications such as gas adsorption that take advantage of the large available surface area and tailorable pore size.²⁵⁰ RUMs similar to those present in other NTE oxides lead to thermomiotic behavior in MOF-5 [$\text{Zn}_4\text{O}(\text{1,4-benzenedicarboxylate})_3$] ($\alpha_\ell \approx -16 \times 10^{-6} \text{ K}^{-1}$ to $-10 \times 10^{-6} \text{ K}^{-1}$ from 4 K to 600 K) where the ZnO_4 tetrahedra and phenyl rings act as rigid units and the carboxylate groups serve as the flexible units allowing large amplitude transverse vibrations (Figure 1.8).²⁵¹

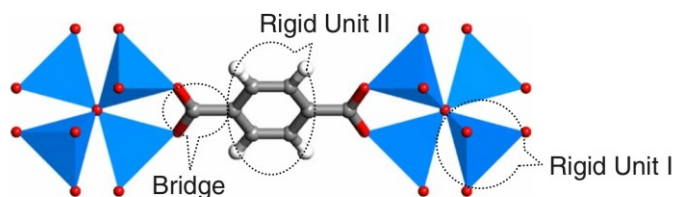


Figure 1.8: A partial structure of MOF-5, showing that the ZnO_4 tetrahedra and the phenyl rings serve as the rigid units (I and II, respectively in the figure), while the carboxyl groups serve as a bridging unit. Negative thermal expansion in this material arises from the large amplitude transverse vibrations of the bridging carboxyl groups. From reference 251, with permission. Copyright 2008 the American Physical Society.

The MOF material $\text{Cu}_3(1,3,5\text{-benzenetricarboxylate})_2$ also exhibits NTE with $\alpha_t \approx -4 \times 10^{-6} \text{ K}^{-1}$ in the temperature range 50 K to 500 K.²⁵² Molecular simulations have correctly predicted the sign and the magnitude of the thermal expansion coefficients of MOFs.^{119,251,253}

1.6.3.2 NaSICON

Sodium super-ionic conductors (abbreviated NaSICON or NASICON) are based on $\text{NaZr}_2(\text{PO}_4)_3$ (abbrev. NZP) where substitutions of the metal ions can lead to thermal expansion properties that differ greatly²⁵⁴ and allow for tailoring of the CTE. The thermal expansion behavior of these materials are anisotropic, and can be negative either along the *c*-axis or the *a*-axis, depending on the crystal space group.²⁵⁵ One material that has NTE along the *a*-axis from 20 °C to 700 °C is $\text{NbTi}(\text{PO}_4)_3$ with α_a ranging from -4.3 to $-0.1 \times 10^{-6} \text{ K}^{-1}$; although α_c is positive, α_V is negative.²⁵⁶

1.6.3.3 Nanomaterials

There is a strong theoretical background for the vibrational contribution to CTE in nanomaterials,¹⁷¹ predicting higher CTEs for nanomaterials in comparison to their bulk counterparts arising from the shallower and asymmetric potential for surface atoms due to their incomplete coordination, compared to the bulk atoms.²⁵⁷

However there are some reports of non-vibrational effects on CTE of nanosized materials where nanometric CuO shows giant NTE ($\alpha_V = -110 \times 10^{-6} \text{ K}^{-1}$) below its Néel temperature ($T_N \approx 200 \text{ K}$),²⁵⁸ whereas bulk CuO has near zero CTE in the same

temperature range. Similarly, nanometric $\text{Mn}_3(\text{Cu}_{1-x}\text{Ge}_x)\text{N}$ presents much more pronounced NTE than its bulk counterpart²⁵⁹ and gold nanoparticles show a change in the sign of the thermal expansion coefficient at 125 K.²⁶⁰ The NTE is attributed to the effects of the valence electron potential on the equilibrium lattice separations.

1.6.3.4 Other Structures

Water contracts from 273 K to 277 K with the NTE due to compression breaks up tetrahedral hydrogen bonds, increasing the entropy, resulting in NTE.⁴ Ice (Ih phase) also exhibits NTE for $T < 60$ K,²⁶¹ and this also is attributed to changes in hydrogen bonding.

NTE also occurs in some organic materials, however most exhibit anisotropic CTEs, and have $\alpha_V > 0$.^{262,263,264} NTE is known for C_{60} at $T < 3$ K,²⁶⁵ and is attributed to loss of free rotation and onset of libration.²⁶⁶ Graphene exhibits NTE of $-7 \times 10^{-6} \text{ K}^{-1}$.²⁶⁷ Other nanomaterials could be expected to exhibit NTE, as suggested by simulations for carbon nanotubes²⁶⁸ and Si nanowires.²⁶⁹

The simple molecular solid CH_4 exhibits NTE at very low temperatures ($T < 9$ K) in the solid state,²⁷⁰ associated with quantum effects.

1.7 COMPOSITE MATERIALS

Reduction of the positive CTE of a material by inclusion of thermomiotic filler, forming a composite, has been reported for a wide variety of matrices, including cement,²⁷¹ polymers,^{122,166} metals,^{272,273} and ceramics.¹⁸⁶ Many of these composites

include ZrW_2O_8 as the filler material, although molybdate-,²⁷⁴ LAS-²⁷⁵, and nitride-based²⁷⁶ composites have also been reported. ZrW_2O_8 is advantageous because of its isotropic NTE, wide temperature range of thermal stability, lack of moisture sensitivity and commercial availability, but it is expensive.

The ZrO_2 - ZrW_2O_8 composite system is of special interest because ZrW_2O_8 can be formed *in situ* during sintering *via* solid-state reaction of ZrO_2 and WO_3 .^{277,278} The composition can be tailored to produce nearly zero CTE materials, outside of the temperature range in which the α - to β -phase transition occurs.^{186,277,278,279} However, the resulting composites are difficult to densify because the thermal stability limit of ZrW_2O_8 is below the optimal sintering temperature for ZrO_2 , resulting in a reduced stiffness.²⁷⁷ The densification can be improved by the addition of a small amount of Al_2O_3 , which forms an $\text{Al}_2\text{W}_3\text{O}_{12}$ liquid phase.²⁷⁷ Finite element method simulations indicate that the ZrW_2O_8 in these composites is subject to significant thermal stress, potentially producing the undesirable γ -phase.^{70,112}

When the thermomiotic material in a composite is not formed *in situ*, additional considerations of matrix-filler bonding and dispersion arise.^{122,166} To increase the homogeneity of the composite, the thermomiotic filler particles should be small so that they mix well with the polymer;¹²² thermomiotic nanoparticles can be prepared hydrothermally.¹²² The particles need to be surface-modified to improve matrix-filler bonding,^{122,166} which improves the composite's CTE.¹⁶⁶ Matrix-filler bonding is also a factor in the production of ceramic composites, for example in the SiC - ZrW_2O_8 system, where borosilicate glass has been used as a bonding agent.¹⁶⁰

1.8 SOLID SOLUTIONS

Solid solutions are homogeneous solids. Interstitial solid solutions form when a small solute occupies a hole or interstice in the lattice. To date there are no thermomiotic systems reported for interstitial solid solutions, likely because they prevent low-frequency modes that can lead to NTE.

However, substitutional solid solutions, formed when atoms of one type in a crystal lattice are partially replaced by atoms of a second type in either a disordered or ordered fashion, are far more practical for thermomiotic materials. Such substitutions follow the Hume-Rothery rules:¹⁸ each component should have the same type of crystal structure; there should be no more than 15 % difference in atomic radius; the solute and solvent should have similar electronegativities; and the solute and solvent should have similar valence.

There have been several investigations of ZrW_2O_8 solid solutions to improve the physical properties, including CTE. $ZrW_{2-x}Mo_xO_8$ solid solutions can improve the thermal and mechanical properties of ZrW_2O_8 .^{280,281, 282} Replacement of Zr by Sn^{4+} ,²⁸³ Sc^{3+} , Y^{3+} , In^{3+} ,^{284,285} Lu^{3+} ,²⁸⁶ Eu^{3+} , Er^{3+} , and Yb^{3+} ,²⁸⁷ improves the mechanical properties while having very little impact on the CTE.²⁸⁸

There has been some investigation of solid solutions of the $A_2M_3O_{12}$ family primarily to explore the CTE.^{128, 134, 274, 289, 290, 291, 292, 293} Li *et al.* and Dasgupta *et al.* have also investigated the effects of replacing Y^{3+} with Fe^{3+} in $Y_2Mo_3O_{12}$ to reduce the hygroscopic nature of the material and the potential of $Al_{2-x}Sc_xW_3O_{12}$ systems as infrared transmitting windows, respectively.^{191,294}

1.9 RESEARCH GOALS

As shown previously, in Section 1.3.2, the low-frequency optic phonons associated with NTE can reduce the phonon mean free path and lead to low values of thermal conductivity in ZrW_2O_8 ⁵⁷ and HfMo_2O_8 .⁷¹ If this reduction in thermal conductivity is a general phenomenon for thermomiotic materials, and other members of the families associated with NTE materials, then the resulting poor thermal fracture resistance (see equation (1.6)) of these materials could reduce their utility in composites or industrial applications that are exposed to thermal cycling. Improvements in the thermal fracture resistance of materials could instead be accomplished by developing homogeneous materials with near-zero coefficients of thermal expansion.

Towards this end, several materials in the $A_2\text{Mo}_3\text{O}_{12}$ family have been synthesized using a variety of techniques: sol-gel, the solid-state reaction method, and mechanical activation. These compounds have been selected for their large range of CTE values (from low positive to large negative; see Table 1.3), similarities in crystal structure, and ease of synthesis to develop a test set of materials from which to gain a better understanding of the thermal properties associated with NTE. Although some are known to be hygroscopic, care has been taken to select candidates with negligible hygroscopicity where possible. Difficulties associated with accurately determining the properties of hygroscopic materials will be discussed where applicable.

Within the existing literature, it is difficult to delineate which thermal properties are exclusively related to thermomiotic behavior since comparisons must be made between families of compounds. By developing a range of materials, in one

compositional family, with low-positive, near-zero, low-negative, and large-negative CTE values, the role of low-frequency modes in these materials can be more clearly understood.

To this end, $\text{Y}_2\text{Mo}_3\text{O}_{12}$, $\text{Al}_2\text{Mo}_3\text{O}_{12}$, $\text{In}_2\text{Mo}_3\text{O}_{12}$, $\text{HfMgMo}_3\text{O}_{12}$, and two solid solutions, $\text{In}(\text{HfMg})_{0.5}\text{Mo}_3\text{O}_{12}$ and $\text{In}_{1.5}(\text{HfMg})_{0.25}\text{Mo}_3\text{O}_{12}$, have been synthesized to determine the relationship between the mechanisms of negative thermal expansion in the $A_2\text{Mo}_3\text{O}_{12}$ family and low-frequency phonon modes of these materials through their thermal conductivity and heat capacity. In particular, the question of whether the low thermal conductivity that has been observed in ZrW_2O_8 ⁵⁷ and HfMo_2O_8 ⁷¹ is a general property of open-framework materials with negative, near-zero or low-positive thermal expansion is addressed. Sample composition and particle morphology was determined using scanning electron microscopy and X-ray powder diffraction was used to confirm the phase purity of all the samples. X-ray powder diffraction and dilatometry were used to determine the intrinsic and extrinsic (bulk) thermal expansion coefficients in a step towards zero thermal expansion materials.

CHAPTER 2 SAMPLE PREPARATION

In this section the synthesis and sample preparation methods will be discussed in detail. Synthetic methodologies were chosen based on ease of synthesis, purity of the final product, and time constraints, while sample preparation and measurements were performed following two distinct routes depending on the air stability of the samples.

Unless otherwise stated, all sample preparation and characterization has been carried out by the author, Kimberly J. Miller. Contributions from other parties to sample preparation, characterization and data analysis are credited as appropriate throughout this thesis.

2.1 SYNTHETIC METHODS

The ceramic samples that were prepared to examine the thermal properties of members of the $A_2Mo_3O_{12}$ family (Table 2.1) were synthesized *via* three routes; two are standard solid-state reaction methods and the third is a simplified sol-gel approach designed to simplify the synthesis of these materials and lower the energy cost. In this section the three synthetic routes are explored in detail.

Table 2.1: Members of the $A_2\text{Mo}_3\text{O}_{12}$ family synthesized by three reaction methods: solid-state reaction (SSR), mechanical activation (MA), and a simplified sol-gel approach.

Material	Method	Material	Method
$\text{Y}_2\text{Mo}_3\text{O}_{12}$	MA	$\text{In}_{1.5}(\text{HfMg})_{0.25}\text{Mo}_3\text{O}_{12}$	MA
$\text{Y}_{1.5}\text{In}_{0.5}\text{Mo}_3\text{O}_{12}$	MA	$\text{In}(\text{HfMg})_{0.5}\text{Mo}_3\text{O}_{12}$	MA
$\text{YInMo}_3\text{O}_{12}$	SSR, MA	$\text{HfMgMo}_3\text{O}_{12}$	MA
$\text{Y}_{0.5}\text{In}_{1.5}\text{Mo}_3\text{O}_{12}$	SSR	$\text{Al}_2\text{Mo}_3\text{O}_{12}$	Sol-Gel
$\text{In}_2\text{Mo}_3\text{O}_{12}$	MA		

The two solid-state routes, solid-state reaction and mechanical activation, require much the same preparation and reagents, the difference being in the initial steps of the synthesis. The reactions were performed over the course of three weeks in Brazil, in the laboratory of collaborator Dr. Bojan Marinkovic, at Pontificia Universidade Católica de Rio de Janeiro – PUC-Rio, Brazil, during which time all the samples needed for this study had were prepared. For this reason, mechanical activation was the synthesis method of choice for the majority of the samples since this method required half as much time as the standard solid-state reaction approach.

The materials used for the three reaction methods are listed with their suppliers and purities in Table 2.2.

Table 2.2: Suppliers and purities of reagents used for the three synthetic routes.

Material	Supplier
Molybdenum oxide (MoO ₃)	Fluka 99.98%
Yttrium oxide (Y ₂ O ₃)	Labosi 99.9%
Indium oxide (In ₂ O ₃)	Fluka 99.9 %
Hafnium oxide (HfO ₂)	Aldrich 98 %
Magnesium oxide (MgO)	Fluka 99.5 %
Aluminum nitrate (Al(NO ₃) ₃ .9H ₂ O)	Vetec, 98%
Ammonium molybdate ((NH ₄) ₆ Mo ₇ O ₂₄ .4H ₂ O)	Vetec, 99%
Polyvinyl alcohol (PVA)	Vetec

2.1.1 SOLID-STATE REACTION METHOD

As mentioned previously, the solid-state reaction and mechanical activation methods are both similar in approach and design, the difference being in the activation of the materials in the latter. For both methods, the component oxides must first be treated to remove impurities and moisture. The oxides (~5 g each) were heated at a rate of 30 K per minute from room temperature to 773 K and held isothermally for 3 h except MoO₃ (Fluka 99.98 %) which was calcined at 873 K for 6 h. Following the heat treatment, reagents were stored in a furnace at 373 K until use.

Materials produced by the solid-state reaction method were prepared by combining a stoichiometric mixture of reagents (to a total of 5 g), mixed and homogenized in agate mortar and then heat treated in air in alumina crucibles at 973 K for 48 h, with grinding every 12 h, and then heated to 1053 K for 20 h, followed by cool down in the furnace. Powder patterns were collected *via* X-ray powder diffraction

(XRPD) to check for the presence of starting materials. If there was unreacted starting material, the samples were heated further at 1053 K, then cooled to room temperature, until no reactants were detectable by XRPD. The average time for completion of the synthesis process was 84 h. The resulting powder was then pressed into 1 cm pellets using a Schulz Tecnologia de Vanguarda press with a pressure of 250 MPa and then the pellets were heated to 1003 K for 18 h. Heat treatment of the component oxides and the precursor solutions were both carried out in a Tubular Maitec – INTI FET 1600/H furnace.

2.1.2 MECHANICAL ACTIVATION

The average time for the completion of a synthesis *via* mechanical activation was 42 h, half the amount of time required for the standard solid-state synthesis approach. Therefore, this approach was more highly favoured with the time constraints.

Samples were prepared using a solid-state reaction technique involving activation of precursor oxides *via* a mechanical activation step. Similarly to the solid-state process, sample impurities were removed by the same heat treatment mentioned in Section 2.1.1. Following the heat treatment, reagents were stored in a furnace at 373 K until use. The component oxides were stoichiometrically measured, homogenized for 15 minutes with an agate mortar and pestle, and then mechanically activated, using a steel vial and balls, in a SPEX 1000M mixer for two 5 h intervals, 1 h apart, followed by calcination at 973 K for 12 h. The resulting powder was then pressed into 1 cm pellets using a Schulz Tecnologia de Vanguarda press with a pressure of 250 MPa and then heated to 1003 K for 18 h. Heat treatments of the component oxides and the precursor solutions were both

carried out in a Tubular Maitec – INTI FET 1600/H furnace. XRPD was used to confirm sample purity and monophasic composition of the samples.

2.1.3 SIMPLIFIED SOL-GEL SYNTHESIS[†]

Aluminum molybdate was prepared through a PVA assisted sol-gel technique from a stoichiometric mixture of aluminum nitrate $[\text{Al}(\text{NO}_3)_3 \cdot 9\text{H}_2\text{O}]$ and ammonium molybdate $[(\text{NH}_4)_6\text{Mo}_7\text{O}_{24} \cdot 4\text{H}_2\text{O}]$ in either a 1:2 or 1:8 mole ratio of reagents to PVA. The PVA (5 g) was first dissolved in 50 mL distilled water and heated to 373 K with magnetic stirring until the solution was viscous. The reactants, $\text{Al}(\text{NO}_3)_3 \cdot 9\text{H}_2\text{O}$ and $(\text{NH}_4)_6\text{Mo}_7\text{O}_{24} \cdot 4\text{H}_2\text{O}$, were then dissolved (in appropriate amounts to achieve the 1:2 and 1:8 mole ratio with respect to PVA) into 50 mL of distilled water, added to the PVA solution and held at 373 K for 24 h until a precursor gel was formed. Two grams of the gel was placed in an alumina crucible and then heated at 30 K min^{-1} to 873 K or 973 K and held isothermally for 20 min or 15 min, respectively, before being allowed to cool within the furnace. Ratios of metal ions to PVA, calcination temperature, and calcination times were altered in order to tailor particle size.

The precursor gels prepared with 1:2 and 1:8 metal-to-PVA ratios were studied by thermogravimetric analysis (TGA) in a Shimadzu 51H instrument (In Dr. Bojan Marinkovic's lab at PUC-Rio, Brazil), using a heating rate of 10 K min^{-1} , in order to

[†] Adapted and used with permission from: Ari, M.; Miller, K. J.; Marinkovic, B. A.; Jardim, P. M.; de Avillez, R.; Rizzo F.; White M. A. *J. Sol-Gel Sci. Technol.* **2011**, *58*, 121–125. K.J. Miller's contribution to the work in this manuscript was: developing the synthetic technique and performing the preliminary sol-gel experiments with M. Ari as well as consultations on experimental results. Contributions also included drafting and writing most of the first draft of the manuscript and subsequent editing.

determine the temperatures of redox reaction between PVA and nitrates, and of organic residue decomposition.²⁹⁵

2.2 SAMPLE PREPARATION AND SINTERING METHODOLOGIES

Sample preparation is as crucial to measurements as the purity of the samples themselves. The measurement procedures for thermal conductivity and dilatometry measurements require sample pellets able to withstand thermal stress (temperature gradient across a sample) and mechanical stress (sample mounted between two plates or held between a pushrod and sample chamber). Samples were prepared for thermal conductivity and heat capacity measurements following the same protocol, producing samples with diameters of ~ 2 mm and heights of ~1 mm, but samples for dilatometry required a modified procedure to further improve the mechanical stability of larger samples with diameters of 5 mm and sample heights > 2 mm.

In addition to preparing robust samples, there was the additional complication of hygroscopic samples. While $\text{In}_2\text{Mo}_3\text{O}_{12}$, $\text{HfMgMo}_3\text{O}_{12}$, and their solid solutions were not hygroscopic, $A_2\text{Mo}_3\text{O}_{12}$ materials containing large cations, such as yttrium, contain molecular channels large enough for water molecules to enter and disrupt the vibrational modes responsible for NTE and cause amorphization.¹¹⁵ It was experimentally determined that the method of preparation for most the air-stable samples was not suitable for hygroscopic samples and so two separate methods were developed, each tailored to the materials' specific requirements.

2.2.1 SAMPLE PREPARATION

The majority of samples could be prepared and sintered following the same procedure and produced consistently robust samples suitable for measurements. Methanol, ethanol, or propanol was added to the sample powder to act as a binding agent to create a slurry which was then allowed to air dry until tacky. For heat capacity and thermal conductivity measurements the moist sample was then loaded into a 2.8 mm die and pressed to ~0.5 GPa. The pellets were removed and allowed to air dry further at room temperature for 1 h. The green bodies were then ramped to 1063 K at a rate of 5 K min⁻¹ and sintered in air for 12 h before cooling at 5 K min⁻¹ to room temperature. Samples for dilatometry were prepared with 5 % mass polyethylene glycol incorporated and mixed with a small amount of water until tacky and pressed to 1.0 GPa. The sintering temperature and conditions were otherwise consistent between sample preparation methods. Sintering produced robust pellets suitable for thermal property, thermal expansion, and dilatometry measurements. XRPD was used to confirm the crystallinity and space group of each sample material following the final sintering step.

2.2.2 HYGROSCOPIC SAMPLE PREPARATION

At room temperature both $\text{Y}_2\text{Mo}_3\text{O}_{12}$ and $\text{Y}_{2-x}\text{In}_x\text{Mo}_3\text{O}_{12}$ ($x = 0, 0.5, 1, 1.5$) exist as hydrates and readily absorb moisture from the air. As discussed, the water molecules are suspected to inhibit the rocking motion of the tetrahedra, preventing negative thermal expansion below 403 K and destroying the Pbcn framework.^{114,141,189} Therefore, to measure the thermal properties of these compounds it is necessary to dehydrate the

materials. Due to the extremely hygroscopic nature of these materials, dehydration, sample preparation, handling, and storage have proven to be challenging.

To prepare a hygroscopic specimen for measurement, approximately 50 mg of sample was placed in a pellet press and the entire assembly was heated to 423 K for an hour (Figure 2.1). The assembly was then removed from the oven and 2000 lbs (~0.5 GPa) of pressure was applied using a Carver Laboratory Press, model C (Fred S. Carver, Inc.). The assembly was allowed to cool on the press until tactile before removing the pellet.

Once a suitable pellet was obtained it was then divided using a sharp blade and then stored in an oven at 423 K until used. Samples could also be stored under ambient conditions until needed if preheated prior to measurements.

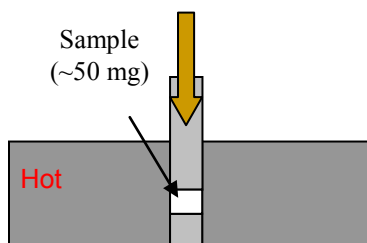


Figure 2.1: Approximately 50 mg of hydrated sample was loaded into a pellet press and heated prior to compression.

To ensure that the samples were kept free of contaminants during storage and transport between buildings an aluminum sample holder was constructed. The aluminum sample holder also allowed for minimal handling of the fragile samples and prevented the chipping and fragmenting that was observed when samples were transported in glass vials.

While this method was effective, the pellet press was not specifically designed to be heated and was not hardened steel and, therefore, subject to deformation. The combination of heating and high pressing pressures resulted in the deterioration of the pellet press. In addition, the delicate care required while handling the samples was not ideal. For these reasons, a specialized die and alternate sample preparation method was developed. This die model was subsequently used for all pellet preparation following its completion. The design was less likely to jam and suffer damage than the previous model. An image and schematic diagram of the new die assembly is shown in Figure 2.2.

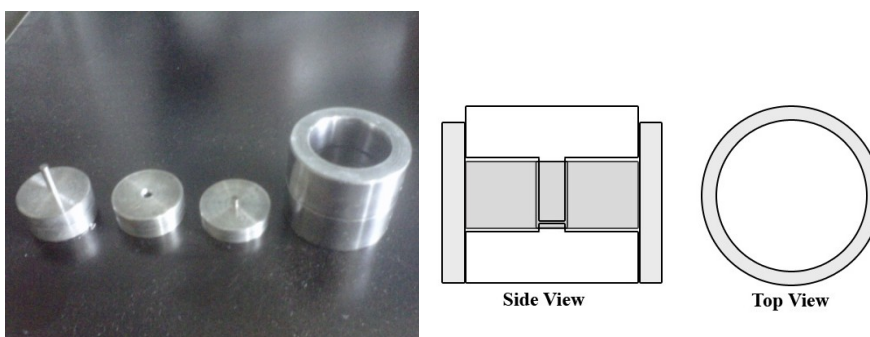


Figure 2.2: Between 5 mg and 20 mg of sample was loaded into the die assembly and 1 GPa of pressure is applied.

Upon completion of the new die, samples were prepared in a more similar fashion to those in Section 2.2.1. However, methanol, ethanol, and propanol acted as poor binders and produced samples that were flakey and prone to crack formation. This was likely due to interactions between the incorporated water molecules and the organic solvents and dehydration/hydration effects. The best binder was water, which produced robust pellets for sintering. The green bodies were then ramped to 1063 K at a rate of 5 K min⁻¹ and sintered in air for 12 h before quenching back to room temperature. Samples for dilatometry were prepared with 5 % mass polyethylene glycol incorporated and mixed

with a small amount of water until tacky and pressed to 1.0 GPa. The sintering temperature and conditions were otherwise consistent between sample preparation methods. Hygroscopic samples intended for heat capacity measurements were stored in a desiccator or oven at 373 K until used.

CHAPTER 3 CHARACTERIZATION

Unless otherwise stated, all sample preparation and characterization has been carried out by the author, Kimberly J. Miller. Contributions from other parties to sample preparation, characterization and data analysis are credited as appropriate.

3.1 SCANNING ELECTRON MICROSCOPY (SEM)

An Hitachi S-4700 cold-field emission analytical scanning electron microscope (FE-SEM) (located in the Faculty of Engineering at Dalhousie University and managed by the Institute for Research in Materials), equipped with an energy-dispersive spectrometer (EDS) was used to observe particle morphology, size, and effectiveness of sintering using secondary electron imaging operating with a 3 kV accelerating voltage, and to verify the chemical composition of the as-synthesized samples. Sintered samples were mounted on carbon tape and measured without coating. The chemical composition of the samples, measured by EDS, was only semi-quantitative since the surfaces of the samples were not polished prior to measurement. In an attempt to obtain a statistically representative estimate of the true composition of the synthesized compounds five measurements were conducted on each sample.

3.2 TRANSMISSION ELECTRON MICROSCOPY (TEM)

Transmission electron microscopy (TEM) images were recorded using a Gatan CCD camera on a JEOL-2010 microscope operating at 200 kV (located at the Departamento de Engenharia de Materiais, Pontificia Universidade Católica de Rio de Janeiro – PUC-Rio, Brazil). TEM specimens were prepared by dispersing the powder samples in alcohol *via* ultrasonic treatment and then dropping onto a porous carbon film supported by a copper grid.

3.3 THERMOGRAVIMETRIC ANALYSIS

A TA Instruments SDT Q600 thermogravimetric analyzer (TGA) (located in Dr. Jeff Dahn's lab in the Department of Physics and Atmospheric Science at Dalhousie University) was employed to determine the water content of hygroscopic samples, and to determine the dry mass of hygroscopic samples. A Shimadzu 51H thermogravimetric analyzer (located at the Departamento de Engenharia de Materiais, Pontificia Universidade Católica de Rio de Janeiro – PUC-Rio, Brazil) was used to monitor the redox reaction and decomposition of organic materials in the simplified sol-gel system.

The precursor gels prepared with 1:2 and 1:8 metal-to-PVA ratios were studied by thermogravimetric analysis employing the Shimadzu 51H instrument, using a heating rate of 10 K min^{-1} , in order to determine the temperatures of redox reaction between PVA and nitrates, and of organic residue decomposition.²⁹⁵

The TA Instruments Q600 TGA was used to determine the accurate dehydrated mass of hygroscopic samples. For the majority of materials a microgram balance was adequate, however with the hygroscopic samples the water content prior to measurements could not be accurately predicted and had to be determined for each sample. The dry mass of the hygroscopic sample fragments was obtained by thermogravimetric analysis. Samples were placed in aluminum pans and monitored against an empty pan as the temperature was increased to at least 403 K under argon atmosphere. By monitoring the change in mass as a function of temperature it was possible to observe the dehydration of the molybdates until completion. In order to obtain a final mass the last ten data points from the TGA run were averaged and taken as accurate within the instrumental error of ± 0.0001 mg. The samples were then transported and stored in the aluminum pan until use (Figure 3.1).

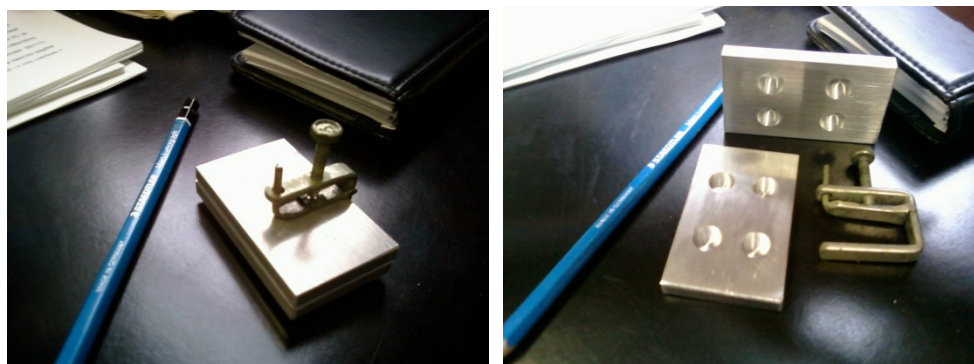


Figure 3.1: Aluminum sample holder for heating and transporting hygroscopic samples.

3.4 DIFFERENTIAL SCANNING CALORIMETRY (DSC)

In addition to TGA, differential scanning calorimetry (DSC) is another useful instrument for characterizing the thermal properties of compounds. In a DSC the power difference required to heat a sample and reference at a constant rate is monitored.¹⁸ By monitoring the power difference a graph outlining the differential heat flow as a function of temperature is generated and can be used to detect any thermal anomalies.

DSC measurements on the samples were conducted using a TA Instruments Q200 series differential scanning calorimeter (located in Dr. Mary Anne White's research lab at Dalhousie University and managed by the Institute for Research in Materials) equipped with either a liquid nitrogen cooling system (LNCS) cooling head or a forced air cooling system (FACS) and a helium atmosphere, depending on the temperature range of interest. Samples larger than 45 mg were loaded into a steel DSC pan to accommodate the larger sample size needed to resolve the phase transitions; the temperature ranges examined varied from 170 K to 700 K with a heating rate of 10 K min⁻¹. The DSC was calibrated using indium, either a 5.12 mg sample loaded in an aluminum pan or a 46.18 mg sample in a stainless steel pan; In has $T_{fus} = 429.74$ K and $\Delta_{fus}H = 28.6624$ J g⁻¹.²⁹⁶ A typical baseline for DSC scans is shown in Appendix D.

3.5 DILATOMETRY

Dilatometric studies were carried out on the sintered pellets using a Netzsch Dilatometer DIL 402C (located at the Departamento de Engenharia de Materiais, Pontifícia Universidade Católica de Rio de Janeiro – PUC-Rio, Brazil) with a resolution of 0.125 nm / 1.25 nm in the temperature range from 300 K to 970 K. A standard α -alumina sample, supplied by Netzsch and made from the same α -alumina used for the push rod and the sample holder, was run for the calibration measurement. The data ($\Delta L/L_0$ vs. T) for this calibration measurement were used in the Netzsch Proteus Thermal Analysis software to perform a push rod and sample holder correction and to obtain $\Delta L/L_0$ vs. T data free of any sample holder and push rod effect. The heating rate during measurements was 10 K min^{-1} , while the cooling rate was not controlled. The accuracy of the instrument was assessed using an α -alumina rod supplied by Netzsch. The CTE of the α -alumina rod was determined to be $7.85 \times 10^{-6} \text{ K}^{-1}$ at 737.15 K, well within the range of reported values, $7.2 \times 10^{-6} \text{ K}^{-1}$ to $8.8 \times 10^{-6} \text{ K}^{-1}$,¹²⁴ indicating good precision. The measurements were remarkably reproducible. The upper and lower bounds of the CTE were calculated based on 1% accuracy in $\Delta L/L_0$ for the dilatometer.²⁹⁷

Analysis of the bulk average α_t was performed on the cooling measurements in order to minimize the contribution of crack healing, creep, and sintering effects during the measurements. Microcrack healing upon heating has a tendency induce a drastic change in the observed coefficient of thermal expansion during the heating cycles, *i.e.*, α_t at temperatures higher than 800 K is inaccurate during the heating portion of the

measurement.²⁹⁸ The sample measurements were taken to be reproducible to within $0.1 \times 10^{-6} \text{ K}^{-1}$ over the measured temperature ranges based on duplicate measurements.

3.6 X-RAY POWDER DIFFRACTION

3.6.1 INSTRUMENTS

Various XRD instruments were used depending on the location of the sample, the requirements of the measurements, and the availability of the equipment. Under the supervision of Dr. Bojan Marinkovic, a Siemens D-5000 diffractometer (located at the Departamento de Engenharia de Materiais, Pontificia Universidade Católica de Rio de Janeiro – PUC-Rio, Brazil) was used to characterize the synthesized samples before shipment to Dalhousie University. A Siemens D-500 powder diffractometer was employed under the supervision of Andy George, Department of Physics and Atmospheric Science, Dalhousie University, in order to confirm the purity of samples as well as to conduct qualitative variable temperature experiments. A PANalytical X'Pert Pro Bragg-Brentano diffractometer at the University of Manitoba was used to perform quantitative variable-temperature experiments under the supervision of Dr. Mario Bieringer.

3.6.1.1 Siemens D-5000 Diffractometer

X-ray powder diffraction (XRPD), carried out at room temperature using a Siemens D-5000 diffractometer equipped with a Cu-sealed tube and graphite

monochromator, was used to determine the phase content and space group of the final product. The data were recorded in steps of 0.02° (8 s per step) from 10° to 60° (2θ). Qualitative phase and space group analysis of the as-obtained samples were performed using the Le Bail method with Topas-Academic Software. Measurements on this instrument were conducted by Prof. Bojan Marinkovic at PUC-Rio.

3.6.1.2 Siemens D-500 Powder Diffractometer

XRPD was carried out using a Siemens D-500 powder diffractometer in θ - 2θ Bragg-Brentano configuration with $\text{CuK}\alpha$ radiation ($\lambda = 1.541(8) \text{ \AA}$) and a diffracted beam graphite monochromator. Low-temperature measurements were made in the range between 80 K and 297 K using a continuous flow cryostat (Oxford Instruments Ltd., model CF1108). Data were recorded for 2 s at each 2θ in steps of 0.05° from 10° to 38° (2θ). Qualitative phase analysis and space group determination were performed using the Le Bail method and Topas-Academic Software.²⁹⁹ Measurements at room temperature and lower temperatures were carried out using a zero-background Si-(510) wafer. Room-temperature samples were prepared by casting a thin film on the wafer from a slurry of methanol. For low-temperature measurements the vertical position of the sample platform required that a small amount of silicone vacuum greased be used as a support.

The Siemens D-500 instrument was used for low-temperature XRPD as well as simple XRPDs where high resolution was not crucial.

3.6.1.3 PANalytical X'Pert Pro Bragg-Brentano Diffractometer

Room-temperature powder X-ray diffractograms were collected on a PANalytical X'Pert Pro Bragg-Brentano diffractometer equipped with CuK α radiation ($\lambda = 1.541(8)$ Å), a sample spinner, and an X'Celerator detector, 1° divergence slits and 0.04 rad soller slits. The sample was mounted on a Si-(510) zero background sample holder and data were collected over $10^\circ \leq 2\theta \leq 90^\circ$ in 0.0084° steps and 200 s / step counting time.

Variable-temperature powder X-ray diffractograms were collected on the same PANalytical X-pert Pro diffractometer equipped with a self-masking Anton Paar HTK2000 high-temperature camera. The sample was mounted as a thin layer on the 10 mm Pt resistive heating element and heated in 25 K increments from room temperature to 973 K in air. The temperature of the furnace is accurate within 5 K between room temperature and 1473 K. Diffractograms spanning $10^\circ \leq 2\theta \leq 65^\circ$ and $\Delta 2\theta = 0.0167^\circ$ step size were collected with 100 s / step counting times during heating and cooling.

All unit cell dimensions were determined using Le Bail fitting with FullProf 2k (Version 4.00).²⁹⁹ The peak shape parameters and asymmetry parameters as well as background functions were determined at room temperature and held fixed for all high-temperature refinements. For the furnace data the (111) and (200) Pt peaks and all peaks with $2\theta \leq 21.4^\circ$ were excluded because of excessive asymmetry. The instrument parameters have been verified by adjusting the set parameters to the diffraction pattern collected from a LaB₆ NIST standard specimen. For the high-temperature refinements the unit cell parameters and the sample height were refined. Note that the sample height remained constant ($\approx -0.06(3)$ mm) within statistical error over the entire temperature

range (298 K to 973 K). The least squares refinements resulted in χ^2 values between 2 and 7 for all temperatures.

3.6.2 REFINEMENT METHODS

Both the Le Bail²⁹⁹ and Rietveld³⁰⁰ refinement methods were employed to determine the coefficients of thermal expansion and the space groups of the materials in this work. The Le Bail method was employed when there was insufficient data to determine the atomic positions of the atoms within the unit cell.

3.6.2.1 Rietveld Method Using Rietica

Rietveld analysis is a reproducible and qualitative analysis first developed by H.M. Rietveld^{173, 300} which analyses the profile intensities obtained by step-scanning a sample and is favoured for accuracy and minimizing correlations between peak intensities and shape. Rietica is a free-for-use software package that operates as a Windows front end for the Lucas Heights Research Laboratories (LHPM) computer program for Rietveld analysis of X-ray and neutron powder diffraction patterns.³⁰¹

The Rietveld method relates the background intensity, y_{ib} (where B_m is one of six refinable background parameters ($B_1 \dots B_6$)),³⁰⁰

$$y_{ib} = \sum_{m=-1}^n B_m (2\theta)^m, \quad (3.1)$$

and the intensity (I_k) of the k^{th} Bragg diffraction to the net intensity (y_{ic}) at point i .³⁰⁰

$$y_{ic} = y_{ib} + \sum_p \sum_{k=k_1^p}^{k_2^p} G_{ik}^p I_k, \quad (3.2)$$

where G_{ik} is the peak profile function and k_1 and k_2 are the reflections which contribute to the intensity at point i , and p corresponds to the phases in the sample. The intensity of the k^{th} Bragg diffraction is in turn defined as:³⁰⁰

$$I_k = S_f M_k L_k |F_k|^2 P_k A_k E_k, \quad (3.3)$$

where S_f is a scale factor, M_k is the multiplicity, L_k is the Lorentz-polarization factor, P_k describes the effects of preferred orientation ($P_k = 1$ for powders unaffected by preferred orientation), A_k is a correction of absorption, and E_k is the correction for extinction. F_k is the structure factor.³⁰⁰

A pseudo-Voigt peak shape function,³⁰⁰

$$G_{ik} = \gamma_m \frac{C_0^{1/2}}{H_k \pi} [1 + C_0 X_{ik}^2]^{-1} + (1 - \gamma_m) \frac{C_1^{1/2}}{H_k \pi^{1/2}} \exp[-C_1 X_{ik}^2], \quad (3.4)$$

was selected as the peak profile function, where $C_0 = 4$, $C_1 = 4 \ln 2$, γ_m is a refinable mixing parameter, that for the Gaussian and Lorentzian can range from 0 to 1, and $X_{jk} = (2\theta_i - 2\theta_k)/H_k$. H_k is the full-width at half maximum (FWHM) of the k^{th} Bragg reflection,³⁰⁰

$$H_k = (U_b \tan^2 \theta + V_b \tan \theta + W_b)^{1/2}, \quad (3.5)$$

where U_b is a refinable parameter associated with broadening due to strain³⁰⁰ and V_b and W_b are also refinable parameters. These three halfwidth parameters take into account peak broadening due to particle size and the variation of halfwidth with scattering angle.

The least-squares refinement was carried out using the Newton-Raphson algorithm³⁰² which, when near the desired root, can converge rather quickly. Convergence however, is dependent on an initial guess which must be sufficiently close

to the actual value and the algorithm can fail to reach the convergence conditions if the initial parameters are vastly different from the actual parameters.³⁰⁰

The reliability factors (*R*-factors), are a measure of the fit of a calculated pattern to an experimental sample and are given as the weighted *R*-factor (R_{wp}),³⁰³

$$R_{wp} = 100 \left\{ \frac{\sum w_i (y_{io} - y_{ic})^2}{\sum w_i (y_{io})} \right\}^{1/2}, \quad (3.6)$$

where y_{io} is the observed net intensity and w_i is:

$$w_i = \frac{1}{\delta y_{io}}, \quad (3.7)$$

and δy_{io} is the uncertainty in y_{io} ; the profile *R*-factor (R_p),³⁰³

$$R_p = 100 \frac{\sum |y_{io} - y_{ic}|}{\sum y_{io}}; \quad (3.8)$$

and the expected *R*-factor (R_{exp}),³⁰³

$$R_{exp} = 100 \left\{ \frac{(N - P_a)}{\sum w_c (y_{io})^2} \right\}^{1/2}, \quad (3.9)$$

where N is the number of observations and P_a is the number of adjusted parameters, and w_c is the weight where:

$$w_c = \frac{1}{y_{ic}}. \quad (3.10).$$

In addition there is the Bragg *R*-factor (R_B),³⁰³

$$R_B = 100 \left\{ \frac{\sum (I_o - I_c)^2}{\sum (I_o)^2} \right\}^{1/2}, \quad (3.11)$$

where I_o is the observed intensity, I_c is the calculated intensity. The goodness of fit, or χ^2 value, is given as the ratio R_{wp} / R_{exp} .³⁰³

3.6.2.2 Le Bail Fitting

Le Bail fitting is a quick alternative to Rietveld analysis that uses generated hkl peaks defined by the unit cell and space group in order to fit a pattern. The technique is typically employed when atomic positions are unknown and it is employable even with patterns of lower quality. The Le Bail method is also useful for identifying secondary phases within a sample.³⁰⁴

The Le Bail method is a modification of the Rietveld approach to obtain estimates of the structure-factor magnitudes extended to situations where no structural model is present. Initially all the integrated peak intensities of the reflections are considered equal. In the case of isolated peaks the area is easy to evaluated, however it can be complicated by overlapping peaks. For two overlapping peaks, this assumption does not impact the overall result of the fitting since³⁰⁴

$$A_1(obs) + A_2(obs) = \sum_i (obs(i) - back(i)), \quad (3.12)$$

where $A_1(obs)$ and $A_2(obs)$ are the observed integrated intensities and $obs(i)-back(i)$ are the observed peak contributions at the i^{th} point in the diffraction pattern.

The Le Bail method is a further extension of the Rietveld method by employing a recursive approach to determining the calculated peak areas where the observed structure-factor magnitude of the r^{th} iteration is used for the calculated peak area for the $(r+1)^{\text{th}}$ iterations.³⁰⁴

3.7 HEAT CAPACITY

Heat capacity was determined using a commercial relaxation calorimeter (Physical Property Measurement System (PPMS) model 6000 from Quantum Design located in Dr. Mary Anne White's research lab at Dalhousie University and managed by the Institute for Research in Materials) which determines heat capacity at constant pressure,

$$C_p = \left(\frac{dq}{dT} \right)_p, \quad (3.13)$$

by measuring the heat (q) added/removed from a sample with a change in temperature.

3.7.1 PPMS INSTRUMENT OVERVIEW

The PPMS is a unique instrument capable of accurately measuring the heat capacity of very small sample sizes (1 mg to 200 mg). Typically sample masses between 4 mg and 20 mg were used in order to keep the relaxation times at a reasonable level. If a sample was too large it could result in relaxation times that would render an experiment impractical based on time constraints. However, if a sample mass was too small then the addenda heat capacity would be much greater than the heat capacity of the sample and introduce too much uncertainty.

To obtain accurate measurements, heat capacity on the PPMS is measured using a specially designed sample holder (Figure 3.2) under a high vacuum which is maintained at ~ 0.01 mTorr. This ensures that the thermal conductance is limited to the wires securing the 3 mm \times 3 mm sapphire sample platform to the puck. Samples are typically affixed to

the sapphire platform using Apiezon[®] thermal grease to ensure good thermal contact (Figure 3.2).

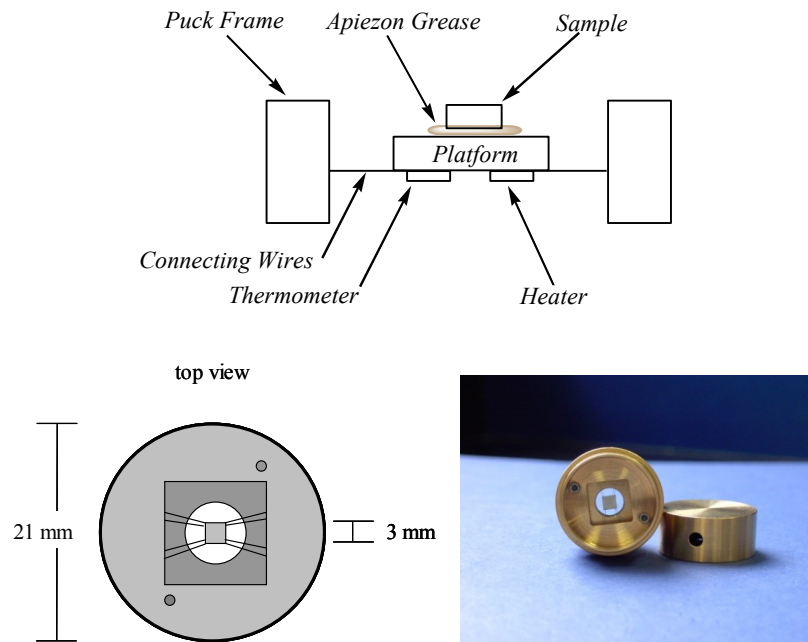


Figure 3.2: Schematic diagrams outlining the sample and platform setup and photo of the heat capacity puck.

A Cernox sensor[™] and a thin film resistive RuO platform heater are attached directly to the bottom side of the platform and are electrically and thermally connected to the puck frame by a series of eight small thermally conductive wires. These wires also serve as the structural support for the platform.³⁰⁵

Since the platform thermometer is buried in the platform itself the temperature reading it takes is considered to be the sample temperature. A second thermometer on the puck frame provides the temperature of the thermal bath, T_0 .³⁰⁵

3.7.2 HEAT CAPACITY ANALYSIS MODELS

During a heat capacity run the heater supplies a constant power, \dot{q} , over a time, t , and the instrument records the temperature response of the sample during and after the heating process (Figure 3.3). To convert the raw data collected into quantitative heat capacities of the materials being studied, two models are typically used: the simple single-tau model for systems with good thermal contact with the sapphire base or the two-tau modelTM for samples with poor thermal contact.

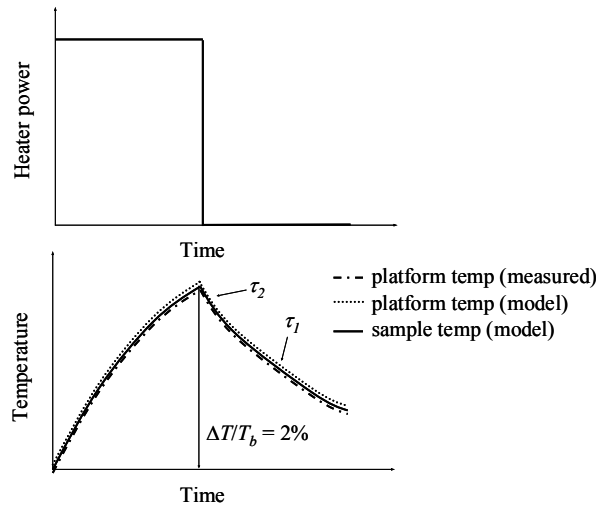


Figure 3.3: The temperature response to an applied power during the heat capacity measurement showing the two-tauTM method to model temperature decay.³⁰⁵

The single-tau model is the simpler method and assumes that the sample and platform have good thermal contact. The total heat capacity (sample and addenda) is:³⁰⁵

$$C_{total} = \frac{dT}{dt} = -K_w(T_p - T_b) + \dot{q}(t), \quad (3.14)$$

where T_p is the temperature of platform, T_b is the temperature of the puck frame, t is time, K_w is the thermal conductance of the supporting wires, and $\dot{q}(t)$ is the heater power.

Typically the single-tau model is only used for addenda measurements when there is only a thin layer of thermal grease on the platform.

The temperature difference between the sample and platform, due to thermal attachment, can be accurately accounted for using the two-tauTM model. The two-tauTM model is used to simulate the heat flow from the platform to the sample by considering the heat capacity of the platform ($C_{platform}$):³⁰⁵

$$C_{platform} \frac{dT_p}{dt} = \dot{q}(t) - K_w (T_p(t) - T_b) + K_g (T_s(t) - T_p(t)) \quad (3.15)$$

and the heat capacity of the sample (C_{sample}):³⁰⁵

$$C_{sample} \frac{dT_s}{dt} = -K_g (T_s(t) - T_p(t)), \quad (3.16)$$

where K_g is the thermal conductance between the sample and platform due to the grease, and T_s is the temperature of the sample.

The Quantum Design PPMS can accurately determine the heat capacity of a sample to within 1 % for the temperature range of 5 K to 300 K as long as the sample mass is optimized so that the heat capacity of the sample contributes at least one third of the total heat capacity, and provided that there is good thermal contact.³⁰⁶

Thermally conductive grease is used to ensure adequate thermal contact to the sample platform and to obtain accurate heat capacity measurements. Apiezon[®] N grease is typically used for low-temperature measurements since it remains thermally conductive at low temperatures, has a high vapor pressure, and is inert. For high-temperature experiments, Apiezon[®] T or Apiezon[®] H grease can be used as Apiezon[®] N grease melts and loses thermal contact with the sample at temperatures greater than 320 K.³⁰⁷

Due to the limitations of the thermal contact greases available and the conditions required to dry the samples *in situ* using only one thermal contact grease was not feasible. Apiezon[®] N grease was used for low-temperature experiments since it has well known characteristics at low temperatures and is a good thermal conductor. However, the yttrium trimolybdate samples required heating to 340 K for one hour prior to sample measurements and at high temperatures Apiezon[®] N grease was found to melt off the platform so Apiezon[®] H and T grease were used in its place. A list of properties of the three Apiezon[®] greases is given in Table 3.1.

Table 3.1: Selected properties for Apiezon[®] greases.

	Apiezon [®] N ³⁰⁷	Apiezon [®] T ³⁰⁸	Apiezon [®] H ³⁰⁹
$T_{\text{fus}} / \text{K}$	312 to 322	385 to 446	Does not melt
Vapor Pressure / Torr	6×10^{-10}	4.6×10^{-9}	1.7×10^{-9}
Thermal conductivity / $\text{W m}^{-1} \text{K}^{-1}$	303 K: 0.194 2 K: 0.095	Not reported	303 K: 0.216
Working Temperature Range	2 K – 300 K	2 K – 340 K	210 K – 390 K
Limitations	Melts off the platform and loses thermal contact at $T > 320 \text{ K}$	Can creep into the sample at $T > 360 \text{ K}$ for extended periods	Looses thermal contact at $T < 210 \text{ K}$

3.7.3 HEAT CAPACITY ACCURACY CRITERIA

In order to ensure the accuracy and precision of the heat capacity measurements the heat capacity was determined three times at each measurement temperature. The recorded values were evaluated in terms of sample contribution to the total heat capacity ($C_{\text{sample}} / C_{\text{total}}$), thermal contact, and reproducibility ($\delta C_{\text{sample}} / C_{\text{sample}} \times 100 \%$).³⁰⁶

The sample contribution to the heat capacity should be greater than 30 % for the entire temperature range³⁰⁶ and the thermal coupling between the platform and the sample is acceptable above 70 %, although higher values are preferred. The calculated reproducibility should be within 2 % for temperatures above 10 K and within 5 % for 2 K to 10 K.³⁰⁶ Typically the heat capacity was determined three times at each temperature and averaged values are reported.

3.8 THERMAL CONDUCTIVITY

The thermal conductivity (κ) of a solid can vary greatly between materials depending on the structure, composition, grain sizes, lattice defects, dislocations, impurities, anharmonicity, etc.⁶⁹ The thermal conductivity is defined by

$$\kappa = \frac{\dot{q}}{A_c} \frac{dx}{dT}, \quad (3.17)$$

where \dot{q} is the power applied at one end of the sample of cross-sectional area A_c . The heat is lost at the same rate at the other end, with a temperature gradient of dT/dx (Figure 3.4). In a steady-state system with 1D heat flow along a sample with length, L , κ is determined by measuring the steady-state temperature differential, ΔT_∞ , across a sample which is proportional to \dot{q} by:

$$\dot{q} = K\Delta T_\infty, \quad (3.18)$$

where K is the thermal conductance of the sample and

$$K = \frac{\kappa A_c}{L}. \quad (3.19)$$

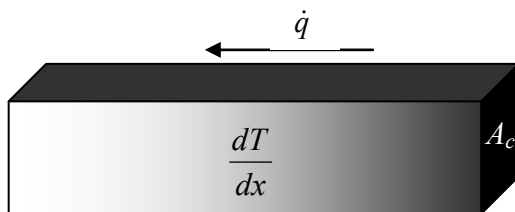


Figure 3.4: Determination of the thermal conductivity of a sample with a cross-sectional area, A_c , by applying power, \dot{q} , to the right side of the sample, and creating a temperature gradient (dT/dx).

While steady-state techniques are more direct in terms of calculating κ from experimental results, continuous measurement techniques allow for rapid and high-density data acquisition. Methods for obtaining thermal conductivity results from continuous measurement techniques are examined in Section 3.8.2.

3.8.1 PPMS INSTRUMENT OVERVIEW

To accurately measure the thermal conductivity of a solid, the PPMS uses the thermal transport option (TTO) to monitor the temperature drop along a sample of known dimensions as a known power is applied to the sample. The TTO employs convenient sample mounting, a 2 k Ω heater, and CernoxTM thermometry in conjunction with sophisticated software to model the heat flow through the sample and correct for heat loss.

The TTO system (Figure 3.5) measures the thermal conductance by applying heat from a heater shoe to create a temperature differential (typically $\sim 3\%$ of the absolute T).

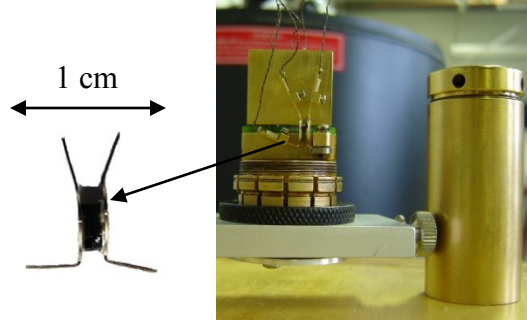


Figure 3.5: Sample mounted on leads in a 2-probe configuration (left) and loaded onto the measurement platform and connected to a heater, heat sink, and thermometers (right).

The PPMS can measure thermal conductivity over the temperature range 2 K to 400 K under high vacuum ($\sim 10^{-5}$ Torr) with the option of having a magnetic field (0 T to 9 T). The TTO uses either a continuous or a steady-state measurement mode to determine the thermal conductivity which can be specified in accordance with the experiment.³⁰⁵

3.8.1.1 Steady-State Measurement

In steady-state mode the cryostat is set to a selected temperature and the TTO software monitors the thermometry attached to the sample, both at the hot end (T_{hot}) and cold end (T_{cold}). When the average sample temperature stabilizes (typically $dT/dt \leq 0.1\%$), T_{hot} and T_{cold} are calculated over 60 s to determine ΔT_{OFF} . The heater power is then turned on such that $\Delta T = 3\%$ of the cryostat T and the system again waits for the stability criterion to be met before determining ΔT_{ON} . During single-measurement mode it is assumed that $\Delta T_{\infty} = \Delta T_{ON} - \Delta T_{OFF}$. Figure 3.6 shows the steady-state response to a heat pulse and the resulting time-based response of the hot and cold thermometers during measurement.

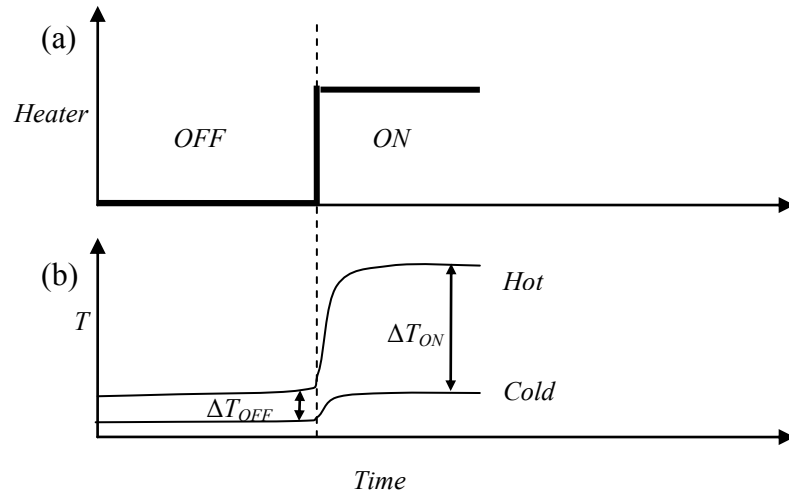


Figure 3.6: An idealized temperature response to the heater power, in the steady-state measurement mode, showing the (a) heater power, (b) the time-based response of the hot and cold thermometers during measurement.

In steady-state measurement mode, κ is measured as either stability or time-based measurements. In the stability mode, a user-specified stability criterion must be met at the hot and cold thermometer probes before a specified heater power is applied.³⁰⁵ The power then remains on until the stability criterion is again met. Data points are only collected during the times when the stability requirements are met before and after the heat pulse. Timed measurements are similar in operation to stability measurements, except that instead of waiting for a stability requirement to be met during heating, the heater power is applied for a set time and then turned off.³⁰⁵

While steady-state measurements are the classical method to obtain κ and provide good results, the steady-state measurement mode is slower than the continuous mode and requires the system to reach a steady-state in both the heater “off” and “on” states before taking a measurement. While slower, the single measurement mode does not require curve fitting calculations, making the interpretation of data more straightforward.³⁰⁵

3.8.1.2 Continuous-Measurement Mode

The continuous mode takes measurements continuously while optimizing the heater power continually over the course of the measurement. This process is ideal for non-equilibrium conditions, such as slow skew rates of system variables such as temperature and magnetic field. This method has the advantage of being quite rapid in comparison to the steady-state measurement mode. Since it does not require the system to reach equilibrium, the continuous mode uses curve fitting software to determine the steady-state thermal properties of the material in response to a short heat pulse (Figure 3.7).³⁰⁵

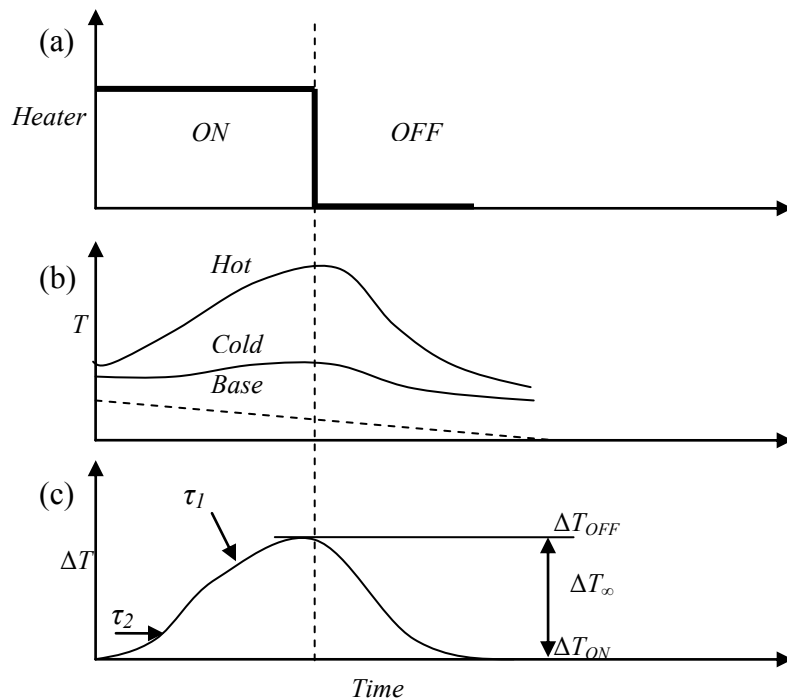


Figure 3.7: The idealized temperature response to a heat pulse, in continuous measurement mode, showing the (a) heater power, (b) the time based response of the hot and cold thermometers during measurement, and (c) the temperature differentials, ΔT , across a sample, the estimated time constants, τ_1 and τ_2 , and the asymptotic differential, ΔT_∞ .

When measurements are taken in the continuous mode, the software, developed for the TTO option, employs an adaptive algorithm consisting of a non-linear least squares fitting routine to give a modeled temperature rise (ΔT_m):³⁰⁵

$$\Delta T_m = \Delta T_\infty \times \left\{ 1 - \frac{\left[\tau_1 \times \exp\left(-\frac{t}{\tau_1}\right) - \tau_2 \times \exp\left(-\frac{t}{\tau_2}\right) \right]}{(\tau_1 - \tau_2)} \right\}, \quad (3.20)$$

that fits the data over the heat pulse range to an empirical formula where ΔT_∞ is the asymptotic temperature differential across the sample (Figure 3.7) and τ_1 and τ_2 are the long and short empirical time constants for the sample.³⁰⁵ The fitting routine adjusts the empirical time constants and ΔT_∞ until a satisfactory fit is achieved for the heating ($\Delta T_{m, heating}$) and cooling cycles ($\Delta T_{m, cooling}$) where the cooling cycle is given by:³⁰⁵

$$\Delta T_{m, cooling} = A - \Delta T_{m, heating}, \quad (3.21)$$

and A is a constant. From this fit, the total thermal conductance (K_{tot}) of the assembly can be calculated as a ratio of the heater power to ΔT_∞ (from Equation 3.20),³⁰⁵

$$K_{tot} = \frac{(\dot{q} - P_{rad})}{\Delta T_\infty}, \quad (3.22)$$

where the radiative loss, P_{rad} , can be estimated by

$$P_{rad} = \sigma_T \left(\frac{S_A}{2} \right) \varepsilon (T_{hot}^4 - T_{cold}^4), \quad (3.23)$$

and where S_A is the total surface area, σ_T is the Stefan–Boltzmann constant ($\sigma_T = 5.67 \times 10^{-8} \text{ W m}^{-2} \text{ K}^{-4}$), $T_{hot/cold}$ are the average temperatures of the hot and cold thermometers and the factor of $1/2$ is an estimate that only half of the sample surface area is radiating heat.³⁰⁵ The emissivity, ε , is the relative ability of a surface to emit energy by

radiation and quantifies the radiative thermal conduction from the hot end of the sample to the surrounding thermal shield. If the exact quantity is unknown an approximation based on known samples will suffice. For ceramics and highly oxidized metals the value can be assumed to be ~ 1 .

The sample conductance, K_{sample} , can then be determined by

$$K_{sample} = K_{tot} - K_{shoes}. \quad (3.24)$$

K_{shoes} is the thermal conductance of the leads and the shoe assembly as determined by factory calibration,

$$K_{shoes} = aT + bT^2 + cT^3, \quad (3.25)$$

where a , b , and c are all constants.³⁰⁵

Once the thermal conductance of the sample is determined from the total thermal conductance it can be related to the thermal conductivity of the sample (κ_{sample}) through sample geometry:

$$\kappa_{sample} = \frac{K_{sample}L}{A_c}. \quad (3.26)$$

For all samples studied in this thesis, continuous mode thermal conductivity measurements were employed to collect high density thermal conductivity data over a large temperature range (2 K to 300 K). Values of L ranged from 1 mm to 2 mm and typical values of A_c were $\sim 10 \text{ mm}^2$.

4.1 MOTIVATIONS FOR DEVELOPMENT

Developing the sol-gel technique was driven by the desire to reduce the total synthesis time and reduce the energy cost of the synthesis. While the development process did not afford the opportunity to synthesize additional novel samples of NTE materials at the time of development, its success presents the opportunity for synthesis of thermomiotic materials at lower temperatures than traditional methods and with a shortened synthesis time.^{132,280,137,138,139,140,141,142,143,144,145,146,147}

Since the mid-1990s, the crystallographic phases of the $A_2M_3O_{12}$ family have received increased attention owing to their potential to exhibit negative thermal expansion or unusually low positive thermal expansion. Following the initial observation of thermomiotic behavior by Evans *et al.*,^{38,310} much effort has been dedicated to understanding the mechanisms behind NTE in these ceramics.^{35,38,81,134,190,195} However, there has not been as much focus on the development of these materials for commercial applications. Several studies have been dedicated to fabrication of composites,^{274,311} and to the development and optimization of new synthetic routes for the production of $A_2M_3O_{12}$ -type phases.^{280,140,147,158} The well-known solid-state reaction route is still the principal way to produce NTE phases of the $A_2M_3O_{12}$ family. However, there are

[‡] Adapted and used with permission from: Ari, M.; Miller, K. J.; Marinkovic, B. A.; Jardim, P. M.; de Avillez, R.; Rizzo F.; White M. A. *J. Sol-Gel Sci. Technol.* **2011**, *58*, 121–125. K.J. Miller's contribution to the work in this manuscript was: developing the synthetic technique and performing the preliminary sol-gel experiments with M. Ari as well as consultations on experimental results. TGA, XRPD, and TEM experiments were carried out by M. Ari and Dr. B.A. Marinkovic. Contributions also included writing most of the first draft of the manuscript and subsequent editing.

substantial drawbacks to this classical approach: it is time consuming, it requires high energy costs and it does not result in uniform or nanometric powders.

The development of new synthetic routes for $A_2M_3O_{12}$ -type phases has generally consisted of two different approaches. Liang *et al.*¹⁵⁸ produced $Y_2Mo_3O_{12}$ through rapid solidification after the use of a continuous-wave CO_2 laser. This synthesis method is extremely rapid; however, it depends on expensive equipment and it is not suitable for large-scale production of thermomiotic materials. The other main method^{140,141} is based on non-hydrolytic sol-gel processing which offers an alternative to conventional sol-gel synthesis and relies on ethers and metal halides to produce alkoxides *in situ*. This approach, proposed by Gates *et al.*,^{140,141} was able to produce $Y_2Mo_3O_{12}$ and a metastable form of $Ga_2Mo_3O_{12}$ ¹⁴⁰ via a sophisticated, time-consuming, but powerful method that can form metastable phases and fine tune properties. This method even allows synthesis of ternary oxides from the $AA'M_3O_{12}$ family, such as $HfMgW_3O_{12}$ and $ZrMgW_3O_{12}$.¹⁴² Another non-hydrolytic sol-gel process is the stearic acid route used for the synthesis of $Al_2W_2MoO_{12}$.¹⁴⁷ Since many salts dissolve in melted stearic acid, this can be a convenient way to produce nanostructured mixed oxides.

An assisted sol-gel process using PVA (polyvinyl alcohol) has also been developed, for the synthesis of multicomponent monophasic oxides.^{295,312,313} PVA acts as a metal chelating agent and thereby inhibits the segregation of metals.^{314,315} It has been demonstrated that PVA-assisted sol-gel processes can result in uniform, monophasic and even nanosized particles for many multicomponent oxides such as spinels ($NiFe_2O_4$, $LiMn_2O_4$, $CoFe_2O_4$),^{295,312,315} $YBa_2Cu_3O_{7-x}$ ³¹⁴ and PLZT (lanthanum modified lead zirconate titanate) ceramics.³¹³

4.2 METHODS

$\text{Al}_2\text{Mo}_3\text{O}_{12}$ was synthesized by the sol-gel method described in Section 2.1.3 and characterized using XPRD (as described in Section 3.6.1.1 and Section 3.6.2.1), SEM (by Dr. Bojan Marinkovic and Monica Ari, as described in Section 3.1), TEM (by Dr. Bojan Marinkovic and Monica Ari, as described in Section 3.2), and TGA (by Dr. Bojan Marinkovic and Monica Ari, as described in Section 3.3).

4.3 RESULTS AND DISCUSSION

The resulting raw product from low-temperature sol-gel processing was typically a dark brown (1:8 mole ratio of reagents to PVA) or light brown (1:2 ratio) porous material, where the color indicates the presence of organic residue.²⁹⁵ The thermal decomposition of organic matter in PVA assisted sol-gel reactions has previously been shown to be complete, for different spinel phases, at temperatures around 400 °C.^{295,312} However, the thermal decomposition of organic residue in the raw $\text{Al}_2\text{Mo}_3\text{O}_{12}$ samples, presented in this report, occurred at higher temperatures, 550 °C for the 1:8 ratio and 605 °C for the 1:2 ratio as illustrated in Figure 4.1. According to previous studies,^{295,312} the redox reaction between PVA and nitrates, resulting in the decomposition of both nitrates and PVA, occurs at 140 °C. Therefore, higher decomposition temperatures were required to allow this reaction, which the TG/DTG curves (Figure 4.1) indicate as taking place over the temperature range ~ 140 to 180 °C. Therefore, following a brief and

relatively mild heat treatment, $\text{Al}_2\text{Mo}_3\text{O}_{12}$ could readily (after 15-20 min) be crystallized as a white solid at temperatures between 600 °C and 700 °C. By following this simple approach to the sol-gel method, the molar ratio of PVA can be varied with no influence on the quality of material produced. The product is monophasic with no evidence of amorphous residue. However a small MoO_3 impurity was present in some samples following calcination. Most advantageously, the crystalline product can be formed at lower temperatures and shorter calcinations times than previously reported.^{104,142}

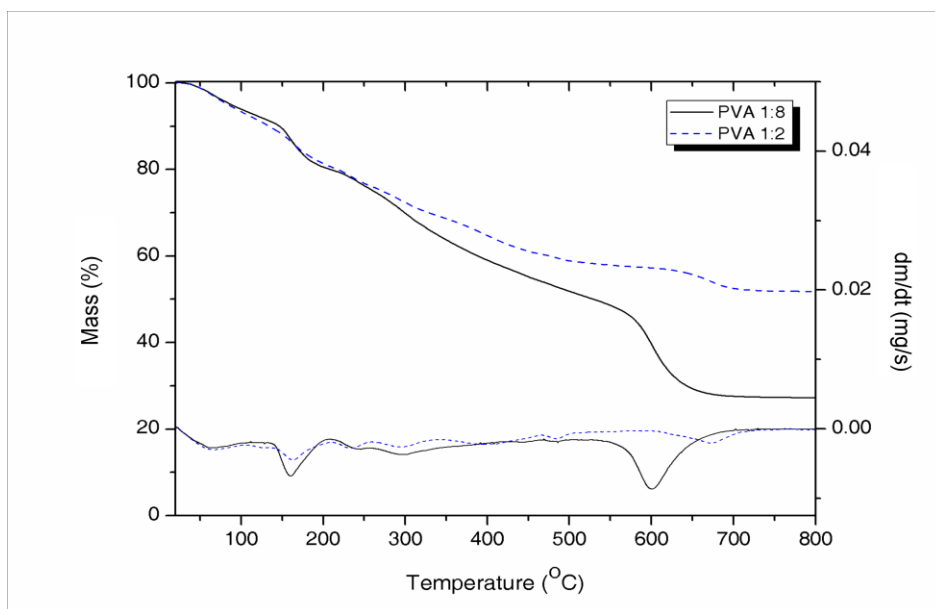


Figure 4.1: TGA and derivative TGA curves for $\text{Al}_2\text{Mo}_3\text{O}_{12}$ samples with 1:2 (dashed line) and 1:8 (solid line) metal to PVA ratios prepared using the assisted sol-gel method. Reprinted with permission from Ari, M.; Miller, K. J.; Marinkovic, B. A.; Jardim, P. M.; de Avillez, R.; Rizzo F.; White M. A. *J. Sol-Gel Sci. Technol.* **2011**, *58*, 121–125. Copyright 2010 Springer.

Similar sol-gel techniques have been employed by Lind *et al.*, Xu *et al.*, and Baiz *et al.* in the fabrication of $\text{Al}_2\text{W}_2\text{MoO}_{12}$, $\text{HfMgW}_3\text{O}_{12}$ and $\text{ZrMgW}_3\text{O}_{12}$.^{104,142,147} While the method employed by Xu *et al.* is relatively simple, it employs stearic acid and requires ignition of the raw material in order to remove solvents prior to calcination.¹⁴⁷

The variable temperature of combustion does not allow for fine control of the reaction

conditions, which can greatly impact attempts to use temperature and calcination times to tailor a specific particle size. While the method of Baiz *et al.*¹⁴² does provide fine control, the method is rather complex, both time consuming and requiring the use of a Schlenk line and glovebox. They also noted that while temperatures of 540 °C could produce some crystalline material, these relatively low temperatures also induced the formation of tungsten and tungsten (VI) oxide. The removal of those impurities and the formation of highly crystalline material could only be achieved when the material was heated to temperatures in excess of 1000 °C.¹⁴² Conversely, a comparative non-hydrolytic sol-gel approach by Lind *et al.*, while superior in terms of tailoring particle size, has reaction times on the order of days.¹⁰⁴ The assisted sol-gel synthesis approach presented in this chapter is rapid, energy efficient and allows for fine tuning of calcination times, temperatures and metal/PVA ratios.

Rietveld refinement (Figure 4.2) showed that the $\text{Al}_2\text{Mo}_3\text{O}_{12}$ specimens with 1:8 metal to PVA mole ratio, prepared by heat treatment at 600 °C for 20 min, were monoclinic $P2_1/a$, the same structure as the solid-state reaction product.¹²⁸ Furthermore, calcination temperature and time could be modified with no effect on the resulting morphology and phase purity. The mean particle size of the 1:8/600 °C / 20 min sample was calculated using the X-ray results and the size-strain analysis embedded in the Rietveld refinement program Topas-Academic and found to be ~300 nm. SEM images of $\text{Al}_2\text{Mo}_3\text{O}_{12}$ obtained from the same sample observed in back scatter and secondary electron modes show that the sample is chemically uniform and consists of submicron particles (Figure 4.3 (a) and 4.3 (b)). A thorough TEM analysis of these samples showed

only $\text{Al}_2\text{Mo}_3\text{O}_{12}$, particles with sizes comparable to the results from X-ray diffraction and SEM analyses (Figure 4.3 (c)).

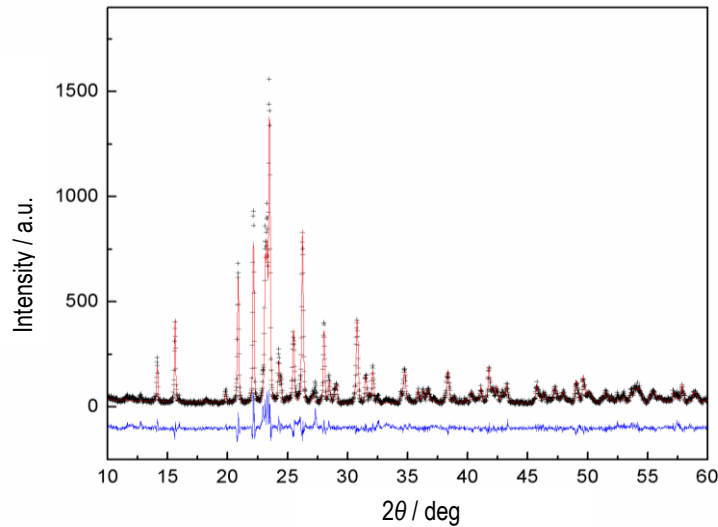


Figure 4.2: Experimental X-ray powder diffraction pattern (black), Rietveld fit (red) and residual (blue) for $\text{Al}_2\text{Mo}_3\text{O}_{12}$ prepared using PVA assisted sol-gel with 1:8 metal to PVA ratio after calcination at 600°C for 20 min. The poor fit between 10° and 13° , in 2θ , indicates the presence of unreacted MoO_3 . Reprinted with permission from Ari, M.; Miller, K. J.; Marinkovic, B. A.; Jardim, P. M.; de Aveliz, R.; Rizzo F.; White M. A. *J. Sol-Gel Sci. Technol.* **2011**, 58, 121–125. Copyright 2010 Springer.

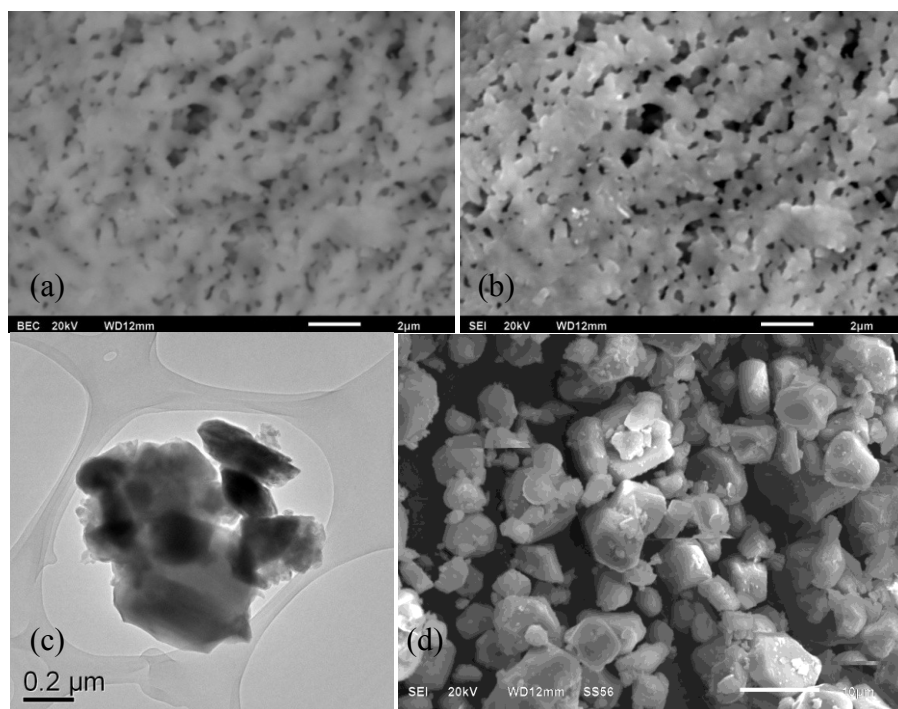


Figure 4.3: Micrographs of $\text{Al}_2\text{Mo}_3\text{O}_{12}$ prepared using the PVA-assisted sol-gel method and calcination at $600\text{ }^\circ\text{C}$ for 20 min. (a) SEM in back scattering mode, (b) SEM in secondary electron mode (c) TEM, (d) secondary electron mode for the sample prepared by solid-state reaction with mechanical-activation. Reprinted with permission from Ari, M.; Miller, K. J.; Marinkovic, B. A.; Jardim, P. M.; de Avillez, R.; Rizzo F.; White M. A. *J. Sol-Gel Sci. Technol.* **2011**, 58, 121–125. Copyright 2010 Springer.

Note that thermal decomposition of the organic residue (approx. 40 mass percent for the 1:2 reaction mixture and 70 mass percent for the 1:8 reaction mixture), which started at $540\text{ }^\circ\text{C}$ (Figure 4.1), is a strong exothermic reaction,^{295,312} and therefore the real (local) temperature of calcination is higher than the nominal temperature of $600\text{ }^\circ\text{C}$. This could be the reason why the process gives sub-micron particles ($\sim 300\text{ nm}$) at such low nominal temperatures, rather than nanometric material. The fine porous nature of the material produced *via* sol-gel reactions (Figure 4.3 (a) and (b)) has previously been explained as resulting from dispersion caused by the evolution of CO_2 , CO , and H_2O gases during the combustion of the organic matrix.²⁹⁵ Conversely, an $\text{Al}_2\text{Mo}_3\text{O}_{12}$ sample

synthesized using a standard mechanical-activation solid-state reaction technique has much larger particle sizes (~1-10 μm) and rougher surfaces (Figure 4.3 (d)).

In order to understand the effect of metal-to-PVA ratio on the mean particle size of $\text{Al}_2\text{Mo}_3\text{O}_{12}$, samples synthesized using two different ratios, 1:2 and 1:8, were treated to identical calcination conditions of 700 °C for 15 min. SEM micrographs of the resulting products (Figure 4.4a and 4.4b) show that substantially larger particles were formed in the sample with higher PVA content. This shows that the metal/PVA ratio could be an important tool for tailoring particle size. Higher PVA content leads to much larger particles due to the greater exothermicity of thermal decomposition of the organic residue.

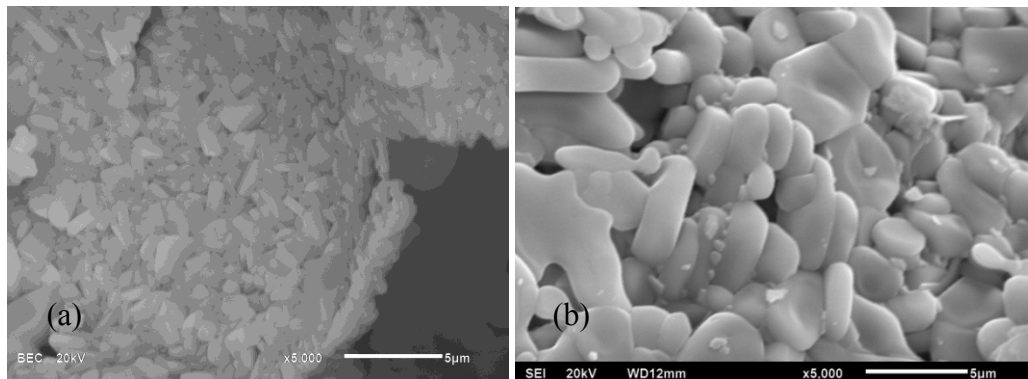


Figure 4.4: SEM micrographs of the monophasic $\text{Al}_2\text{Mo}_3\text{O}_{12}$ powder prepared through PVA-assisted sol-gel method and calcined at 700 °C for 15 min using (a) 1:2 and (b) 1:8 metal to PVA ratio. Reprinted with permission from Ari, M.; Miller, K. J.; Marinkovic, B. A.; Jardim, P. M.; de Avillez, R.; Rizzo F.; White M. A. *J. Sol-Gel Sci. Technol.* **2011**, 58, 121–125. Copyright 2010 Springer.

4.4 CONCLUSIONS

Monophasic, submicron (~300 nm) $\text{Al}_2\text{Mo}_3\text{O}_{12}$ was synthesized successfully using a simplified PVA assisted sol-gel technique with shorter calcination times and lower temperatures than standard mechanical-activation solid-state reaction techniques. It was observed that metal to PVA ratio, together with calcination temperature and time, could be used as a control parameter to tailor the particle size of the final product. The results suggest possible synthetic routes for other members of the $A_2M_3O_{12}$ family using a similar approach.

5.1 INTRODUCTION

Generally, it is assumed that low-energy transverse thermal vibrations of two-coordinate atoms along with possible contributions from translational modes are responsible for negative thermal expansion in open-framework orthorhombic structures.^{6,21,25,26,27,28,29,33,34,35,36,38,39}

Since the $A_2M_3O_{12}$ family has a large degree of chemical flexibility within the orthorhombic *Pbcn* (No. 60) space group there exists a large range of variation of linear coefficients of thermal expansion for the orthorhombic $A_2M_3O_{12}$ phases.^{135, 201} However, another important characteristic of the $A_2M_3O_{12}$ family is the existence of the orthorhombic to monoclinic phase transition, because low-temperature monoclinic counterparts of the orthorhombic phases have coefficients of thermal expansion that are highly positive.^{38,76} Some authors have shown a correlation between the temperature of the phase transition (T_{trs}) in this family and electronegativity of A ,^{38,78} with more electronegative A atoms exhibiting higher phase transition temperatures (Table 5.1).

[§] Portions of this chapter are excerpted and used with permission from: Marinkovic, B. A.; Ari, M.; de Avillez, R.; Rizzo F.; Ferreira, F.F.; Miller, K. J.; Johnson, M.B.; White, M. A. *Chem. Mater.* **2009**, *21*, 2886-2894. K.J. Miller's contribution to the work in this manuscript was: determination of the low-temperature heat capacity, TGA and DSC results, and writing a first draft of that section of the manuscript. The material characterization and the thermal expansion coefficients were determined by Dr. Bojan Marinkovic and will not be discussed at length in this chapter, but this material included for completion and to provide a context for the heat capacity and DSC results.

Table 5.1: Phase transition temperatures of select $A_2M_3O_{12}$ materials

Material	$T_{\text{trs}} / \text{K}$	Material	$T_{\text{trs}} / \text{K}$
$\text{Al}_2\text{Mo}_3\text{O}_{12}$	475, ²⁰¹ 473 ⁷⁸	$\text{AlFeMo}_3\text{O}_{12}$	642 ²⁰¹
$\text{Sc}_2\text{Mo}_3\text{O}_{12}$	178, ⁷⁶ 282 ⁷⁸	$\text{AlCrMo}_3\text{O}_{12}$	557 ²⁰¹
$\text{In}_2\text{Mo}_3\text{O}_{12}$	608 ⁷⁸	$\text{CrFeMo}_3\text{O}_{12}$	738 ²⁰¹
$\text{Cr}_2\text{Mo}_3\text{O}_{12}$	658, ⁷⁸ 676 ²⁰¹	$\text{Al}_2\text{W}_3\text{O}_{12}$	267 ⁷⁸
$\text{Fe}_2\text{Mo}_3\text{O}_{12}$	772, ⁷⁸ 786 ²⁰¹	$\text{In}_2\text{W}_3\text{O}_{12}$	525 ⁷⁸

The thermal expansion and phase transition of the orthorhombic $\text{Y}_2\text{Mo}_3\text{O}_{12}$ phase (with *Pbcn* space group) were recently studied for the first time, and it was observed that this phase presents very high NTE between 403 K and 1073 K.¹⁸⁹ Note that at temperatures lower than 823 K this phase is metastable (another orthorhombic phase with *Pba2* space group is stable), but it is kinetically preferred.¹⁴¹ However, the *Pbcn* phase is hygroscopic and poorly crystalline in air at room temperature; therefore it needs to be thermally treated to assume its anhydrous crystalline orthorhombic (*Pbcn*) NTE form. This is especially important because the presence of water hinders the motions of the polyhedra.¹⁹⁰

There is little information about the orthorhombic *Pbcn* $\text{Y}_2\text{Mo}_3\text{O}_{12}$ phase below room temperature. Therefore, the aim of this study was to shed more light on thermal expansion,²²⁷ heat capacity, and possible phase transitions of $\text{Y}_2\text{Mo}_3\text{O}_{12}$ in the temperature range between 2 K and 450 K.

5.2 METHODS

$\text{Y}_2\text{Mo}_3\text{O}_{12}$ was synthesized by Dr. Bojan Marinkovic using the solid-state reaction method described in Section 2.1.1 and characterized using high resolution XPRD (HRXRPD) from data collected by Dr. Bojan Marinkovic, in vacuum (8-10 mTorr), at four different temperatures (20 K, 150 K, 300 K and 450 K), using a commercial closed-cycle He cryostat (Advanced Research Systems), at the X-Ray Powder Diffraction (D10B-XPD) beamline²¹ of the Brazilian Synchrotron Light Laboratory (LNLS). X-rays of 1.23989 Å wavelength were selected and data were recorded at different temperatures for 2 s at each 2θ in steps of 0.004° from 10° to 70° . Rietveld refinement was performed using Topas-Academic software (as described in Section 3.6.2.1).^{**}

The sample was characterized using SEM (by Dr. Bojan Marinkovic, as described in Section 3.1), TGA (as described in Section 3.3), DSC (as described in Section 3.4), and heat capacity measurements (as described in Section 3.7).

^{**} For further information on the equipment and parameters selected for data collection and refinement at the LNLS please see the original manuscript, Marinkovic, B. A.; Ari, M.; de Avillez, R.; Rizzo F.; Ferreira, F.F.; Miller, K. J.; Johnson, M.B.; White M. A. *Chem. Mater.* **2009**, *21*, 2886-2894.

5.3 PHASE PURITY OF $Y_2Mo_3O_{12}$

The $Y_2Mo_3O_{12}$ sample was investigated by HRXRPD over the temperature range 10 K to 450 K (by Dr. Bojan Marinkovic) and no traces of the precursor phases or bi-products were observed. The purity was confirmed by SEM analysis of this sample in back-scattering mode. It was observed that no first-order phase transition occurred in the investigated temperature range (10 K to 450 K); see below for details. The absence of an orthorhombic to monoclinic phase transition for $Y_2Mo_3O_{12}$ was confirmed through Rietveld refinement of the whole diffraction pattern (Figure 5.1). Therefore, the $Y_2Mo_3O_{12}$ phase maintained the orthorhombic $Pbcn$ structure from 450 K to 20 K, or lower.

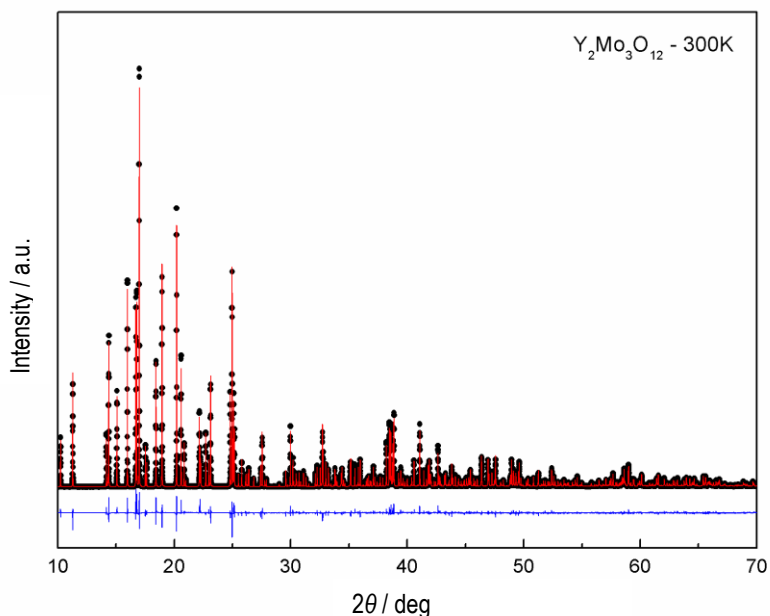


Figure 5.1: High-resolution XRPD pattern for $Y_2Mo_3O_{12}$ at $T = 300$ K. Experimental profile (black points), calculated (red full lines) and difference profiles (blue full lines). Reprinted with permission from Marinkovic, B. A.; Ari, M.; de Avillez, R.; Rizzo F.; Ferreira, F.F.; Miller, K. J.; Johnson, M.B.; White M. A. *Chem. Mater.* **2009**, *21*, 2886-2894. Copyright 2009 American Chemical Society.

5.4 HEAT CAPACITY AND DSC OF $Y_2Mo_3O_{12}$

5.4.1 DIFFERENTIAL SCANNING CALORIMETRY

Figure 5.2 shows the DSC results for anhydrous $Y_2Mo_3O_{12}$. Within the limit of detection (1 J g^{-1} for the small sample of $Y_2Mo_3O_{12}$), there are no features in the temperature range from 103 K to 673 K.

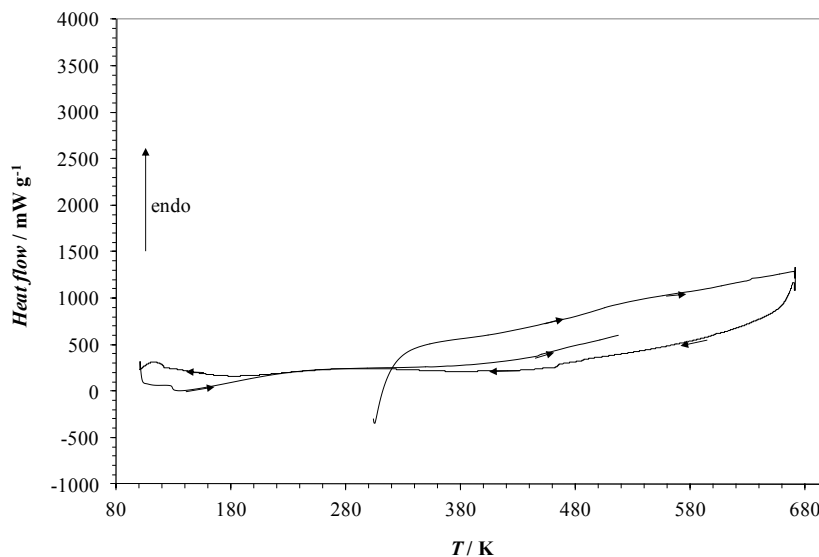


Figure 5.2: DSC results for 4.826 mg of anhydrous $Y_2Mo_3O_{12}$ measured in a helium atmosphere from 103 K to 673 K with a heating rate of 10 K min^{-1} . The arrows indicate the direction of the scan, starting at room temperature. Reprinted with permission from Marinkovic, B. A.; Ari, M.; de Avillez, R.; Rizzo F.; Ferreira, F.F.; Miller, K. J.; Johnson, M.B.; White M. A. *Chem. Mater.* **2009**, *21*, 2886-2894. Copyright 2009 American Chemical Society.

5.4.2 HEAT CAPACITY

In order to obtain accurate heat capacity results below 373 K, it was necessary to determine the experimental condition necessary for *in situ* dehydration of $Y_2Mo_3O_{12}$.

After heating the samples to 403 K for 4 min in a TA Instruments SDT Q600, using an aluminum pan under argon, the water was fully removed (limit of detection, 0.1 mol %

water) (Figure 5.3). Subsequent runs indicated that holding at 373 K in air for 10 min also was sufficient for drying the samples.

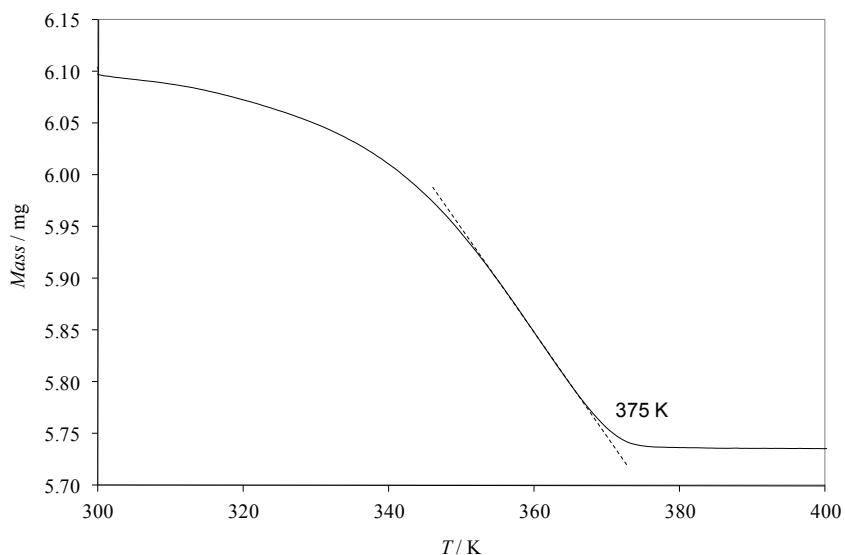


Figure 5.3: TGA of a sample of $Y_2Mo_3O_{12}$ heated under argon to 400 K in order to determine the dehydrated mass of the sample.

The heat capacity results were evaluated in terms of their sample contribution to the total heat capacity ($C_{\text{sample}} / C_{\text{total}} \times 100 \%$), the calculated reproducibility ($\delta C_{\text{sample}} / C_{\text{sample}} \times 100 \%$), and coupling constant (sample contribution, reproducibility and coupling constant data are provided in Appendix A) show no thermal anomalies over the examined temperature range, 2 K to 390 K (Full data sets for the heat capacity of $Y_2Mo_3O_{12}$ are provided in Appendix B). Furthermore, the heat capacity shows no dependence on sample mass over the range 4.9491 mg to 13.9403 mg (sample mass dependence can be indicative of low thermal conductivity, leading to uncertainty in heat capacity results).³⁰⁶ Taking into account the full temperature range of the DSC and heat capacity results, no thermal anomalies were observed in $Y_2Mo_3O_{12}$ over the temperature

range 2 K to 670 K, supporting the absence of an orthorhombic to monoclinic phase transition over this temperature range.

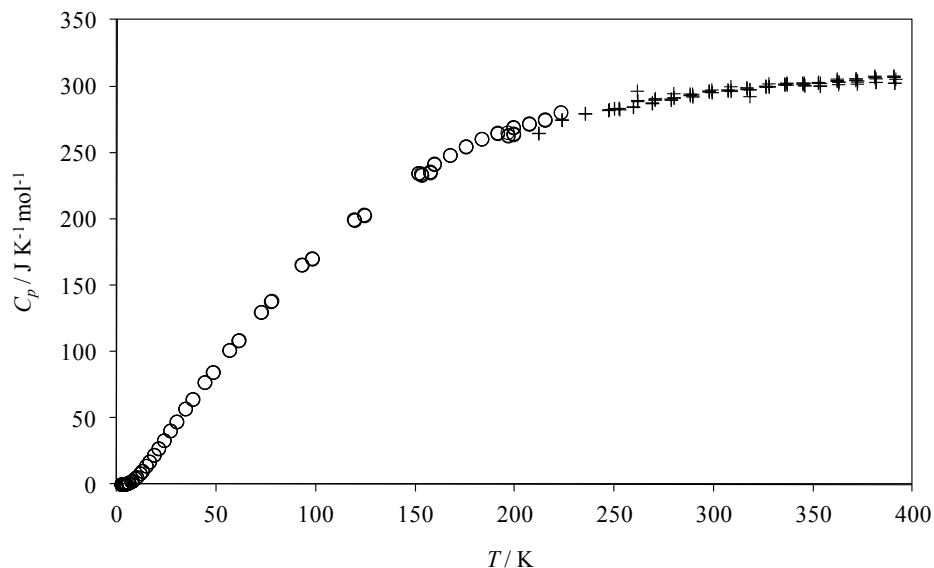


Figure 5.4: Heat capacity data for $\text{Y}_2\text{Mo}_3\text{O}_{12}$ samples ranging in size from 4.9491 mg to 13.9403 mg from 2 K to 390 K. Lower temperature samples were measured using Apiezon[®] T grease, ○, and higher temperature samples were measured using Apiezon[®] H grease, +. Samples required heating to 340 K prior to measurements to ensure sample dehydration, as explained in Section 5.4.2, therefore, the low-temperature Apiezon[®] N grease was unsuitable for measurements with this system. Reprinted with permission from Marinkovic, B. A.; Ari, M.; de Avillez, R.; Rizzo F.; Ferreira, F.F.; Miller, K. J.; Johnson, M.B.; White M. A. *Chem. Mater.* **2009**, *21*, 2886-2894. Copyright 2009 American Chemical Society.

5.5 DETERMINATION OF THE INTRINSIC CTE AND POLYHEDRAL DISTORTION

5.5.1 COEFFICIENT OF THERMAL EXPANSION

The variation of unit-cell parameters of $\text{Y}_2\text{Mo}_3\text{O}_{12}$ in the range of 20 K to 400 K is shown in Figure 5.5. The *b*- and *c*-axes diminish with increasing temperature throughout the temperature range. On the other hand, the *a*-axis increases from 20 K to 300 K, but then remains unchanged between 300 K and 450 K. This behavior of the cell

parameters leads to a nearly linear reduction of the cell volume as a function of temperature. The net volume coefficient of thermal expansion, α_V , of $\text{Y}_2\text{Mo}_3\text{O}_{12}$ in the range 20 K to 450 K was highly negative, $-27.1 \times 10^{-6} \text{ K}^{-1}$, giving an average linear coefficient of expansion, $\alpha_\ell (= \alpha_V/3)$ of $-9.02 \times 10^{-6} \text{ K}^{-1}$ over this temperature range.

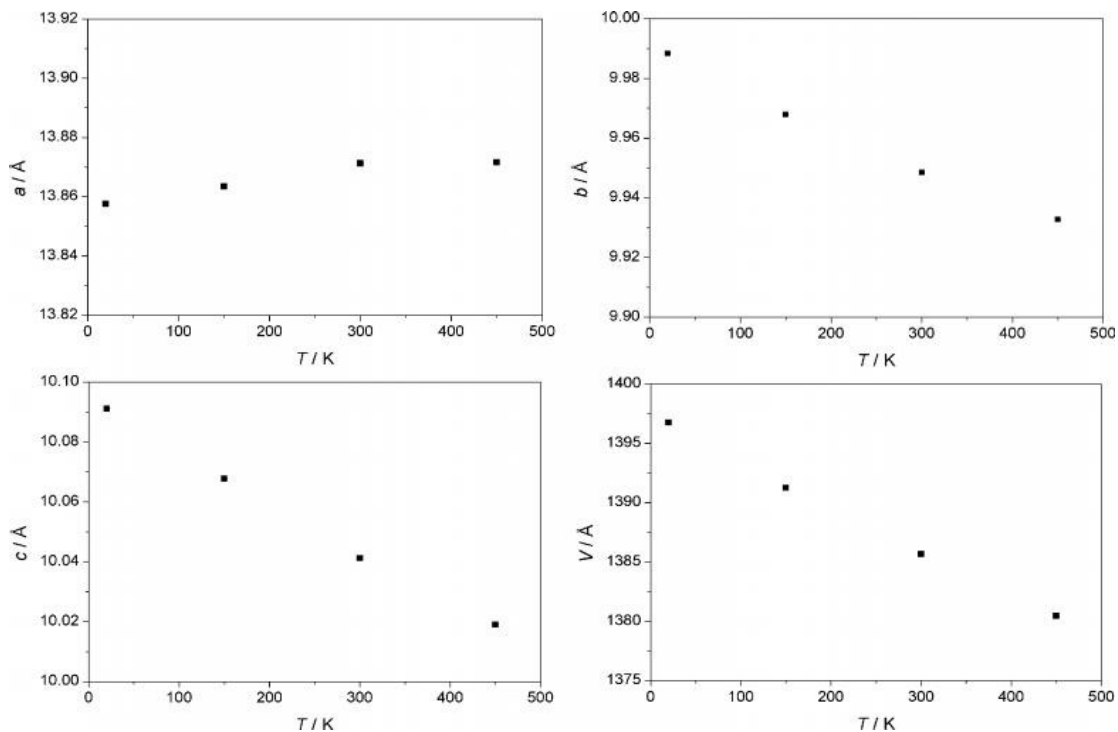


Figure 5.5: Lattice parameters of $\text{Y}_2\text{Mo}_3\text{O}_{12}$ vs. temperature. Standard uncertainties are included but are too small to be visible in the graphs. Reprinted with permission from Marinkovic, B. A.; Ari, M.; de Avillez, R.; Rizzo F.; Ferreira, F.F.; Miller, K. J.; Johnson, M.B.; White M. A. *Chem. Mater.* **2009**, *21*, 2886-2894. Copyright 2009 American Chemical Society.

5.6 $\text{Y}_2\text{Mo}_3\text{O}_{12}$ IN THE LOW-TEMPERATURE RANGE

The temperature of the orthorhombic to monoclinic phase transition in several $A_2M_3O_{12}$ compounds has been correlated to the electronegativities of the A atoms.³⁸ The concept is that as the electronegativity of the A atom increases, the electron density on the

bridging oxygen atom atoms should decrease, causing the oxygen-oxygen attraction to increase, leading to structural transition at higher temperatures. However, the structure is very ionic and the correlation was with the electronegativities of the neutral atoms³¹⁶ (although referred to as that of A^{3+} ions).³⁸ Correlations of the orthorhombic to monoclinic phase transition temperature with the electronegativities of the A^{3+} ions³¹⁷ was not as strong (Figure 5.6), and neither model could accurately predict whether or not there would be an orthorhombic to monoclinic phase transition in $Y_2Mo_3O_{12}$. There is no such transition in $Y_2W_3O_{12}$ over the temperature range 15 K to 1373 K.¹⁹⁷ In $Sc_2Mo_3O_{12}$ this transition occurs at $T = 178$ K,¹⁹⁵ whereas it is absent in the tungstate counterpart⁷⁶ suggesting that the M^{6+} ions might play a role. It is also not clear why some other molybdates have higher temperatures of phase transition than their tungstate counterparts (for example, $InMo_3O_{12}/InW_3O_{12}$ see Table 5.1).¹⁹⁴

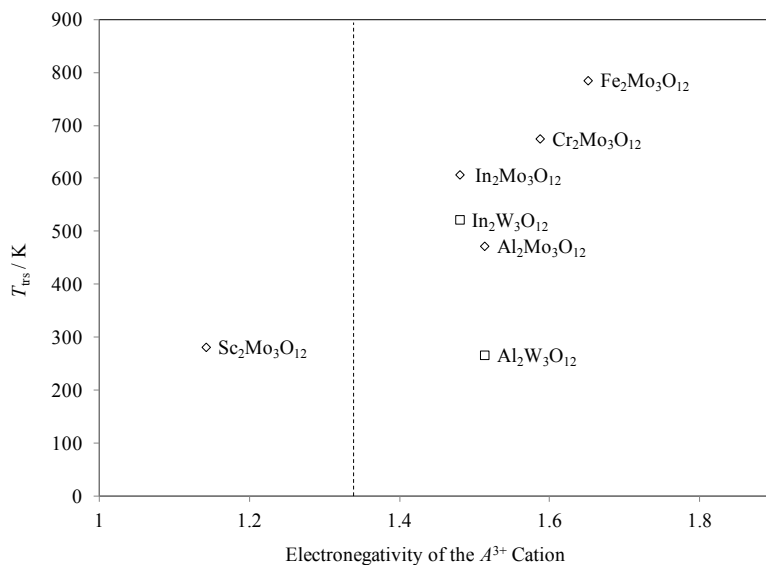


Figure 5.6: Temperature of the orthorhombic to monoclinic phase transitions in $A_2Mo_3O_{12}$ and $A_2W_3O_{12}$ as a function of the electronegativity of A^{3+} ions (Li-Xue scale).³¹⁷ A dashed line is included at 1.340 on the Li-Xue scale, indicating the electronegativity of Y^{3+} .³¹⁷

The nature of the a -axis variation with temperature, as shown in Figure 5.5, could be a sign of subtle changes. For example, $\text{Y}_2\text{Mo}_3\text{O}_{12}$ and related $A_2M_3\text{O}_{12}$ materials could be candidates for cationic migration.³¹⁸ This feature in the temperature dependence of the a -axis of $\text{Y}_2\text{Mo}_3\text{O}_{12}$ is unexpected was not previously explicitly discussed in the literature, although Forster and Sleight¹⁹⁷ showed that the slope of the a -axis of $\text{Y}_2\text{W}_3\text{O}_{12}$ (b -axis in the nonstandard $Pnca$ space group) changes sign, from positive to negative, at $T > 295$ K. The alteration of sign of the a -axis thermal expansion in $\text{Y}_2\text{Mo}_3\text{O}_{12}$ was not followed by a change in the space group symmetry, whereas a slight change in the negative thermal expansion coefficient at 430 K in ZrW_2O_8 is accompanied by a phase transition from $P2_13$ to $Pa-3$.⁵⁸ If the observed temperature dependence of the a -axis were a consequence of a second-order phase transition, it would be accompanied by other anomalies, but the heat capacity (Figure 5.4) shows no evidence of even a subtle second-order phase transition in $\text{Y}_2\text{Mo}_3\text{O}_{12}$.

Possibly, the change in sign of thermal expansion along the a -axis is promoted by a mechanism similar to that recently proposed³¹⁹ for cubic Cu_2O , which changes its thermal expansion from negative to positive near room temperature.^{10,217} This change of thermal expansion in Cu_2O is not attributed to a phase transition, but related to the subtle competition between the two contributions, different at the atomic level, to the thermal expansion behavior in solids.^{217,319} These competing interactions in Cu_2O are the asymmetrical potential between the first neighbors, responsible for the positive thermal expansion, and the transversal vibrations of the two-coordinate atoms (a low-energy soft vibrational mode), responsible for negative thermal expansion. The change of the sign of thermal expansion along the a -axis in $\text{Y}_2\text{Mo}_3\text{O}_{12}$ can be understood as a change in the

balance of two different contributions to thermal expansion between 300 K and 450 K. Taking into account the findings of Liang *et al.*,¹⁵⁷ there are both high-energy optical phonons contributing to NTE in $Y_2Mo_3O_{12}$, together with the well-known low-energy (soft) modes (translational and librational motions). The temperature dependence of these modes leads to thermomiotic behavior, relative to the positive thermal expansion contributions, and provokes the change of sign in thermal expansion along the a -axis, from positive to negative (*i.e.*, the addition of high-energy modes tips the balance to NTE at higher temperatures). It is worth mentioning that this kind of change in the a -axis thermal expansion never occurs in members of the $A_2M_3O_{12}$ family with less pronounced thermomiotic behavior, such as ScW_3O_{12} ¹⁹⁵ and $ScMo_3O_{12}$,⁷⁶ this axis showing positive thermal expansion over the whole temperature range. On the other hand, low-energy translational and librational modes predominate over positive thermal expansion contributions along the b - and c -axes in $Y_2Mo_3O_{12}$ already from the lowest temperatures. This weighting of the soft phonon modes over the positive thermal contribution has been used earlier by Smith and White³²⁰ to explain the negative thermal expansion in Ge and several III-V and II-VI compounds below 80 K. The same mechanism explains the switch from NTE to PTE at higher temperature in Si and CuCl.¹⁰

The details of the mechanism that promotes NTE in $A_2M_3O_{12}$ were not as well understood as for the AM_2O_8 family,^{117,321} until recently.¹⁹⁰ It had been generally assumed for $A_2M_3O_{12}$ that transverse low-energy phonon modes of two-coordinate oxygens are responsible for this phenomenon, while their polyhedra are quasi-rigid, whereas the polyhedra in AM_2O_8 are fully rigid. The low-frequency modes present in $Y_2Mo_3O_{12}$ are discussed further in Chapter 9.

5.7 CONCLUSIONS

Thermal properties of orthorhombic *Pbcn* $\text{Y}_2\text{Mo}_3\text{O}_{12}$, such as thermal expansion, stability and heat capacity were investigated over a wide temperature range, as low as 2 K (heat capacity) and as high as 670 K (DSC). The orthorhombic to monoclinic phase transition, commonly observed in $A_2M_3O_{12}$ structures, is absent over the temperature range 2 K to 670 K. In its orthorhombic *Pbcn* phase, $\text{Y}_2\text{Mo}_3\text{O}_{12}$ exhibited large negative thermal expansion ($\alpha_\ell = -9.02 \times 10^{-6} \text{ K}^{-1}$, averaged over $T = 20 \text{ K}$ to $T = 450 \text{ K}$). The unit-cell parameter, a , shows anomalous behavior, increasing in the range between 20 K and 300 K, then decreasing as the temperature is increased further. The latter is not due to a phase transition, but can be explained through a change of balance of atomic-level mechanisms contributing to expansion and reduction of interatomic distances.

6.1 INTRODUCTION

$\text{HfMgMo}_3\text{O}_{12}$ can be classified as a cousin to the $A_2M_3\text{O}_{12}$ family, with a slightly different space group, and two A^{3+} ions replaced by Hf^{4+} and Mg^{2+} .^{81,203,199} Both $\text{HfMgMo}_3\text{O}_{12}$ ¹⁹⁹ and $\text{HfMgW}_3\text{O}_{12}$ ^{81,203} have been characterized previously at temperatures above 298 K, but, with the exception of some neutron diffraction data collected by Gindhart *et al.* on $\text{HfMgW}_3\text{O}_{12}$,⁸¹ no work has been reported on the low-temperature properties of either the tungstate or molybdate analogue. Furthermore, the room-temperature structure of $\text{HfMgW}_3\text{O}_{12}$ was first reported by Suzuki and Omote²⁰³ to be orthorhombic, space group $Pnma$, while Gindhart *et al.*⁸¹ suggest the monoclinic space group, $P2_1/a$, with a transition to $Pnma$ between 400 K and 473 K. $\text{HfMgMo}_3\text{O}_{12}$ crystallizes at room temperature in the orthorhombic $Pnma$ (62) space group¹⁹⁹ which likely forms an open-framework structure with easily excited low-frequency transverse vibrations, although its full crystal structure is not yet resolved. However, while $\text{HfMgW}_3\text{O}_{12}$ has an average linear thermal expansion coefficient, α_ℓ , of $-1.2 \times 10^{-6} \text{ K}^{-1}$ (400 K to 800 K),⁸¹ $\text{HfMgMo}_3\text{O}_{12}$ has a low positive coefficient of thermal expansion, $\alpha_\ell = 1.2 \times 10^{-6} \text{ K}^{-1}$ (293 K to 1013 K).¹⁹⁹

^{††} Adapted and used with permission from: Miller, K. J.; Johnson, M. B.; White, M. A.; Marinkovic, B. A. *Solid State Commun.* **2012**, *152*, 1748-1752. K.J. Miller's contribution to the work in this manuscript was: synthesis, determination of the low temperature heat capacity and thermal conductivity, obtaining DSC measurements, the initial refinement of the XRPD patterns, writing most of the first draft of the manuscript and subsequent editing.

The phase transition of $\text{HfMgW}_2\text{O}_{12}$ from monoclinic to orthorhombic was characterized as being second-order between 400 K and 473 K, from XRPD and neutron diffraction.⁸¹ A continuous phase transition could lead to less stress in the material than a first-order phase change, due to the volume discontinuity associated with the latter.

This chapter reports studies concerning the presence of a sub-ambient phase transition from a monoclinic low-temperature phase to an orthorhombic higher-temperature phase in $\text{HfMgMo}_3\text{O}_{12}$.

6.2 METHODS

$\text{HfMgMo}_3\text{O}_{12}$ was synthesized according to ref 199. The low-temperature XRPD patterns were collected as described in Section 3.6.1.2 and analyzed according to methods described in Section 3.6.2.2. SEM (as described in Section 3.1) was used to determine the grain size and structure and DSC (as described in Section 3.4) and heat capacity (as described in Section 3.7) were used to determine the phase transition temperature.

6.3 RESULTS AND DISCUSSION

6.3.1 SAMPLE CHARACTERIZATION AND PHASE TRANSITION

Samples of $\text{HfMgMo}_3\text{O}_{12}$ sintered at 1063 K for 12 h were more robust compared to other $A_2\text{Mo}_3\text{O}_{12}$ compounds.³⁵ SEM images of the sintered sample show that the sintering conditions produced well-fused homogenous grains (Figure 6.1).

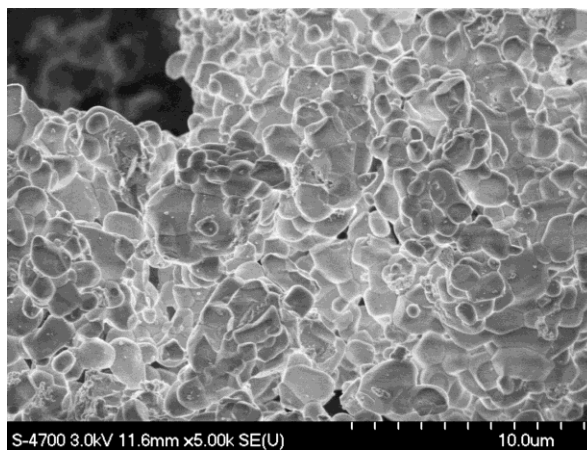


Figure 6.1: SEM image of $\text{HfMgMo}_3\text{O}_{12}$ showing the homogeneous particle morphology and excellent sintering between the grains. Reprinted with permission from Miller, K. J.; Johnson, M. B.; White, M. A.; Marinkovic, B. A. *Solid State Commun.* **2012**, *152*, 1748-1752. Copyright 2012 Elsevier.

A 59.5 mg sample $\text{HfMgMo}_3\text{O}_{12}$ was analysed in a steel DSC pan to accommodate the larger sample size needed to resolve the phase transition; the temperature range was from 103 K to 273 K with a heating rate of 10 K min^{-1} . The sub-ambient DSC results (Figure 6.2) show a subtle endotherm (monoclinic to orthorhombic phase transition; see below), with an enthalpy change ($\Delta_{\text{trs}}H$) of 0.27 kJ mol^{-1} at an onset temperature of 173 K. The corresponding transition entropy change, $\Delta_{\text{trs}}S$ is $1.6 \text{ J K}^{-1} \text{ mol}^{-1}$, in good agreement with the values reported for other members of the $A_2M_3O_{12}$ family.¹⁹³ The small value has been attributed to the subtle change in structure

where the polyhedra undergo a static rotation.¹⁹³ No other features were seen in the DSC in the examined temperature range. A typical baseline for DSC scans is shown in Appendix D.

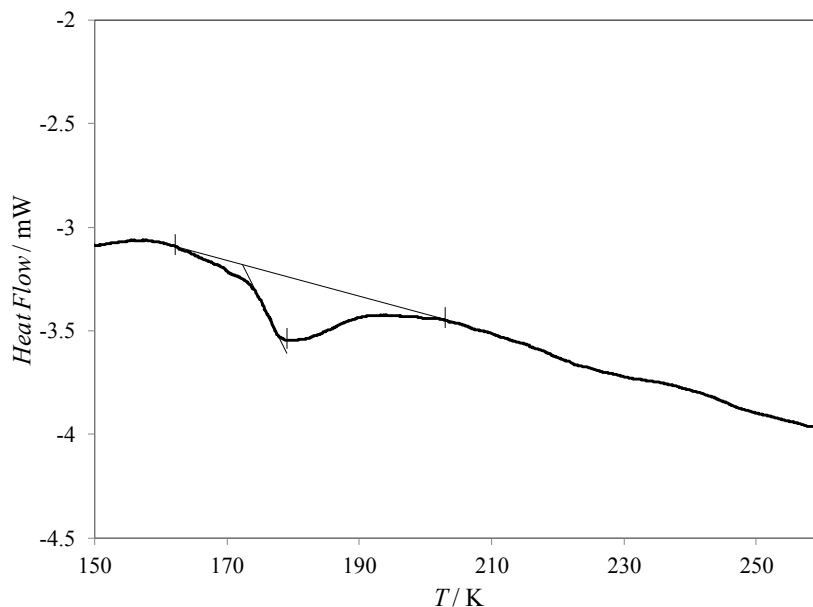


Figure 6.2: The DSC scan for HfMgMo₃O₁₂ at a heating rate of 10 K min⁻¹ (exotherm up) shows the phase transition with an enthalpy change of 0.27 kJ mol⁻¹ at an onset temperature of 173 K. Reprinted with permission from Miller, K. J.; Johnson, M. B.; White, M. A.; Marinkovic, B. A. *Solid State Commun.* **2012**, *152*, 1748-1752. Copyright 2012 Elsevier.

XRPD patterns taken at temperatures of 80 K, 120 K, 160 K, 180 K, 240 K and 297 K were analyzed by the Le Bail method to investigate the space group of HfMgMo₃O₁₂ below room temperature. The higher-angle data had poor signal-to-noise ratio so the refinement was confined to $\leq 38^\circ$ in 2θ . Diffraction patterns taken at 297 K, 240 K and 180 K (Figure 6.3) give excellent fits for the orthorhombic *Pnma* space group. However, for the pattern taken at 160 K, a weak new peak was present at $\sim 25.8^\circ$ in 2θ , indicating a reduction in symmetry (Figure 6.4). At 120 K and 80 K this peak was more intense and better defined as well as accompanied by the appearance of a second peak at $\sim 23.7^\circ$ in 2θ . The pattern taken at $T = 160$ K could not be fit to higher-symmetry

orthorhombic space groups, such as $Pnma$ and $Pbcn$, or lower symmetry space groups, either orthorhombic or monoclinic, possibly indicating the presence of multiple phases. The diffraction patterns at $T = 120$ K and 80 K exhibited an excellent fit within the lower symmetry monoclinic $P2_1/a$ space group (Figure 6.5). The unsatisfactory fit for the $T = 160$ K pattern using just one phase (orthorhombic or monoclinic) can be understood in the light of the DSC results (Figure 6.2): the XRPD at $T = 160$ K arises from the co-existence of two $\text{HfMgMo}_3\text{O}_{12}$ phases, orthorhombic $Pnma$ (60) and monoclinic $P2_1/a$ (14).

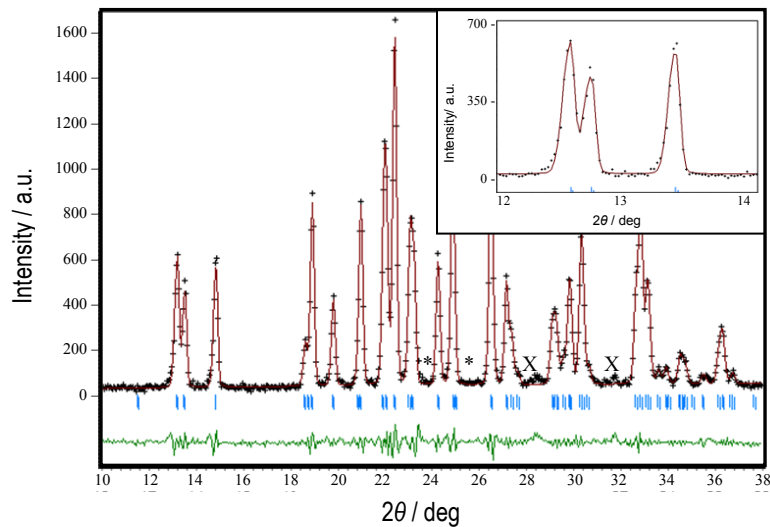


Figure 6.3: XRPD patterns for $\text{HfMgMo}_3\text{O}_{12}$ showing the measured pattern in black, the fitted pattern in red, and the difference plot in green. Peaks from the sample holder are marked with an \times , and $*$ marks correspond to the regions of the new peaks associated with the low-temperature phase for $T = 180$ K showing an excellent fit to the orthorhombic $Pnma$ space group. The inset shows the quality of fit at low angles. Adapted from Miller, K. J.; Johnson, M. B.; White, M. A.; Marinkovic, B. A. *Solid State Commun.* **2012**, *152*, 1748-1752. Copyright 2012 Elsevier.

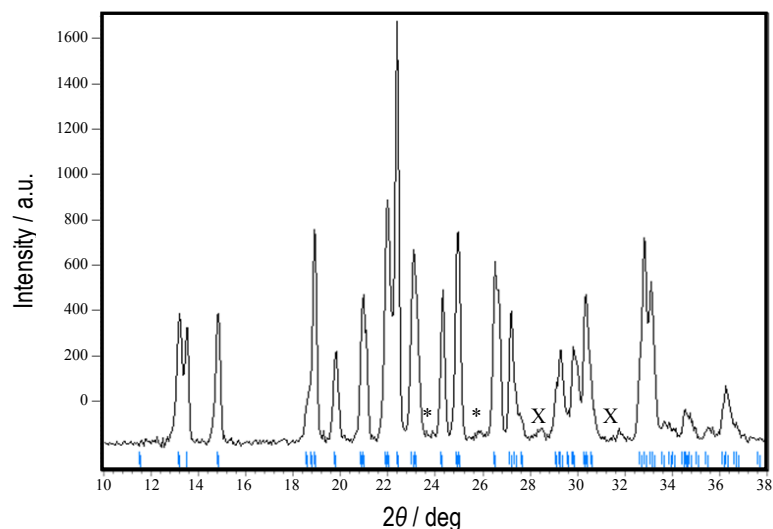


Figure 6.4: XRPD patterns for HfMgMo₃O₁₂ showing the measured pattern in black. Peaks from the sample holder are marked with an x, and * marks correspond to the regions of the new peaks associated with the low-temperature phase for $T = 160$ K which could not be fit as a single phase material and showed both *Pnma* and *P2₁/a* character. Tick marks correspond to the orthorhombic *Pnma* peak positions. Adapted from Miller, K. J.; Johnson, M. B.; White, M. A.; Marinkovic, B. A. *Solid State Commun.* **2012**, *152*, 1748-1752. Copyright 2012 Elsevier.

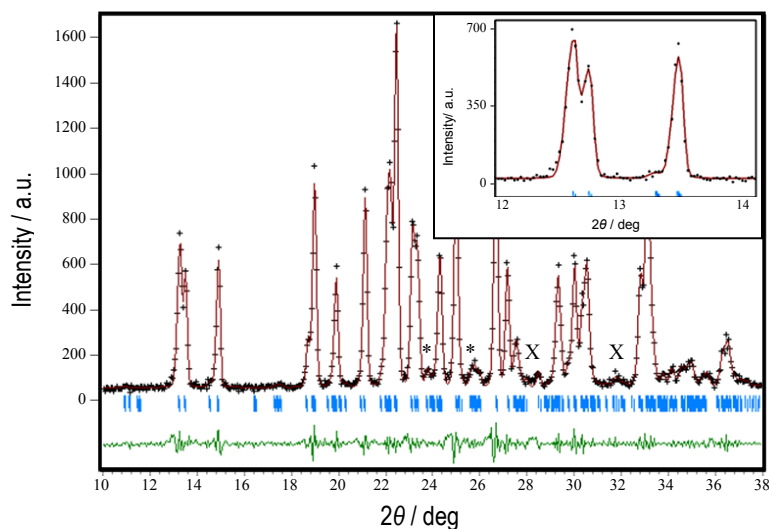


Figure 6.5: XRPD patterns for HfMgMo₃O₁₂ showing the measured pattern in black, the fitted pattern in red, and the difference plot in green. Peaks from the sample holder are marked with an x, and * marks correspond to the regions of the new peaks associated with the low-temperature phase for $T = 80$ K showing an excellent fit for the monoclinic *P2₁/a* space group. The inset shows the quality of fit at low angles. Adapted from Miller, K. J.; Johnson, M. B.; White, M. A.; Marinkovic, B. A. *Solid State Commun.* **2012**, *152*, 1748-1752. Copyright 2012 Elsevier.

The transition to a monoclinic phase at lower temperature is not unexpected since various *Pbcn* orthorhombic phases of compounds in this family exhibit such a transition,¹⁹³ as does HfMgW₃O₁₂.⁸¹ In the case of HfMgMo₃O₁₂ the phase transition from *P2₁/a* to *Pnma* is subtle, as observed by the DSC results (above) and the heat capacity (*vide infra*). The XRPD shows about 2% increase in the unit-cell volume from the *P2₁/a* phase at 120 K to *Pnma* phase at 180 K (Table 6.1), at the same level as previously found for some of the phase transitions in this crystal family,^{193,196} but more data closer to the transition would be required to say definitively whether or not the transition is first order.

Table 6.1: Lattice constants and space groups for HfMgMo₃O₁₂ at 180 K and 120 K.

<i>a</i> / Å	<i>b</i> / Å	<i>c</i> / Å	β / °	<i>V</i> (Å ³) – for 4 chemical formulae	<i>T</i> / K	Space group
9.56(5)	13.144(1)	9.47(8)	-	1191(5)	180	<i>Pnma</i>
16.13(7)	9.497(1)	18.75(7)	125.7(1)	1167(1)	120	<i>P2₁/a</i>

The low-temperature heat capacity of HfMgMo₃O₁₂, measured using relaxation calorimetry, from 5 K to 300 K also shows a small anomaly associated with the change in phase at *T* ~ 175 K (Figure 6.6; full data set in Appendix B), consistent with the DSC and XRPD results.

The goal of the XRPD study was space group determination and phase transition delineation, which was achieved. The unit cell volumes are reasonably accurate for those purposes but the small 2θ range and lack of internal thermal expansion standard mean that thermal expansion coefficients could not be determined accurately from these XRPD data.

6.3.2 HEAT CAPACITY

Heat capacity measurements were performed on two samples of $\text{HfMgMo}_3\text{O}_{12}$ of masses 13.26 mg and 14.69 mg shown in Figure 6.6. Smaller sample sizes did not resolve the low energy phase transition clearly and were therefore omitted from the analysis. Following the phase transition at $T \sim 175$ K, the sample coupling decreased remarkably, as shown in Appendix A, with values remaining constant at about 70 % for the rest of the measurement range. All data points were evaluated in terms of their sample contribution to the total heat capacity ($C_{\text{sample}} / C_{\text{total}} \times 100$ %) and the calculated reproducibility ($\delta C_{\text{sample}} / C_{\text{sample}} \times 100$ %) (Appendix A). Data for samples which did not contribute more than 25 % to the total heat capacity and/or which had a calculated deviation from reproducibility of more than 1.5 % were omitted from further analysis.

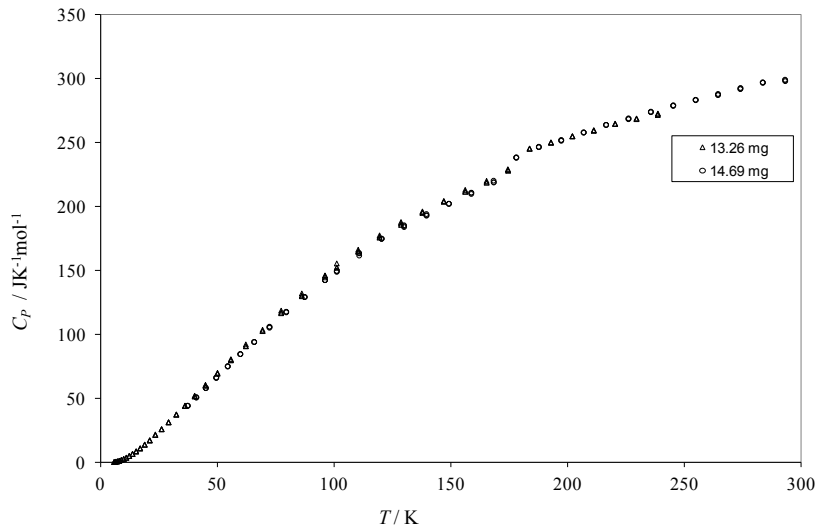


Figure 6.6: Experimental heat capacity data for $\text{HfMgMo}_3\text{O}_{12}$ for two samples (Δ , 13.26 mg; \circ , 14.69 mg) showing an anomaly at $T \sim 175$ K. Reprinted with permission from Miller, K. J.; Johnson, M. B.; White, M. A.; Marinkovic, B. A. *Solid State Commun.* **2012**, *152*, 1748-1752. Copyright 2012 Elsevier.

Heat capacity data analysis can reveal significant features concerning the lattice dynamics in solids and a detailed discussion concerning this material and other members of this family is presented in Chapter 9.

6.4 CONCLUSIONS

Heat capacity and DSC results of $\text{HfMgMo}_3\text{O}_{12}$ indicate a transition from the low-temperature monoclinic phase, $P2_1/a$, to the high-temperature phase, $Pnma$, at 175 K. The enthalpy and entropy changes associated with the orthorhombic to monoclinic structure are similar to values reported previously for similar structures, and demonstrate that only a small rearrangement is required for the phase transformation.

7.1 MOTIVATIONS

Orthorhombic $\text{In}_2\text{Mo}_3\text{O}_{12}$ (*Pnca*) has a low negative average intrinsic linear thermal expansion coefficient ($\alpha_\ell = -1.85 \times 10^{-6} \text{ K}^{-1}$ from 643 K to 1033 K) in the orthorhombic (*Pnca*) phase and is monoclinic (*P2₁/a*) ($\alpha_\ell = 12.4 \times 10^{-6} \text{ K}^{-1}$ from 373 K to 593 K) at room temperature.¹⁹⁶ Since $\text{HfMgMo}_3\text{O}_{12}$ (discussed in Chapter 6) and $\text{In}_2\text{Mo}_3\text{O}_{12}$ share the same monoclinic and similar orthorhombic space groups and have similar crystal ionic radii (85 pm for Hf^{4+} , 86 pm for Mg^{2+} , and 94 pm for In^{3+}),³²² this system could provide candidates for solid solutions with tailorable CTEs between those of the parent compounds, $\text{In}_2\text{Mo}_3\text{O}_{12}$ and $\text{HfMgMo}_3\text{O}_{12}$. Since $\text{HfMgMo}_3\text{O}_{12}$ has a low positive CTE ($\alpha_\ell = -1.2 \times 10^{-6} \text{ K}^{-1}$ from 400 K to 800 K) and $\text{In}_2\text{Mo}_3\text{O}_{12}$ has a correspondingly low negative CTE, in their respective orthorhombic phases, a solid solution of the two materials has the potential to produce a near-zero thermal expansion material.

This chapter reports information for a sample of $\text{In}_2\text{Mo}_3\text{O}_{12}$ characterized by XRPD to ensure sample purity. DSC results are presented to investigate the monoclinic to orthorhombic phase transition above room temperature and the low-temperature heat capacity was determined to investigate any thermal anomalies down to 2 K. Chapter 9 expands on the heat capacity results obtained for $\text{In}_2\text{Mo}_3\text{O}_{12}$ and $\text{HfMgMo}_3\text{O}_{12}$ (Chapter 6) with respect to their solid solutions.

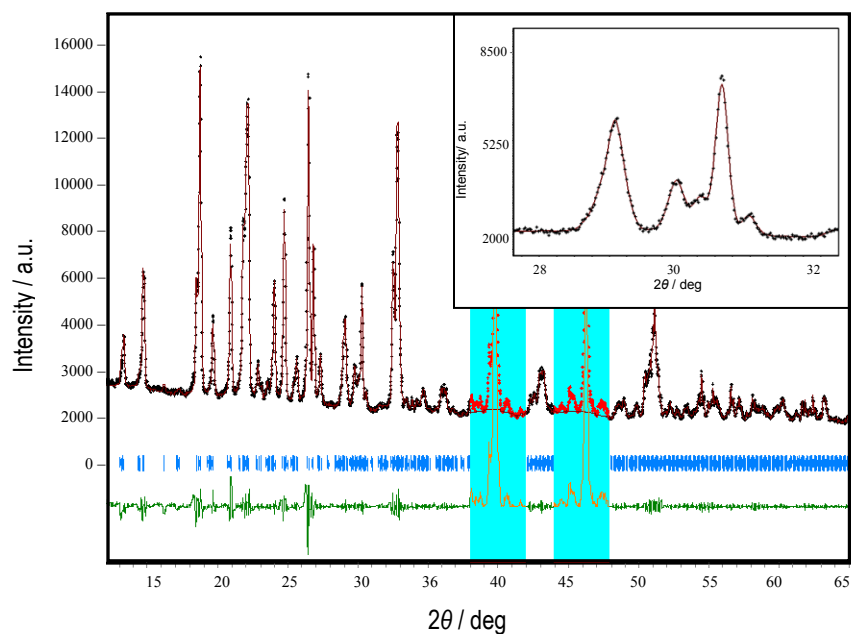
7.2 METHODS

$\text{In}_2\text{Mo}_3\text{O}_{12}$ was synthesized by solid-state reactions (as described in Section 2.2.1) and provided by Dr. Bojan Marinkovic. XRPD patterns were collected as described in Section 3.6.1.3, to confirm the phase purity, and analyzed according to methods described in Section 3.6.2.2. The sample was analyzed using DSC (as described in Section 3.4) and heat capacity (as described in Section 3.7).

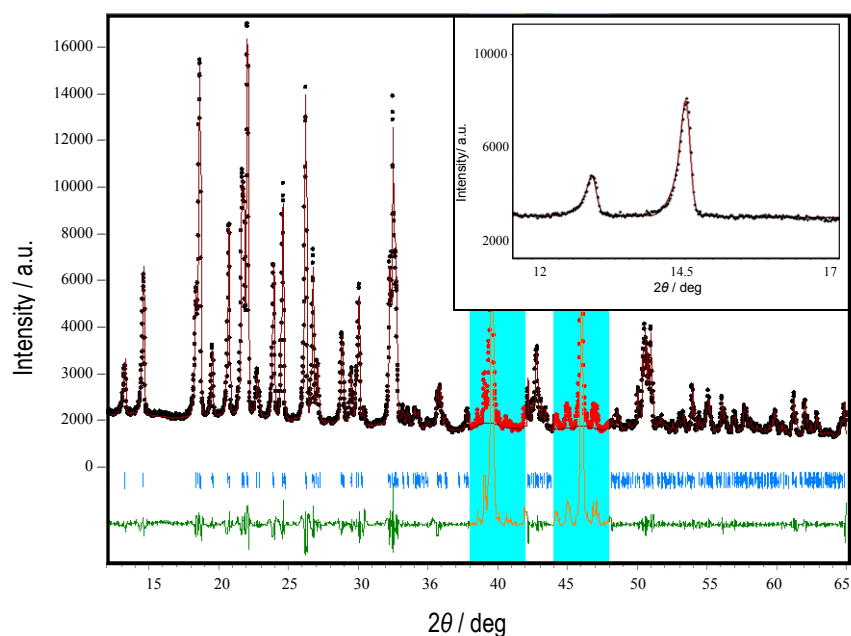
7.3 RESULTS AND DISCUSSION

7.3.1 SAMPLE CHARACTERIZATION AND PHASE TRANSITION

To confirm the monophasic nature of the sample, two XRPD patterns of $\text{In}_2\text{Mo}_3\text{O}_{12}$ were collected at temperatures above and below the reported T_{trs} at 610.5 K.¹⁹³ The patterns collected at room temperature and 838 K confirmed the monophasic nature of the monoclinic ($P2_1/a$) phase (Figure 7.1 (a)) and the orthorhombic ($Pnca$) phase (Figure 7.2 (b)), respectively.¹⁹⁶ The χ^2 (defined in Section 3.6.2) and R_B (Equation 3.11) for both patterns were below 9 and 0.2, respectively.



(a)



(b)

Figure 7.1: XRPD pattern for $\text{In}_2\text{Mo}_3\text{O}_{12}$ illustrating a Le Bail fit to (a) the monoclinic $P2_1/a$ space group at 298 K and (b) the orthorhombic $Pnca$ space group at 838 K; the measured pattern is in black, the fitted pattern is red, and the difference plot is green. The highlighted regions ($38^\circ < 2\theta < 42^\circ$ and $44^\circ < 2\theta < 48^\circ$) were excluded from refinement due to contributions from the platinum stage and the inset regions show the quality of the fitted patterns.

The unit cell parameters determined from XRPD were in agreement with values reported by Marinkovic *et al.* determined from high-resolution data collected at the Brazilian Synchrotron Light Laboratory (LNLS) (Table 7.1).¹⁹⁶

Table 7.1: Lattice constants and space groups for $\text{In}_2\text{Mo}_3\text{O}_{12}$ at 298 K and 838 K compared to the literature values at 373 K and 773 K determined by Marinkovic *et al.*.¹⁹⁶

	$a / \text{\AA}$	$b / \text{\AA}$	$c / \text{\AA}$	$\beta / ^\circ$	$V (\text{\AA}^3) - \text{for 4 chemical formulae}$	T / K	Space group
Present	9.5540(4)	13.3198(6)	9.6537(9)	-	1228.5(3)	838	$Pnca$
Literature ¹⁹⁶	13.320	9.557	9.669	-	1230.9	773	$Pbcn$
Present	16.2746(8)	9.5995(7)	18.9344(3)	125.1(1)	1209.9(6)	298	$P2_1/a$
Literature ¹⁹⁶	16.272	9.592	18.921	125.2	1206	373	$P2_1/a$

In the DSC experiment, a 12.54 mg powder sample of $\text{In}_2\text{Mo}_3\text{O}_{12}$ was analysed from 580 K to 640 K in an aluminum pan with heating rates of 5 K min^{-1} or 10 K min^{-1} (specified below) in helium flow. The DSC results, for the experiment using a heating rate of 10 K min^{-1} , (Figure 7.2) show an endotherm (monoclinic to orthorhombic phase transition; see below), with an enthalpy change ($\Delta_{\text{trs}}H$) of $(3.2 \pm 0.3) \text{ kJ mol}^{-1}$ at an onset temperature of 615 K. The corresponding transition entropy change, $\Delta_{\text{trs}}S$, is $(5.3 \pm 0.4) \text{ J K}^{-1} \text{ mol}^{-1}$. A second scan with a slower heating rate of 5 K min^{-1} confirmed the onset temperature of 615 K (graph shown in Appendix D). A typical baseline for DSC scans is also shown in Appendix D.

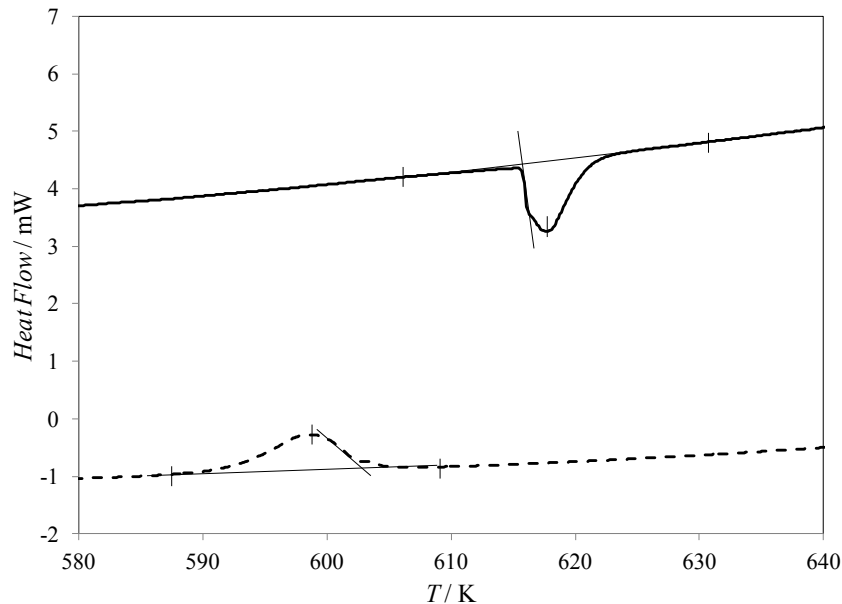


Figure 7.2: The DSC scan for 12.54 mg $\text{In}_2\text{Mo}_3\text{O}_{12}$, during heating (—) and cooling (---), at a heating rate of 10 K min^{-1} (exotherm up) shows the phase transition with an enthalpy change of 3.2 kJ mol^{-1} at an onset temperature of 615 K.

These values notably differ from those reported by Varga *et al.* which characterized the monoclinic to orthorhombic transition at $T_{\text{trs}} = 610.45 \text{ K}$ with a $\Delta_{\text{trs}}H$ of 0.89 kJ mol^{-1} , and $\Delta_{\text{trs}}S$ of $1.46 \text{ J K}^{-1} \text{ mol}^{-1}$.¹⁹³ The measurements performed by Varga *et al.* were carried out at a heating rate of 20 K min^{-1} on 50 mg to 100 mg pelletized samples said to be phase pure. While the average of the present T_{trs} , obtained on heating and cooling, was in good agreement with the values reported by Varga *et al.*, the discrepancy in the T_{trs} obtained on heating is outside the usual uncertainty and not likely linked to the fast scanning rate used in ref 193. The enthalpy and entropy changes associated with the static rotation of the polyhedra during the phase transition are larger for the present results, but both sets of results show quite low values, consistent with other members of the $A_2M_3O_{12}$ family.¹⁹³ No other features were seen in the DSC in the examined temperature range.

7.3.2 HEAT CAPACITY

Heat capacity results for separate measurements of four samples of $\text{In}_2\text{Mo}_3\text{O}_{12}$ of masses 9.94 mg, 18.62 mg, 20.64 mg, and 24.26 mg are shown in Figure 7.3 (full data sets in Appendix B). The coupling constants for all the samples, using Apiezon[®] N grease to assure good thermal contact, were above 80 % for the entire temperature range and better than 90% below 250 K (Appendix A). The data were evaluated in terms of the sample contribution to the total heat capacity ($C_{\text{sample}} / C_{\text{total}} \times 100 \%$) and the calculated reproducibility ($\delta C_{\text{sample}} / C_{\text{sample}} \times 100 \%$) (Appendix A). Each sample contributed more than 30 % of the total heat capacity and the calculated deviation from reproducibility was less than 0.5 % for most of the temperature range with a maximum of 3.5 % at $T < 25$ K. Larger samples maximized the sample contribution to the total heat capacity with thermal relaxation due to sample size minimally affecting the 24.26 mg sample at 300 K. Heat capacity measurements from 2 K to 300 K were featureless and showed no thermal anomalies over the measured temperature range.

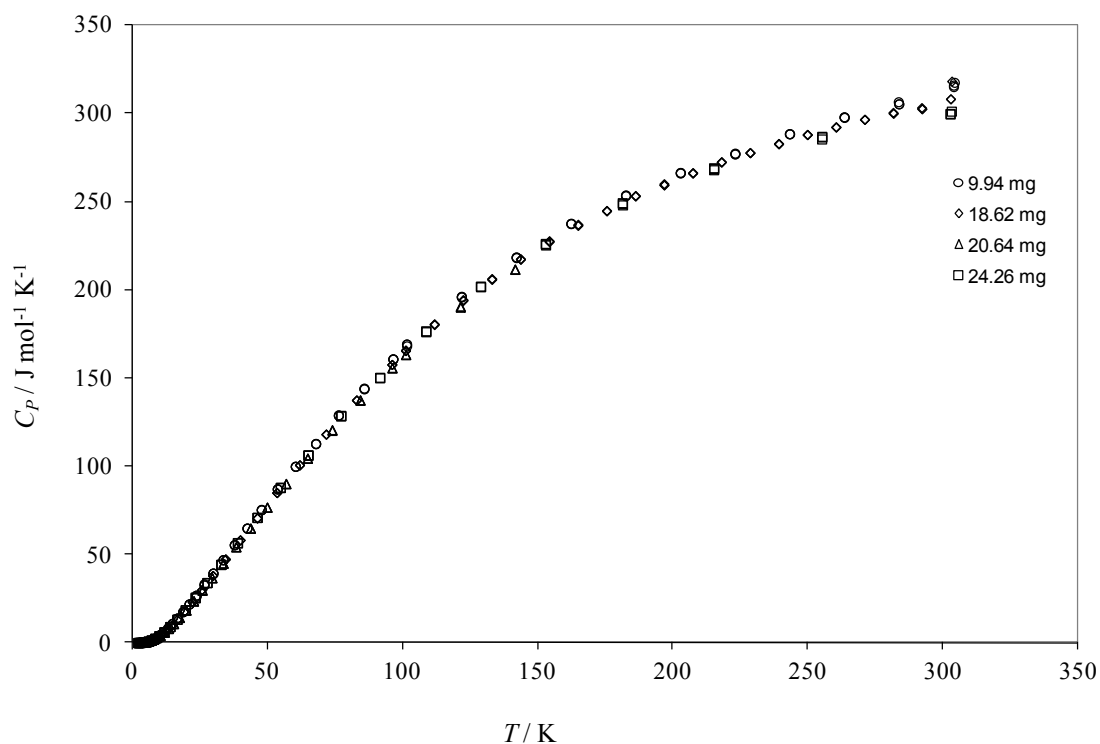


Figure 7.3: Experimental heat capacity data for $\text{In}_2\text{Mo}_3\text{O}_{12}$ for four samples (\circ , 9.94 mg; \diamond , 18.62 mg; \triangle , 20.64 mg; \square , 24.26 mg) showing no thermal anomalies from 2 K to 300 K.

7.4 CONCLUSIONS

The monoclinic, $P2_1/a$, and orthorhombic, $Pnca$, phases of $\text{In}_2\text{Mo}_3\text{O}_{12}$ were confirmed by XRPD at 298 K and 838 K, respectively. The enthalpy and entropy changes associated with the phase transition, $T_{\text{trs}} = 615$ K, are low, consistent with previously reported values.¹⁹³ Low-temperature heat capacity from 2 K to 300 K did not reveal any further thermal events in the examined temperature range.

8.1 MOTIVATIONS

As discussed previously, materials with near-zero thermal expansion would be able to withstand large thermal gradients and would be less subject to failure when exposed to temperature extremes due to their high thermal shock fracture resistance.^{18,20} Near-zero thermal expansion is especially important to reduce thermal stress, *i.e.* to increase thermal shock fracture resistance, because some NTE materials have been shown to have associated low thermal conductivity due to their short phonon mean free paths and the low-frequency vibrations associated with NTE.^{57,66}

As shown in Chapter 6, $\text{HfMgMo}_3\text{O}_{12}$ can be classified as a member of the $A_2M_3O_{12}$ family which crystallizes, at room temperature, in the orthorhombic $Pnma$ (62) space group.¹⁹⁹ Orthorhombic $\text{In}_2\text{Mo}_3\text{O}_{12}$ ($Pnca$) (Chapter 7) has an average intrinsic linear thermal expansion coefficient $\alpha_\ell = -1.85 \times 10^{-6} \text{ K}^{-1}$ (643 K to 1033 K),¹⁹⁶ while $\text{HfMgMo}_3\text{O}_{12}$ has a low positive average intrinsic coefficient of thermal expansion, $\alpha_\ell = 1.2 \times 10^{-6} \text{ K}^{-1}$ (293 K to 1013 K), and undergoes a phase transition to monoclinic $P2_1/a$ (14) at 175 K.^{199,323} $\text{In}_2\text{Mo}_3\text{O}_{12}$ is monoclinic ($P2_1/a$) at room temperature. Since $\text{HfMgMo}_3\text{O}_{12}$ and $\text{In}_2\text{Mo}_3\text{O}_{12}$ share the same monoclinic and similar orthorhombic space

^{‡‡} Information pertaining to the material, $\text{In}(\text{HfMg})_{0.5}\text{Mo}_3\text{O}_{12}$, has been adapted from: Miller, K. J.; Johnson, M. B.; Romao, C. P.; Bieringer, M.; Marinkovic, B. A.; Prisco, L.; White, M. A. White *J. Am. Ceram. Soc.* In Press. K. J. Miller's contribution to the work in this manuscript included: synthesis, sample characterization, variable temperature XRPD and dilatometry measurements, and the initial refinement of the XRPD patterns. Contributions also included drafting and writing most of the first draft of the manuscript and subsequent editing.

groups, and the *A* ions have similar crystal ionic radii (85 pm for Hf⁴⁺, 86 pm for Mg²⁺, and 94 pm for In³⁺),³²² solid solutions are possible.

Two solid solutions of In₂Mo₃O₁₂ and HfMgMo₃O₁₂ were prepared. Dilatometry and temperature variable X-ray powder diffraction (XRPD) were used to determine the bulk and intrinsic CTEs, respectively, and thermal analysis by DSC was used to probe the phase transitions between the monoclinic and orthorhombic structures. The 1:1 and 3:1 stoichiometric ratios of In₂Mo₃O₁₂ and HfMgMo₃O₁₂ were selected to form solid solutions of In(HfMg)_{0.5}Mo₃O₁₂ and In_{1.5}(HfMg)_{0.25}Mo₃O₁₂ as they are predicted by rule of mixtures to yield materials with intrinsic coefficients of thermal expansion close to zero. While the stoichiometric ratio of 1:3 is predicted to have a low intrinsic coefficient of thermal expansion close to $0.5 \times 10^{-6} \text{ K}^{-1}$, bulk CTEs in thermomiotic materials tend to be more positive due to macroscopic effects.³²⁴ Therefore, In_{0.5}(HfMg)_{0.75}Mo₃O₁₂ would not be a likely candidate for a near-zero CTE material on the bulk level. The properties of the solid solutions are compared to the properties of the parent compounds in terms of the intrinsic CTE value (this chapter) and the presence of low-frequency phonon modes (Chapter 9).

8.2 METHODS

In(HfMg)_{0.5}Mo₃O₁₂ and In_{1.5}(HfMg)_{0.25}Mo₃O₁₂ were synthesized according to the method described in Section 2.1.2. The room temperature and variable temperature XRPD patterns were collected as described in Sections 3.6.1.3 and Section 3.6.1.1,

respectively, and analyzed, with assistance from Dr. Bojan Marinkovic (to confirm data interpretation) and Dr. Mario Bieringer (to select instrument settings and experimental parameters as well as to confirm and evaluate data interpretation for measurements conducted by the author at the University of Manitoba) according to methods described in Section 3.6.2.2. Dilatometry (as described in Section 3.5) was used to determine the bulk linear thermal expansion coefficient. SEM (as described in Section 3.1) was used to determine the grain size and structure and DSC (as described in Section 3.4) measurements, using steel DSC pans, were used to determine the temperatures, enthalpy, and entropy changes associated with the phase transitions.

8.3 RESULTS AND DISCUSSION

8.3.1 SAMPLE CHARACTERIZATION

Phase analysis of the XRPD patterns obtained at room temperature, illustrate the monophasic nature of the $\text{In}(\text{HfMg})_{0.5}\text{Mo}_3\text{O}_{12}$ ($\chi^2 = 1.2$) and $\text{In}_{1.5}(\text{HfMg})_{0.25}\text{Mo}_3\text{O}_{12}$ ($\chi^2 = 1.3$) powders, in the monoclinic space group $P2_1/a$ (14) (Figure 8.1 and Figure 8.2).

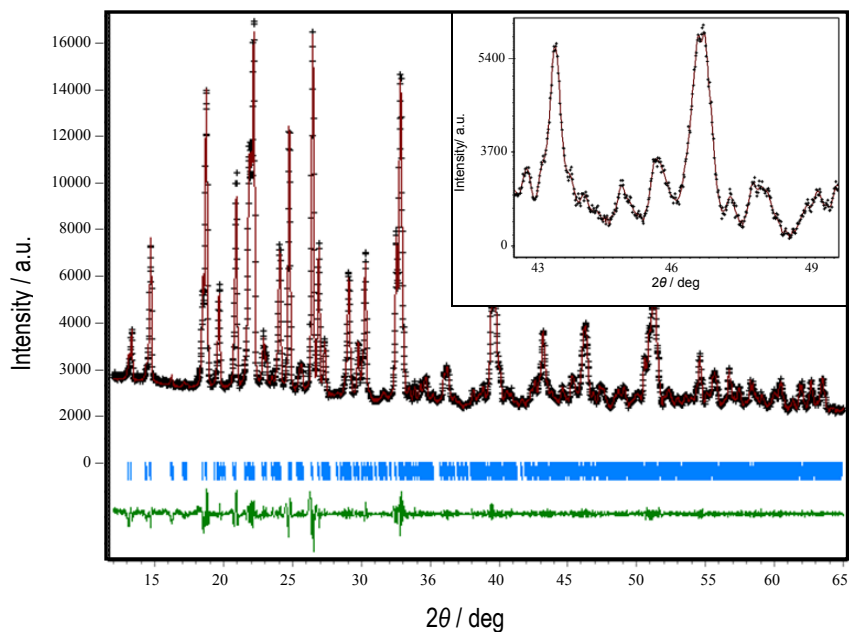


Figure 8.1: XRPD pattern of $\text{In}(\text{HfMg})_{0.5}\text{Mo}_3\text{O}_{12}$ at $T = 298$ K, illustrating an excellent Le Bail fit to the monoclinic $P2_1/a$ space group; the measured pattern is in blue, the fitted pattern is red, and the difference plot is grey. The inset shows the quality of fit at high angles.

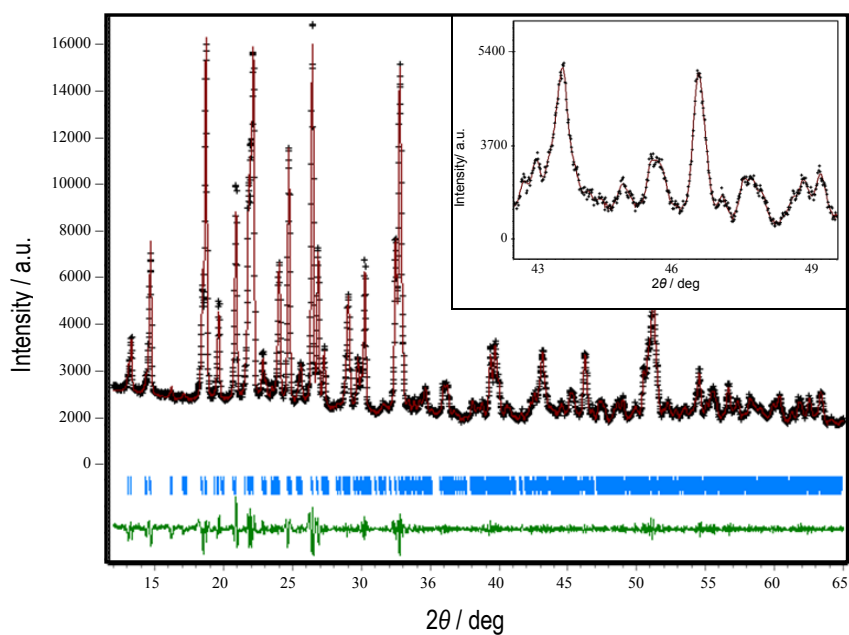


Figure 8.2: XRPD pattern of $\text{In}_{1.5}(\text{HfMg})_{0.25}\text{Mo}_3\text{O}_{12}$ at $T = 298$ K, illustrating an excellent Le Bail fit to the monoclinic $P2_1/a$ space group; the measured pattern is in blue, the fitted pattern is red, and the difference plot is grey. The inset shows the quality of fit at high angles.

Figure 8.3 shows SEM micrographs of $\text{In}(\text{HfMg})_{0.5}\text{Mo}_3\text{O}_{12}$ and $\text{In}_{1.5}(\text{HfMg})_{0.25}\text{Mo}_3\text{O}_{12}$. The particle morphology is consistent with previously examined materials and shows well-fused homogenous grains.³²³

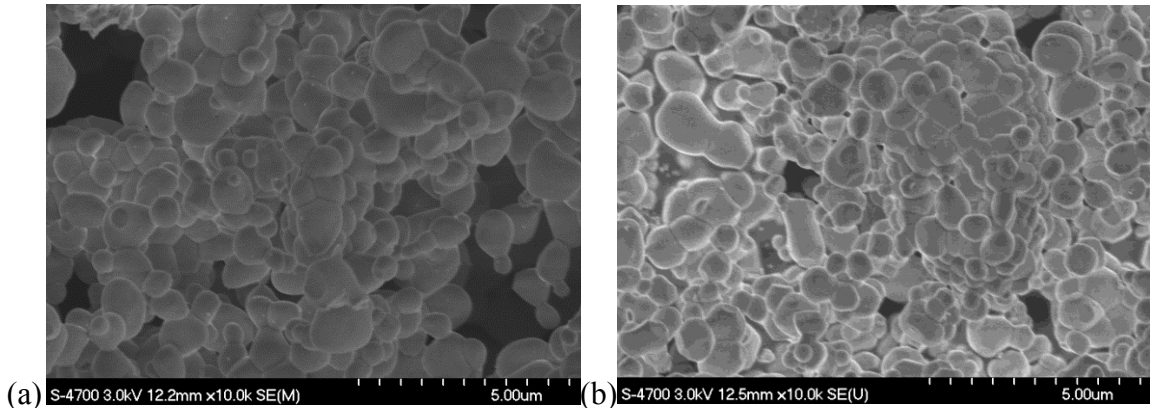


Figure 8.3: FE-SEM secondary electron images showing homogeneous particle morphology and excellent sintering between the grains of (a) $\text{In}(\text{HfMg})_{0.5}\text{Mo}_3\text{O}_{12}$ and (b) $\text{In}_{1.5}(\text{HfMg})_{0.25}\text{Mo}_3\text{O}_{12}$.

Due to the surface roughness of the samples, EDS analysis was only able to afford an approximate experimental composition of the samples (Table 8.1, Table 8.2 and Figure 8.4 (a) and (b)). The values reported are approximations only, but indicate the relative quantities of each element present in the samples.

Table 8.1: Approximate experimental composition of $\text{In}(\text{HfMg})_{0.5}\text{Mo}_3\text{O}_{12}$ as determined by qualitative EDS analysis. All results are given in atomic %.

Sample #	Magnesium	Molybdenum	Indium	Hafnium
1	2.2	21.6	6.4	3.6
2	2.2	13.0	3.6	2.5
3	2.1	14.5	4.0	2.7
4	2.2	14.2	4.3	2.6
5	2.6	18.2	5.2	3.5
Mean	2.3	16.3	4.7	3.0
Standard Deviation	0.2	3.6	1.1	0.5
Theoretical Values	2.9	17.6	5.8	2.9

Table 8.2: Approximate experimental composition of $\text{In}_{1.5}(\text{HfMg})_{0.25}\text{Mo}_3\text{O}_{12}$ as determined by qualitative EDS analysis. All results are given in atomic %.

Sample #	Magnesium	Molybdenum	Indium	Hafnium
1	1.1	12.4	4.9	1.2
2	1.2	9.1	2.6	1.2
3	1.0	13.8	5.6	1.2
4	1.1	14.2	6.0	1.2
5	1.0	14.7	5.5	1.5
Mean	1.1	13	4.9	1.3
Standard Deviation	0.1	2	1.4	0.2
Theoretical Values	1.5	17.6	8.8	1.5

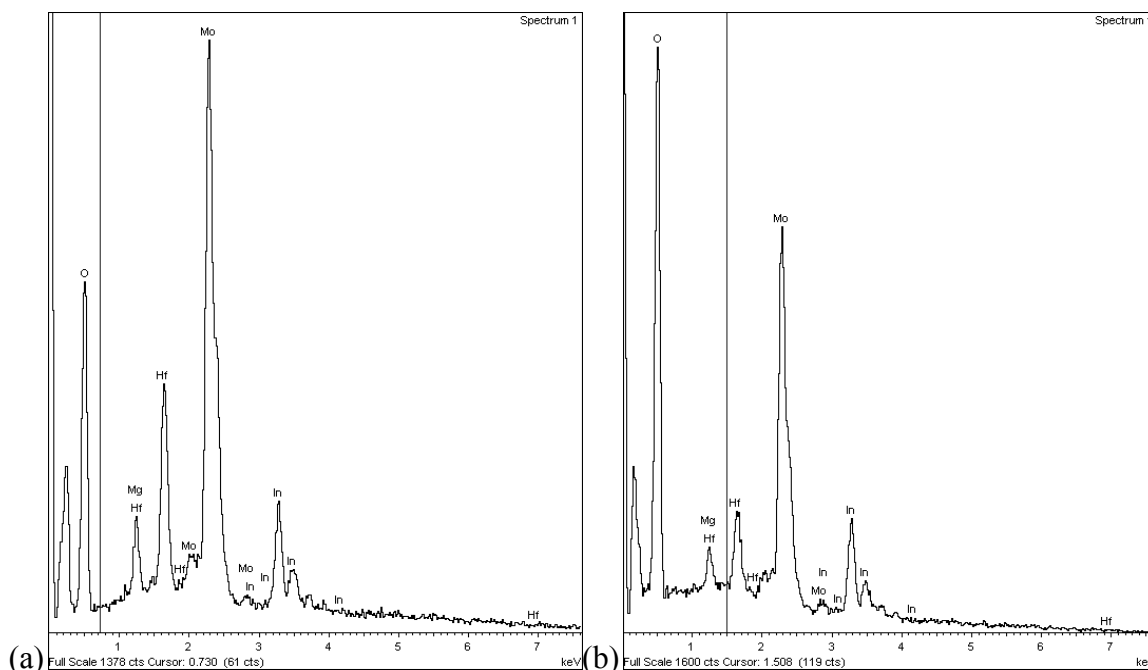


Figure 8.4: Qualitative EDS spectra of (a) $\text{In}(\text{HfMg})_{0.5}\text{Mo}_3\text{O}_{12}$ and (b) $\text{In}_{1.5}(\text{HfMg})_{0.25}\text{Mo}_3\text{O}_{12}$ identifying the elemental compositions of the samples.

8.3.2 PHASE TRANSITIONS

In the DSC experiment, a 53.53 mg powder sample of $\text{In}(\text{HfMg})_{0.5}\text{Mo}_3\text{O}_{12}$ and a 58.52 mg powder sample of $\text{In}_{1.5}(\text{HfMg})_{0.25}\text{Mo}_3\text{O}_{12}$ were analysed from 410 K to 500 K and 450 K to 600 K, respectively, with a heating rate of 10 K min^{-1} in helium flow. The DSC thermograms (Figure 8.5) show subtle endotherms on heating (monoclinic to orthorhombic phase transition; see below), with enthalpy changes ($\Delta_{\text{trs}}H$) of 0.89 kJ mol^{-1} at an onset temperature of 425 K for $\text{In}(\text{HfMg})_{0.5}\text{Mo}_3\text{O}_{12}$ and 1.31 kJ mol^{-1} at an onset temperature of 520 K for $\text{In}_{1.5}(\text{HfMg})_{0.25}\text{Mo}_3\text{O}_{12}$. These transition temperatures fall between the values for $\text{HfMgMo}_3\text{O}_{12}$ and $\text{In}_2\text{Mo}_3\text{O}_{12}$, 173 K and 615 K, respectively (Table 8.3), following a rule of mixtures (Figure 8.6).^{193,323} The corresponding transition entropy changes are the small for both materials, $\Delta_{\text{trs}}S = 2.0 \text{ J K}^{-1} \text{ mol}^{-1}$ for

$\text{In}(\text{HfMg})_{0.5}\text{Mo}_3\text{O}_{12}$ and $2.5 \text{ J K}^{-1} \text{ mol}^{-1}$ for $\text{In}_{1.5}(\text{HfMg})_{0.25}\text{Mo}_3\text{O}_{12}$, in good agreement with the values reported for other members of the $A_2M_3O_{12}$ family.^{193,323} The small values have been attributed to the subtle, entropically favoured, change in structure when the polyhedra undergo a static rotation, and are similar to the values observed for the end members of the solid solutions, $\text{HfMgMo}_3\text{O}_{12}$ and $\text{In}_2\text{Mo}_3\text{O}_{12}$.^{193,323} No other features were seen in the DSC experiments in the examined temperature range. A typical baseline for DSC scans is also shown in Appendix D.

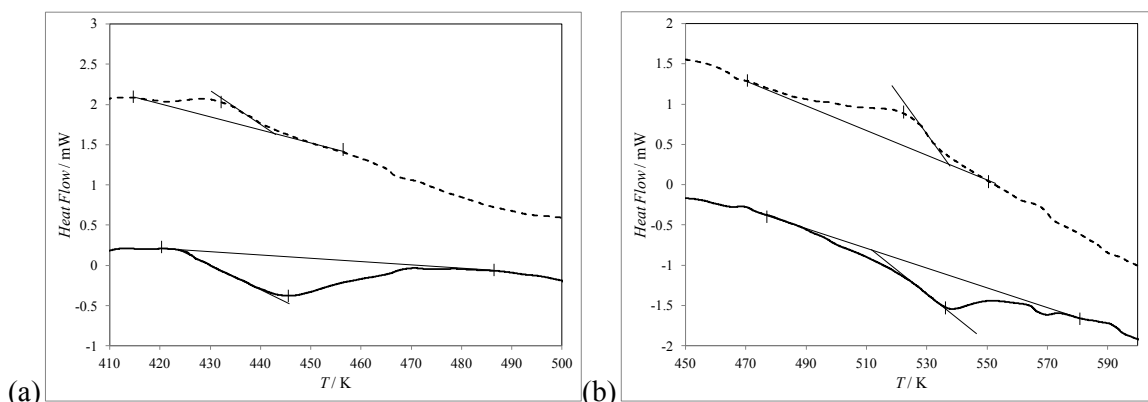


Figure 8.5: DSC thermograms for (a) $\text{In}(\text{HfMg})_{0.5}\text{Mo}_3\text{O}_{12}$ and (b) $\text{In}_{1.5}(\text{HfMg})_{0.25}\text{Mo}_3\text{O}_{12}$ during heating (—) and cooling (---), both at 10 K min^{-1} (exotherm up), showing phase transitions with enthalpy changes of 0.89 kJ mol^{-1} and 1.3 kJ mol^{-1} at onset temperatures of 425 K and 520 K respectively.

Table 8.3: Enthalpy and entropy changes for the monoclinic to orthorhombic phase transition with transition onset temperatures on heating, in helium atmosphere, at a heating rate of 10 K min⁻¹ in aluminum pans for HfMgMo₃O₁₂ and In₂Mo₃O₁₂ and in stainless steel pans for In(HfMg)_{0.5}Mo₃O₁₂ and In_{1.5}(HfMg)_{0.25}Mo₃O₁₂.

Material	Monoclinic	Orthorhombic	T_{trs}	$\Delta_{\text{trs}}H$	$\Delta_{\text{trs}}S$
	Phase	Phase	/ K	/ kJ mol ⁻¹	/ J mol ⁻¹ K ⁻¹
HfMgMo ₃ O ₁₂ ³²³	<i>P2₁/a</i>	<i>Pnma</i>	173 (± 1)	0.27 (± 0.03)	1.6 (± 0.2)
In(HfMg) _{0.5} Mo ₃ O ₁₂	<i>P2₁/a</i>	<i>Pnca</i>	425 (± 2)	0.89 (± 0.04)	2.0 (± 0.1)
In _{1.5} (HfMg) _{0.25} Mo ₃ O ₁₂	<i>P2₁/a</i>	<i>Pnca</i>	520 (± 2)	1.31 (± 0.04)	2.5 (± 0.1)
In ₂ Mo ₃ O ₁₂ ^{§§}	<i>P2₁/a</i>	<i>Pnca</i>	615 (± 1)	3.24 (± 0.3)	5.3 (± 0.5)

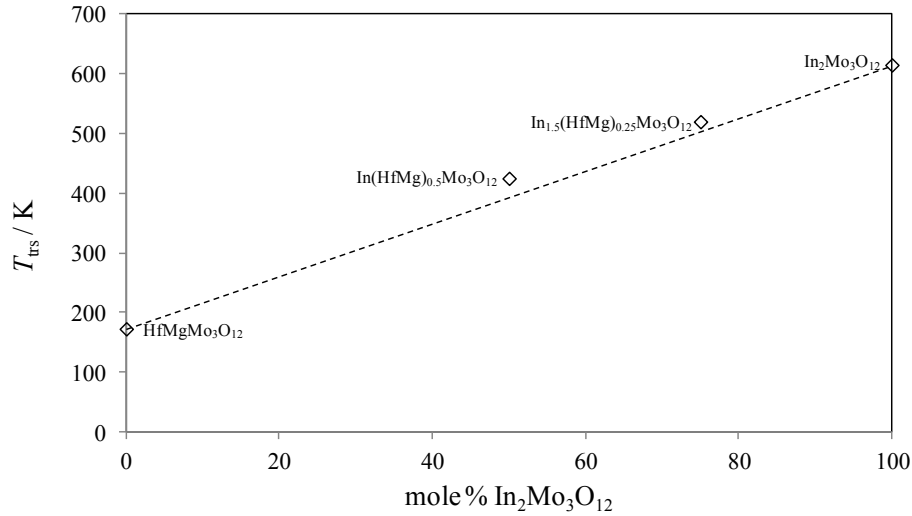


Figure 8.6: The T_{trs} for In₂Mo₃O₁₂, In_{1.5}(HfMg)_{0.25}Mo₃O₁₂, In(HfMg)_{0.5}Mo₃O₁₂, and HfMgMo₃O₁₂ in relation to the percentage of In₂Mo₃O₁₂ in the solid solutions.

^{§§} As presented in Chapter 7.

8.3.3 THERMAL EXPANSION COEFFICIENTS

8.3.3.1 Dilatometry

Dilatometric measurements were carried out on sintered samples of $\text{In}(\text{HfMg})_{0.5}\text{Mo}_3\text{O}_{12}$ and $\text{In}_{1.5}(\text{HfMg})_{0.25}\text{Mo}_3\text{O}_{12}$ from 300 K to 970 K in two heating and cooling cycles for $\text{In}(\text{HfMg})_{0.5}\text{Mo}_3\text{O}_{12}$ and one cycle for $\text{In}_{1.5}(\text{HfMg})_{0.25}\text{Mo}_3\text{O}_{12}$ (sample details listed in Table 8.4). Determination of the bulk α_ℓ was performed on the cooling measurements in order to minimize the possible contributions of crack healing, creep, and sintering effects during the measurements. The dilatometric curves acquired during the heating of $\text{In}_{1.5}(\text{HfMg})_{0.25}\text{Mo}_3\text{O}_{12}$ and the first heating of $\text{In}(\text{HfMg})_{0.5}\text{Mo}_3\text{O}_{12}$ both show a subtle change in slope at temperatures higher than 800 K, a feature which can be attributed to microcrack healing.²⁹⁸

Table 8.4: Size and density of the 5 mm diameter pellets used for dilatometry measurements.

Sample	Thickness / mm	Density / g cm ⁻³	% Theoretical Density
$\text{In}(\text{HfMg})_{0.5}\text{Mo}_3\text{O}_{12}$	3.10	2.65	68
$\text{In}_{1.5}(\text{HfMg})_{0.25}\text{Mo}_3\text{O}_{12}$	2.82	2.79	71

8.3.3.1.1 Dilatometry of $\text{In}(\text{HfMg})_{0.5}\text{Mo}_3\text{O}_{12}$

The monoclinic $P2_1/a$ phase was found to have a bulk $\alpha_\ell = 16.2 \times 10^{-6} \text{ K}^{-1}$ (303 K to 413 K) on the first cooling cycle, and a bulk $\alpha_\ell = 16.3 \times 10^{-6} \text{ K}^{-1}$ (303 K to 413 K) on the second cooling (Figure 8.7). The orthorhombic $Pnca$ phase had a near-zero bulk

linear CTE of $\alpha_\ell = 0.30 \times 10^{-6} \text{ K}^{-1}$ (554 K to 923 K) and $\alpha_\ell = 0.41 \times 10^{-6} \text{ K}^{-1}$ (557 K to 923 K) on cooling during the first and second cycles, respectively. The measurements were remarkably reproducible. Based on 1% accuracy in $\Delta L/L_0$ for the dilatometer,²⁹⁷ the upper and lower bounds of the bulk thermal expansion in the orthorhombic phase are $0.13 \times 10^{-6} \text{ K}^{-1}$ and $0.53 \times 10^{-6} \text{ K}^{-1}$, and $0.29 \times 10^{-6} \text{ K}^{-1}$ and $0.64 \times 10^{-6} \text{ K}^{-1}$, for first and second cooling, respectively, giving an overall bulk thermal expansion on cooling of the orthorhombic phase of $(0.36 \pm 0.18) \times 10^{-6} \text{ K}^{-1}$. The phase transition is visible in the dilatometric measurements at 430 K, corroborating the DSC findings (Figure 8.5 (a)), as the material expands during the monoclinic to orthorhombic phase transition. The change in volume between the heating and cooling cycles is likely due to sintering, as discussed in Section 1.5.3.2.

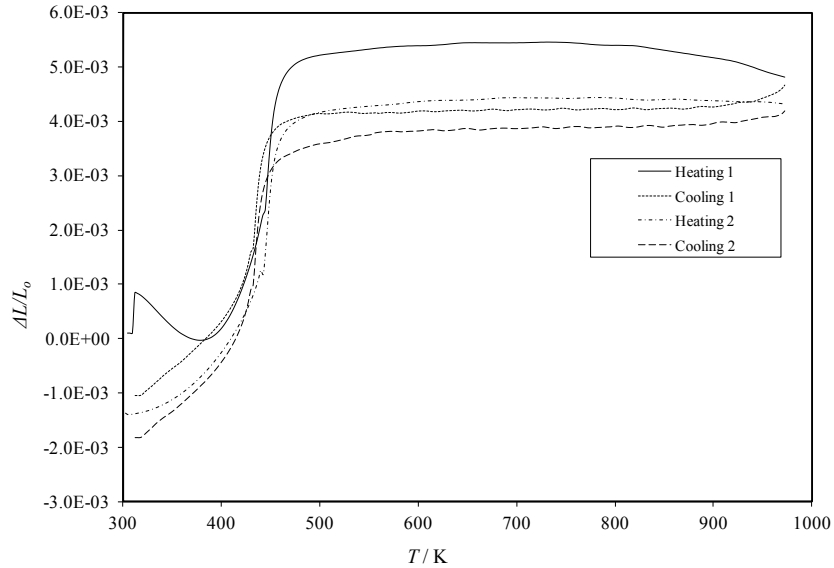


Figure 8.7: Dilatometry results for $\text{In}(\text{HfMg})_{0.5}\text{Mo}_3\text{O}_{12}$ over two heating and cooling cycles showing the change in length with respect to the original length as a function of temperature for: —, the first heating cycle; ---, first cooling cycle; - • -, the second heating cycle; and - - -, the second cooling cycle.

8.3.3.1.2 Dilatometry of $\text{In}_{1.5}(\text{HfMg})_{0.25}\text{Mo}_3\text{O}_{12}$

As seen with $\text{In}(\text{HfMg})_{0.5}\text{Mo}_3\text{O}_{12}$, the monoclinic $P2_1/a$ phase was found to have a large bulk $\alpha_\ell = 13.8 \times 10^{-6} \text{ K}^{-1}$ (314 K to 513 K) while the orthorhombic $Pnca$ phase had a near-zero bulk linear CTE of $\alpha_\ell = 0.10 \times 10^{-6} \text{ K}^{-1}$ (573 K to 927 K) (Figure 8.8). Based on 1% accuracy in $\Delta L/L_0$ for the dilatometer,²⁹⁷ the upper and lower bounds of the bulk thermal expansion in the orthorhombic phase are $0.43 \times 10^{-6} \text{ K}^{-1}$ and $-0.19 \times 10^{-6} \text{ K}^{-1}$, giving an overall bulk thermal expansion on cooling of the orthorhombic phase of $(0.10 \pm 0.3) \times 10^{-6} \text{ K}^{-1}$. The phase transition is visible in the dilatometric measurements at 526 K, corroborating the DSC findings (Figure 8.5 (b)), as the material expands during the monoclinic to orthorhombic phase transition. The change in volume between the heating and cooling cycles is likely due to sintering, as discussed in Section 1.5.3.2.

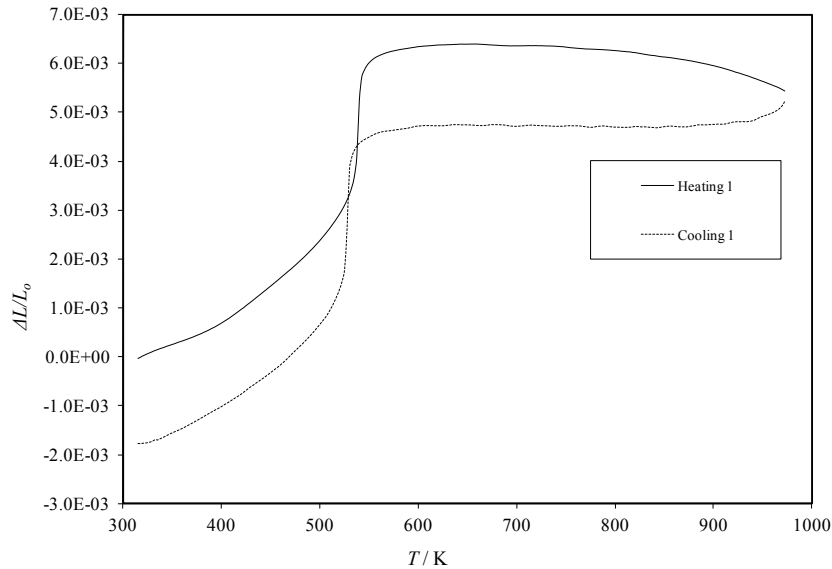


Figure 8.8: Dilatometry results for $\text{In}_{1.5}(\text{HfMg})_{0.25}\text{Mo}_3\text{O}_{12}$ over a heating and cooling cycles showing the change in length with respect to the original length as a function of temperature for: —, heating cycle; - - -, cooling cycle.

8.3.3.2 Temperature-Dependent XRPD^{***}

Temperature-dependent powder X-ray diffraction provides insight concerning the intrinsic thermal expansion of a material arising from the lattice dynamics, in contrast with dilatometry which determines the bulk thermal expansion, including both intrinsic and extrinsic effects. The extrinsic effects have to be considered for eventual applications of a material, and they include microstructural effects such as grain sizes, boundaries and microcrack formation. Combining both X-ray diffraction and dilatometry allows for a direct comparison of the microstructural and intrinsic thermal expansion effects. Lattice constants and the goodness of fit for each refinement are listed in Appendix E.

8.3.3.2.1 Determination of Room-Temperature Parameters

To minimize systematic errors due to parameter correlation for the high-temperature powder X-ray diffraction data analysis, a room-temperature XRD pattern was collected, under the supervision of Dr. Mario Bieringer (selecting instrument settings and experimental parameters as well as confirming and evaluating data interpretation for measurements conducted by the author at the University of Manitoba), on a well-centered spinner stage and the data were analyzed for different angular ranges. Based on this analysis, data for $2\theta < 21.4^\circ$ were excluded due to excessive peak asymmetry. The peak shape, asymmetry parameters and the diffractometer zero point were determined from the

^{***} High-temperature XRPD data were initially fit to the orthorhombic *Pnma* space group; however, taking into account systematic absences, the data were later found to fit the higher symmetry *Pnca* space group better. While the temperature-dependent patterns were refined as *Pnma* for the solid solutions, the lattice constants should be unaffected by this change in space group and subsequent discussions are carried out using the *Pnca* space group.

room-temperature diffractogram and were held constant for the high-temperature Le Bail fits. Figure 8.9 shows the Le Bail fit using the previously determined monoclinic $P2_1/a$ space group (Figure 8.1) for the room-temperature diffraction data of $\text{In}(\text{HfMg})_{0.5}\text{Mo}_3\text{O}_{12}$. Table 8.5 gives the lattice parameters determined from the room-temperature Le Bail fits for both $\text{In}(\text{HfMg})_{0.5}\text{Mo}_3\text{O}_{12}$ and $\text{In}_{1.5}(\text{HfMg})_{0.25}\text{Mo}_3\text{O}_{12}$.

Table 8.5: Lattice parameters for the room-temperature Le Bail fit, with the $P2_1/a$ space group, of $\text{In}(\text{HfMg})_{0.5}\text{Mo}_3\text{O}_{12}$ and $\text{In}_{1.5}(\text{HfMg})_{0.25}\text{Mo}_3\text{O}_{12}$.

Material	$a / \text{\AA}$	$b / \text{\AA}$	$c / \text{\AA}$	$\beta / ^\circ$	$V / \text{\AA}^3$
$\text{In}(\text{HfMg})_{0.5}\text{Mo}_3\text{O}_{12}$	16.214(7)	9.5582(4)	18.879(7)	125.39(6)	2385.2(2)
$\text{In}_{1.5}(\text{HfMg})_{0.25}\text{Mo}_3\text{O}_{12}$	16.223(6)	9.5614(5)	18.879(7)	125.35(7)	2388.4(6)

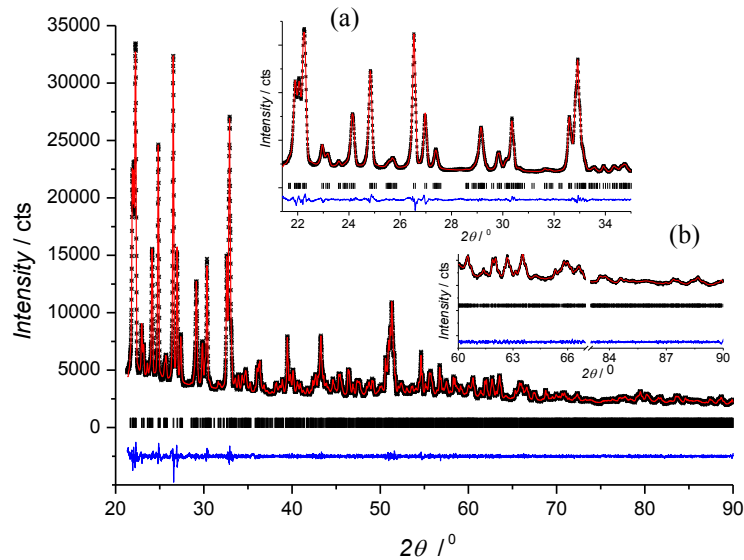


Figure 8.9: Le Bail fit for the room-temperature powder X-ray diffractogram of $\text{In}(\text{HfMg})_{0.5}\text{Mo}_3\text{O}_{12}$. Inset (a) emphasizes the low-angle region and inset (b) illustrates the fit quality for the high-angle regions. Black crosses = experimental data, red line = fit, blue line = difference, black markers = Bragg positions. $\chi^2 = 2.27$.

8.3.3.2.2 Determination of the CTEs by XRPD

The contour plot of $\text{In}(\text{HfMg})_{0.5}\text{Mo}_3\text{O}_{12}$ in Figure 8.10 clearly shows the large temperature dependence of the monoclinic diffraction peak positions and the nearly negligible temperature dependence in the orthorhombic phase, and Figure 8.11 illustrates the fitting quality of the powder X-ray data collected at 973 K.

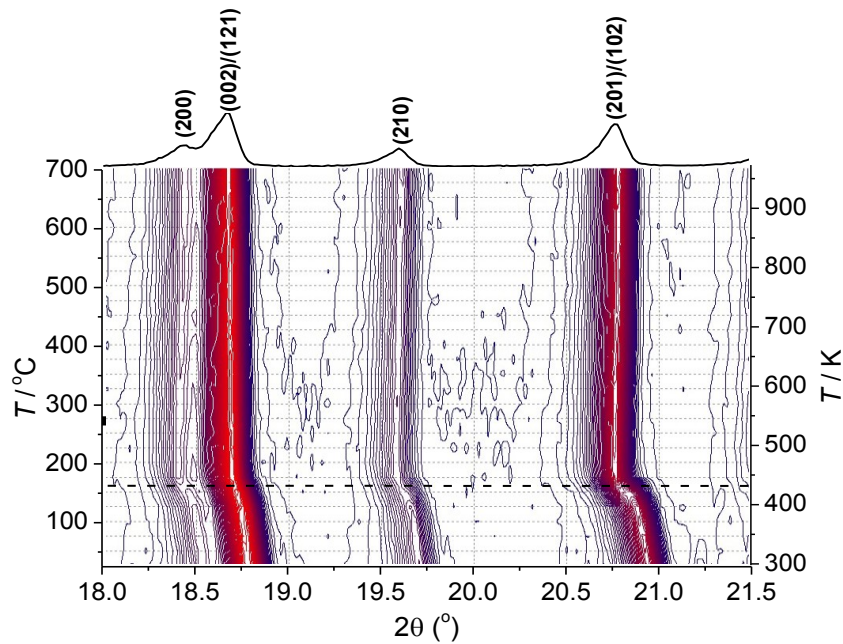


Figure 8.10: Powder X-ray diffraction contour plot covering $18^\circ \leq 2\theta \leq 21.5^\circ$ for $\text{In}(\text{HfMg})_{0.5}\text{Mo}_3\text{O}_{12}$. The dashed line indicates the monoclinic ($P2_1/a$) to orthorhombic ($Pnca$) phase transition temperature at 436 K. The Miller indices at the top of the figure refer to the orthorhombic phase (space group: $Pnca$). Intensities are indicated as contours in constant increments from blue (lowest intensity) to red (highest intensity).

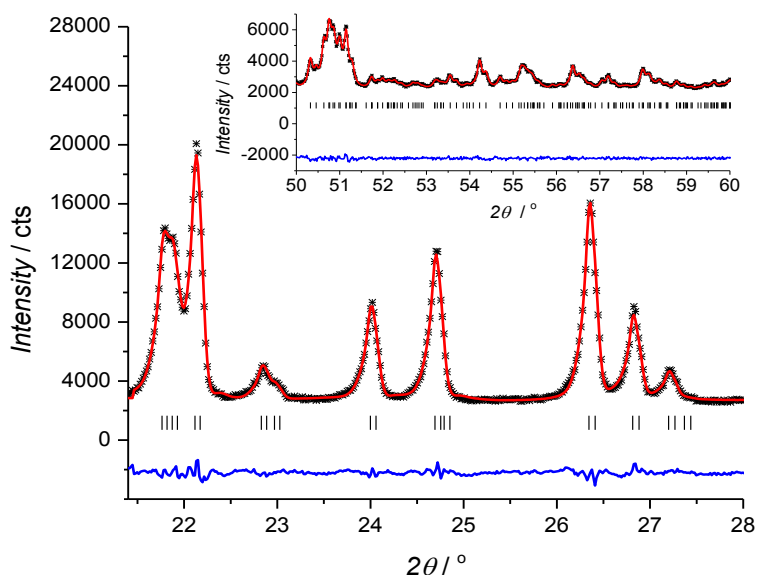
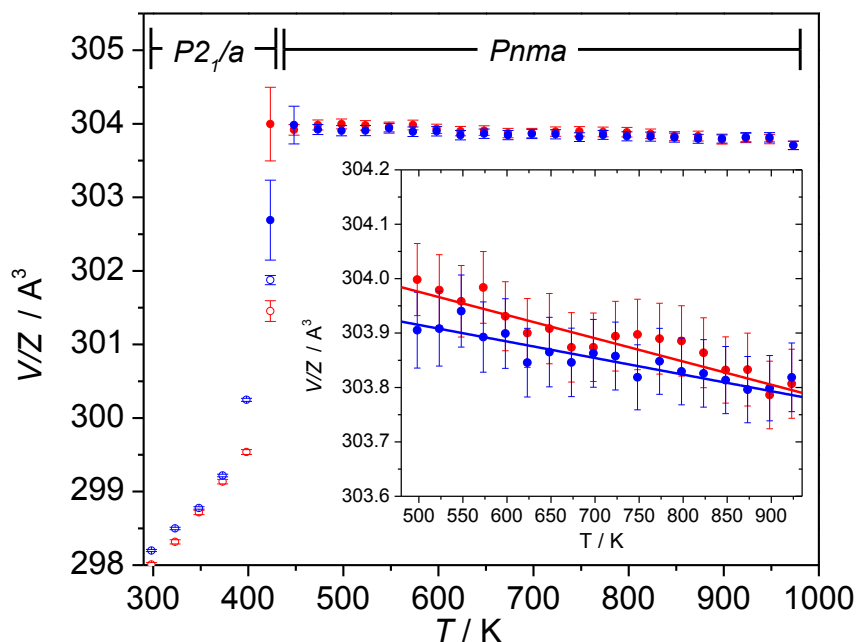


Figure 8.11: Le Bail fit for $\text{In}(\text{HfMg})_{0.5}\text{Mo}_3\text{O}_{12}$ for 973 K powder X-ray diffractogram during heating. Black crosses = experimental data, red line = fit, blue line = difference, black markers = Bragg positions. $\chi^2 = 2.48$.

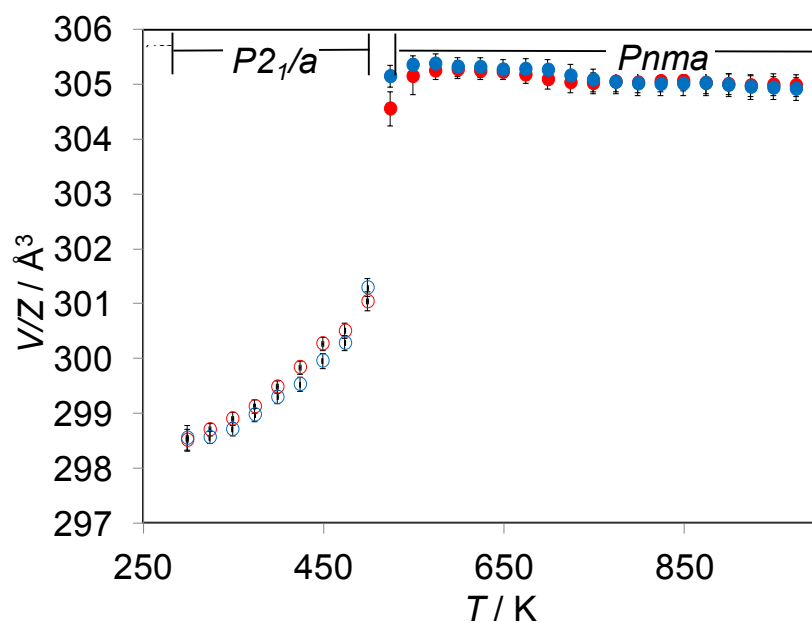
For the monoclinic phases of both materials, the intrinsic thermal expansion is positive along all three cell axes (Table 8.6) with an average intrinsic linear expansion coefficient of $\alpha_l = 20 \times 10^{-6} \text{ K}^{-1}$ (298 K to 398 K) and $\alpha_l = 14 \times 10^{-6} \text{ K}^{-1}$ (298 K to 520 K) for $\text{In}(\text{HfMg})_{0.5}\text{Mo}_3\text{O}_{12}$ and $\text{In}_{1.5}(\text{HfMg})_{0.25}\text{Mo}_3\text{O}_{12}$, respectively. The CTE along the individual axes in $\text{In}_{1.5}(\text{HfMg})_{0.25}\text{Mo}_3\text{O}_{12}$ were similar to those reported for $\text{In}_2\text{Mo}_3\text{O}_{12}$,¹⁹⁶ however, α_b for $\text{In}(\text{HfMg})_{0.5}\text{Mo}_3\text{O}_{12}$ was nearly twice the value observed for $\text{In}_2\text{Mo}_3\text{O}_{12}$ and $\text{In}_{1.5}(\text{HfMg})_{0.25}\text{Mo}_3\text{O}_{12}$. The fitted formula unit volume evolutions as a function of temperature are illustrated for $\text{In}(\text{HfMg})_{0.5}\text{Mo}_3\text{O}_{12}$ and $\text{In}_{1.5}(\text{HfMg})_{0.25}\text{Mo}_3\text{O}_{12}$ in Figure 8.12.

Table 8.6: Intrinsic thermal expansion coefficients (α) for $\text{In}(\text{HfMg})_{0.5}\text{Mo}_3\text{O}_{12}$ and $\text{In}_{1.5}(\text{HfMg})_{0.25}\text{Mo}_3\text{O}_{12}$ as obtained from powder X-ray diffraction experiments and literature values for $\text{In}_2\text{Mo}_3\text{O}_{12}$ ¹⁹⁶ and $\text{HfMgMo}_3\text{O}_{12}$.¹⁹⁹ Here α_t represents the spatially averaged linear thermal expansion coefficient, and $\Delta\alpha_{max}$, the thermal expansion anisotropy, is the maximum difference in the axial thermal expansion coefficients.

Structure	Fit Range / K	α_a / 10^{-6} K^{-1}	α_b / 10^{-6} K^{-1}	α_c / 10^{-6} K^{-1}	α_t / 10^{-6} K^{-1}	$\Delta\alpha_{max}$ / 10^{-6} K^{-1}
$\text{In}(\text{HfMg})_{0.5}\text{Mo}_3\text{O}_{12}$						
Monoclinic ($P2_1/a$)	298 – 398	15	25	22	20	
Orthorhombic ($Pnca$)	498 – 923	-4.2(1)	5.0(1)	-2.0(1)	-0.4	9.2
$\text{In}_{1.5}(\text{HfMg})_{0.25}\text{Mo}_3\text{O}_{12}$						
Monoclinic ($P2_1/a$)	298 – 520	13	14	22	14	
Orthorhombic ($Pnca$)	573 – 973	-5.1(1)	4.6(7)	-2.7(5)	-1.0	9.7
$\text{In}_2\text{Mo}_3\text{O}_{12}$						
Monoclinic ($P2_1/a$) ¹⁹⁶	373 – 598	12	13	19	12	
Orthorhombic ($Pnca$) ¹⁹⁶	643 – 1033	-4.4	5.46	-6.41	-1.85	11.87
$\text{HfMgMo}_3\text{O}_{12}$						
Orthorhombic ($Pnma$) ¹⁹⁹	298 – 1013	-3.44	8.0	-1.49	1.02	11.44



(a)



(b)

Figure 8.12: Formula unit volume (V/Z) evolution in (a) $\text{In}(\text{HfMg})_{0.5}\text{Mo}_3\text{O}_{12}$ and (b) $\text{In}_{1.5}(\text{HfMg})_{0.25}\text{Mo}_3\text{O}_{12}$. ●, ○ = heating, ●, ○ = cooling, ○, ○ = monoclinic phase ($P2_1/a$), ●, ● = orthorhombic ($Pnca$) phase. The data show the large positive unit cell expansion for the monoclinic phases and almost zero expansion for the orthorhombic phases, with the structural phase transition between 423 K and 448 K and 505 K and 525 K, respectively. The inset in (a) shows the linear fits to the heating (red) and cooling (blue) for the orthorhombic phase over the temperature range from 498 K to 923 K. Note that V/Z for heating and cooling are the same within the uncertainty.

Intrinsic thermal expansion coefficients were obtained by linear regression and the results are summarized in Table 8.6. The orthorhombic phase shows small intrinsic contractions along the *a*- and *c*-axes and a small expansion along the *b*-axis for both solid solutions. $\text{In}(\text{HfMg})_{0.5}\text{Mo}_3\text{O}_{12}$ and $\text{In}_{1.5}(\text{HfMg})_{0.25}\text{Mo}_3\text{O}_{12}$ have overall average linear expansion coefficients of $\alpha_\ell = -0.4 \times 10^{-6} \text{ K}^{-1}$, from $T = 498$ to 923 K , and $\alpha_\ell = -1.0 \times 10^{-6} \text{ K}^{-1}$, from $T = 573$ to 973 K .

In contrast, the bulk linear expansion coefficients derived from the dilatometric measurements are $\alpha_\ell = 0.36 \times 10^{-6} \text{ K}^{-1}$ for $\text{In}(\text{HfMg})_{0.5}\text{Mo}_3\text{O}_{12}$ and $\alpha_\ell = -0.10 \times 10^{-6} \text{ K}^{-1}$ for $\text{In}_{1.5}(\text{HfMg})_{0.25}\text{Mo}_3\text{O}_{12}$ over similar temperature ranges. The near zero values of α_ℓ determined for both materials place them in the category of a zero thermal expansion (ZTE) material.^{324,325} The more positive values for the bulk measurements, compared with the intrinsic thermal expansions, were likely indicative of microstructural effects which, on cooling, can add a small positive component to the intrinsic linear expansion coefficient.¹⁸³ Furthermore, the present results along with the previously reported intrinsic expansion coefficients for $\text{In}_2\text{Mo}_3\text{O}_{12}$ ¹⁹⁶ indicate that substitution of In atoms in $\text{In}_2\text{Mo}_3\text{O}_{12}$ with (Hf,Mg) only significantly changes α_c (from $-6.4 \times 10^{-6} \text{ K}^{-1}$ to $-2.0 \times 10^{-6} \text{ K}^{-1}$ and $-2.7 \times 10^{-6} \text{ K}^{-1}$), while α_a and α_b change by less than 10 %; the overall effect is that the average intrinsic α_ℓ changes from $-1.85 \times 10^{-6} \text{ K}^{-1}$ in $\text{In}_2\text{Mo}_3\text{O}_{12}$ ¹⁹⁶ to $-0.4 \times 10^{-6} \text{ K}^{-1}$ in $\text{In}(\text{HfMg})_{0.5}\text{Mo}_3\text{O}_{12}$ and $-1.0 \times 10^{-6} \text{ K}^{-1}$ in $\text{In}_{1.5}(\text{HfMg})_{0.25}\text{Mo}_3\text{O}_{12}$ (Figure 8.13). The average linear thermal expansion coefficient for the solid solutions of $\text{In}_2\text{Mo}_3\text{O}_{12}$ and $\text{HfMgMo}_3\text{O}_{12}$ adhere to the rule of mixtures in that the average CTE can be accurately predicted by the mole percent composition.

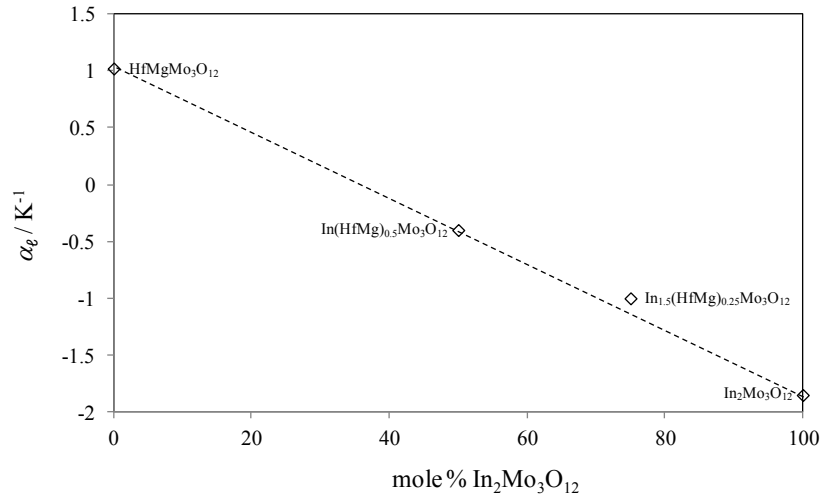


Figure 8.13: The average intrinsic linear thermal expansion coefficients of the orthorhombic phases of HfMgMo₃O₁₂,¹⁹⁹ In₂Mo₃O₁₂ (643 K to 1033 K),¹⁹⁶ In(HfMg)_{0.5}Mo₃O₁₂ (498 K to 923 K), and In(HfMg)_{0.5}Mo₃O₁₂ (573 K to 973 K) in relation to the composition of In₂Mo₃O₁₂, where the dashed line indicates the rule of mixtures prediction.

The thermal expansion anisotropies of the solid solutions were smaller than that of In₂Mo₃O₁₂ and HfMgMo₃O₁₂ (Table 8.6), further reducing the amount of thermal stress the material experiences. Thermal expansion anisotropy is quantitatively expressed for orthorhombic phases as $\Delta\alpha_{max}$, the maximum difference in the axial thermal expansion coefficients.

8.4 CONCLUSIONS

Both solid solutions, In(HfMg)_{0.5}Mo₃O₁₂ and In_{1.5}(HfMg)_{0.25}Mo₃O₁₂, adopt monoclinic (*P2₁/a*) structures at low temperature and undergo phase transitions, at 425 K for In(HfMg)_{0.5}Mo₃O₁₂ and 520 K for In_{1.5}(HfMg)_{0.25}Mo₃O₁₂, to an orthorhombic phase (*Pnca*). The enthalpy and entropy changes associated with the orthorhombic to

monoclinic structural transition are small and similar to values reported previously for similar structures, and demonstrate that only a small rearrangement is required for the structural phase transformation. Thermal expansion is positive in the low-temperature monoclinic phases. However, both solid solutions have near-zero thermal expansion coefficients in the high-temperature orthorhombic phases, with average linear intrinsic coefficients of thermal expansions of $\alpha_\ell = -0.4 \times 10^{-6} \text{ K}^{-1}$ ($\text{In}(\text{HfMg})_{0.5}\text{Mo}_3\text{O}_{12}$) and $-1.0 \times 10^{-6} \text{ K}^{-1}$ ($\text{In}_{1.5}(\text{HfMg})_{0.5}\text{Mo}_3\text{O}_{12}$), and average linear bulk coefficient of thermal expansions of $\alpha_\ell = 0.4 \times 10^{-6} \text{ K}^{-1}$ ($\text{In}(\text{HfMg})_{0.5}\text{Mo}_3\text{O}_{12}$) and $-0.2 \times 10^{-6} \text{ K}^{-1}$ ($\text{In}_{1.5}(\text{HfMg})_{0.5}\text{Mo}_3\text{O}_{12}$). Furthermore, the anisotropies of the thermal expansion coefficients (quantitatively defined as $\Delta\alpha_{max}$) were less than for the parent compounds, which is promising for reduced stress on large thermal excursions. The slight difference in the intrinsic and bulk results is attributable to microstructural effects.

CHAPTER 9 HEAT CAPACITY AND THERMAL CONDUCTIVITY OF THE $A_2\text{Mo}_3\text{O}_{12}$ FAMILY^{†††}

9.1 MOTIVATIONS

Analysis of the low-temperature heat capacity and thermal conductivity can reveal information concerning lattice dynamics, in particular regarding the low-frequency phonon modes responsible for negative thermal expansion which are easily excited at low temperatures.^{57,66,323} In this chapter the heat capacity and thermal conductivity of members of the $A_2\text{Mo}_3\text{O}_{12}$ family with a range of thermal expansion coefficients ranging from largely negative to low positive are examined to better understand the connection between low-frequency modes and the magnitude and sign of the CTE.

It should be noted that, of the compounds studied, each was found to undergo a solid-solid phase transition upon cooling with the exception of $\text{Y}_2\text{Mo}_3\text{O}_{12}$. Although $\text{In}_2\text{Mo}_3\text{O}_{12}$, $\text{HfMgMo}_3\text{O}_{12}$, and their solid solutions are monoclinic at low temperatures, the low-frequency phonon modes linked to thermomiotic behavior are still active and while the crystal structure of the monoclinic phase is not in itself thermomiotic, an understanding of the role of phonon modes can still be obtained as they relate to the orthorhombic phase. Throughout this chapter, comparisons of the low-frequency modes

^{†††} Portions of this chapter, pertaining to the heat capacity analysis of $\text{HfMgMo}_3\text{O}_{12}$, were adapted and used with permission from: Miller, K. J.; Johnson, M. B.; White, M. A.; Marinkovic, B. A. *Solid State Commun.* **2012**, *152*, 1748-1752. K.J. Miller's contribution to the work in this manuscript was: synthesis, determination of the low temperature heat capacity and thermal conductivity, obtaining DSC measurements, and the initial refinement of the XRPD patterns. Contributions also included writing most of the first draft of the manuscript and subsequent editing.

and their relationship to coefficient of thermal expansion in the orthorhombic phases will be made.

9.2 METHODS

Samples for heat capacity measurements were prepared according to Section 2.2.1 and Section 2.2.2 for air stable ($\text{HfMgMo}_3\text{O}_{12}$, $\text{In}_2\text{Mo}_3\text{O}_{12}$, $\text{In}(\text{HfMg})_{0.5}\text{Mo}_3\text{O}_{12}$, and $\text{In}_{1.5}(\text{HfMg})_{0.5}\text{Mo}_3\text{O}_{12}$) and hygroscopic samples ($\text{Y}_2\text{Mo}_3\text{O}_{12}$) respectively. Measurements were carried out according to methods and criteria described in Section 3.7. Samples for thermal conductivity measurements were prepared according to Section 2.2.1 and measurements were carried out according to the methods and criteria described in Section 3.8.

9.3 HEAT CAPACITY RESULTS

9.3.1 HEAT CAPACITY RESULTS FOR $\text{HfMgMo}_3\text{O}_{12}$, $\text{In}_2\text{Mo}_3\text{O}_{12}$, AND $\text{Y}_2\text{Mo}_3\text{O}_{12}$

The heat capacity results the two solid solution end members, $\text{HfMgMo}_3\text{O}_{12}$ (Figure 9.1; Chapter 6, Section 6.3.2) and $\text{In}_2\text{Mo}_3\text{O}_{12}$ (Figure 9.2; Chapter 7, Section 7.3.2) and for $\text{Y}_2\text{Mo}_3\text{O}_{12}$ (Figure 9.3; Chapter 5, Section 5.4.2) have been presented in previous chapters. Measurements of the respective compounds showed consistency in the measurements, comprising samples of varying masses, for each of the compounds.

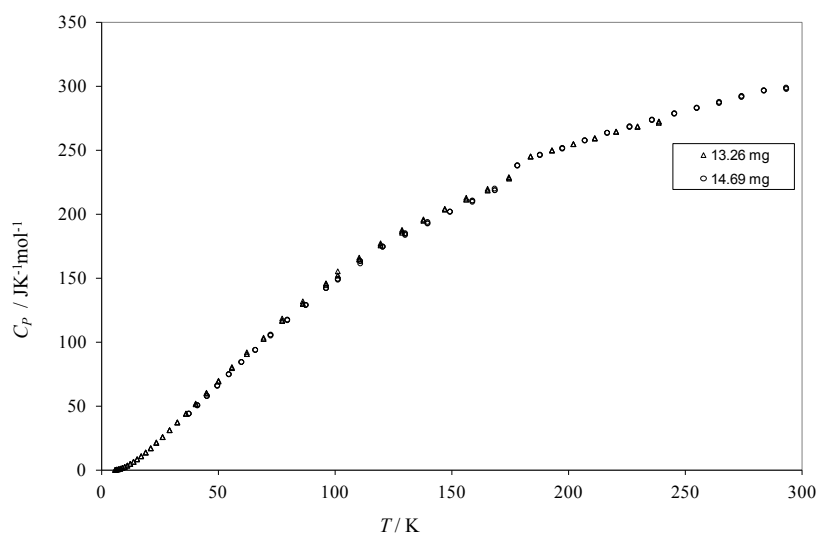


Figure 9.1: Experimental heat capacity data for $\text{HfMgMo}_3\text{O}_{12}$ for two samples (Δ , 13.26 mg; \circ , 14.69 mg) showing an anomaly at $T \sim 175$ K (from Chapter 6, Section 6.3.2). Reprinted with permission from Miller, K. J.; Johnson, M. B.; White, M. A.; Marinkovic, B. A. *Solid State Commun.* **2012**, *152*, 1748-1752. Copyright 2012 Elsevier.

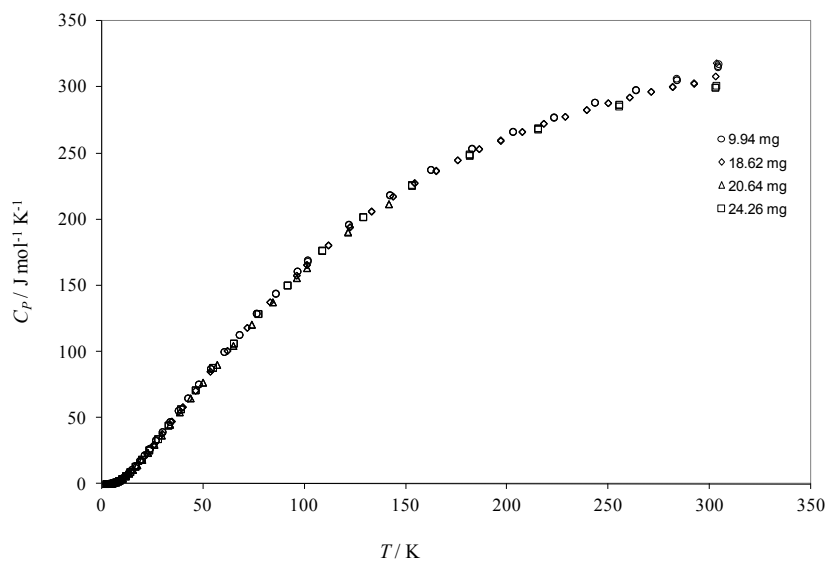


Figure 9.2: Experimental heat capacity data for $\text{In}_2\text{Mo}_3\text{O}_{12}$ for four samples (\circ , 9.94 mg; \diamond , 18.62 mg; Δ , 20.64 mg; \square , 24.26 mg) showing no thermal anomalies from 2 K to 300 K (from Chapter 7, Section 7.3.2).

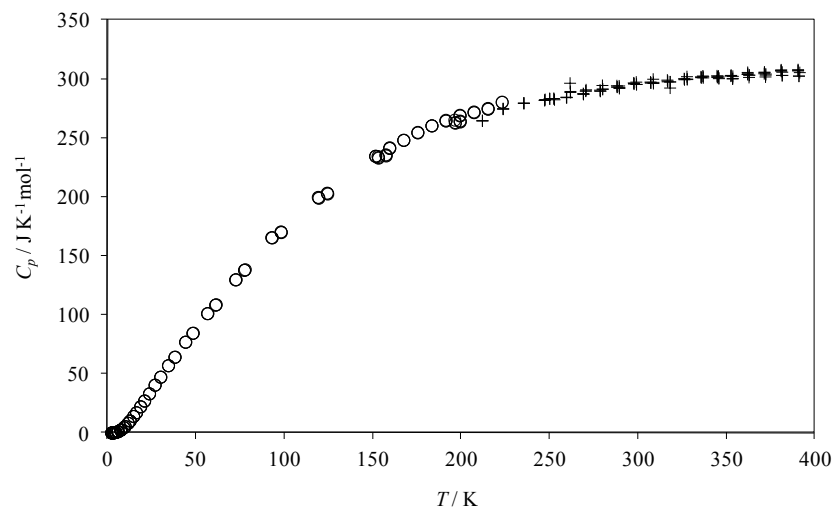


Figure 9.3: Heat capacity data for $\text{Y}_2\text{Mo}_3\text{O}_{12}$ samples ranging in size from 4.9491 mg to 13.9403 mg from 2 K to 390 K. Lower temperature samples were measured using Apiezon[®] T grease, ○, and higher temperature samples were measured using Apiezon[®] H grease, +. Samples required heating to 340 K prior to measurements to ensure sample dehydration, as explained in Section 5.4.2, therefore, the low-temperature Apiezon[®] N grease was unsuitable for measurements with this system (From Chapter 5, Section 5.4.2). Reprinted with permission from Marinkovic, B. A.; Ari, M.; de Avillez, R.; Rizzo F.; Ferreira, F.F.; Miller, K. J.; Johnson, M.B.; White M. A. *Chem. Mater.* **2009**, *21*, 2886-2894. Copyright 2009 American Chemical Society.

9.3.2 HEAT CAPACITY OF $\text{In}(\text{HfMg})_{0.5}\text{Mo}_3\text{O}_{12}$

Heat capacity results for separate measurements of three samples of $\text{In}(\text{HfMg})_{0.5}\text{Mo}_3\text{O}_{12}$ of masses 6.05 mg, 9.34 mg, and 16.10 mg (from 2 K to 300 K) are shown in Figure 9.4 (full data sets in Appendix B). The coupling constants for the 6.05 mg and 9.34 mg samples, using Apiezon[®] N grease to assure good thermal contact, were above 80 % for the entire temperature range. However, the coupling constant for the larger, 16.10 mg, sample dropped to less than 75 % above 117 K and was omitted from analysis above this temperature (Appendix A). All data were evaluated in terms of the sample contribution to the total heat capacity ($C_{\text{sample}} / C_{\text{total}} \times 100 \%$) and the calculated

reproducibility ($\delta C_{\text{sample}} / C_{\text{sample}} \times 100 \%$) (Appendix A). Each sample contributed more than 30 % of the total heat capacity over the entire temperature range with the exception of the 6.05 mg sample which fell below 30 % at ~ 170 K, but remained above 25 %. The calculated deviation from reproducibility was less than 0.5 % for most of the temperature range with a maximum of 2.5 % at $T < 25$ K. Heat capacity measurements from 2 K to 300 K were featureless and showed no thermal anomalies over the measured temperature range.

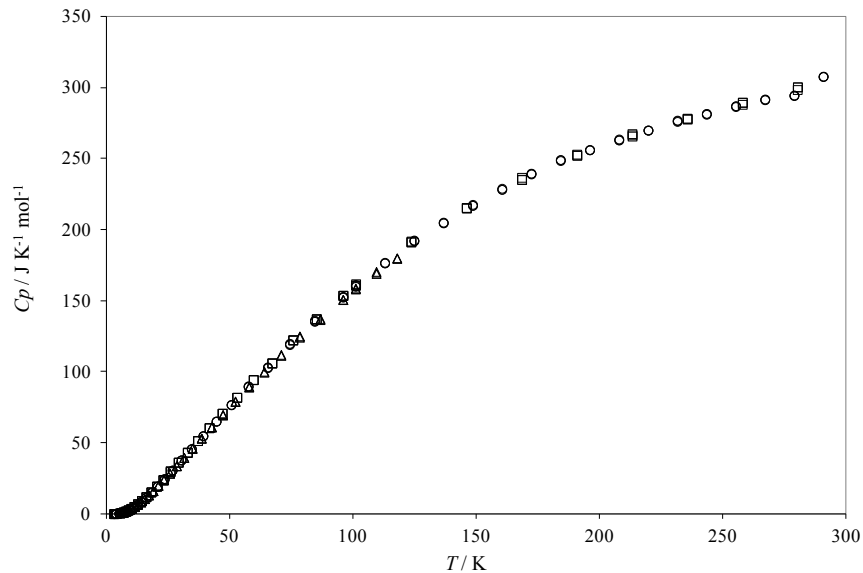


Figure 9.4: Experimental heat capacities for three samples of $\text{In}(\text{HfMg})_{0.5}\text{Mo}_3\text{O}_{12}$ (Δ , 16.10 mg; \circ , 9.34 mg; \square , 6.05 mg) showing no thermal anomalies from 2 K to 300 K.

9.3.3 HEAT CAPACITY OF $\text{In}_{1.5}(\text{HfMg})_{0.25}\text{Mo}_3\text{O}_{12}$

Heat capacity results for separate measurements of three samples of $\text{In}_2(\text{HfMg})_{0.25}\text{Mo}_3\text{O}_{12}$ of masses 7.33 mg, 15.01 mg, and 15.89 mg (from 2 K to 400 K)

are shown in Figure 9.5 (full data sets in Appendix B). The coupling constants for all the samples, using Apiezon[®] N grease for the 7.33 mg and 15.89 mg sample and Apiezon[®] H grease for the 15.01 mg sample, to assure good thermal contact, were above 80 % for the 15.01 mg and 15.89 mg samples for the entire temperature range while the 7.33 sample was better than 75 % below 250 K, but then degraded at higher temperatures (Appendix A). The data were evaluated in terms of the sample contribution to the total heat capacity ($C_{\text{sample}} / C_{\text{total}} \times 100 \%$) and the calculated reproducibility ($\delta C_{\text{sample}} / C_{\text{sample}} \times 100 \%$) (Appendix A). Each of the larger samples contributed more than 30 % of the total heat capacity over the entire temperature range. The smaller, 7.33 mg sample had a smaller contribution to the total heat capacity above 250 K ($> 20 \%$). The calculated deviation from reproducibility was less than 1 % for most of the temperature range with a maximum of 4.5 % at $T < 25$ K. Larger samples maximized the sample contribution to the total heat capacity with thermal relaxation due to sample size minimally affecting the 15.89 mg sample at 300 K. Heat capacity measurements from 2 K to 400 K were featureless and showed no thermal anomalies over the measured temperature range.

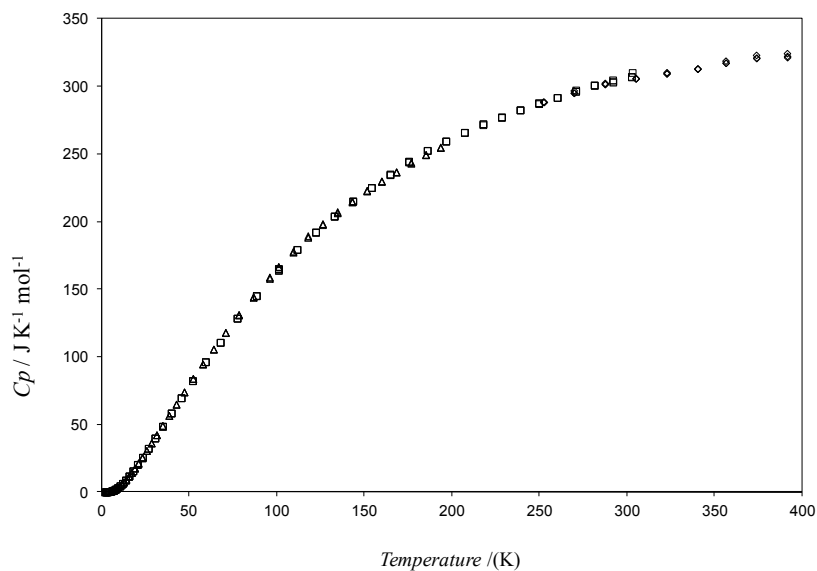


Figure 9.5: Experimental heat capacities for three samples of $\text{In}_{1.5}(\text{HfMg})_{0.25}\text{Mo}_3\text{O}_{12}$ (Δ , 7.33 mg; \diamond , 15.01 mg; \square , 15.89 mg) showing no thermal anomalies from 2 K to 400 K.

9.4 ESTIMATING THE HEAT CAPACITY OF $A_2\text{Mo}_3\text{O}_{12}$ MATERIALS

9.4.1 CONSTITUENT ADDITIVITY MODEL

The simplest model for estimating heat capacities is the Neumann-Kopp law, in which the heat capacity of a solid is well modeled over a wide temperature range by the appropriated weighted sum of the heat capacities of the solid elements from which it is composed.¹⁸ While the Neumann-Kopp law works well for simple solids and alloys it does not adequately model complex oxides, such as sodalite ($\text{Na}_8\text{Al}_6\text{Si}_6\text{O}_{24}\text{Cl}_2$).⁶⁴ However, a constituent additivity model, based on constituent compounds, can yield accurate heat capacities, to within a few percent, over a temperature range from a few kelvin to $T > 1000$ K.⁶⁴

Given the success of the constituent additivity model to approximate the heat capacity of complex oxides, such as sodalite, it is somewhat surprising that this model fails to accurately predict the heat capacity of open-framework oxides in families with thermomiotic properties.^{57,323} $\text{Y}_2\text{Mo}_3\text{O}_{12}$, which has a large negative coefficient of thermal expansion, $\alpha_\ell = -9.02 \times 10^{-6} \text{ K}^{-1}$ from 20 K to 450 K, illustrates that the appropriately weighted sum of the heat capacities of the component oxides, Y_2O_3 ³²⁶ and MoO_3 ,³²⁷ underestimates the experimental data at low temperature as it fails to account for large contribution of the low-frequency modes (Figure 9.6).

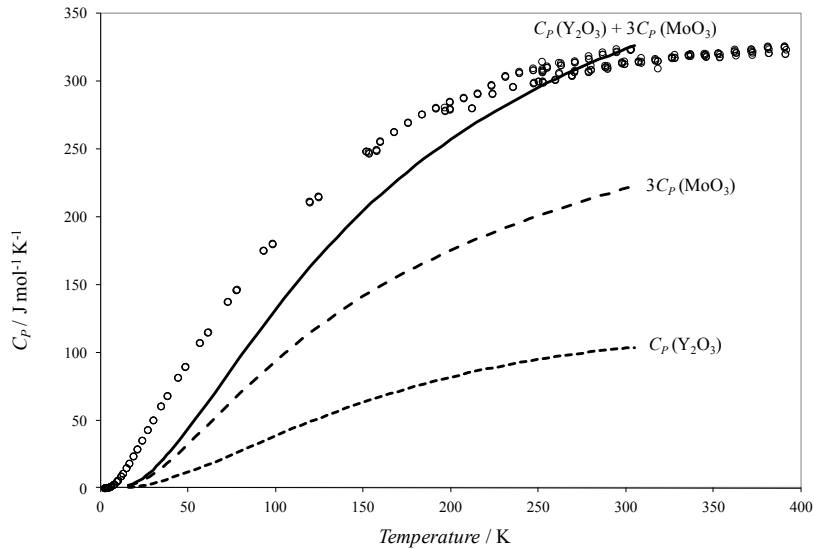


Figure 9.6: Experimental heat capacities for $\text{Y}_2\text{Mo}_3\text{O}_{12}$ (\circ) and —, the constituent additivity heat capacity of $\text{Y}_2\text{Mo}_3\text{O}_{12}$ calculated from the weighted sums of - - -, $C_p(\text{Y}_2\text{O}_3)$ ³²⁶ and — — $C_p(\text{MoO}_3)$.³²⁷

$\text{In}_2\text{Mo}_3\text{O}_{12}$ and $\text{HfMgMo}_3\text{O}_{12}$, while having orthorhombic open framework structures similar to $\text{Y}_2\text{Mo}_3\text{O}_{12}$ (see Chapter 6 and Chapter 7), have much smaller absolute values of thermal expansion coefficients. The low values of the CTE indicate the presence of low-frequency modes interfering with the more intuitive mechanisms of

positive thermal expansion, but not to the same extent as those present in $\text{Y}_2\text{Mo}_3\text{O}_{12}$. As seen in $\text{Y}_2\text{Mo}_3\text{O}_{12}$, the appropriately weighted heat capacities of In_2O_3 ,³²⁸ MoO_3 ,³²⁷ MgO ,³²⁹ and HfO_2 ³³⁰ fall below the measured heat capacities of $\text{In}_2\text{Mo}_3\text{O}_{12}$ and $\text{HfMgMo}_3\text{O}_{12}$ due to the absence of low-frequency modes in the component oxides (Figure 9.7 and Figure 9.8). Similarly the solid solutions, $\text{In}(\text{HfMg})_{0.5}\text{Mo}_3\text{O}_{12}$ and $\text{In}_{1.5}(\text{HfMg})_{0.25}\text{Mo}_3\text{O}_{12}$, are also poorly represented by the constituent additivity model (Figure 9.9 and Figure 9.10), especially at low temperatures where the low-frequency modes are most important.

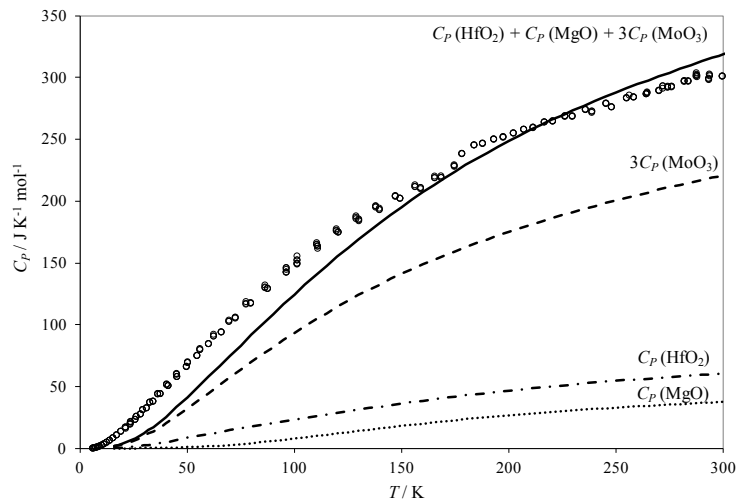


Figure 9.7: The constituent additivity heat capacities, —, calculated from the weighted heat capacities of; $-\bullet-\bullet-$, $C_p(\text{In}_2\text{O}_3)$,³²⁸ $-\cdot-\cdot-$, $C_p(\text{HfO}_2)$,³³⁰ $\bullet\bullet\bullet$, $C_p(\text{MgO})$ ³²⁹ and $- - -$, $C_p(\text{MoO}_3)$,³²⁷ compared to the experimental heat capacities for $\text{HfMgMo}_3\text{O}_{12}$ (\circ) (Chapter 6). Reprinted with permission from Miller, K. J.; Johnson, M. B.; White, M. A.; Marinkovic, B. A. *Solid State Commun.* **2012**, *152*, 1748-1752. Copyright 2012 Elsevier.

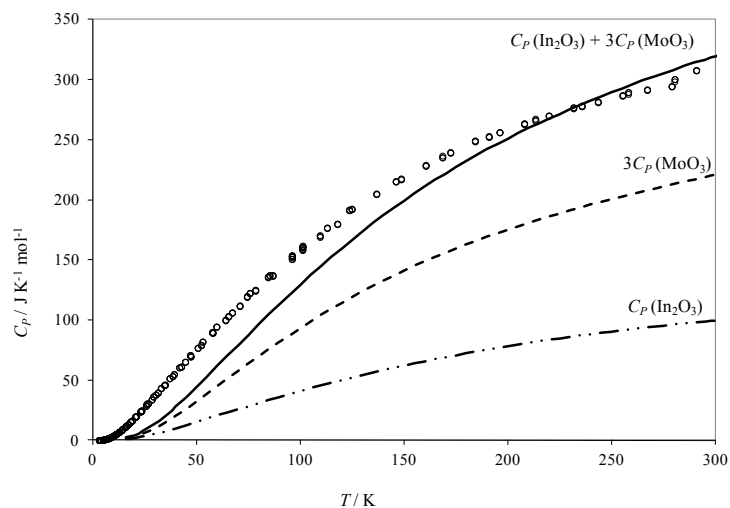


Figure 9.8: The constituent additivity heat capacities, —, calculated from the weighted heat capacities of; $-\bullet-\bullet-$, $C_p(\text{In}_2\text{O}_3)$,³²⁸ $-\bullet-$, $C_p(\text{HfO}_2)$,³³⁰ $\bullet\bullet\bullet$, $C_p(\text{MgO})$ ³²⁹ and $- -$, $C_p(\text{MoO}_3)$,³²⁷ compared to the experimental heat capacities for $\text{In}_2\text{Mo}_3\text{O}_{12}$ (\circ) (Chapter 7).

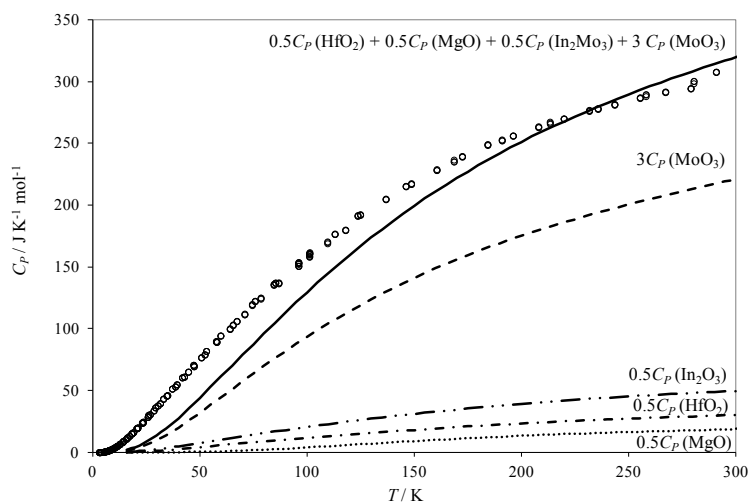


Figure 9.9: The constituent additivity heat capacities, —, calculated from the weighted heat capacities of; $-\bullet-\bullet-$, $C_p(\text{In}_2\text{O}_3)$,³²⁸ $-\bullet-$, $C_p(\text{HfO}_2)$,³³⁰ $\bullet\bullet\bullet$, $C_p(\text{MgO})$ ³²⁹ and $- -$, $C_p(\text{MoO}_3)$,³²⁷ compared to the experimental heat capacities for $\text{In}(\text{HfMg})_{0.5}\text{Mo}_3\text{O}_{12}$.

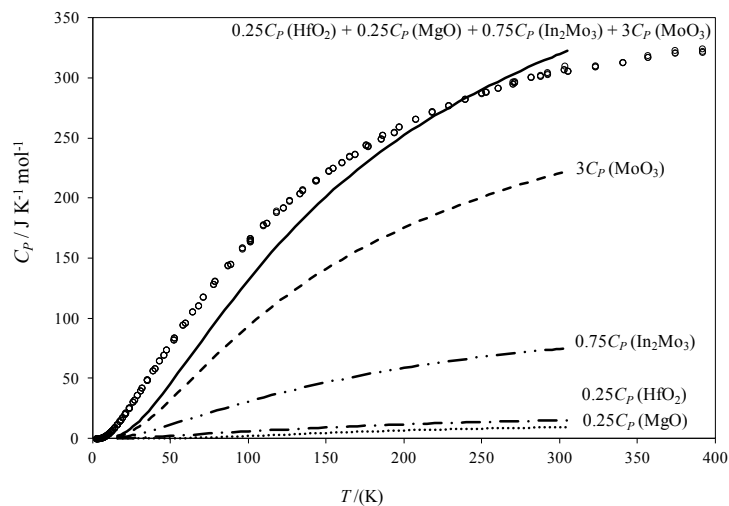


Figure 9.10: The constituent additivity heat capacities, —, calculated from the weighted heat capacities of; $-\bullet-\bullet-$, $C_p(\text{In}_2\text{O}_3)$,³²⁸ $-\cdot-\cdot-$, $C_p(\text{HfO}_2)$,³³⁰ $\bullet\bullet\bullet$, $C_p(\text{MgO})$ ³²⁹ and $-\cdot-$, $C_p(\text{MoO}_3)$,³²⁷ compared to the experimental heat capacities for $\text{In}_{1.5}(\text{HfMg})_{0.25}\text{Mo}_3\text{O}_{12}$ (\circ).

9.4.2 HEAT CAPACITY BY THE RULE OF MIXTURES

While it has been shown that predicting the heat capacity of thermomiotic oxides using constituent additivity is not an accurate model, it should be possible to obtain a reasonable approximation of the heat capacities of solid solutions of materials by weighing the heat capacities of the solid solution end members appropriately, *i.e.* rule of mixtures. The heat capacity of $\text{In}(\text{HfMg})_{0.5}\text{Mo}_3\text{O}_{12}$, the 1:1 ratio solid solution of $\text{HfMgMo}_3\text{O}_{12}$ and $\text{In}_2\text{Mo}_3\text{O}_{12}$, can be accurately predicted using this rule of mixtures approach over a wide temperature range (5 K to 300 K) (Figure 9.11).

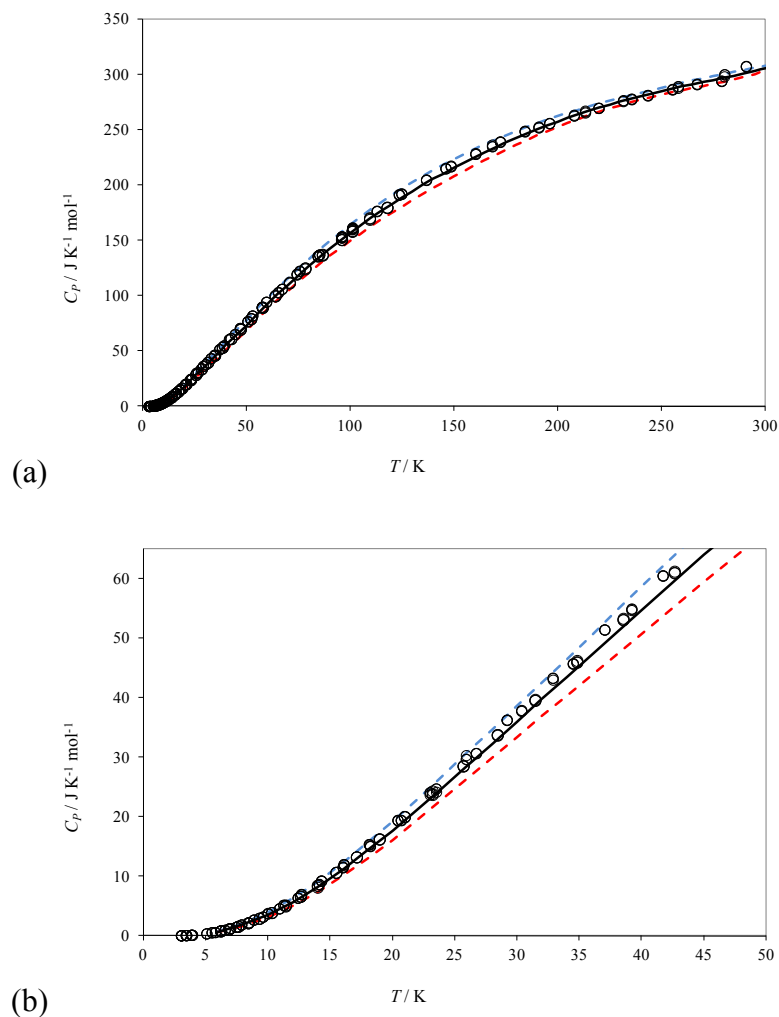


Figure 9.11: The rule of mixtures heat capacity, —, calculated from the averaged heat capacities of - - -, $\text{HfMgMo}_3\text{O}_{12}$ and - - -, $\text{In}_2\text{Mo}_3\text{O}_{12}$ compared to the experimental heat capacities of $\text{In}(\text{HfMg})_{0.5}\text{Mo}_3\text{O}_{12}$ for (a) $5 \text{ K} < T < 265 \text{ K}$ and (b) $5 \text{ K} < T < 50 \text{ K}$.

However, $\text{In}_{1.5}(\text{HfMg})_{0.25}\text{Mo}_3\text{O}_{12}$ was not modeled as effectively at $T < 50 \text{ K}$, with the heat capacity more closely mirroring that of the end member, $\text{In}_2\text{Mo}_3\text{O}_{12}$ (Figure 9.12). The failure of the rule of mixtures to accurately predict the low temperature heat capacity of $\text{In}_{1.5}(\text{HfMg})_{0.25}\text{Mo}_3\text{O}_{12}$ is likely due to a non-linear increase in low-frequency modes responsible for NTE not represented by this simple stoichiometric model.

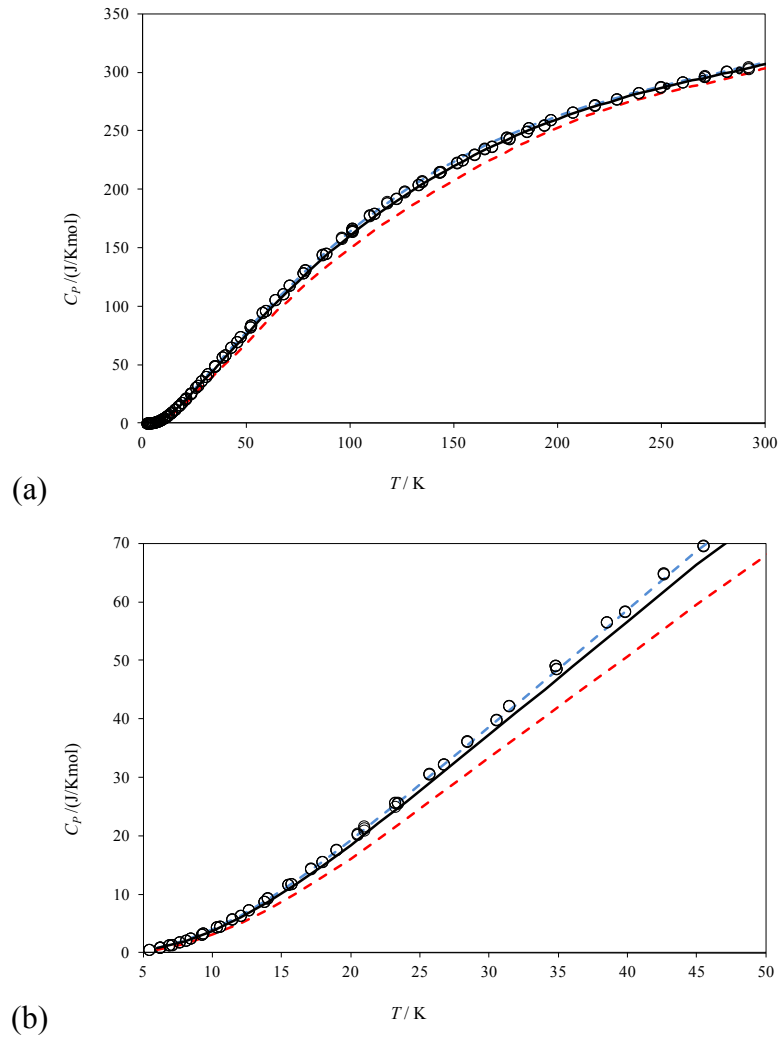


Figure 9.12: The rule of mixtures heat capacity, —, calculated from the averaged heat capacities of, ---, $\text{HfMgMo}_3\text{O}_{12}$ and ---, $\text{In}_2\text{Mo}_3\text{O}_{12}$ compared to the experimental heat capacities of $\text{In}_{1.5}(\text{HfMg})_{0.25}\text{Mo}_3\text{O}_{12}$ for (a) $15 \text{ K} < T < 265 \text{ K}$ and (b) $15 \text{ K} < T < 50 \text{ K}$.

9.5 ANOMALOUS LOW-FREQUENCY MODES

It was recently confirmed that the parent compound, $\text{HfMgMo}_3\text{O}_{12}$, while not a thermomiotic material itself and monoclinic in the low temperature region, has low-frequency phonon modes typically present in NTE materials.³²³ By assessing C_P in the

$\lim T \rightarrow 0$, where, based on lattice contributions to C_p , $C_p \propto aT^3 + bT^5 + \dots$ so $C_p T^{-3}$ should be linear in T^2 for a typical solid, it is possible to compare the low-frequency phonon modes present in the solid solutions to those found in the parent compounds $\text{HfMgMo}_3\text{O}_{12}$ and $\text{In}_2\text{Mo}_3\text{O}_{12}$. The series of compounds, ranging from low-positive thermal expansion in the orthorhombic phase of $\text{HfMgMo}_3\text{O}_{12}$ and low-negative thermal expansion in the orthorhombic phase of $\text{In}_2\text{Mo}_3\text{O}_{12}$, is an ideal system to delineate the contribution of low-frequency modes to the magnitude and sign of the thermal expansion coefficient.

A more illustrative way to present the temperature-dependence of $C_p T^{-3}$ is by plotting it as a function of $\log(T / \text{K})$. Such a plot is given in Figure 9.13 for $\text{In}_2\text{Mo}_3\text{O}_{12}$, $\text{In}_{1.5}(\text{HfMg})_{0.25}\text{Mo}_3\text{O}_{12}$, $\text{In}(\text{HfMg})_{0.5}\text{Mo}_3\text{O}_{12}$, $\text{HfMgMo}_3\text{O}_{12}$, $\text{Sc}_2\text{Mo}_3\text{O}_{12}$,⁷⁴ and $\text{Y}_2\text{Mo}_3\text{O}_{12}$. It shows the presence of low-frequency modes at low temperatures, regardless of the phase or coefficient of thermal expansion for these materials. These bell-shaped curves are typical of thermomiotic materials in this family⁷⁴ and other NTE families.^{66,70}

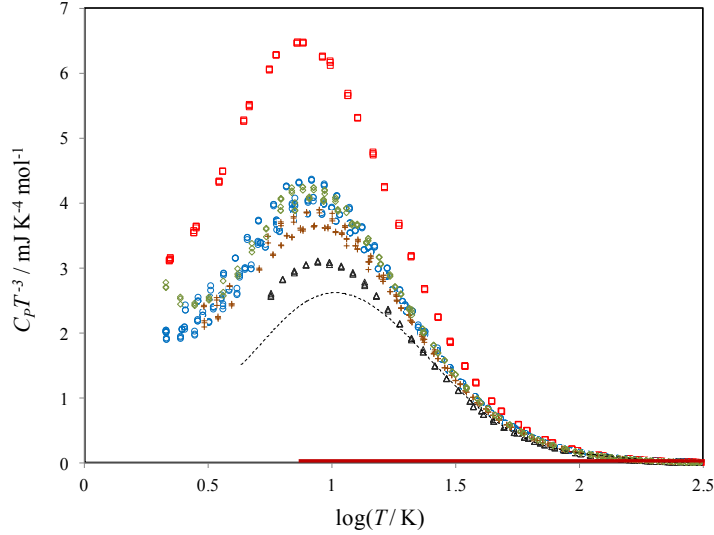


Figure 9.13: $C_p T^{-3}$ vs. $\log(T/K)$ for, Δ , $\text{HfMgMo}_3\text{O}_{12}$; 199 $+$, $\text{In}(\text{HfMg})_{0.5}\text{Mo}_3\text{O}_{12}$; \diamond , $\text{In}_{1.5}(\text{HfMg})_{0.25}\text{Mo}_3\text{O}_{12}$; \circ , $\text{In}_2\text{Mo}_3\text{O}_{12}$; \square , $\text{Y}_2\text{Mo}_3\text{O}_{12}$; $---$, $\text{Sc}_2\text{Mo}_3\text{O}_{12}$ (monoclinic at $T < 178$ K); $—$, and sapphire.⁶⁸

$\text{HfMgMo}_3\text{O}_{12}$, a low-positive thermal expansion material ($\alpha_\ell = 1.02 \times 10^{-6} \text{ K}^{-1}$), has a small number of low-energy modes excited compared to the other compounds studied. As the CTEs approach zero and become negative in the solid solutions, $\text{In}(\text{HfMg})_{0.5}\text{Mo}_3\text{O}_{12}$ ($\alpha_\ell = -0.4 \times 10^{-6} \text{ K}^{-1}$) and $\text{In}_{1.5}(\text{HfMg})_{0.25}\text{Mo}_3\text{O}_{12}$ ($\alpha_\ell = -1.0 \times 10^{-6} \text{ K}^{-1}$), the presence of low-frequency modes increases and approaches the total populated modes of the low-negative thermal expansion end member, $\text{In}_2\text{Mo}_3\text{O}_{12}$ ($\alpha_\ell = -1.84 \times 10^{-6} \text{ K}^{-1}$). $\text{Y}_2\text{Mo}_3\text{O}_{12}$, which is more thermomiotic compared to the other compounds, has a much stronger presence of low-frequency modes as indicated by the higher magnitude of the curve in the plot of $C_p T^{-3}$ vs. $\log(T / K)$. Interestingly, $\text{Sc}_2\text{Mo}_3\text{O}_{12}$, which exhibits NTE ($\alpha_\ell = -2.1 \times 10^{-6} \text{ K}^{-1}$ from 180 K to 300 K)⁷⁶ in the orthorhombic phase and undergoes a transition to the monoclinic phase at $T_{\text{trs}} = 178$ K, has a smaller number of low-frequency modes active at low temperatures than $\text{HfMgMo}_3\text{O}_{12}$.⁷⁴ It is unclear why the low-temperature anomaly in $\text{Sc}_2\text{Mo}_3\text{O}_{12}$ is smaller

than that of $\text{HfMgMo}_3\text{O}_{12}$ (which has low-positive thermal expansion in the orthorhombic phase).

Within the set of compounds examined in this thesis, an interesting trend is observed between the $C_p T^{-3}$ peak temperature and the value of the average linear thermal expansion coefficient (Table 9.1 and Figure 9.14). As the presence of low-frequency phonon modes increases, the bell-shaped curve not only increases in magnitude, but the maximum of the distribution shifts to lower temperatures. The magnitude of the peak is intuitively linked to NTE; as the magnitude of NTE increases it makes sense that the contribution of low-frequency modes would also increase. The peak shift to lower temperatures is less intuitive, but indicates that the low-frequency modes responsible for NTE are activated more easily as the CTE decreases and becomes negative. Raman and inelastic neutron scattering experiments on these compounds would yield valuable insight into this behavior and should be examined in future work.

Table 9.1: Peak temperature of the low-temperature anomalous heat capacity and the average linear thermal expansion coefficients for the orthorhombic phases of $A_2\text{Mo}_3\text{O}_{12}$ materials.

Material	Orthorhombic Phase	$\alpha_l / \times 10^{-6} \text{ K}^{-1}$	Temperature Range / K	Peak Temperature / K
$\text{HfMgMo}_3\text{O}_{12}$ ¹⁹⁹	<i>Pnma</i>	1.02	298 – 1013	8.72 (± 0.01)
$\text{In}(\text{HfMg})_{0.5}\text{Mo}_3\text{O}_{12}$	<i>Pnca</i>	-0.4	498 – 923	8.46 (± 0.01)
$\text{In}_{1.5}(\text{HfMg})_{0.25}\text{Mo}_3\text{O}_{12}$	<i>Pnca</i>	-1.0	573 – 973	8.40 (± 0.01)
$\text{In}_2\text{Mo}_3\text{O}_{12}$ ¹⁹⁶	<i>Pnca</i>	-1.85	643 – 1033	8.24 (± 0.01)
$\text{Y}_2\text{Mo}_3\text{O}_{12}$ ³⁵	<i>Pbcn</i>	-9.02	20 – 450	7.19 (± 0.01)
$\text{Sc}_2\text{Mo}_3\text{O}_{12}$ ⁷⁶	<i>Pbcn</i>	-2.2	180 – 300	10 (± 0.1)

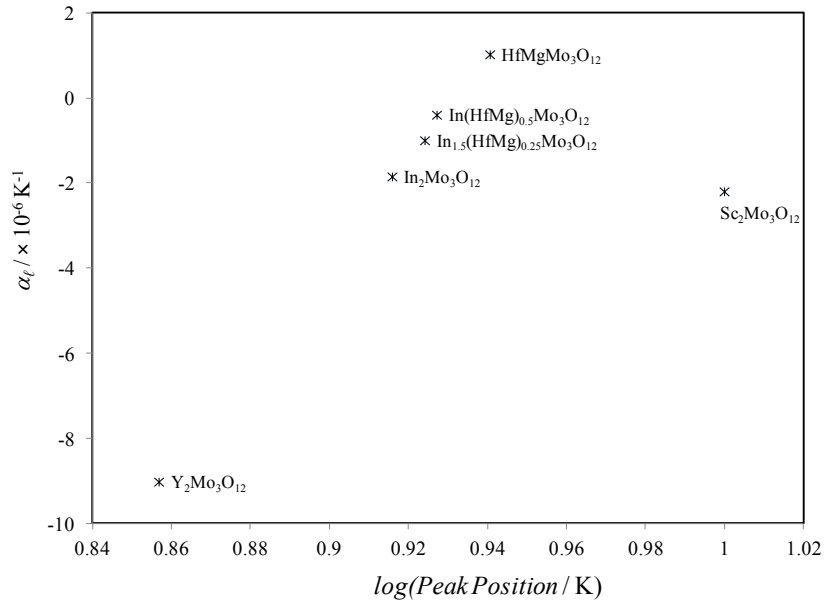


Figure 9.14: Correlation of peak temperature of the low-temperature anomalous heat capacity with the average linear thermal expansion coefficients for the orthorhombic phases of $A_2\text{Mo}_3\text{O}_{12}$ materials (Table 9.1). Error bars for $\log(\text{Peak Position} / \text{K})$ are too small to be visible.

9.6 DEBYE TEMPERATURE

The effective acoustic modes of $\text{In}(\text{HfMg})_{0.5}\text{Mo}_3\text{O}_{12}$ can be quantified from the effective Debye temperature θ_D^e determined from the Debye- T^3 law (Section 1.3.1) using the heat capacity in the lowest temperature ranges 3 K to 8 K, assuming that $C_V = C_P$ and treating all degrees of freedom ($3 \times 17 \times 4$ for 17 atoms per formula unit and 4 formula units per unit cell) with the Debye model (Table 9.2). Figure 9.15 shows the linear fit of $C_P T^{-3}$ against T^2 used to calculate the effective Debye temperature for $\text{Y}_2\text{Mo}_3\text{O}_{12}$ and Figure 9.16 shows the fits for the $\text{In}_2\text{Mo}_3\text{O}_{12}$ - $\text{HfMgMo}_3\text{O}_{12}$ series.

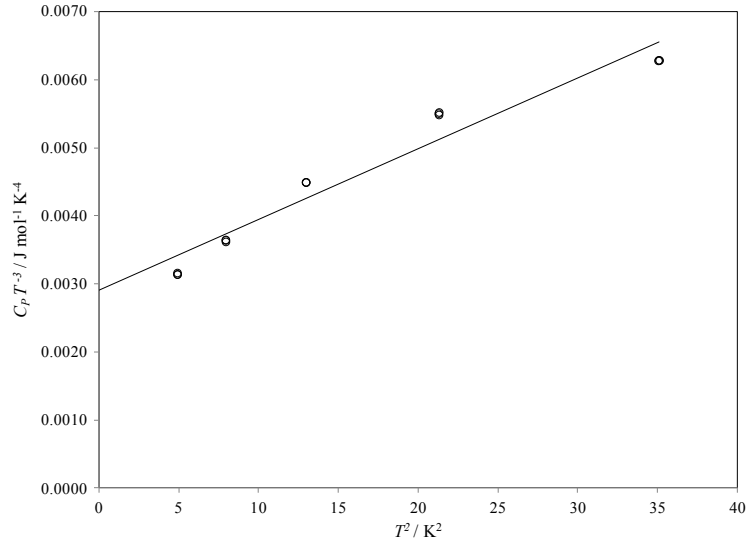


Figure 9.15: The low temperature heat capacity of $\text{Y}_2\text{Mo}_3\text{O}_{12}$ (\circ) (Chapter 5) plotted as $C_p T^{-3}$ against T^2 to determine θ_D^e from the linear fit.

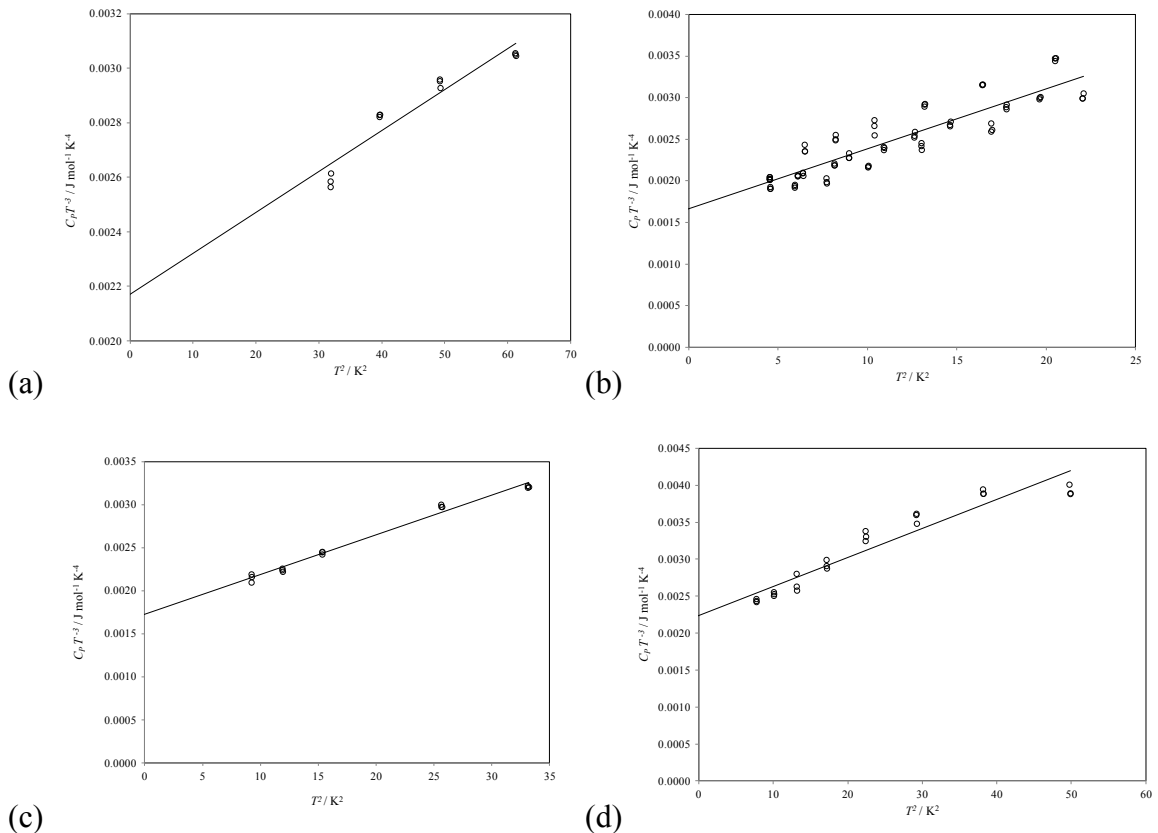


Figure 9.16: The low temperature heat capacities of (a) $\text{HfMgMo}_3\text{O}_{12}$ (\circ) (Chapter 6), (b) $\text{In}_2\text{Mo}_3\text{O}_{12}$ (\circ) (Chapter 7), (c) $\text{In}(\text{HfMg})_{0.5}\text{Mo}_3\text{O}_{12}$ (\circ), and (d) $\text{In}_{1.5}(\text{HfMg})_{0.25}\text{Mo}_3\text{O}_{12}$ (\circ) plotted as $C_p T^{-3}$ against T^2 to determine θ_D^e from the linear fits.

Table 9.2: Young's moduli and the effective speeds of sound for members of the $A_2\text{Mo}_3\text{O}_{12}$ family calculated from θ_D^e .

Structure	θ_D^e / K	$v^{eff} / \text{m s}^{-1}$	E / GPa
HfMgMo₃O₁₂ ¹⁹⁹	248 (±9)	2165	17.8
In(HfMg)_{0.5}Mo₃O₁₂	267 (±4)	2339	21.2
In_{1.5}(HfMg)_{0.25}Mo₃O₁₂	257 (±8)	2247	19.7
In₂Mo₃O₁₂	270 (±9)	2368	22.0
Y₂Mo₃O₁₂	250 (±10)	2266	16.2

These values of θ_D^e place an upper bound on the true Debye temperature, θ_D , calculated by subtraction of the contribution of the optic modes and treating the remaining 3 modes as Debye-like: for example, for HfMo_2O_8 $\theta_D = 82 \text{ K}$,⁶⁶ whereas $\theta_D^e = 307 \text{ K}$.⁶⁷

From θ_D^e , the effective speed of sound, v^{eff} , can be determined from

$$v^{eff} = \left(\frac{2\pi k \theta_D^{eff}}{h} \right) \left(\frac{V}{6\pi^2 N} \right)^{1/3}, \quad (9.1)$$

where $N/V =$ number density of atoms. The use of θ_D^e to calculate Young's modulus (Table 9.2) from

$$E = \rho(v^{eff})^2, \quad (9.2)$$

where ρ is the theoretical density, provides a reasonable approximation for the stiffness of the materials. While these values of Young's modulus are relatively low for ceramic materials, they are similar on the same order as the experimentally determined values for ZrW_2O_8 (88 GPa)³³¹ and consistent with the flexibility of the $A\text{-O-M}$ framework, which also gives rise to the anomalously high heat capacity at low temperatures.^{66,67,323}

9.7 THERMAL CONDUCTIVITY

Thermal conductivity measurements were conducted in continuous mode on samples of the $A_2\text{Mo}_3\text{O}_{12}$ family from 300 K down to 2 K. Details of the sample dimensions and their % theoretical densities are shown in Table 9.3.

Table 9.3: Size and density of the 2.8 mm diameter pellets used to measure thermal conductivity.

Sample	Thickness / mm	Density / g cm^{-3}	% Theoretical Density
HfMgMo₃O₁₂ (A1)	0.76	2.24	59
HfMgMo₃O₁₂ (A2)	0.66	2.25	59
HfMgMo₃O₁₂ (A3)	1.55	2.59	68
In(HfMg)_{0.5}Mo₃O₁₂ (B1)	1.13	2.89	75
In(HfMg)_{0.5}Mo₃O₁₂ (B2)	1.08	2.47	64
In(HfMg)_{0.5}Mo₃O₁₂ (B3)	1.13	2.45	63
In_{1.5}(HfMg)_{0.25}Mo₃O₁₂ (C1)	1.00	2.98	76
In_{1.5}(HfMg)_{0.25}Mo₃O₁₂ (C2)	1.29	2.79	71
In_{1.5}(HfMg)_{0.25}Mo₃O₁₂ (C3)	1.12	2.45	62
In₂Mo₃O₁₂ (D1)	1.18	2.53	64
In₂Mo₃O₁₂ (D2)	1.57	2.49	63
In₂Mo₃O₁₂ (D3)	1.57	2.49	63
Y₂Mo₃O₁₂ (E1)	0.91	2.02	63
Y₂Mo₃O₁₂ (E2)	1.57	2.11	67
Y₂Mo₃O₁₂ (E3)	0.91	1.92	61

The temperature dependence of the thermal conductivity data, κ , for three independent samples of each material were determined (full data sets in Appendix C) and the values scaled up to full density using Klemens' model ($\kappa = \kappa_m(1 - (4/3)f)$, where κ_m is the scaled up conductivity and f is the volume fraction)³³² and the experimental densities (Table 9.3). Figure 9.17 shows the experimental data for $\text{HfMgMo}_3\text{O}_{12}$, with an anomaly at $T = 170$ K corresponding to the orthorhombic to monoclinic phase transition and slight loss of thermal contact, as well as the fully densified data. Polycrystalline data treated with the Klemens' model to determine the densified thermal conductivity can give a good approximation of the properties of high purity single crystal samples with densified data being within 5 % of the crystalline data above 30 K.³³³

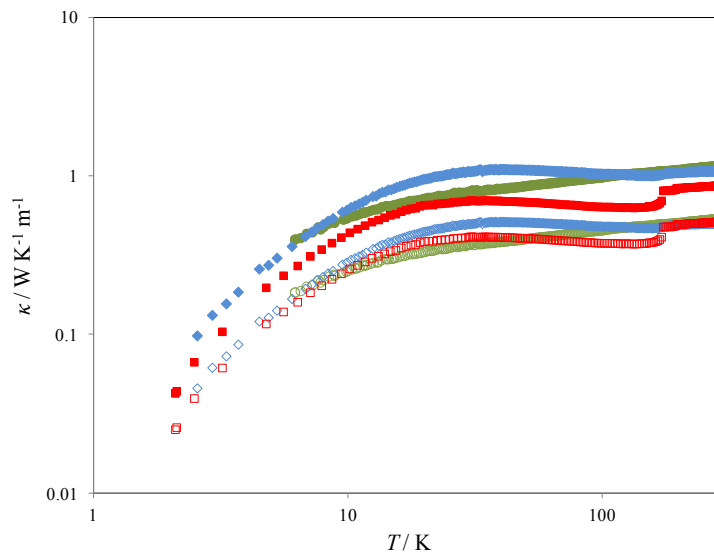


Figure 9.17: Temperature dependence of the experimental thermal conductivity data for $\text{HfMgMo}_3\text{O}_{12}$ (\circ , A1; \diamond , A2; \square , A3; where samples are described in Table 9.3). Open symbols represent the experimental data and closed circles represent the corresponding fully densified data calculated using the Klemens' model.³³²

Figures 9.18, 9.19, 9.20, 9.21, and 9.22 show the fully densified data and the theoretical minimum conductivities, κ_{\min} , for fully coupled phonons:³³⁴

$$\kappa_{\min} = \frac{1}{2.48} k_B n^{2/3} v_i 2 \left(\frac{T}{\theta_D^e} \right)^2 \int_0^{\theta_D^e/T} \frac{x^3 e^x}{(e^x - 1)^2} dx, \quad (9.3)$$

where k_B is Boltzmann's constant, n is the number density, and v_i is the contribution from the longitudinal and two transverse speeds of sound and κ_{\min} is the sum of these two contributions. The mean speeds of sound, $v^{eff} = v_m$, were calculated from the effective Debye temperature (Section 9.6) in order to calculate κ_{\min} for each material.

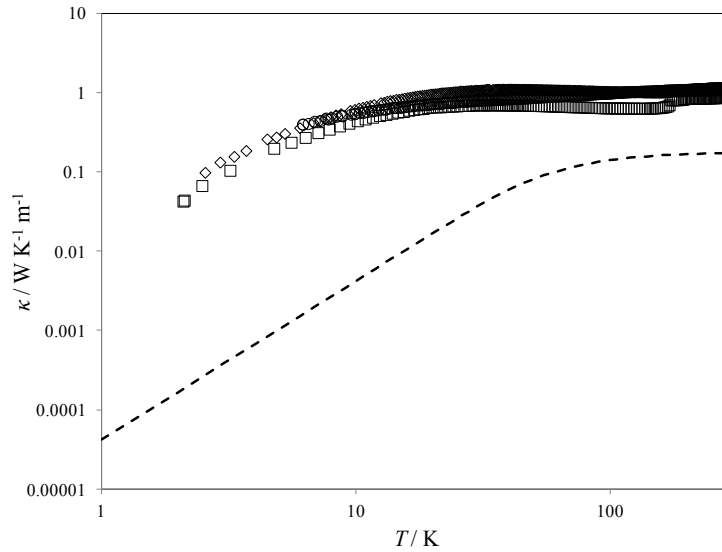


Figure 9.18: Temperature dependence of the fully dense thermal conductivity of $\text{HfMgMo}_3\text{O}_{12}$ (\circ , A1; \diamond , A2; \square , A3; where samples are described in Table 9.3); - - - denotes the theoretical minimum thermal conductivity. Reprinted with permission from Miller, K. J.; Johnson, M. B.; White, M. A.; Marinkovic, B. A. *Solid State Commun.* **2012**, *152*, 1748-1752. Copyright 2012 Elsevier.

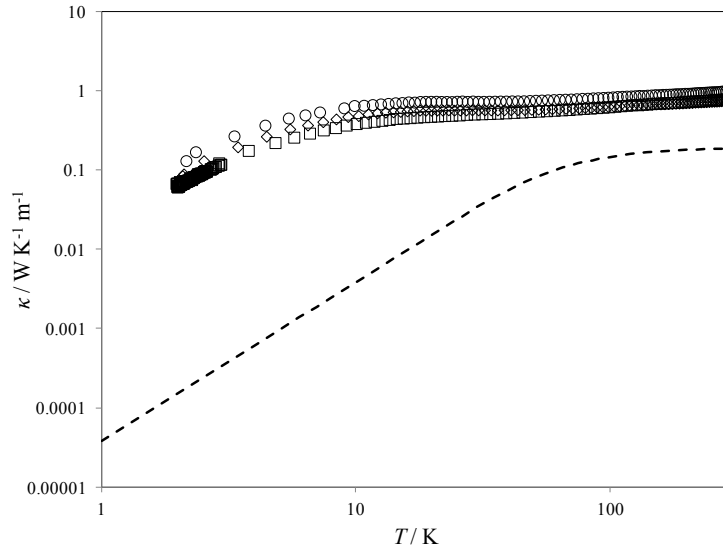


Figure 9.19: Temperature dependence of the fully dense thermal conductivity $\text{In}(\text{HfMg})_{0.5}\text{Mo}_3\text{O}_{12}$ (\circ , B1; \diamond , B2; \square , B3; where samples are described in Table 9.3); - - - denotes the theoretical minimum thermal conductivity.

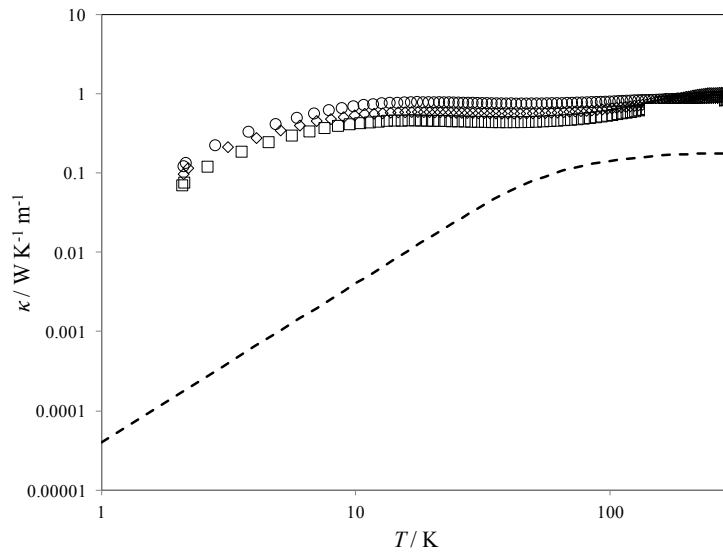


Figure 9.20: Temperature dependence of the fully dense thermal conductivity $\text{In}_{1.5}(\text{HfMg})_{0.25}\text{Mo}_3\text{O}_{12}$ (\circ , C1; \diamond , C2; \square , C3; where samples are described in Table 9.3); - - - denotes the theoretical minimum thermal conductivity.

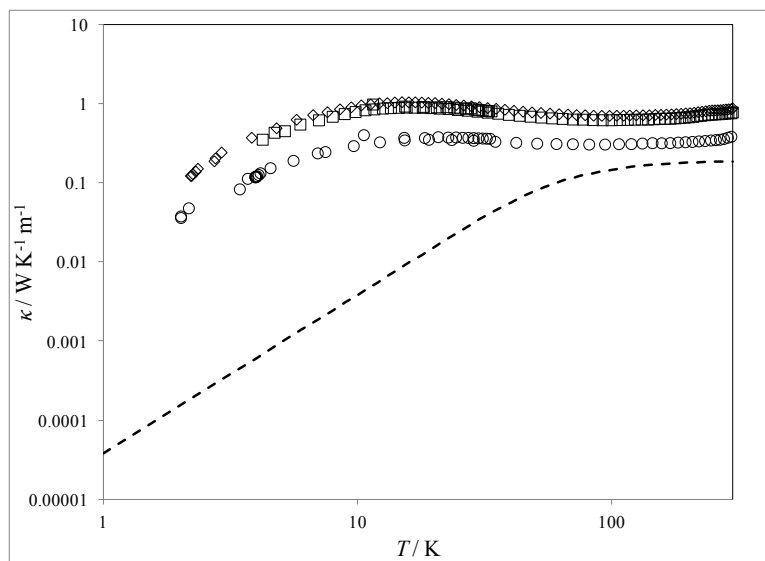


Figure 9.21: Temperature dependence of the fully dense thermal conductivity $\text{In}_2\text{Mo}_3\text{O}_{12}$ (\circ , D1; \diamond , D2; \square , D3; where samples are described in Table 9.3); - - - denotes the theoretical minimum thermal conductivity.

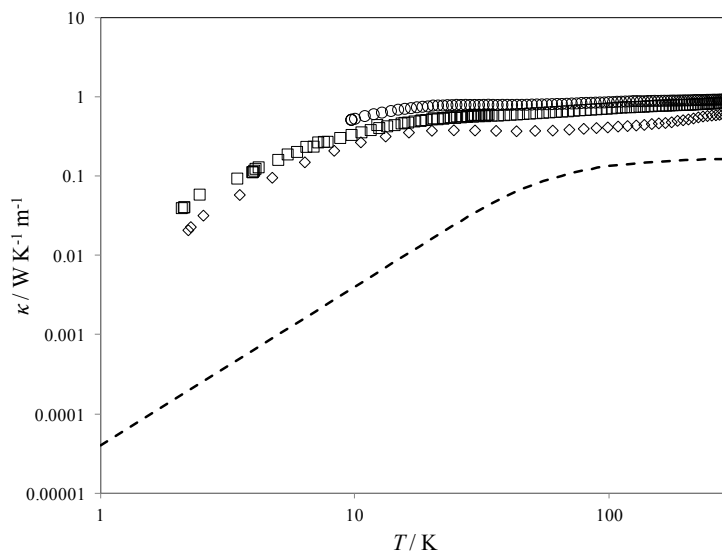


Figure 9.22: Temperature dependence of the fully dense thermal conductivity of $\text{Y}_2\text{Mo}_3\text{O}_{12}$ (\circ , E1; \diamond , E2; \square , E3; where samples are described in Table 9.3); - - - denotes the theoretical minimum thermal conductivity.

As observed for the low-positive CTE parent compound, $\text{HfMgMo}_3\text{O}_{12}$ (Figure 9.18), the thermal conductivities of the solid-solutions, $\text{In}(\text{HfMg})_{0.5}\text{Mo}_3\text{O}_{12}$ and $\text{In}_{1.5}(\text{HfMg})_{0.25}\text{Mo}_3\text{O}_{12}$ (Figure 9.19 and Figure 9.20), and the other end member,

$\text{In}_2\text{Mo}_3\text{O}_{12}$ (Figure 9.21), are all low, but considerably above the minimum value throughout the examined temperature range, indicating that while the systems are anharmonic, they are not as anharmonic as some thermomiotic materials.^{57,71} Somewhat surprisingly, $\text{Y}_2\text{Mo}_3\text{O}_{12}$ (Figure 9.22), which has a large negative CTE, has a thermal conductivity similar to the low-positive, near-zero, and low-negative $A_2\text{Mo}_3\text{O}_{12}$ materials.

Figure 9.23 shows the fully densified thermal conductivities determined from the measured values of the $\text{HfMgMo}_3\text{O}_{12} - \text{In}_2\text{Mo}_3\text{O}_{12}$ solid solutions. Interestingly, the low PTE material, $\text{HfMgMo}_3\text{O}_{12}$, has a more glass like thermal conductivity compared to the low NTE material, $\text{In}_2\text{Mo}_3\text{O}_{12}$, which retains a more crystalline character with a peak at low temperatures. The indium-rich compound, $\text{In}_{1.5}(\text{HfMg})_{0.25}\text{Mo}_3\text{O}_{12}$, also retains the low-temperature thermal conductivity peak to a greater extent than $\text{In}(\text{HfMg})_{0.5}\text{Mo}_3\text{O}_{12}$, which could be indicative of a higher degree of crystallinity or a more harmonic system. These findings are somewhat unexpected since it has been shown previously that the thermomiotic material, ZrW_2O_8 , has unusually low and glass-like thermal conductivity.⁵⁷

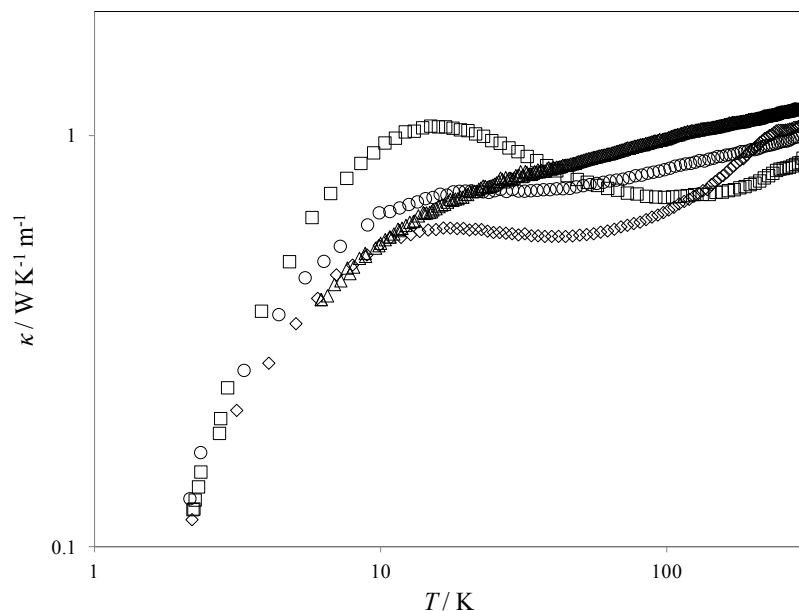


Figure 9.23: Temperature dependence of the fully dense thermal conductivities of: Δ (A1, from Table 9.3), $\text{HfMgMo}_3\text{O}_{12}$; \circ (B2, from Table 9.3), $\text{In}(\text{HfMg})_{0.5}\text{Mo}_3\text{O}_{12}$; \diamond (C2, from Table 9.3), $\text{In}_{1.5}(\text{HfMg})_{0.25}\text{Mo}_3\text{O}_{12}$; and \square (D2, from Table 9.3), $\text{In}_2\text{Mo}_3\text{O}_{12}$, *i.e.* the highest thermal conductivity for each compound, scaled up to fully densified values.

Intuitively, it was expected that materials with thermomiotic behavior would have thermal conductivities more similar to the glass-like thermal conductivity observed in ZrW_2O_8 ⁵⁷ due to the flexibility of the framework structure and the presence of low-frequency modes. However it should be noted that the members of the $\text{In}_2\text{Mo}_3\text{O}_{12}$ and $\text{HfMgMo}_3\text{O}_{12}$ set of compounds are monoclinic, with positive coefficients of thermal expansion, at low temperatures while ZrW_2O_8 is in a space group that exhibits NTE. $\text{Y}_2\text{Mo}_3\text{O}_{12}$, which has a large negative CTE ($\alpha_\ell = -9.02 \times 10^{-6} \text{ K}^{-1}$) and maintains the orthorhombic structure at low temperatures,³⁵ follows this trend as can be seen in Figure 9.16. In addition, materials having lower coefficients of thermal expansion in their orthorhombic phases, such as $\text{HfMgMo}_3\text{O}_{12}$ ($\alpha_\ell = 1.02 \times 10^{-6} \text{ K}^{-1}$),¹⁹⁹ $\text{In}_2\text{Mo}_3\text{O}_{12}$ ($\alpha_\ell = -1.85 \times 10^{-6} \text{ K}^{-1}$),¹⁹⁶ and the solid solutions ($\text{In}(\text{HfMg})_{0.5}\text{Mo}_3\text{O}_{12}$

($\alpha_\ell = -0.4 \times 10^{-6} \text{ K}^{-1}$) and $\text{In}_{1.5}(\text{HfMg})_{0.25}\text{Mo}_3\text{O}_{12}$ ($\alpha_\ell = -1 \times 10^{-6} \text{ K}^{-1}$), also have fewer low-frequency modes to impact the thermal conductivity of these crystalline materials.

While the low-frequency modes do not appear to contribute as strongly to the thermal resistance in these materials, the more glass-like thermal conductivity seen in the low PTE material, $\text{HfMgMo}_3\text{O}_{12}$, could instead be a result of greater disorder, due to a mixture of *A* cations, in the crystal structure of the material. As the content of $\text{In}_2\text{Mo}_3\text{O}_{12}$ increases in the solid solutions, the materials would take on a more ordered structure. However, in order to fully understand the role of order and disorder in these systems further studies should be carried out, especially to solve the crystal structures of these materials.

9.8 EFFECTIVE PHONON MEAN FREE PATH

Using the heat capacity, velocity of sound, and thermal conductivity data, the effective phonon mean free path, λ , can be calculated from¹⁸

$$\kappa = \frac{C v_m \lambda}{3}, \quad (6.2)$$

where *C* is the heat capacity per unit volume. Generally, the effective mean free path underestimates the true mean free path as calculated by models which include dispersion effects, which is why this is referred to as “effective”.³³⁵ However, the dispersion effects should be similar for all members of the $A_2M_3O_{12}$ family, allowing useful comparisons here.

The results for $\text{Y}_2\text{Mo}_3\text{O}_{12}$ are similar to other open framework structures that have been known to give rise to NTE: the effective phonon mean free path is quite small despite the material being crystalline (Figure 9.24). The effective mean free path decreases with increasing temperature, from greater than 100 nm at 5 K to less than 10 nm above 50 K.

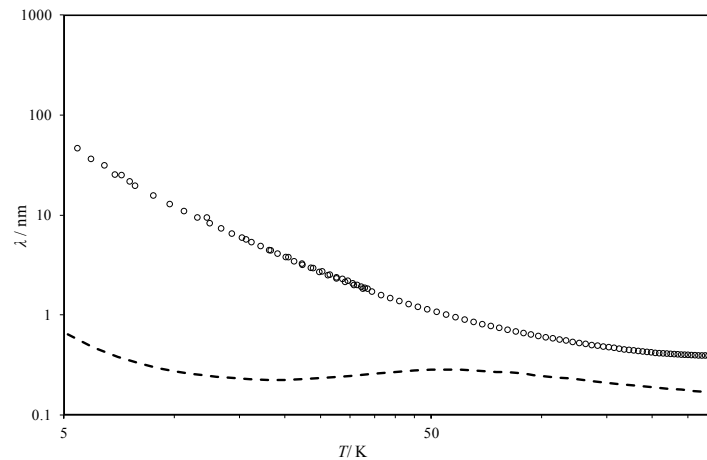


Figure 9.24: Temperature dependence of the effective phonon mean free path of $\text{Y}_2\text{Mo}_3\text{O}_{12}$ from the average fully densified thermal conductivity data, \circ , and the minimum phonon mean free path κ_{\min} , - - -.

Similarly, the effective phonon mean free paths for the solid solutions of $\text{In}(\text{HfMg})_{0.5}\text{Mo}_3\text{O}_{12}$ and $\text{In}_{1.5}(\text{HfMg})_{0.25}\text{Mo}_3\text{O}_{12}$ and the end members $\text{In}_2\text{Mo}_3\text{O}_{12}$ and $\text{HfMgMo}_3\text{O}_{12}$ are also quite small despite the materials being crystalline (Figure 9.25, 9.26, 9.27, and 9.27).

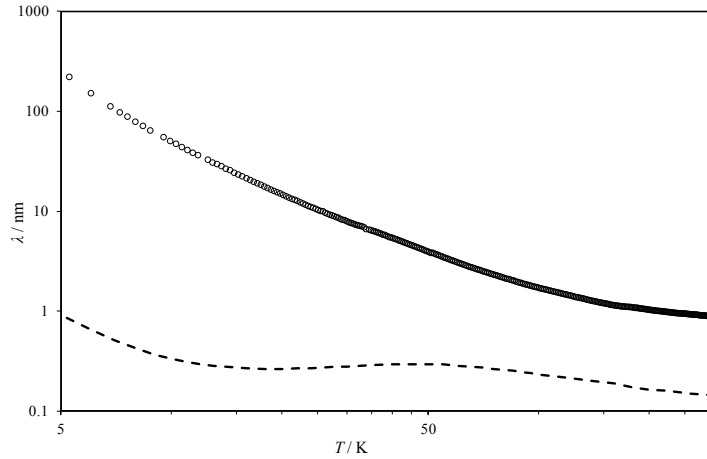


Figure 9.25: Temperature dependence of the effective phonon mean free path of $\text{HfMgMo}_3\text{O}_{12}$ calculated from the average fully densified thermal conductivity data, \circ , and the minimum phonon mean free path κ_{\min} , - - -. Reprinted with permission from Miller, K. J.; Johnson, M. B.; White, M. A.; Marinkovic, B. A. *Solid State Commun.* **2012**, *152*, 1748-1752. Copyright 2012 Elsevier.

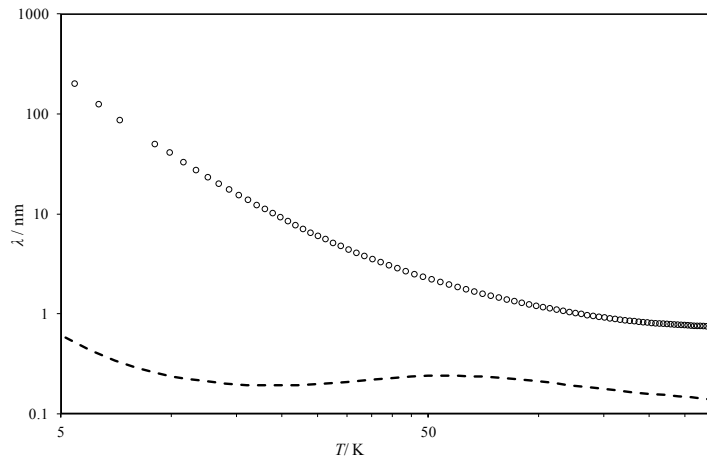


Figure 9.26: Temperature dependence of the effective phonon mean free path of $\text{In}(\text{HfMg})_{0.5}\text{Mo}_3\text{O}_{12}$ calculated from the average fully densified thermal conductivity data, \circ , and the minimum phonon mean free path κ_{\min} , - - -.

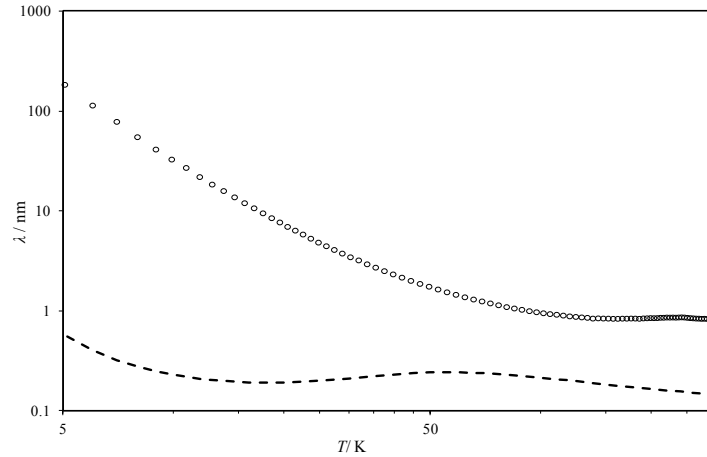


Figure 9.27: Temperature dependence of the effective phonon mean free path of $\text{In}_{1.5}(\text{HfMg})_{0.25}\text{Mo}_3\text{O}_{12}$ calculated from the average fully densified thermal conductivity data, \circ , and the minimum phonon mean free path κ_{\min} , - - -.

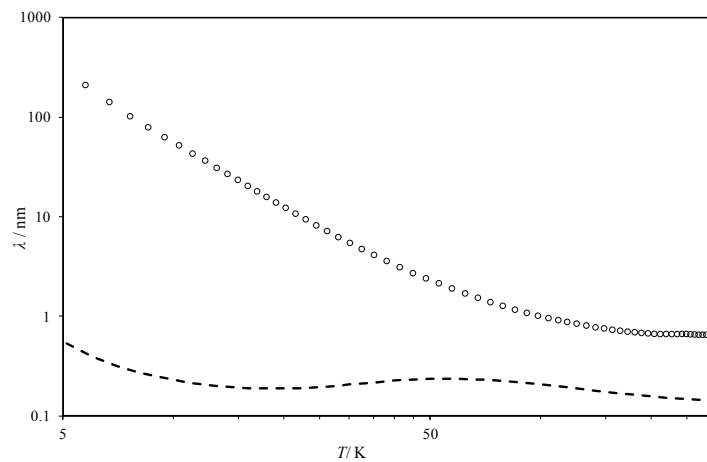


Figure 9.28: Temperature dependence of the effective phonon mean free path of $\text{In}_2\text{Mo}_3\text{O}_{12}$ calculated from the average fully densified thermal conductivity data, \circ , and the minimum phonon mean free path κ_{\min} , - - -.

Interestingly, the phonon mean free paths of the solid solutions, $\text{In}(\text{HfMg})\text{Mo}_3\text{O}_{12}$ and $\text{In}_{1.5}(\text{HfMg})_{0.25}\text{Mo}_3\text{O}_{12}$, are similar to those determined for the two end members (Figure 9.26). From room temperature to ~ 20 K, $\text{HfMgMo}_3\text{O}_{12}$ has been found to have a longer mean free path consistent with the information presented in Section 9.5 which showed that $\text{HfMgMo}_3\text{O}_{12}$, being a low PTE material, has fewer low-frequency phonon modes and therefore a higher thermal conductivity (Figure 9.23) at $T > 50$ K.

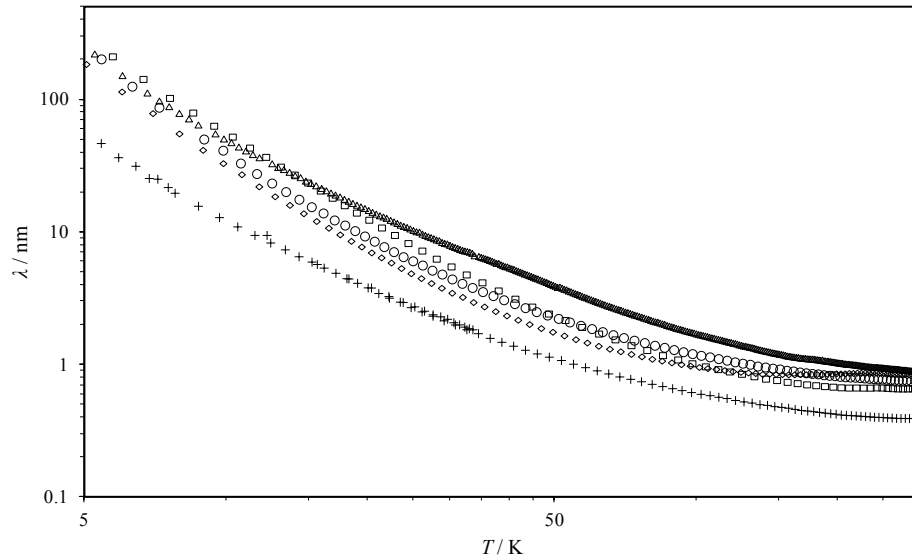


Figure 9.29: Temperature dependence of the effective phonon mean free path of: Δ , $\text{HfMgMo}_3\text{O}_{12}$; \circ , $\text{In}(\text{HfMg})_{0.5}\text{Mo}_3\text{O}_{12}$; \diamond , $\text{In}_{1.5}(\text{HfMg})_{0.25}\text{Mo}_3\text{O}_{12}$; and \square , $\text{In}_2\text{Mo}_3\text{O}_{12}$, and $+$, $\text{Y}_2\text{Mo}_3\text{O}_{12}$ calculated from the maximum fully densified thermal conductivity data for each sample.

$\text{In}_2\text{Mo}_3\text{O}_{12}$ should, intuitively, have the longest effective phonon mean free path as it has the most ordered structure. $\text{HfMgMo}_3\text{O}_{12}$, having a mixture of A cations, would be expected to have a shorter mean free path. However, this trend was not observed. Instead, Figure 9.29 clearly shows that the effective phonon mean free paths, for all of the materials examined in the $\text{In}_2\text{Mo}_3\text{O}_{12} - \text{HfMgMo}_3\text{O}_{12}$ series, are quite similar.

The effective phonon mean free paths of all the materials studied in this thesis are quite low with $\lambda < 2$ nm at $T > 100$ K for all materials and $\lambda < 100$ nm at $T < 30$ K.

$\text{Y}_2\text{Mo}_3\text{O}_{12}$, which has the most NTE of the materials studied, has the shortest mean free path with $\lambda < 1$ nm at $T > 50$ K and with $\lambda < 10$ nm at $T < 10$ K. The low mean free path in $\text{Y}_2\text{Mo}_3\text{O}_{12}$ (almost half an order of magnitude lower than the others) can be understood in terms of a greater number of highly coupled phonons and greater thermal resistance of the material. These results are consistent with those of Kennedy *et al.*, for ZrW_2O_8 ⁵⁷ and

HfMo₂O₈,⁷¹ who proposed that unusually low thermal conductivity could be a general feature for NTE materials.^{57,71} In contrast, a single crystal of the PTE pyrochlore, Y₂Ti₂O₇, has a much larger effective phonon mean free path, particularly at low temperatures, $\lambda > 100$ nm at $T < 50$ K and $\lambda > 1$ nm at $T < 100$ K.³³⁶

9.9 CONCLUSIONS

A series of materials of the general formula $A_2\text{Mo}_3\text{O}_{12}$ with coefficients of thermal expansion ranging, in their orthorhombic phase, from large-negative (Y₂Mo₃O₁₂, $-9.02 \times 10^{-6} \text{ K}^{-1}$ from 20 K to 450 K),³⁵ low-negative (In₂Mo₃O₁₂, $\alpha_\ell = -1.84 \times 10^{-6} \text{ K}^{-1}$ from 643 K to 1033 K),¹⁹⁶ near-zero (In(HfMg)_{0.5}Mo₃O₁₂ ($\alpha_\ell = -0.4 \times 10^{-6} \text{ K}^{-1}$ from 498 K to 923 K) and In_{1.5}(HfMg)_{0.25}Mo₃O₁₂ ($\alpha_\ell = -1.0 \times 10^{-6} \text{ K}^{-1}$ from 573 K to 973 K)), and low-positive (HfMgMo₃O₁₂, $\alpha_\ell = 1.02 \times 10^{-6} \text{ K}^{-1}$ from 298 K to 1013 K)¹⁹⁹ have demonstrated that the heat capacity and thermal conductivity below room temperature show the presence of easily excited low-frequency phonon modes which have been associated with thermomiotic materials. For all members of the $A_2\text{Mo}_3\text{O}_{12}$ family studied, a clear qualitative connection between the orthorhombic CTE and the magnitude of the low temperature peak in $C_p T^{-3}$ vs $\ln(T)$ can be seen. As the CTE becomes more negative the peak increases in magnitude, due to the increase in the contribution of low-frequency modes; the peak also shifts to lower temperatures. The thermal conductivity and effective phonon mean free path for members of the $A_2\text{Mo}_3\text{O}_{12}$ family are consistently low and in line with values observed for other NTE materials.^{57,71}

CHAPTER 10 CONCLUSIONS AND FUTURE WORK

Several materials in the $A_2\text{Mo}_3\text{O}_{12}$ family were successfully synthesized using standard solid-state reaction and mechanical activation methods in order to obtain a set of compounds with CTEs ranging from large-negative to low-positive. In addition to the standard techniques, a simplified sol-gel method was developed to synthesize monophasic, submicron (~ 300 nm) $\text{Al}_2\text{Mo}_3\text{O}_{12}$ (Chapter 4) with shorter calcination times and lower temperatures than standard mechanical-activation and solid-state reaction techniques. It was observed that the metal to PVA ratio, together with calcination temperature and time, could be used as a control parameter to tailor the particle size of the final product. The success of this PVA-assisted sol-gel approach has the potential to reduce reaction times and simplify the synthesis of other members of the $A_2M_3O_{12}$ family using a similar approach.

The coefficients of thermal expansion and some thermal properties of $\text{Y}_2\text{Mo}_3\text{O}_{12}$ (Chapter 5), $\text{HfMgMo}_3\text{O}_{12}$ (Chapter 6), and $\text{In}_2\text{Mo}_3\text{O}_{12}$ (Chapter 7) had been previously characterized and were available in the literature.^{141,157,189,199,196} However, little was known about the thermal properties below room temperature. In particular, it was unknown if $\text{Y}_2\text{Mo}_3\text{O}_{12}$ and $\text{HfMgMo}_3\text{O}_{12}$ underwent a monoclinic to orthorhombic phase transition below room temperature and no information was known concerning the thermal conductivity or heat capacity of these materials over any temperature range. However, these members of the $A_2M_3O_{12}$ family were ideal candidates for probing the low-frequency modes of open-framework materials and determining if the unusually low

and glass-like thermal conductivity observed in ZrW_2O_8 ⁵⁷ and HfMo_2O_8 ⁷¹ was a general feature of thermomiotic materials with an open framework structure.

$\text{Y}_2\text{Mo}_3\text{O}_{12}$ presented the largest challenge of the materials examined. While $\text{Y}_2\text{Mo}_3\text{O}_{12}$ is very thermomiotic it is also quite hygroscopic and presented unique challenges towards obtaining good quality data. Brief exposure, on the order of seconds, to ambient conditions is enough for the material to become hydrated. It was found that excellent results for X-ray powder diffraction, heat capacity, DSC, and thermal conductivity measurements could be obtained after *in situ* dehydration of the samples. Low-temperature measurements of the crystalline sample showed that $\text{Y}_2\text{Mo}_3\text{O}_{12}$ was thermomiotic ($\alpha_t = -9.02 \times 10^{-6} \text{ K}^{-1}$ from 20 K to 450 K) and remained in the orthorhombic (*Pbcn*) phase down to 2 K.

$\text{HfMgMo}_3\text{O}_{12}$ and $\text{In}_2\text{Mo}_3\text{O}_{12}$ did not exhibit hydration-induced amorphization and were air stable. DSC was used to determine the enthalpy change associated with the monoclinic to orthorhombic phase transition in $\text{In}_2\text{Mo}_3\text{O}_{12}$ at $T_{\text{trs}} = 615 \text{ K}$ (*P2₁/a* to *Pnca*) and to characterize the T_{trs} at 175 K in $\text{HfMgMo}_3\text{O}_{12}$ (*P2₁/a* to *Pnma*). The enthalpy and entropy changes associated with the phase transitions for $\text{In}_2\text{Mo}_3\text{O}_{12}$ and $\text{HfMgMo}_3\text{O}_{12}$ are low and consistent with previously reported values¹⁹³ and demonstrate that only a small rearrangement is required for the structural phase transformation. The monoclinic and orthorhombic phases, for both materials, were confirmed by variable-temperature X-ray powder diffraction.

Two solid solutions, $\text{In}(\text{HfMg})_{0.5}\text{Mo}_3\text{O}_{12}$ and $\text{In}_{1.5}(\text{HfMg})_{0.25}\text{Mo}_3\text{O}_{12}$, were synthesized to produce materials with near-zero thermal expansion in the orthorhombic phase. Both solid solutions adopt monoclinic (*P2₁/a*) structures at low temperature and

undergo phase transitions, at 425 K for $\text{In}(\text{HfMg})_{0.5}\text{Mo}_3\text{O}_{12}$ and 520 K for $\text{In}_{1.5}(\text{HfMg})_{0.25}\text{Mo}_3\text{O}_{12}$, to an orthorhombic phase (*Pnca*) with enthalpy and entropy changes consistent with the parent compounds, $\text{In}_2\text{Mo}_3\text{O}_{12}$ and $\text{HfMgMo}_3\text{O}_{12}$. Thermal expansion is positive in the low-temperature monoclinic phases of $\text{In}(\text{HfMg})_{0.5}\text{Mo}_3\text{O}_{12}$ and $\text{In}_{1.5}(\text{HfMg})_{0.25}\text{Mo}_3\text{O}_{12}$. However, both solid solutions have the anticipated near-zero thermal expansion coefficients (as predicted by the rule of mixtures) in their high-temperature orthorhombic phases, with average linear intrinsic coefficients of thermal expansions of $\alpha_\ell = -0.4 \times 10^{-6} \text{ K}^{-1}$ ($\text{In}(\text{HfMg})_{0.5}\text{Mo}_3\text{O}_{12}$) and $\alpha_\ell = -1.0 \times 10^{-6} \text{ K}^{-1}$ ($\text{In}_{1.5}(\text{HfMg})_{0.5}\text{Mo}_3\text{O}_{12}$), and average linear bulk coefficient of thermal expansions of $\alpha_\ell = 0.4 \times 10^{-6} \text{ K}^{-1}$ ($\text{In}(\text{HfMg})_{0.5}\text{Mo}_3\text{O}_{12}$) and $-0.2 \times 10^{-6} \text{ K}^{-1}$ ($\text{In}_{1.5}(\text{HfMg})_{0.5}\text{Mo}_3\text{O}_{12}$).

With the successful synthesis and characterization of these two solid solutions with near-zero thermal expansion in the orthorhombic phases a more complete picture of the thermal properties of thermomiotic materials over a range of CTEs has been constructed. The low-temperature heat capacity of these materials shows the presence of easily excited low-frequency phonon modes regardless of the magnitude and sign of the coefficient of thermal expansion. However, a qualitative connection between the orthorhombic phase CTE and the magnitude of the low temperature peak in $C_P T^{-3}$ vs $\log(T)$ can be seen within this family. As the CTE becomes more negative the $C_P T^{-3}$ peak increases in magnitude, due to the increase in the contribution of low-frequency modes; the peak also shifts to lower temperatures.

The thermal conductivities and effective phonon mean free paths for members of the $A_2\text{Mo}_3\text{O}_{12}$ family are consistently low and in line with values observed for ZrW_2O_8 ⁵⁷ and HfMo_2O_8 ⁷¹ indicating that these low values are most likely a consistent feature of

open-framework structures. This finding stresses the need to develop homogeneous materials with near-zero thermal expansion rather than composites incorporating positive and negative thermal expansion materials, in order to increase thermal shock fracture resistance.

While the results herein add valuable understanding to the role of low-frequency modes to the coefficient of thermal expansion in the $A_2\text{Mo}_3\text{O}_{12}$ family, they also show that it is not simply a matter of low-frequency modes being active or inactive. In $\text{HfMgMo}_3\text{O}_{12}$, which has low-positive thermal expansion in the orthorhombic phase, low-frequency modes were clearly contributing to the low-temperature heat capacity. As the coefficient of thermal expansion of the orthorhombic phase becomes smaller and changes sign, the contribution of the low-frequency modes increases. A clearer picture concerning which modes are being excited in each system is a subject for future work.

Raman spectroscopy and inelastic neutron scattering have been invaluable tools in probing the low-frequency modes of thermomiotic materials and would allow for a direct comparison between these members of the $A_2\text{Mo}_3\text{O}_{12}$ family, further building on this work.

Determination of the full crystal structures from high resolution synchrotron data should be a high priority for developing a better understanding of these results. The lattice parameters only provide insight into the coefficient of thermal expansion and the anisotropies of the thermal expansion coefficients. However, with information on atomic positions of the atoms in the unit cell it would be possible to look more closely at polyhedral distortion and to model the vibrational modes probed by Raman spectroscopy and inelastic neutron scattering.

APPENDIX A – SUPPLEMENTARY DATA FOR HEAT CAPACITY MEASUREMENTS

A1 $Y_2Mo_3O_{12}$

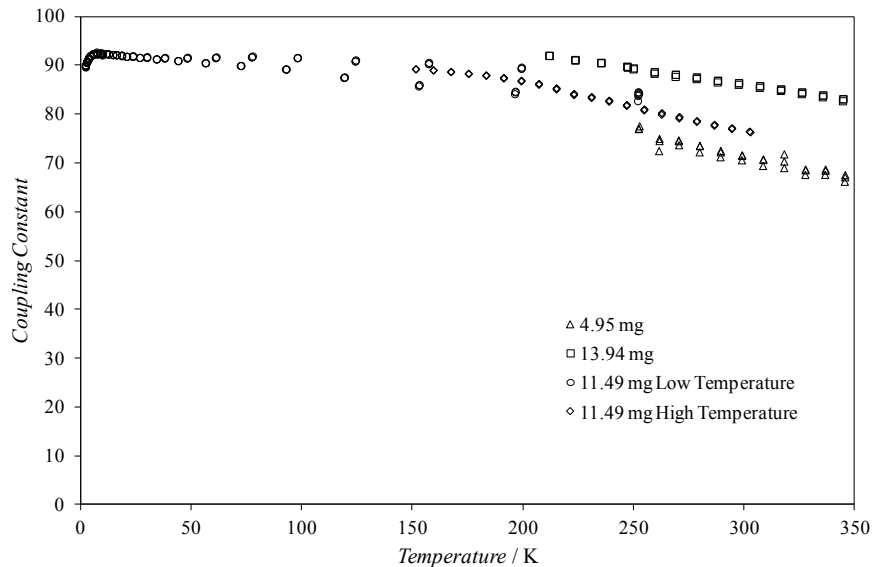


Figure A1.1: The coupling constant between the sample and the platform for four samples of $Y_2Mo_3O_{12}$ (Δ , 4.95 mg; \square , 13.94 mg; \circ , 11.94 mg low-temperature sample; \diamond , 11.94 mg high-temperature sample).

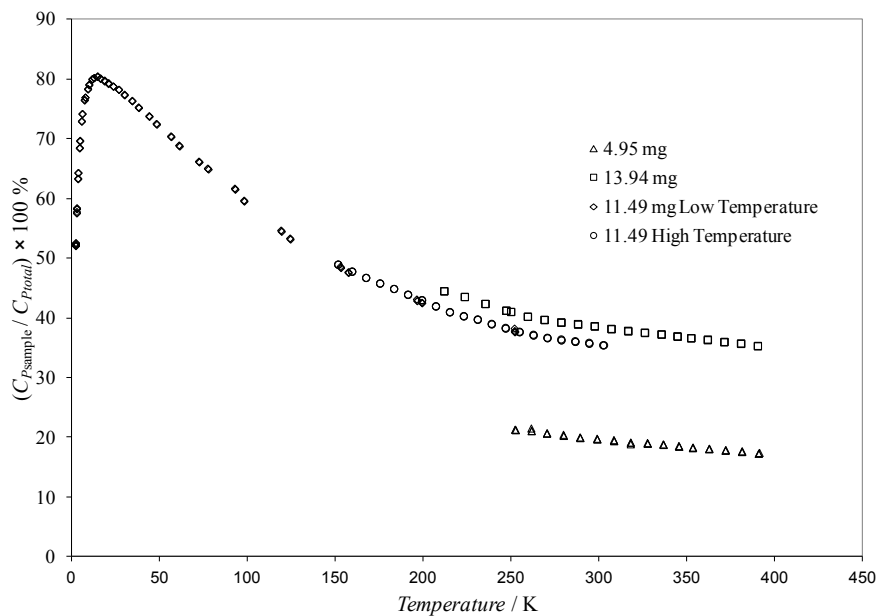


Figure A1.2: The sample contribution to the total heat capacity ($C_{\text{sample}} / C_{\text{total}} \times 100 \%$) for four samples of $Y_2Mo_3O_{12}$ (Δ , 4.95 mg; \square , 13.94 mg; \circ , 11.94 mg low-temperature sample; \diamond , 11.94 mg high-temperature sample).

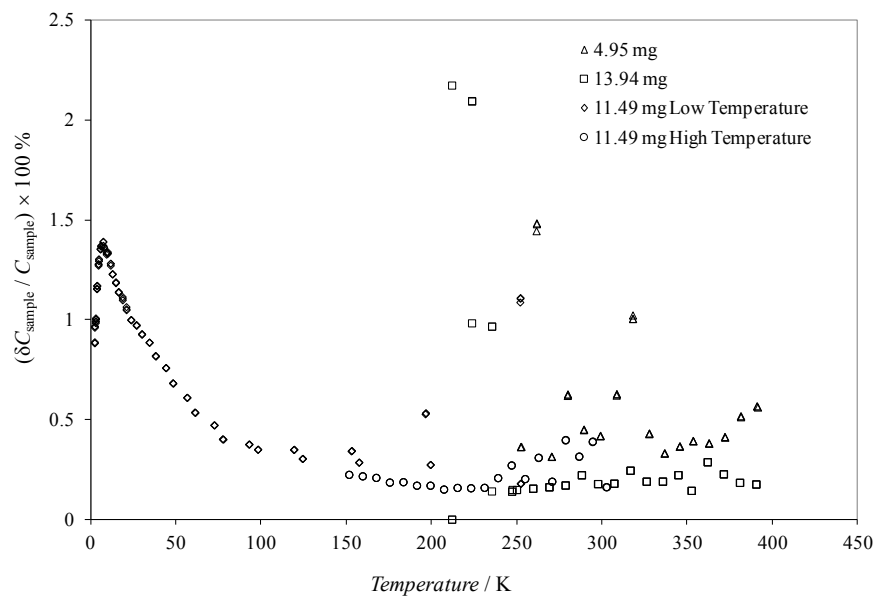


Figure A1.3: The reproducibility ($\delta C_{\text{sample}} / C_{\text{sample}} \times 100 \%$) for four samples of $\text{Y}_2\text{Mo}_3\text{O}_{12}$ (Δ , 4.95 mg; \square , 13.94 mg; \circ , 11.94 mg low-temperature sample; \diamond , 11.94 mg high-temperature sample).

A2 HfMgMo₃O₁₂

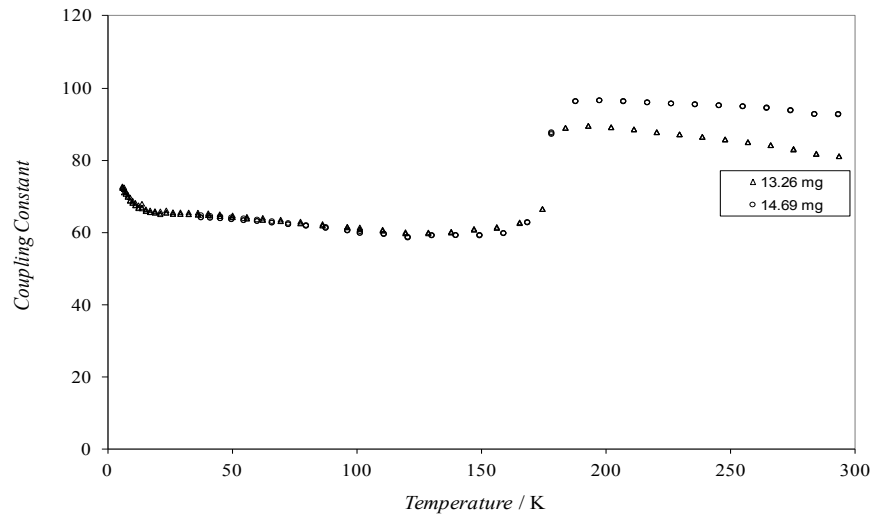


Figure A2.1: The coupling constant between the sample and the platform for two samples of HfMgMo₃O₁₂ (Δ , 13.26 mg; \circ , 14.69 mg).

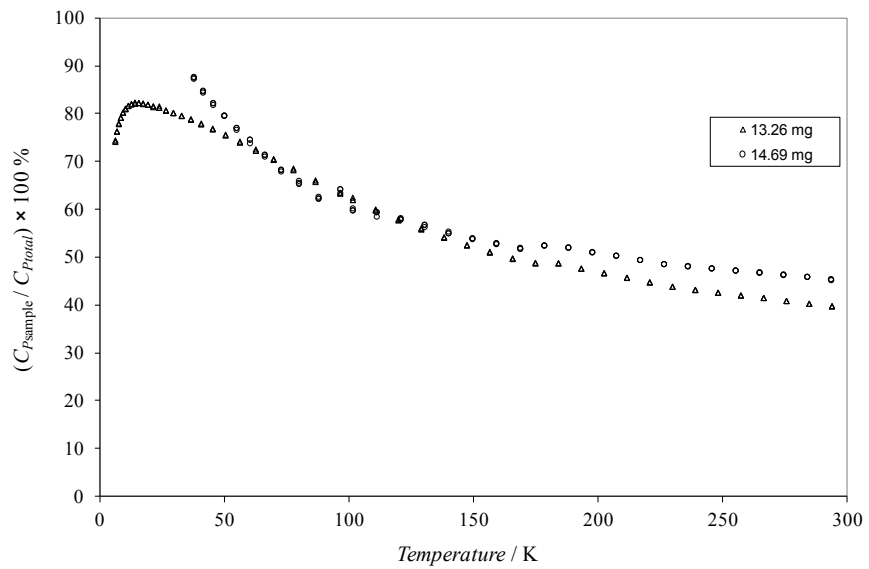


Figure A2.2: The sample contribution to the total heat capacity ($C_{\text{sample}} / C_{\text{total}} \times 100 \%$) for two samples of HfMgMo₃O₁₂ (Δ , 13.26 mg; \circ , 14.69 mg).

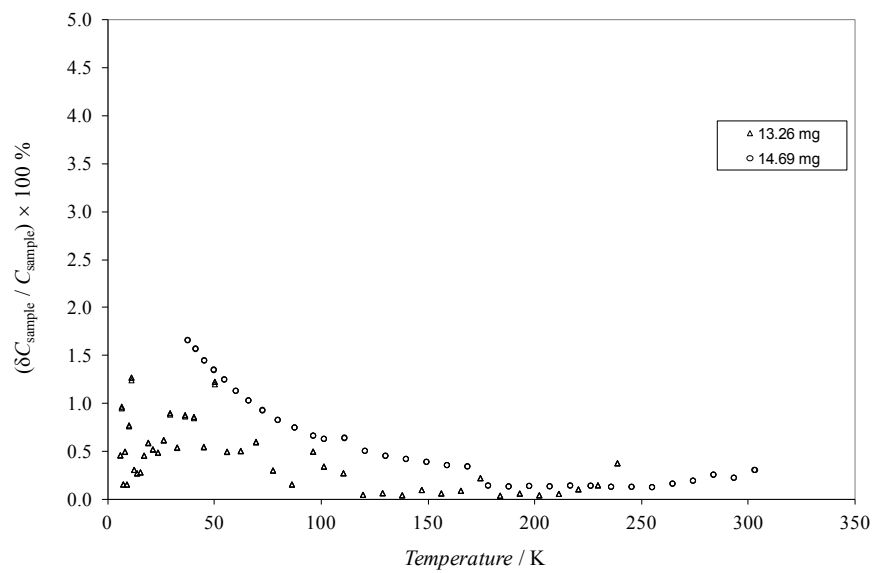


Figure A2.3: The reproducibility $(\delta C_{\text{sample}} / C_{\text{sample}} \times 100 \%)$ for two samples of $\text{HfMgMo}_3\text{O}_{12}$ (Δ , 13.26 mg; \circ , 14.69 mg).

A3 $\text{In}_2\text{Mo}_3\text{O}_{12}$

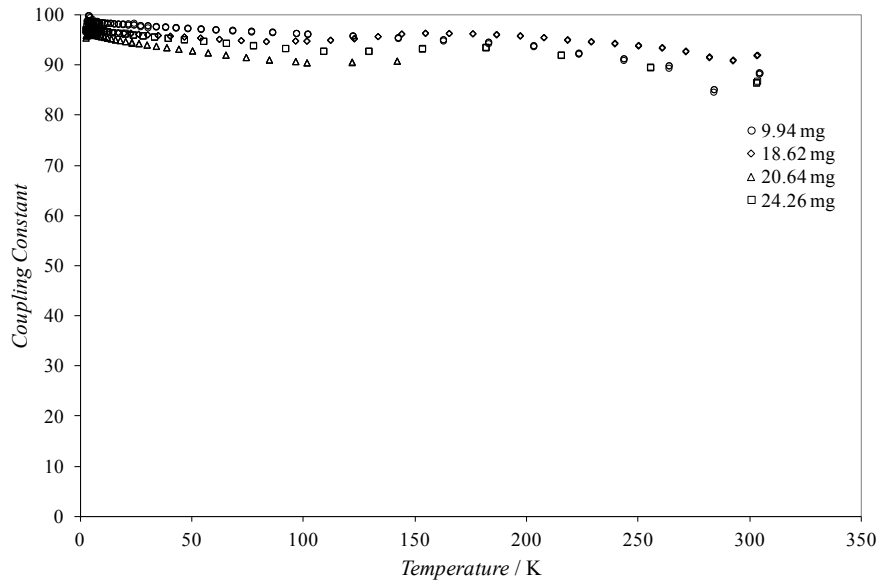


Figure A3.1: The coupling constant between the sample and the platform for four samples of $\text{In}_2\text{Mo}_3\text{O}_{12}$ (\circ , 9.94 mg; \diamond , 18.62 mg; Δ , 20.64 mg; \square , 24.26 mg).

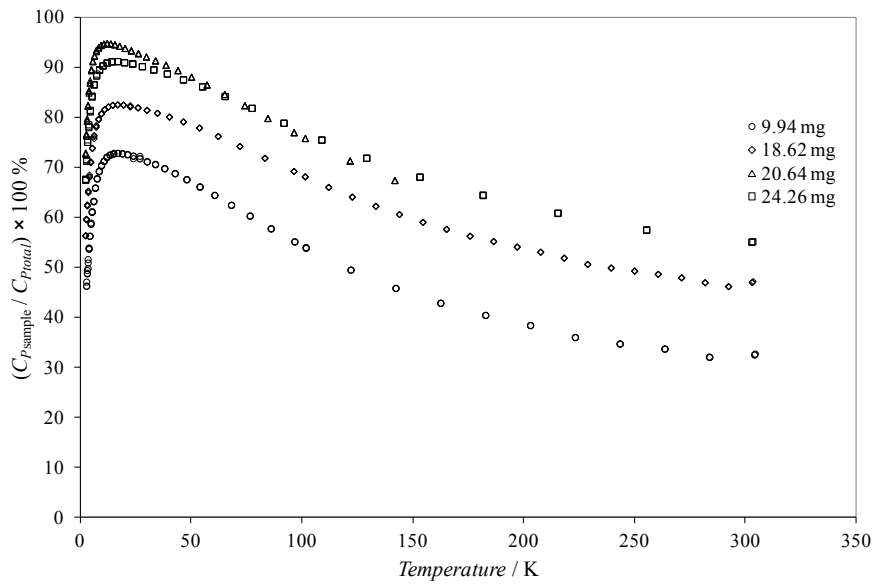


Figure A3.2: The sample contribution to the total heat capacity ($C_{\text{sample}} / C_{\text{total}} \times 100 \%$) for four samples of $\text{In}_2\text{Mo}_3\text{O}_{12}$ (\circ , 9.94 mg; \diamond , 18.62 mg; Δ , 20.64 mg; \square , 24.26 mg).

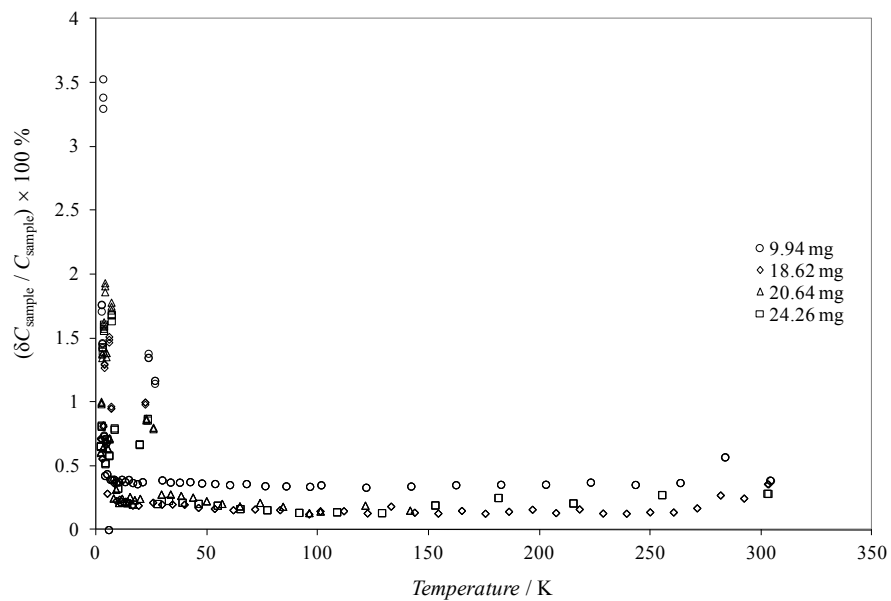


Figure A3.3: The reproducibility ($\delta C_{\text{sample}} / C_{\text{sample}} \times 100 \%$) for four samples of $\text{In}_2\text{Mo}_3\text{O}_{12}$ (○, 9.94 mg; ◇, 18.62 mg; △, 20.64 mg; □, 24.26 mg).

A4 $\text{In}(\text{HfMg})_{0.5}\text{Mo}_3\text{O}_{12}$

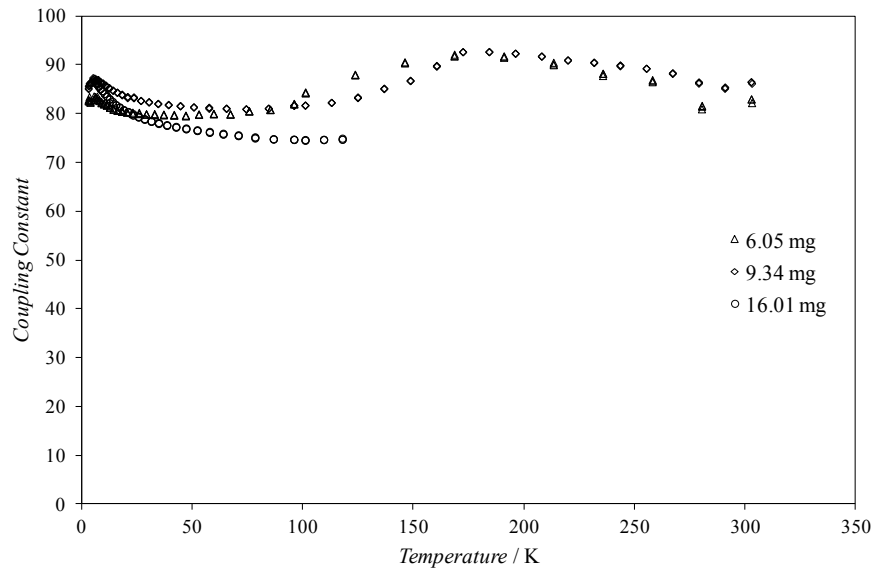


Figure A4.1: The coupling constant between the sample and the platform for three samples of $\text{In}(\text{HfMg})_{0.5}\text{Mo}_3\text{O}_{12}$ (Δ , 6.05 mg; \diamond , 9.34 mg; \circ , 16.01 mg).

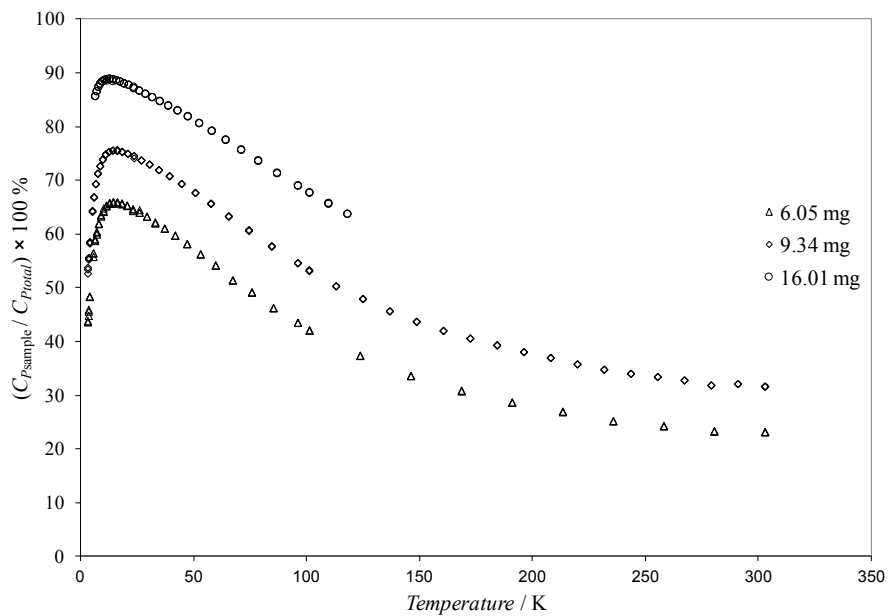


Figure A4.2: The sample contribution to the total heat capacity ($C_{\text{sample}} / C_{\text{total}} \times 100 \%$) for three samples of $\text{In}(\text{HfMg})_{0.5}\text{Mo}_3\text{O}_{12}$ (Δ , 6.05 mg; \diamond , 9.34 mg; \circ , 16.01 mg).

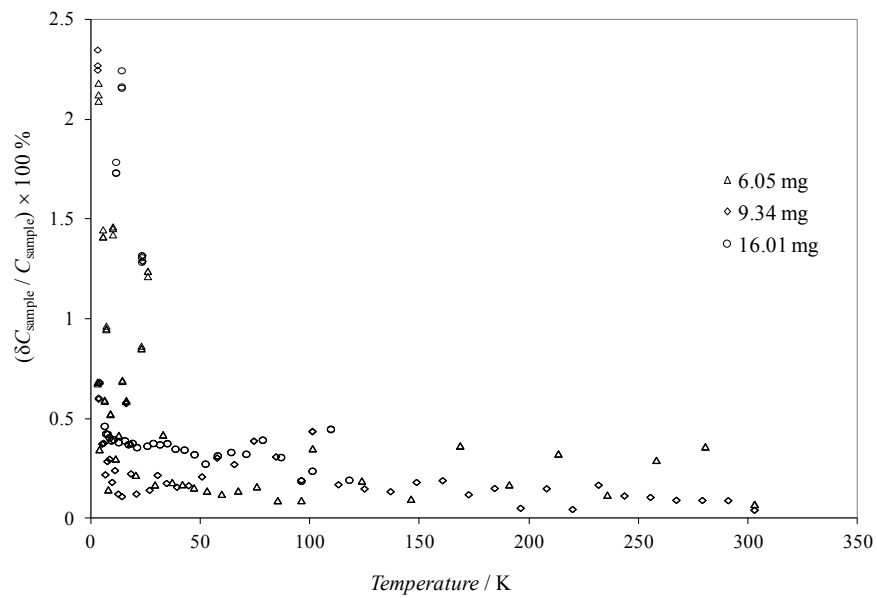


Figure A4.3: The reproducibility ($\delta C_{\text{sample}} / C_{\text{sample}} \times 100 \%$) for three samples of $\text{In}(\text{HfMg})_{0.5}\text{Mo}_3\text{O}_{12}$ (Δ , 6.05 mg; \diamond , 9.34 mg; \circ , 16.01 mg).

A5 $\text{In}_{1.5}(\text{HfMg})_{0.25}\text{Mo}_3\text{O}_{12}$

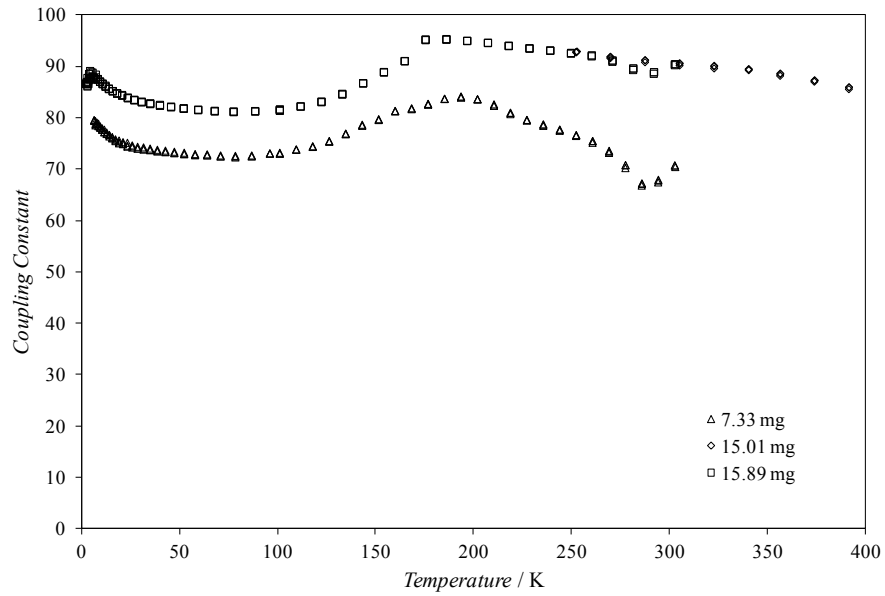


Figure A5.1: The coupling constant between the sample and the platform for three samples of $\text{In}_{1.5}(\text{HfMg})_{0.5}\text{Mo}_3\text{O}_{12}$ (Δ , 7.33 mg; \diamond , 15.01 mg; \square , 15.89 mg).

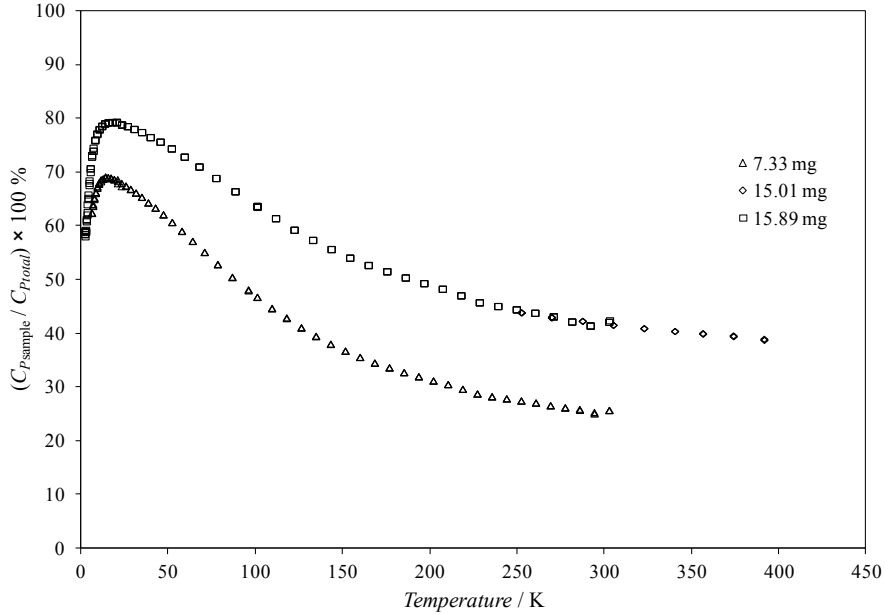


Figure A5.2: The sample contribution to the total heat capacity ($C_{\text{sample}} / C_{\text{total}} \times 100 \%$) for three samples of $\text{In}_{1.5}(\text{HfMg})_{0.5}\text{Mo}_3\text{O}_{12}$ (Δ , 7.33 mg; \diamond , 15.01 mg; \square , 15.89 mg).

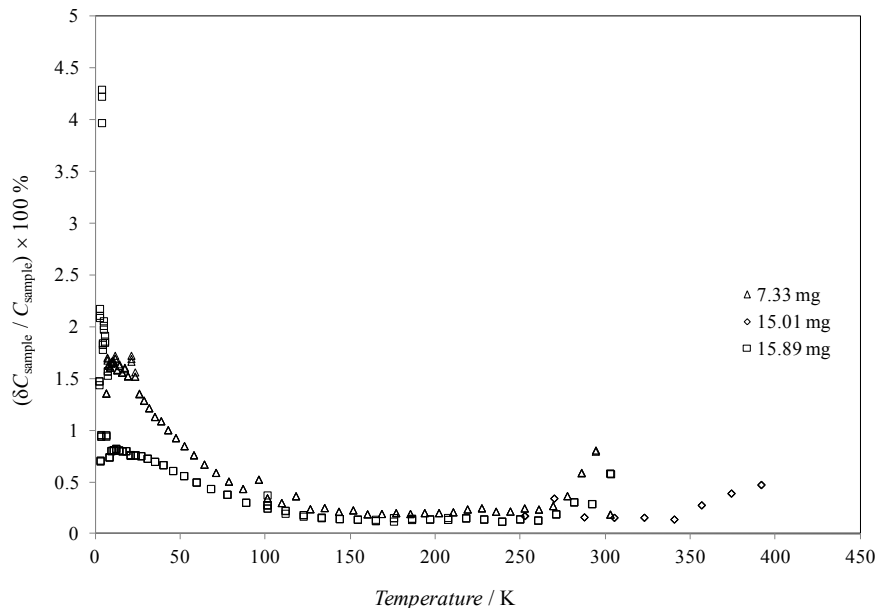


Figure A5.3: The reproducibility ($\delta C_{\text{sample}} / C_{\text{sample}} \times 100 \%$) for three samples of $\text{In}_{1.5}(\text{HfMg})_{0.5}\text{Mo}_3\text{O}_{12}$ (Δ , 7.33 mg; \diamond , 15.01 mg; \square , 15.89 mg).

APPENDIX B - HEAT CAPACITY DATA

B1 Y₂Mo₃O₁₂

Table B1.1: Y₂Mo₃O₁₂ Heat Capacity Data: 4.95 mg sample; in order of data collection.

<i>T</i> / K	<i>C_p</i> / J K ⁻¹ mol ⁻¹	<i>T</i> / K	<i>C_p</i> / J K ⁻¹ mol ⁻¹	<i>T</i> / K	<i>C_p</i> / J K ⁻¹ mol ⁻¹
391.35	323.4	336.51	318.7	299.00	312.8
390.87	320.4	336.72	319.8	299.00	317.5
390.87	320.2	336.71	299.0	308.42	314.7
381.30	320.9	252.62	299.9	308.56	313.7
381.43	323.8	252.27	300.2	308.57	315.0
381.50	320.9	252.22	313.9	318.03	309.6
371.97	319.5	261.43	306.5	318.02	315.1
372.08	321.2	261.60	305.6	318.02	319.8
372.13	322.2	261.61	308.0	327.54	317.7
362.64	319.1	270.47	307.0	327.67	317.2
362.73	321.1	270.32	306.8	327.68	312.8
362.79	321.1	270.32	311.9		
353.34	317.7	279.72	308.7		
353.43	318.2	279.86	308.4		
353.47	320.1	279.86	311.5		
345.38	320.3	289.18	310.1		
345.58	318.6	289.31	309.2		
345.59	318.0	289.32	314.9		
336.51	320.4	298.86	312.8		

Table B1.2: Y₂Mo₃O₁₂ Heat Capacity Data: 13.94 mg sample; in order of data collection.

<i>T</i> / K	<i>C_p</i> / J K ⁻¹ mol ⁻¹	<i>T</i> / K	<i>C_p</i> / J K ⁻¹ mol ⁻¹	<i>T</i> / K	<i>C_p</i> / J K ⁻¹ mol ⁻¹
390.37	326.1	325.95	318.0	268.10	304.0
390.39	325.5	326.13	317.1	259.36	301.4
390.38	325.0	326.12	317.7	259.49	301.1
380.69	325.3	316.45	316.8	259.47	301.0
380.83	325.9	316.63	315.2	249.86	300.2
380.89	324.7	316.61	315.9	249.98	299.8
371.22	322.5	306.94	315.0	247.33	299.3
371.34	323.8	307.10	314.2	247.05	298.7
371.40	323.7	307.09	314.2	247.05	298.5
361.79	321.8	297.42	314.2	235.25	296.2
361.88	323.6	297.59	313.8	235.33	295.9
361.94	322.5	297.58	313.2	235.31	295.9
352.35	320.4	287.90	311.7	223.54	290.9
352.48	321.0	288.07	310.5	223.60	290.7
352.52	320.8	288.05	310.5	223.58	291.1
344.53	320.6	278.39	307.8	211.84	280.3
344.72	319.7	278.54	306.8	211.87	280.1
344.72	319.2	278.52	306.9	211.85	280.3
335.44	319.7	268.88	304.7		
335.64	318.9	269.02	304.2		
335.63	319.1				

Table B1.3: Y₂Mo₃O₁₂ Heat Capacity Data: 11.49 mg sample (high temperature); in order of data collection.

<i>T</i> / K	<i>C_p</i> / J K ⁻¹ mol ⁻¹	<i>T</i> / K	<i>C_p</i> / J K ⁻¹ mol ⁻¹	<i>T</i> / K	<i>C_p</i> / J K ⁻¹ mol ⁻¹
302.82	323.7	254.77	310.3	199.22	284.7
302.38	323.7	246.74	309.7	199.19	284.7
302.37	323.1	246.86	308.2	191.20	280.7
294.31	324.0	246.84	308.4	191.26	280.0
294.46	322.1	238.81	307.3	191.24	280.2
294.45	321.5	238.91	306.4	183.27	275.6
286.38	321.6	238.89	306.1	183.31	275.7
286.53	320.0	230.87	304.3	183.29	275.8
286.51	319.8	230.96	303.4	175.32	269.4
278.44	318.8	230.94	303.5	175.35	269.9
278.59	316.5	222.95	297.6	175.33	269.4
278.57	316.8	223.03	296.7	167.37	262.6
270.52	315.1	223.00	297.0	167.39	262.7
270.65	314.2	215.02	291.4	167.37	262.9
270.63	313.9	215.10	290.8	159.43	255.4
262.58	313.6	215.07	290.6	159.44	255.5
262.72	311.8	207.08	288.2	159.42	256.1
262.70	312.0	207.15	287.5	151.49	248.3
254.67	311.3	207.13	287.6	151.48	248.5
254.79	310.1	199.15	285.2	151.46	248.3

Table B1.4: $\text{Y}_2\text{Mo}_3\text{O}_{12}$ Heat Capacity Data: 11.49 mg sample (low temperature); in order of data collection.

T/K	$C_p/\text{J K}^{-1}\text{ mol}^{-1}$	T/K	$C_p/\text{J K}^{-1}\text{ mol}^{-1}$	T/K	$C_p/\text{J K}^{-1}\text{ mol}^{-1}$
2.21	0.03	118.99	211.5	14.59	14.86
2.21	0.03	119.27	211.2	14.60	14.82
2.22	0.03	119.34	210.6	14.62	14.81
2.82	0.08	152.78	248.2	11.55	8.77
2.82	0.08	153.05	247.2	11.54	8.70
2.82	0.08	153.12	246.7	11.54	8.70
3.60	0.21	196.25	280.8	9.12	4.76
3.60	0.21	196.50	278.6	9.11	4.72
3.60	0.21	196.54	278.0	9.11	4.72
4.61	0.54	251.86	314.7	7.22	2.44
4.61	0.54	251.98	309.3	7.19	2.41
4.62	0.54	252.04	308.3	7.19	2.40
5.92	1.30	252.36	307.8	5.56	1.04
5.92	1.31	252.12	307.0	5.56	1.04
5.93	1.31	252.12	306.7	5.56	1.04
7.60	2.85	199.33	279.1	4.38	0.44
7.61	2.85	199.27	279.7	4.38	0.44
7.61	2.86	199.22	280.0	4.38	0.44
9.78	5.79	157.44	248.6	3.48	0.18
9.80	5.77	157.33	249.2	3.48	0.18
9.80	5.80	157.29	249.7	3.48	0.18
12.64	10.75	124.40	214.5	2.75	0.07
12.64	10.74	124.17	215.0	2.75	0.07
12.64	10.74	124.12	215.3	2.75	0.07
16.24	18.14	98.10	179.8	2.19	0.03
16.23	18.19	98.02	180.2	2.19	0.03
16.23	18.20	97.94	180.5	2.19	0.03
20.78	28.46	77.76	146.6		
20.82	28.75	77.34	145.9		
20.83	28.88	77.28	146.1		
26.68	42.82	61.33	115.1		
26.74	42.90	61.02	114.7		
26.75	43.00	60.97	114.8		
34.25	60.39	48.34	89.67		
34.34	60.44	48.11	89.41		
34.35	60.36	48.09	89.42		
43.92	81.49	38.10	68.15		
44.06	81.58	37.93	67.86		
44.08	81.45	37.90	67.98		
56.33	107.1	30.00	50.12		
56.52	107.2	29.89	49.98		
56.54	107.1	29.88	50.16		
72.22	137.4	23.62	35.19		
72.47	137.6	23.56	35.13		
72.51	137.5	23.54	35.09		
92.66	175.3	18.59	23.51		
92.92	175.3	18.58	23.68		
92.98	175.1	18.54	23.33		

B2 HfMgMo₃O₁₂

Table B2.1: HfMgMo₃O₁₂ Heat Capacity Data: 13.26 mg sample; in order of data collection.

T / K	$C_p / \text{J K}^{-1} \text{mol}^{-1}$	T / K	$C_p / \text{J K}^{-1} \text{mol}^{-1}$	T / K	$C_p / \text{J K}^{-1} \text{mol}^{-1}$
302.97	294.4	156.00	212.2	32.27	37.53
302.62	292.7	146.85	204.8	32.27	37.56
302.62	292.3	146.86	204.4	28.95	31.65
293.38	290.2	146.84	204.2	28.94	31.55
293.47	291.0	137.68	196.6	28.94	31.48
293.46	290.9	137.69	196.1	25.96	26.24
284.25	289.5	137.68	195.4	25.95	26.11
284.32	288.9	128.51	188.3	25.95	26.09
284.30	289.0	128.52	186.1	23.27	22.05
275.11	286.1	128.50	187.1	23.27	21.57
275.18	285.9	119.33	177.9	23.27	21.57
275.16	285.8	119.34	176.1	20.88	17.51
265.96	283.0	119.32	176.7	20.87	17.25
266.02	282.9	110.16	166.6	20.87	17.46
266.00	282.9	110.17	165.4	18.72	14.07
256.81	279.7	110.15	165.0	18.72	14.05
256.87	279.7	100.99	155.9	18.71	14.07
256.85	280.0	101.02	152.6	16.79	11.09
247.66	276.6	101.00	152.7	16.78	11.17
247.71	276.5	95.97	146.2	16.78	11.19
247.70	276.5	95.95	146.5	15.06	8.77
238.51	272.0	95.95	145.0	15.05	8.78
238.55	273.2	86.02	132.4	15.05	8.80
238.54	272.9	86.03	130.2	13.51	6.78
229.37	268.8	86.01	130.8	13.50	6.73
229.41	269.3	77.16	119.0	13.50	6.86
229.39	269.2	77.16	117.5	12.11	5.16
220.22	265.3	77.15	116.9	12.10	5.20
220.26	265.0	69.21	104.0	12.10	5.16
220.24	265.0	69.20	103.1	10.86	3.86
211.07	260.1	69.20	102.9	10.86	3.87
211.10	260.2	62.04	92.54	10.86	3.88
211.08	259.7	62.04	91.14	9.73	2.82
201.90	255.4	62.04	91.08	9.73	2.84
201.94	255.5	55.65	80.99	9.72	2.84
201.92	255.4	55.64	80.09	8.73	2.06
192.74	250.6	55.64	80.16	8.73	2.07
192.77	250.3	49.91	70.29	8.73	2.06
192.75	250.6	49.90	69.69	7.83	1.46
183.57	245.7	49.90	69.69	7.82	1.46
183.60	245.7	44.75	60.85	7.82	1.46
183.58	245.7	44.75	60.33	7.02	1.01
174.29	229.7	44.74	60.28	7.01	1.02
174.38	228.4	40.13	52.40	7.01	1.02
174.35	229.0	40.13	51.89	6.30	0.71
165.17	220.5	40.12	51.83	6.29	0.70
165.20	219.1	35.99	44.64	6.29	0.70
165.17	219.3	35.98	44.36	5.65	0.47
156.00	213.5	35.98	44.25	5.64	0.46
156.02	211.9	32.28	37.72	5.64	0.46

Table B2.2: HfMgMo₃O₁₂ Heat Capacity Data: 14.69 mg sample; in order of data collection.

T/K	$C_p/J\ K^{-1}\ mol^{-1}$	T/K	$C_p/J\ K^{-1}\ mol^{-1}$	T/K	$C_p/J\ K^{-1}\ mol^{-1}$
303.04	305.1	149.01	202.7	33.77	38.29
302.68	304.3	139.42	193.6	33.77	38.41
302.70	303.2	139.41	193.3	30.72	33.04
292.99	299.7	139.40	194.6	30.71	32.99
293.10	298.6	129.82	184.4	30.71	32.97
293.08	299.2	129.80	185.8	27.94	28.14
283.42	297.7	129.80	185.1	27.94	27.96
283.50	297.4	120.19	175.4	27.93	28.09
283.49	297.3	120.19	175.2	25.41	23.65
273.85	292.3	120.18	175.2	25.40	23.70
273.92	293.2	110.60	162.1	25.40	23.69
273.91	292.7	110.57	163.8	23.10	20.40
264.26	287.6	110.57	164.0	23.11	19.86
264.34	288.0	101.00	149.8	23.10	19.86
264.31	288.6	100.98	149.3	21.02	16.45
254.68	284.0	100.97	150.1		
254.74	283.7	95.96	142.9		
254.72	284.0	95.94	142.8		
245.09	279.2	95.93	142.9		
245.14	279.6	87.24	129.7		
245.12	279.6	87.22	129.6		
235.50	274.5	87.22	129.6		
235.55	274.3	79.35	118.1		
235.53	274.7	79.34	118.0		
225.92	268.8	79.33	117.6		
225.96	269.3	72.18	106.4		
225.95	269.4	72.17	106.2		
216.34	264.3	72.17	105.6		
216.37	264.4	65.63	94.52		
216.35	264.3	65.62	94.36		
206.74	258.4	65.61	94.42		
206.77	258.4	59.69	85.00		
206.75	258.4	59.67	84.92		
197.13	251.9	59.67	84.92		
197.16	252.3	54.29	75.52		
197.14	252.5	54.28	75.29		
187.53	246.9	54.28	75.32		
187.55	247.0	49.37	66.71		
187.53	247.3	49.36	66.39		
177.87	238.9	49.36	66.35		
177.90	238.8	44.90	58.45		
177.88	238.6	44.90	58.35		
168.16	220.7	44.89	58.29		
168.24	219.4	40.83	51.20		
168.22	219.3	40.83	50.98		
158.61	211.3	40.83	51.02		
158.63	211.2	37.14	44.61		
158.62	210.3	37.13	44.49		
149.02	202.6	37.13	44.50		
149.02	202.6	33.78	38.50		

B3 In₂Mo₃O₁₂Table B3.1: In₂Mo₃O₁₂ Heat Capacity Data: 9.94 mg sample (low temperature); in order of data collection.

<i>T</i> / K	<i>C_p</i> / J K ⁻¹ mol ⁻¹	<i>T</i> / K	<i>C_p</i> / J K ⁻¹ mol ⁻¹	<i>T</i> / K	<i>C_p</i> / J K ⁻¹ mol ⁻¹
304.28	317.5	67.89	112.7	11.71	6.29
303.94	315.9	60.38	99.95	11.72	6.30
303.95	315.1	60.38	99.86	10.41	4.65
283.53	306.5	60.38	99.83	10.42	4.65
283.72	305.3	53.71	87.21	10.42	4.65
283.68	305.3	53.72	87.04	9.26	3.42
263.43	297.9	53.72	87.01	9.26	3.40
263.53	297.6	47.77	75.47	9.26	3.40
263.49	297.9	47.78	75.27	8.23	2.44
243.21	288.3	47.78	75.26	8.23	2.43
243.30	288.3	42.49	64.94	8.24	2.43
243.27	288.4	42.50	64.80	7.32	1.70
223.03	276.8	42.50	64.79	7.32	1.69
223.10	277.1	37.80	55.49	7.32	1.70
223.06	277.4	37.80	55.41	6.52	1.18
202.83	266.1	37.81	55.34	6.51	1.17
202.87	266.4	33.62	47.02	6.51	1.18
202.83	266.4	33.63	46.88	5.78	0.77
182.59	253.2	33.63	46.87	5.78	0.77
182.62	253.7	29.88	39.32	5.78	0.77
182.58	253.5	29.90	39.40	5.02	0.47
162.36	237.5	29.91	39.35	5.02	0.47
162.37	237.6	26.58	33.34	5.03	0.48
162.33	237.4	26.60	32.66	4.52	0.32
142.12	218.1	26.61	32.69	4.52	0.32
142.11	218.5	23.66	26.24	4.53	0.32
142.08	218.4	23.66	26.89	4.05	0.21
121.84	196.2	23.67	26.84	4.05	0.21
121.82	195.9	21.04	21.86	4.05	0.21
121.80	196.0	21.05	21.84	3.63	0.14
101.59	168.1	21.05	21.83	3.63	0.14
101.55	169.2	18.72	17.49	3.63	0.14
101.54	169.2	18.71	17.51	3.22	0.09
96.49	160.6	18.72	17.49	3.22	0.09
96.48	160.8	16.64	13.85	3.22	0.09
96.48	160.8	16.64	13.84	2.86	0.06
85.81	144.0	16.65	13.85	2.86	0.06
85.79	143.8	14.80	10.87	2.86	0.06
85.78	144.2	14.81	10.82	2.54	0.04
76.33	129.0	14.81	10.81	2.55	0.04
76.33	128.9	13.17	8.32	2.54	0.04
76.32	128.7	13.17	8.31		
67.89	112.9	13.18	8.28		
67.89	112.7	11.71	6.32		

Table B3.2: In₂Mo₃O₁₂ Heat Capacity Data: 18.62 mg sample (low temperature); in order of data collection.

T / K	$C_p / \text{J K}^{-1} \text{mol}^{-1}$	T / K	$C_p / \text{J K}^{-1} \text{mol}^{-1}$	T / K	$C_p / \text{J K}^{-1} \text{mol}^{-1}$
303.28	318.2	133.06	205.8	16.59	13.13
302.84	308.2	133.06	206.3	16.58	13.10
302.85	308.1	133.05	206.1	16.58	13.10
292.12	303.2	122.41	194.3	14.32	9.57
292.25	302.4	122.43	193.8	14.32	9.54
292.24	302.6	122.41	194.3	14.32	9.54
281.56	300.5	111.77	180.6	12.37	6.79
281.66	300.0	111.78	180.2	12.37	6.78
281.64	300.0	111.77	180.5	12.37	6.77
270.98	296.5	101.16	165.4	10.70	4.68
271.07	296.5	101.16	165.6	10.68	4.67
271.05	296.6	101.15	165.8	10.69	4.67
260.38	292.2	96.09	157.6	9.23	3.14
260.47	292.1	96.11	157.6	9.23	3.13
260.44	292.3	96.11	157.6	9.23	3.13
249.78	288.0	83.00	137.5	7.97	2.04
249.86	288.0	82.99	137.4	7.96	2.05
249.84	287.8	82.99	137.4	7.97	2.03
239.18	282.9	71.72	118.2	6.88	1.29
239.26	282.8	71.72	118.1	6.87	1.30
239.23	282.5	71.72	118.0	6.88	1.27
228.59	277.8	61.94	100.8	5.94	0.78
228.66	277.6	61.92	100.7	5.94	0.77
228.64	277.6	61.92	100.6	5.93	0.76
218.00	272.2	53.52	85.04	5.13	0.46
218.06	272.4	53.50	84.98	5.12	0.46
218.03	272.5	53.50	84.95	5.13	0.46
207.40	266.0	46.22	70.70	4.43	0.26
207.44	266.3	46.21	70.57	4.43	0.26
207.42	266.2	46.21	70.59	4.43	0.26
196.79	259.4	39.92	58.25	3.83	0.15
196.83	259.3	39.92	58.15	3.82	0.15
196.79	260.1	39.92	58.10	3.82	0.15
186.19	253.0	34.49	47.41	3.30	0.09
186.21	253.2	34.48	47.33	3.30	0.09
186.19	253.4	34.48	47.30	3.30	0.08
175.56	244.6	29.79	38.07	2.86	0.05
175.58	244.8	29.78	37.98	2.85	0.05
175.55	244.9	29.79	37.99	2.85	0.05
164.94	236.4	25.73	30.01	2.47	0.03
164.95	237.1	25.73	29.93	2.47	0.03
164.94	236.6	25.73	29.90	2.47	0.03
154.31	227.5	22.22	23.38	2.13	0.02
154.32	227.2	22.22	22.95	2.12	0.02
154.30	227.7	22.22	23.02	2.12	0.02
143.69	217.2	19.20	17.64		
143.69	217.5	19.19	17.59		
143.68	217.3	19.19	17.60		

Table B3.3: In₂Mo₃O₁₂ Heat Capacity Data: 20.64 mg sample (low temperature); in order of data collection.

T / K	$C_p / \text{J K}^{-1} \text{mol}^{-1}$	T / K	$C_p / \text{J K}^{-1} \text{mol}^{-1}$	T / K	$C_p / \text{J K}^{-1} \text{mol}^{-1}$
303.32	286.9	49.90	76.86	6.11	0.82
302.91	285.3	49.89	76.63	6.10	0.82
302.92	285.6	49.89	76.67	6.11	0.81
282.70	282.9	43.76	64.96	5.36	0.51
282.80	283.1	43.76	64.80	5.35	0.51
282.80	283.1	43.76	64.78	5.36	0.52
262.59	278.4	38.38	54.41	4.70	0.32
262.65	279.2	38.38	54.24	4.69	0.31
262.64	278.8	38.38	54.21	4.69	0.31
242.47	272.8	33.66	45.09	4.12	0.18
242.51	273.2	33.66	44.95	4.11	0.18
242.49	273.2	33.66	44.94	4.11	0.19
222.34	265.7	29.51	36.86	3.60	0.11
222.36	266.7	29.52	36.70	3.61	0.11
222.34	266.4	29.52	36.68	3.61	0.12
202.20	255.8	25.88	30.05	3.17	0.07
202.19	255.9	25.88	29.72	3.16	0.07
202.17	256.7	25.89	29.59	3.16	0.07
182.02	244.0	22.70	23.78	2.78	0.04
182.00	244.8	22.70	23.74	2.77	0.04
181.99	244.8	22.71	23.40	2.77	0.04
161.84	229.4	19.91	18.44	2.43	0.03
161.81	229.8	19.90	18.41	2.43	0.03
161.80	230.4	19.91	18.42	2.43	0.03
141.66	211.5	17.46	14.25	2.14	0.02
141.62	211.5	17.46	14.20	2.13	0.02
141.61	211.8	17.46	14.22	2.13	0.02
121.46	190.0	15.32	10.77		
121.42	190.8	15.31	10.73		
121.42	190.4	15.31	10.75		
101.22	163.4	13.44	7.98		
101.22	163.3	13.43	7.96		
101.21	163.1	13.43	7.97		
96.15	155.7	11.79	5.82		
96.17	155.6	11.78	5.80		
96.16	155.9	11.78	5.79		
84.33	137.5	10.34	4.12		
84.34	137.6	10.34	4.11		
84.34	137.2	10.34	4.11		
73.96	120.7	9.07	2.86		
73.96	120.6	9.06	2.87		
73.96	120.2	9.06	2.85		
64.86	104.6	7.95	1.92		
64.86	104.4	7.94	1.92		
64.86	104.4	7.94	1.93		
56.88	90.25	6.96	1.26		
56.88	90.06	6.95	1.28		
56.88	90.00	6.96	1.30		

Table B3.4: In₂Mo₃O₁₂ Heat Capacity Data: 24.26 mg sample (low temperature); in order of data collection.

T/K	$C_p/J\ K^{-1}\ mol^{-1}$	T/K	$C_p/J\ K^{-1}\ mol^{-1}$	T/K	$C_p/J\ K^{-1}\ mol^{-1}$
303.16	301.2	54.86	88.01	9.94	3.87
302.70	299.9	54.84	87.84	9.93	3.85
302.71	299.5	54.84	87.88	9.93	3.84
255.16	285.4	46.24	70.98	8.37	2.40
255.25	286.5	46.23	70.91	8.37	2.40
255.22	286.9	46.23	70.85	8.37	2.37
215.19	268.0	38.97	56.67	7.05	1.43
215.21	268.6	38.96	56.53	7.04	1.39
215.18	269.1	38.97	56.53	7.05	1.39
181.47	248.0	32.85	44.40	5.94	0.78
181.43	248.7	32.85	44.23	5.94	0.78
181.39	249.3	32.85	44.24	5.94	0.78
152.99	225.3	27.70	34.04	5.00	0.42
152.93	225.8	27.69	33.96	5.00	0.42
152.91	226.2	27.69	33.99	5.00	0.43
128.95	201.6	23.34	25.80	4.21	0.22
128.90	201.8	23.34	25.44	4.21	0.21
128.89	202.0	23.34	25.39	4.21	0.22
108.68	176.1	19.68	18.39	3.56	0.12
108.65	176.5	19.66	18.56	3.55	0.11
108.64	176.6	19.67	18.56	3.55	0.11
91.60	150.3	16.58	13.22	2.99	0.06
91.58	150.0	16.58	13.19	2.99	0.06
91.58	150.2	16.58	13.18	2.99	0.06
77.21	128.8	13.98	9.09	2.53	0.03
77.19	128.5	13.97	9.06	2.52	0.03
77.19	128.5	13.97	9.05	2.52	0.03
65.07	106.4	11.78	6.06	2.13	0.02
65.06	106.2	11.78	6.04	2.12	0.02
65.06	106.2	11.78	6.04	2.12	0.02

B4 In(HfMg)_{0.5}Mo₃O₁₂Table B4.1: In(HfMg)_{0.5}Mo₃O₁₂ Heat Capacity Data: 16.10 mg sample; in order of data collection.

T / K	$C_p / \text{J K}^{-1} \text{mol}^{-1}$	T / K	$C_p / \text{J K}^{-1} \text{mol}^{-1}$	T / K	$C_p / \text{J K}^{-1} \text{mol}^{-1}$
117.86	180.1	34.82	45.95	8.41	2.16
117.87	179.7	31.46	39.73	8.41	2.16
117.86	179.8	31.46	39.54	7.61	1.57
109.46	170.5	31.46	39.60	7.60	1.58
109.47	169.0	28.44	33.82	7.60	1.58
109.45	169.9	28.42	33.81	6.87	1.13
101.07	158.9	28.43	33.69	6.86	1.13
101.07	158.1	25.69	28.62	6.86	1.12
101.05	158.3	25.68	28.52	6.21	0.80
95.92	150.9	25.68	28.53	6.20	0.80
96.02	150.7	23.21	24.33	6.20	0.80
96.01	150.6	23.21	23.72		
86.73	137.4	23.20	23.91		
86.73	136.6	20.98	20.03		
86.72	136.9	20.97	19.97		
78.38	124.9	20.97	20.05		
78.37	125.1	18.96	16.30		
78.37	124.2	18.95	16.21		
70.83	112.2	18.94	16.26		
70.83	111.6	17.12	13.25		
70.82	111.5	17.11	13.24		
63.98	100.3	17.11	13.25		
63.97	99.67	15.48	10.67		
63.97	99.75	15.47	10.65		
57.82	89.67	15.47	10.63		
57.81	89.24	13.98	8.48		
57.81	89.14	13.98	8.15		
52.24	79.34	13.97	8.45		
52.24	79.01	12.62	6.63		
52.23	78.96	12.62	6.64		
47.20	69.90	12.62	6.62		
47.20	69.56	11.42	5.13		
47.20	69.47	11.41	5.14		
42.65	61.27	11.42	4.98		
42.64	61.07	10.30	3.88		
42.64	60.99	10.30	3.88		
38.54	53.36	10.30	3.90		
38.53	53.17	9.32	2.93		
38.53	53.09	9.31	2.92		
34.82	46.27	9.31	2.93		
34.82	46.05	8.41	2.17		

Table B4.2: In(HfMg)_{0.5}Mo₃O₁₂ Heat Capacity Data: 6.05 mg sample; in order of data collection.

T/K	$C_p/J K^{-1} mol^{-1}$	T/K	$C_p/J K^{-1} mol^{-1}$	T/K	$C_p/J K^{-1} mol^{-1}$
95.99	153.6	20.41	19.45	3.02	0.07
96.00	153.8	18.13	15.30	3.02	0.07
96.00	153.5	18.12	15.41	303.00	310.1
85.22	137.0	18.12	15.40	302.78	309.7
85.20	137.2	16.10	11.92	302.77	310.2
85.20	137.2	16.08	12.04	280.34	298.5
75.68	122.5	16.09	12.04	280.43	300.3
75.66	122.1	14.29	9.21	280.39	300.4
75.66	122.5	14.28	9.30	258.04	288.0
67.18	106.3	14.28	9.26	258.08	289.7
67.17	106.0	12.68	6.96	258.04	289.3
67.16	106.1	12.67	7.02	235.66	278.1
59.64	94.33	12.67	6.99	235.69	277.7
59.62	94.50	11.25	5.17	235.64	278.3
59.62	94.32	11.24	5.17	213.33	266.6
52.95	81.93	11.24	5.20	213.33	265.7
52.93	81.93	9.99	3.72	213.27	267.4
52.93	81.94	9.98	3.83	190.92	252.2
47.00	70.70	9.98	3.74	190.90	252.4
46.99	70.71	8.86	2.68	190.85	253.0
46.99	70.69	8.85	2.71	168.52	235.1
41.72	60.55	8.85	2.70	168.48	236.7
41.71	60.59	7.87	1.88	168.45	235.4
41.71	60.51	7.86	1.88	146.11	215.1
37.04	51.44	7.86	1.88	146.06	215.3
37.03	51.49	6.98	1.26	146.02	215.5
37.03	51.47	6.97	1.28	123.64	191.9
32.89	43.03	6.97	1.28	123.60	191.2
32.87	43.38	6.20	0.87	123.57	191.4
32.87	43.31	6.19	0.88	101.17	161.8
29.20	36.34	6.19	0.88	101.15	160.9
29.18	36.25	5.50	0.57	101.12	160.8
29.18	36.28	5.49	0.58		
25.91	30.35	5.49	0.58		
25.91	29.69	3.84	0.15		
25.90	29.73	3.84	0.15		
23.01	24.06	3.84	0.15		
23.00	23.74	3.41	0.10		
23.00	24.12	3.41	0.10		
20.43	19.39	3.41	0.10		
20.42	19.47	3.03	0.07		

Table B4.3: In(HfMg)_{0.5}Mo₃O₁₂ Heat Capacity Data: 9.34 mg sample; in order of data collection.

T/K	$C_p/J\ K^{-1}\ mol^{-1}$	T/K	$C_p/J\ K^{-1}\ mol^{-1}$	T/K	$C_p/J\ K^{-1}\ mol^{-1}$
303.01	304.9	124.79	192.6	18.19	15.11
302.70	304.7	112.92	176.9	18.19	15.10
302.71	304.6	112.92	176.5	16.02	11.51
290.77	307.6	112.91	176.5	16.01	11.62
290.86	307.9	101.05	161.3	16.01	11.50
290.85	307.7	101.06	160.0	14.10	8.68
278.98	294.2	101.04	160.4	14.09	8.69
279.03	294.6	95.96	152.4	14.09	8.67
279.01	294.5	95.99	153.0	12.41	6.39
267.14	291.3	95.99	152.7	12.40	6.38
267.19	291.8	84.44	136.2	12.40	6.37
267.16	291.5	84.44	135.8	10.92	4.58
255.30	286.5	84.44	135.4	10.91	4.60
255.34	287.1	74.33	119.9	10.91	4.60
255.32	286.9	74.33	119.5	9.60	3.19
243.44	281.0	74.33	119.0	9.59	3.20
243.48	281.6	65.39	103.3	9.59	3.20
243.46	281.6	65.39	102.9	8.46	2.21
231.61	276.0	65.38	102.8	8.45	2.20
231.64	276.6	57.54	90.03	8.45	2.20
231.62	276.9	57.54	89.56	7.44	1.47
219.78	270.0	57.53	89.55	7.43	1.48
219.80	269.8	50.64	76.96	7.43	1.48
219.77	270.0	50.63	76.69	6.55	0.98
207.93	262.9	50.63	76.68	6.54	0.98
207.94	263.7	44.56	65.28	6.54	0.98
207.92	263.1	44.55	65.14	5.76	0.61
196.07	256.1	44.55	65.06	5.75	0.61
196.08	256.3	39.21	55.00	5.75	0.61
196.06	256.0	39.20	54.91	5.07	0.39
184.22	248.5	39.20	54.74	5.06	0.39
184.22	249.2	34.51	45.81	5.06	0.39
184.20	249.1	34.49	45.76	3.92	0.14
172.34	239.4	34.49	45.71	3.92	0.15
172.35	239.0	30.36	37.94	3.92	0.15
172.32	239.6	30.35	37.78	3.45	0.09
160.47	228.2	30.35	37.86	3.45	0.09
160.47	229.0	26.72	30.71	3.45	0.09
160.44	228.3	26.71	30.69	3.04	0.06
148.59	217.7	26.71	30.69	3.04	0.06
148.59	217.0	23.52	24.19	3.04	0.06
148.56	217.0	23.50	24.76		
136.72	204.8	23.50	24.72		
136.70	204.6	20.70	19.42		
136.69	205.2	20.70	19.44		
124.82	192.1	20.68	19.46		
124.81	192.1	18.21	15.05		

B5 In_{1.5}(HfMg)_{0.25}Mo₃O₁₂Table B5.1: In_{1.5}(HfMg)_{0.25}Mo₃O₁₂ Heat Capacity Data: 7.33 mg sample (low temperature); in order of data collection.

<i>T</i> / K	<i>C_p</i> / J K ⁻¹ mol ⁻¹	<i>T</i> / K	<i>C_p</i> / J K ⁻¹ mol ⁻¹	<i>T</i> / K	<i>C_p</i> / J K ⁻¹ mol ⁻¹
193.48	301.0	86.64	144.2	20.93	21.69
193.52	300.9	78.30	131.3	18.93	17.63
193.50	300.2	78.29	130.8	18.92	17.69
185.09	298.0	78.28	130.9	18.92	17.61
185.11	293.9	70.76	118.1	17.09	14.36
185.09	293.9	70.75	117.8	17.09	14.41
176.68	301.1	70.74	117.9	17.09	14.49
176.70	298.3	63.91	105.7	15.45	11.69
176.68	297.9	63.90	105.5	15.44	11.69
168.28	294.6	63.90	105.7	15.44	11.67
168.29	293.6	57.75	94.76	13.96	9.41
168.27	292.9	57.74	94.48	13.96	9.31
159.87	289.6	57.74	94.64	13.96	9.41
159.87	289.1	52.18	83.91	12.60	7.32
159.86	289.0	52.17	83.82	12.60	7.34
151.46	287.1	52.17	84.01	12.60	7.36
151.46	286.8	47.14	73.93	11.40	5.71
151.44	287.3	47.13	73.90	11.39	5.80
143.05	283.9	47.13	74.01	11.39	5.80
143.04	283.4	42.59	64.77	10.29	4.39
143.03	283.7	42.58	64.98	10.28	4.42
134.64	279.9	42.58	64.88	10.28	4.45
134.63	279.8	38.48	56.56	9.30	3.34
134.62	280.3	38.47	56.56	9.30	3.37
126.22	276.2	38.48	56.60	9.30	3.38
126.21	275.0	34.77	49.09	8.40	2.50
126.20	275.5	34.76	49.15	8.40	2.51
117.79	271.6	34.77	49.17	8.40	2.51
117.80	271.7	31.42	42.28	7.60	1.84
117.78	272.1	31.41	42.29	7.59	1.86
109.38	268.3	31.41	42.21	7.59	1.86
109.38	268.9	28.39	36.11	6.85	1.34
109.37	268.2	28.38	36.25	6.85	1.36
100.98	264.5	28.38	36.24	6.85	1.35
100.98	265.0	25.65	30.67	6.20	0.97
100.97	264.5	25.64	30.53	6.20	0.97
95.88	258.8	25.64	30.67	6.20	0.96
95.93	259.3	23.18	25.03		
95.92	259.2	23.17	25.73		
86.65	255.1	23.17	25.67		
86.64	254.6	20.94	21.35		

Table B5.2: $\text{In}_{1.5}(\text{HfMg})_{0.25}\text{Mo}_3\text{O}_{12}$ Heat Capacity Data: 15.01 mg sample (low temperature); in order of data collection.

T/K	$C_p/\text{J K}^{-1}\text{ mol}^{-1}$	T/K	$C_p/\text{J K}^{-1}\text{ mol}^{-1}$	T/K	$C_p/\text{J K}^{-1}\text{ mol}^{-1}$
252.67	288.4	322.70	309.4	391.48	324.5
252.28	288.3	322.71	310.4	391.56	322.4
252.26	288.7	322.74	309.7	391.57	321.5
269.68	296.9	340.36	313.0		
269.74	295.1	340.36	312.9		
269.76	295.2	340.36	313.2		
287.42	302.5	356.38	318.9		
287.46	301.6	356.45	317.4		
287.47	301.8	356.47	317.3		
305.06	305.8	373.85	323.2		
305.09	305.8	373.97	320.8		
305.10	306.0	373.99	321.2		

Table B5.3: $\text{In}_{1.5}(\text{HfMg})_{0.25}\text{Mo}_3\text{O}_{12}$ Heat Capacity Data: 15.89 mg sample (low temperature); in order of data collection.

T/K	$C_p/\text{J K}^{-1}\text{ mol}^{-1}$	T/K	$C_p/\text{J K}^{-1}\text{ mol}^{-1}$	T/K	$C_p/\text{J K}^{-1}\text{ mol}^{-1}$
303.08	310.2	132.88	204.2	17.91	15.59
302.63	307.3	122.25	192.4	17.90	15.61
302.63	306.9	122.26	192.1	15.68	11.80
291.88	304.8	122.25	191.9	15.67	11.82
292.02	303.8	111.62	179.2	15.67	11.81
292.01	303.0	111.62	179.4	13.73	8.76
281.33	301.1	111.63	179.4	13.72	8.78
281.44	300.7	101.01	165.1	13.72	8.79
281.42	300.7	101.02	163.8	12.02	6.36
270.75	296.2	101.01	164.8	12.01	6.40
270.85	296.4	100.98	165.0	12.01	6.38
270.84	297.3	101.02	164.0	10.53	4.52
260.17	291.7	101.01	165.2	10.52	4.53
260.25	291.8	88.41	145.2	10.51	4.54
260.25	291.7	88.40	145.0	9.22	3.15
249.57	287.8	88.40	145.3	9.21	3.16
249.66	287.1	77.41	128.6	9.21	3.17
249.65	287.7	77.40	128.5	8.07	2.14
238.98	282.5	77.40	128.5	8.06	2.15
239.05	282.4	67.77	110.8	8.06	2.14
239.04	282.7	67.76	110.6	7.06	1.37
228.40	276.9	67.76	110.6	7.06	1.37
228.46	277.3	59.32	96.38	7.05	1.41
228.46	277.3	59.31	96.20	6.18	0.92
217.81	271.5	59.31	96.25	6.17	0.93
217.85	272.3	51.93	82.35	6.18	0.91
217.85	272.2	51.92	82.28	5.41	0.55
207.21	265.8	51.92	82.19	5.40	0.57
207.25	266.0	45.46	69.71	5.40	0.57
207.24	265.9	45.46	69.58	4.73	0.35
196.60	259.6	45.46	69.62	4.73	0.34
196.64	259.5	39.79	58.45	4.73	0.36
196.63	259.4	39.79	58.37	4.14	0.20
186.01	252.5	39.79	58.33	4.14	0.21
186.03	252.5	34.84	48.63	4.14	0.21
186.01	252.6	34.83	48.56	3.63	0.12
175.38	243.9	34.83	48.58	3.62	0.12
175.40	244.4	30.50	39.90	3.62	0.13
175.39	244.7	30.49	39.90	3.17	0.08
164.74	234.6	30.50	39.81	3.17	0.08
164.76	235.2	26.70	32.29	3.17	0.08
164.75	234.7	26.70	32.22	2.78	0.05
154.12	225.1	26.70	32.30	2.77	0.05
154.13	225.2	23.38	25.58	2.77	0.05
154.13	225.1	23.37	25.73	2.43	0.04
143.50	214.9	23.37	25.58	2.43	0.04
143.51	215.1	20.46	20.45	2.43	0.04
143.50	215.2	20.45	20.31	2.12	0.02
132.88	203.8	20.46	20.21	2.12	0.02
132.88	204.0	17.92	15.57	2.12	0.03

APPENDIX C - THERMAL CONDUCTIVITY DATA

C1 HfMgMo₃O₁₂

Table C1.1: HfMgMo₃O₁₂ Thermal Conductivity Data: A1(as described in Chapter 9, Table 9.3); in order of data collection; where κ_m is the bulk thermal conductivity data as determined from the Klemen's model.³³²

T / K	$\kappa / \text{W m}^{-1} \text{K}^{-1}$	$\kappa_m / \text{W m}^{-1} \text{K}^{-1}$	T / K	$\kappa / \text{W m}^{-1} \text{K}^{-1}$	$\kappa_m / \text{W m}^{-1} \text{K}^{-1}$	T / K	$\kappa / \text{W m}^{-1} \text{K}^{-1}$	$\kappa_m / \text{W m}^{-1} \text{K}^{-1}$
304.67	0.54	1.17	234.17	0.52	1.13	167.99	0.50	1.07
302.69	0.54	1.16	232.59	0.52	1.12	166.53	0.50	1.07
300.00	0.54	1.16	231.00	0.52	1.12	165.06	0.50	1.07
297.77	0.54	1.16	229.41	0.52	1.12	163.60	0.49	1.07
295.67	0.54	1.16	227.83	0.52	1.12	162.13	0.49	1.07
293.75	0.54	1.16	226.24	0.52	1.12	160.65	0.49	1.06
291.84	0.54	1.16	224.66	0.52	1.12	159.17	0.49	1.06
290.02	0.54	1.16	223.07	0.52	1.12	157.70	0.49	1.06
288.31	0.54	1.16	221.50	0.52	1.12	156.23	0.49	1.06
286.60	0.54	1.16	219.93	0.52	1.12	154.76	0.49	1.06
284.88	0.54	1.16	218.35	0.52	1.12	153.30	0.49	1.06
283.22	0.54	1.16	216.78	0.52	1.11	151.82	0.49	1.06
281.65	0.54	1.16	215.20	0.51	1.11	150.35	0.49	1.05
280.08	0.54	1.16	213.62	0.51	1.11	148.88	0.49	1.05
278.50	0.54	1.16	212.05	0.51	1.11	147.41	0.49	1.05
276.91	0.54	1.16	210.48	0.51	1.10	145.94	0.49	1.05
275.32	0.54	1.16	208.89	0.51	1.10	144.47	0.49	1.05
273.73	0.54	1.16	207.31	0.51	1.10	143.00	0.48	1.05
272.15	0.53	1.16	205.73	0.51	1.10	141.53	0.48	1.04
270.57	0.53	1.15	204.15	0.51	1.10	140.05	0.48	1.04
268.98	0.53	1.15	202.57	0.51	1.10	138.58	0.48	1.04
267.39	0.53	1.15	200.99	0.51	1.10	137.11	0.48	1.04
265.81	0.53	1.15	199.42	0.51	1.10	135.68	0.48	1.04
264.22	0.53	1.15	197.83	0.51	1.10	134.30	0.48	1.04
262.65	0.53	1.15	196.26	0.51	1.09	132.93	0.48	1.04
261.07	0.53	1.15	194.68	0.51	1.09	131.56	0.48	1.04
259.49	0.53	1.14	193.09	0.51	1.09	130.18	0.48	1.03
257.91	0.53	1.15	191.51	0.50	1.09	128.80	0.48	1.03
256.33	0.53	1.14	189.92	0.50	1.09	127.42	0.48	1.03
254.75	0.53	1.14	188.34	0.50	1.09	126.04	0.48	1.03
253.17	0.53	1.14	186.75	0.50	1.08	124.67	0.48	1.03
251.59	0.53	1.14	185.16	0.50	1.08	123.30	0.48	1.03
250.02	0.53	1.14	183.60	0.50	1.08	121.92	0.48	1.03
248.44	0.53	1.14	182.02	0.50	1.08	120.54	0.47	1.02
246.86	0.53	1.14	180.45	0.50	1.08	119.20	0.47	1.02
245.28	0.53	1.14	178.87	0.50	1.08	117.90	0.47	1.02
243.68	0.53	1.13	177.29	0.50	1.08	116.61	0.47	1.02
242.10	0.53	1.14	175.71	0.50	1.08	115.31	0.47	1.02
240.52	0.52	1.13	174.13	0.50	1.08	114.01	0.47	1.01
238.93	0.52	1.13	172.55	0.50	1.08	112.71	0.47	1.01
237.33	0.52	1.13	170.97	0.50	1.08	111.41	0.47	1.01
235.75	0.52	1.13	169.46	0.50	1.08	110.11	0.47	1.01

Table C1.1 continued: HfMgMo₃O₁₂ Thermal Conductivity Data: A1 (as described in Chapter 9, Table 9.3); in order of data collection; where κ_m is the bulk thermal conductivity data as determined from the Klemen's model.³³²

T / K	$\kappa / \text{W m}^{-1} \text{K}^{-1}$	$\kappa_m / \text{W m}^{-1} \text{K}^{-1}$	T / K	$\kappa / \text{W m}^{-1} \text{K}^{-1}$	$\kappa_m / \text{W m}^{-1} \text{K}^{-1}$	T / K	$\kappa / \text{W m}^{-1} \text{K}^{-1}$	$\kappa_m / \text{W m}^{-1} \text{K}^{-1}$
108.81	0.47	1.01	63.91	0.42	0.91	37.18	0.38	0.82
107.54	0.46	1.00	63.07	0.42	0.90	36.72	0.38	0.82
106.31	0.46	1.00	62.23	0.42	0.90	36.26	0.38	0.82
105.09	0.46	1.00	61.41	0.42	0.90	35.81	0.38	0.82
103.87	0.46	1.00	60.59	0.42	0.90	35.36	0.38	0.83
102.63	0.46	0.99	59.80	0.42	0.90	34.92	0.38	0.81
101.40	0.46	0.99	59.02	0.41	0.89	34.48	0.38	0.82
100.17	0.46	0.98	58.24	0.41	0.89	34.06	0.37	0.81
98.94	0.46	0.98	57.48	0.41	0.89	33.63	0.37	0.81
97.73	0.45	0.98	56.72	0.41	0.89	33.21	0.37	0.81
96.56	0.45	0.98	55.98	0.41	0.89	32.79	0.37	0.80
95.40	0.45	0.98	55.25	0.41	0.89	32.38	0.38	0.81
94.19	0.45	0.98	54.53	0.41	0.88	31.98	0.38	0.82
93.04	0.45	0.97	53.81	0.41	0.88	31.57	0.37	0.80
91.90	0.45	0.97	53.12	0.41	0.88	31.17	0.37	0.80
90.78	0.45	0.97	52.44	0.41	0.88	30.77	0.38	0.82
89.68	0.45	0.97	51.76	0.40	0.87	30.39	0.37	0.80
88.58	0.45	0.97	51.09	0.40	0.87	30.00	0.37	0.80
87.47	0.45	0.96	50.43	0.40	0.87	29.62	0.37	0.80
86.38	0.44	0.96	49.78	0.40	0.87	29.23	0.37	0.79
85.28	0.44	0.96	49.14	0.40	0.86	28.85	0.36	0.78
84.22	0.44	0.96	48.51	0.40	0.86	28.46	0.36	0.79
83.14	0.44	0.95	47.89	0.40	0.86	28.08	0.36	0.79
82.07	0.44	0.95	47.28	0.40	0.86	27.69	0.36	0.78
81.00	0.44	0.95	46.67	0.40	0.85	27.31	0.37	0.79
79.94	0.44	0.95	46.08	0.40	0.85	26.94	0.36	0.77
78.91	0.44	0.95	45.49	0.39	0.85	26.56	0.36	0.78
77.88	0.44	0.94	44.91	0.39	0.85	26.18	0.37	0.79
76.87	0.44	0.94	44.34	0.39	0.85	25.80	0.36	0.77
75.88	0.43	0.94	43.79	0.39	0.85	25.42	0.36	0.77
74.90	0.43	0.94	43.23	0.39	0.85	25.05	0.35	0.76
73.90	0.43	0.93	42.68	0.39	0.84	24.65	0.35	0.76
72.93	0.43	0.93	42.15	0.39	0.84	24.27	0.35	0.75
71.97	0.43	0.93	41.62	0.39	0.84	23.90	0.35	0.75
71.03	0.43	0.93	41.11	0.39	0.84	23.52	0.35	0.75
70.11	0.43	0.92	40.59	0.39	0.83	23.14	0.35	0.75
69.21	0.43	0.92	40.09	0.39	0.84	22.76	0.35	0.75
68.31	0.43	0.92	39.59	0.38	0.83	22.38	0.35	0.75
67.42	0.42	0.92	39.09	0.38	0.83	21.99	0.34	0.74
66.52	0.42	0.91	38.60	0.39	0.84	21.62	0.34	0.73
65.64	0.42	0.91	38.12	0.38	0.83	21.24	0.34	0.73
64.77	0.42	0.91	37.65	0.38	0.82	20.86	0.34	0.73

Table C1.1 continued: HfMgMo₃O₁₂ Thermal Conductivity Data: A1 (as described in Chapter 9, Table 9.3); in order of data collection; where κ_m is the bulk thermal conductivity data as determined from the Klemen's model.³³²

T / K	$\kappa / \text{W m}^{-1} \text{K}^{-1}$	$\kappa_m / \text{W m}^{-1} \text{K}^{-1}$	T / K	$\kappa / \text{W m}^{-1} \text{K}^{-1}$	$\kappa_m / \text{W m}^{-1} \text{K}^{-1}$	T / K	$\kappa / \text{W m}^{-1} \text{K}^{-1}$	$\kappa_m / \text{W m}^{-1} \text{K}^{-1}$
20.49	0.34	0.73	12.23	0.28	0.60	11.61	0.27	0.59
20.11	0.33	0.72	11.85	0.28	0.60	13.16	0.29	0.62
19.73	0.33	0.72	11.47	0.27	0.59	14.23	0.30	0.65
19.36	0.33	0.71	11.10	0.27	0.58	15.04	0.30	0.65
18.98	0.33	0.71	10.72	0.26	0.57			
18.60	0.33	0.70	10.35	0.26	0.56			
18.22	0.32	0.70	9.97	0.25	0.55			
17.85	0.32	0.70	9.58	0.25	0.53			
17.47	0.32	0.70	8.81	0.24	0.52			
17.09	0.32	0.69	8.41	0.23	0.50			
16.71	0.32	0.68	8.02	0.22	0.48			
16.34	0.31	0.68	7.63	0.22	0.48			
15.96	0.31	0.67	7.24	0.21	0.44			
15.58	0.31	0.66	6.88	0.20	0.43			
15.21	0.31	0.66	6.51	0.19	0.41			
14.82	0.30	0.65	6.18	0.19	0.40			
14.44	0.30	0.65	6.18	0.19	0.40			
14.07	0.30	0.65	7.79	0.21	0.46			
13.51	0.30	0.64	8.84	0.24	0.51			
12.99	0.29	0.62	9.84	0.25	0.54			
12.61	0.29	0.62	10.76	0.26	0.57			

Table C1.2: HfMgMo₃O₁₂ Thermal Conductivity Data: A2 (as described in Chapter 9, Table 9.3); in order of data collection; where κ_m is the bulk thermal conductivity data as determined from the Klemen's model.³³²

T / K	$\kappa / \text{W m}^{-1} \text{K}^{-1}$	$\kappa_m / \text{W m}^{-1} \text{K}^{-1}$	T / K	$\kappa / \text{W m}^{-1} \text{K}^{-1}$	$\kappa_m / \text{W m}^{-1} \text{K}^{-1}$	T / K	$\kappa / \text{W m}^{-1} \text{K}^{-1}$	$\kappa_m / \text{W m}^{-1} \text{K}^{-1}$
303.89	0.50	1.07	236.53	0.50	1.07	174.86	0.48	1.03
301.89	0.50	1.07	235.07	0.50	1.07	173.40	0.48	1.03
299.27	0.50	1.07	233.59	0.50	1.07	171.93	0.48	1.03
296.98	0.50	1.07	232.12	0.50	1.07	170.48	0.48	1.03
294.89	0.50	1.07	230.65	0.50	1.07	169.01	0.48	1.02
292.97	0.50	1.07	229.17	0.50	1.07	167.53	0.47	1.02
291.13	0.50	1.07	227.70	0.50	1.07	166.06	0.47	1.02
289.42	0.50	1.07	226.23	0.50	1.07	164.60	0.47	1.02
287.71	0.50	1.07	224.75	0.50	1.07	163.13	0.47	1.01
286.05	0.50	1.08	223.29	0.50	1.07	161.66	0.47	1.01
284.49	0.50	1.08	221.82	0.50	1.07	160.19	0.47	1.01
282.91	0.50	1.08	220.35	0.50	1.07	158.71	0.47	1.01
281.34	0.50	1.08	218.88	0.50	1.07	157.24	0.47	1.01
279.76	0.50	1.08	217.42	0.50	1.07	155.77	0.47	1.01
278.18	0.50	1.08	215.96	0.50	1.07	154.34	0.47	1.01
276.59	0.50	1.07	214.49	0.50	1.06	152.97	0.47	1.01
275.01	0.50	1.07	213.03	0.50	1.06	151.60	0.47	1.01
273.42	0.50	1.07	211.57	0.49	1.06	150.22	0.47	1.01
271.89	0.50	1.08	210.10	0.49	1.06	148.85	0.47	1.01
270.43	0.50	1.08	208.63	0.49	1.06	147.47	0.47	1.01
268.97	0.50	1.08	207.16	0.49	1.06	146.09	0.47	1.01
267.50	0.50	1.08	205.70	0.49	1.06	144.72	0.47	1.01
266.02	0.50	1.08	204.22	0.49	1.06	143.34	0.47	1.01
264.55	0.50	1.08	202.76	0.49	1.06	141.97	0.47	1.01
263.10	0.50	1.08	201.29	0.49	1.05	140.59	0.47	1.01
261.64	0.50	1.08	199.83	0.49	1.06	139.21	0.47	1.01
260.17	0.50	1.07	198.36	0.49	1.05	137.84	0.47	1.01
258.70	0.50	1.08	196.89	0.49	1.05	136.46	0.47	1.01
257.24	0.50	1.08	195.42	0.49	1.05	135.08	0.47	1.01
255.76	0.50	1.08	193.95	0.49	1.05	133.74	0.47	1.02
254.30	0.50	1.07	192.48	0.49	1.05	132.45	0.48	1.02
252.84	0.50	1.08	191.01	0.49	1.05	131.16	0.48	1.02
251.37	0.50	1.08	189.54	0.49	1.05	129.88	0.48	1.02
249.90	0.50	1.07	188.06	0.49	1.05	128.58	0.48	1.02
248.43	0.50	1.08	186.59	0.49	1.05	127.28	0.48	1.02
246.96	0.50	1.08	185.13	0.49	1.06	125.99	0.47	1.02
245.49	0.50	1.08	183.66	0.49	1.04	124.70	0.48	1.02
244.03	0.50	1.07	182.20	0.49	1.05	123.40	0.48	1.02
242.56	0.50	1.07	180.73	0.49	1.04	122.14	0.48	1.03
241.08	0.50	1.07	179.26	0.49	1.04	120.92	0.48	1.03
239.61	0.50	1.07	177.79	0.49	1.04	119.69	0.48	1.02
238.02	0.50	1.07	176.33	0.48	1.04	118.43	0.48	1.03

Table C1.2 continued: HfMgMo₃O₁₂ Thermal Conductivity Data: A2 (as described in Chapter 9, Table 9.3); in order of data collection; where κ_m is the bulk thermal conductivity data as determined from the Klemen's model.³³²

T / K	$\kappa / \text{W m}^{-1} \text{K}^{-1}$	$\kappa_m / \text{W m}^{-1} \text{K}^{-1}$	T / K	$\kappa / \text{W m}^{-1} \text{K}^{-1}$	$\kappa_m / \text{W m}^{-1} \text{K}^{-1}$	T / K	$\kappa / \text{W m}^{-1} \text{K}^{-1}$	$\kappa_m / \text{W m}^{-1} \text{K}^{-1}$
117.24	0.48	1.02	73.91	0.50	1.06	46.50	0.51	1.10
116.02	0.48	1.03	73.08	0.50	1.07	46.01	0.51	1.10
114.80	0.48	1.03	72.26	0.50	1.07	45.52	0.51	1.10
113.60	0.48	1.03	71.45	0.50	1.07	45.03	0.51	1.10
112.43	0.48	1.03	70.65	0.50	1.07	44.56	0.51	1.10
111.27	0.48	1.03	69.84	0.50	1.07	44.08	0.51	1.10
110.11	0.48	1.03	69.07	0.50	1.07	43.61	0.51	1.10
108.94	0.48	1.03	68.31	0.50	1.07	43.15	0.51	1.10
107.78	0.48	1.03	67.55	0.50	1.07	42.69	0.51	1.10
106.61	0.48	1.03	66.79	0.50	1.07	42.24	0.51	1.10
105.47	0.48	1.03	66.05	0.50	1.07	41.79	0.52	1.10
104.36	0.48	1.03	65.31	0.50	1.07	41.35	0.51	1.10
103.24	0.48	1.03	64.58	0.50	1.07	40.91	0.52	1.11
102.13	0.48	1.03	63.85	0.50	1.08	40.48	0.52	1.10
101.02	0.48	1.03	63.14	0.50	1.08	40.05	0.51	1.10
99.90	0.48	1.03	62.45	0.50	1.08	39.63	0.52	1.11
98.82	0.48	1.04	61.75	0.50	1.08	39.20	0.51	1.10
97.75	0.48	1.04	61.07	0.50	1.08	38.79	0.51	1.10
96.69	0.48	1.04	60.39	0.50	1.08	38.38	0.51	1.10
95.62	0.48	1.04	59.72	0.50	1.08	37.97	0.52	1.11
94.56	0.48	1.04	59.06	0.51	1.08	37.56	0.51	1.09
93.52	0.49	1.04	58.41	0.51	1.09	37.17	0.51	1.10
92.52	0.48	1.04	57.77	0.51	1.08	36.77	0.52	1.10
91.51	0.48	1.04	57.14	0.51	1.09	36.38	0.51	1.10
90.50	0.48	1.04	56.51	0.51	1.09	35.99	0.51	1.10
89.51	0.49	1.04	55.89	0.51	1.09	35.60	0.51	1.10
88.53	0.49	1.04	55.29	0.51	1.09	35.22	0.51	1.10
87.56	0.49	1.04	54.69	0.51	1.09	34.84	0.51	1.09
86.58	0.49	1.04	54.09	0.51	1.09	34.45	0.51	1.09
85.57	0.49	1.05	53.50	0.51	1.09	33.73	0.50	1.07
84.63	0.49	1.05	52.93	0.51	1.10	33.35	0.51	1.10
83.67	0.49	1.05	52.35	0.51	1.09	32.95	0.51	1.10
82.74	0.49	1.06	51.79	0.51	1.09	32.56	0.51	1.09
81.82	0.49	1.05	51.23	0.51	1.10	32.18	0.51	1.08
80.90	0.49	1.05	50.67	0.51	1.09	31.80	0.50	1.08
80.00	0.49	1.06	50.13	0.51	1.10	31.41	0.50	1.08
79.11	0.49	1.06	49.59	0.51	1.10	31.04	0.50	1.08
78.22	0.49	1.06	49.06	0.51	1.10	30.66	0.50	1.07
77.34	0.49	1.06	48.53	0.51	1.10	30.29	0.50	1.07
76.47	0.50	1.06	48.02	0.51	1.10	29.91	0.50	1.07
75.60	0.50	1.06	47.51	0.51	1.10	29.53	0.50	1.07
74.75	0.50	1.07	47.00	0.51	1.10	29.15	0.50	1.06

Table C1.2 continued: HfMgMo₃O₁₂ Thermal Conductivity Data: A2 (as described in Chapter 9, Table 9.3); in order of data collection; where κ_m is the bulk thermal conductivity data as determined from the Klemen's model.³³²

T / K	$\kappa / \text{W m}^{-1} \text{K}^{-1}$	$\kappa_m / \text{W m}^{-1} \text{K}^{-1}$	T / K	$\kappa / \text{W m}^{-1} \text{K}^{-1}$	$\kappa_m / \text{W m}^{-1} \text{K}^{-1}$	T / K	$\kappa / \text{W m}^{-1} \text{K}^{-1}$	$\kappa_m / \text{W m}^{-1} \text{K}^{-1}$
28.77	0.49	1.06	12.89	0.35	0.75			
28.39	0.50	1.07	12.52	0.35	0.75			
28.01	0.49	1.06	11.77	0.33	0.71			
27.64	0.49	1.06	11.39	0.32	0.69			
27.26	0.49	1.05	11.02	0.31	0.67			
26.89	0.49	1.04	10.64	0.30	0.65			
26.51	0.49	1.04	10.26	0.30	0.64			
26.14	0.49	1.04	9.89	0.29	0.61			
25.76	0.49	1.05	9.49	0.28	0.59			
25.38	0.48	1.03	8.73	0.25	0.54			
25.01	0.48	1.03	8.34	0.24	0.52			
24.63	0.48	1.03	7.95	0.23	0.50			
24.25	0.48	1.02	7.56	0.22	0.47			
23.86	0.47	1.01	7.21	0.21	0.45			
23.49	0.47	1.00	6.80	0.20	0.42			
23.12	0.47	1.00	6.02	0.17	0.36			
22.74	0.47	1.00	5.25	0.14	0.30			
22.37	0.47	1.00	4.87	0.13	0.27			
21.94	0.46	1.00	4.48	0.12	0.26			
21.60	0.46	0.99	3.70	0.09	0.19			
21.23	0.46	0.98	3.32	0.07	0.16			
20.84	0.45	0.97	2.92	0.06	0.13			
20.47	0.45	0.96	2.55	0.05	0.10			
20.09	0.45	0.96	2.17	0.03	0.07			
19.72	0.45	0.96	2.04	0.03	0.06			
19.34	0.44	0.95	2.04	0.03	0.06			
18.96	0.44	0.94	2.04	0.03	0.06			
18.59	0.43	0.93						
18.21	0.43	0.92						
17.84	0.43	0.91						
17.46	0.42	0.91						
17.07	0.42	0.89						
16.70	0.41	0.88						
16.33	0.41	0.87						
15.96	0.40	0.86						
15.53	0.40	0.85						
15.15	0.39	0.84						
14.77	0.38	0.82						
14.39	0.38	0.82						
14.01	0.37	0.80						
13.64	0.37	0.79						
13.26	0.36	0.78						

Table C1.3: HfMgMo₃O₁₂ Thermal Conductivity Data: A3 (as described in Chapter 9, Table 9.3); in order of data collection; where κ_m is the bulk thermal conductivity data as determined from the Klemen's model.³³²

T / K	$\kappa / \text{W m}^{-1} \text{K}^{-1}$	$\kappa_m / \text{W m}^{-1} \text{K}^{-1}$	T / K	$\kappa / \text{W m}^{-1} \text{K}^{-1}$	$\kappa_m / \text{W m}^{-1} \text{K}^{-1}$	T / K	$\kappa / \text{W m}^{-1} \text{K}^{-1}$	$\kappa_m / \text{W m}^{-1} \text{K}^{-1}$
302.61	0.51	0.86	195.94	0.50	0.84	79.67	0.39	0.65
302.58	0.53	0.90	193.94	0.49	0.82	77.59	0.39	0.66
300.68	0.52	0.89	191.08	0.48	0.82	75.52	0.39	0.66
297.69	0.52	0.89	187.58	0.48	0.82	73.44	0.39	0.66
294.86	0.52	0.88	184.50	0.48	0.81	71.46	0.39	0.66
292.09	0.52	0.88	181.62	0.48	0.81	69.59	0.39	0.66
289.37	0.52	0.88	178.85	0.48	0.81	67.75	0.39	0.67
286.67	0.52	0.88	176.13	0.48	0.81	65.97	0.40	0.67
283.99	0.52	0.87	173.44	0.48	0.81	64.25	0.40	0.67
281.30	0.52	0.87	170.93	0.41	0.70	62.54	0.40	0.67
278.62	0.51	0.87	168.21	0.40	0.68	60.89	0.40	0.67
275.95	0.51	0.87	165.25	0.39	0.66	59.31	0.40	0.68
273.26	0.51	0.87	162.07	0.39	0.66	57.78	0.40	0.68
270.61	0.51	0.87	158.90	0.38	0.65	56.31	0.40	0.68
267.93	0.51	0.86	155.74	0.38	0.64	54.88	0.40	0.68
265.26	0.51	0.86	152.58	0.38	0.65	53.51	0.40	0.68
262.59	0.51	0.86	149.43	0.38	0.64	52.17	0.40	0.69
259.93	0.51	0.86	146.28	0.38	0.64	50.92	0.41	0.69
257.27	0.51	0.86	143.12	0.38	0.64	49.69	0.41	0.69
254.61	0.51	0.86	139.97	0.38	0.64	48.50	0.41	0.69
251.95	0.51	0.86	136.81	0.38	0.63	47.36	0.41	0.69
249.29	0.51	0.86	133.65	0.37	0.63	46.27	0.41	0.69
246.62	0.51	0.86	130.50	0.37	0.63	45.23	0.41	0.69
243.95	0.51	0.86	127.35	0.38	0.64	44.23	0.41	0.69
241.27	0.51	0.86	124.21	0.38	0.64	43.26	0.41	0.70
238.60	0.51	0.86	121.06	0.37	0.63	42.34	0.41	0.69
235.92	0.50	0.85	117.90	0.38	0.64	41.43	0.41	0.70
233.25	0.50	0.85	114.98	0.38	0.64	40.56	0.41	0.70
230.57	0.50	0.85	112.32	0.38	0.64	39.71	0.41	0.70
227.90	0.50	0.85	109.65	0.38	0.64	38.88	0.41	0.70
225.24	0.50	0.85	106.97	0.38	0.64	38.09	0.41	0.70
222.58	0.50	0.85	104.29	0.38	0.64	37.32	0.41	0.70
219.92	0.50	0.85	101.63	0.38	0.64	36.58	0.41	0.70
217.26	0.50	0.85	98.96	0.38	0.64	35.87	0.41	0.70
214.60	0.50	0.85	96.29	0.38	0.64	35.18	0.41	0.70
211.94	0.50	0.85	93.63	0.38	0.64	34.51	0.41	0.70
209.28	0.50	0.84	91.15	0.38	0.65	33.85	0.42	0.70
206.61	0.50	0.84	88.85	0.38	0.65	33.22	0.41	0.70
203.95	0.50	0.84	86.54	0.38	0.65	32.60	0.41	0.70
201.28	0.50	0.84	84.22	0.38	0.65	32.00	0.41	0.70
198.61	0.50	0.84	81.88	0.39	0.65	31.41	0.41	0.70

Table C1.3 continued: HfMgMo₃O₁₂ Thermal Conductivity Data: A3 (as described in Chapter 9, Table 9.3); in order of data collection; where κ_m is the bulk thermal conductivity data as determined from the Klemen's model.³³²

T / K	$\kappa / \text{W m}^{-1} \text{K}^{-1}$	$\kappa_m / \text{W m}^{-1} \text{K}^{-1}$	T / K	$\kappa / \text{W m}^{-1} \text{K}^{-1}$	$\kappa_m / \text{W m}^{-1} \text{K}^{-1}$	T / K	$\kappa / \text{W m}^{-1} \text{K}^{-1}$	$\kappa_m / \text{W m}^{-1} \text{K}^{-1}$
30.84	0.42	0.70						
30.29	0.42	0.70						
29.75	0.41	0.70						
28.95	0.41	0.69						
27.92	0.41	0.69						
26.93	0.41	0.69						
25.96	0.41	0.69						
25.01	0.40	0.68						
24.12	0.40	0.68						
23.24	0.40	0.67						
22.39	0.40	0.67						
21.56	0.39	0.66						
20.74	0.39	0.66						
19.95	0.39	0.66						
19.19	0.38	0.65						
18.42	0.37	0.63						
17.67	0.37	0.62						
16.92	0.36	0.61						
16.16	0.35	0.60						
15.41	0.34	0.58						
14.65	0.33	0.57						
13.91	0.32	0.55						
13.16	0.31	0.53						
12.41	0.30	0.51						
11.65	0.29	0.49						
10.90	0.27	0.46						
10.15	0.26	0.44						
9.40	0.24	0.41						
8.63	0.22	0.38						
7.87	0.20	0.35						
7.10	0.18	0.31						
6.33	0.16	0.27						
5.57	0.14	0.24						
4.76	0.12	0.20						
3.20	0.06	0.10						
2.48	0.04	0.07						
2.12	0.03	0.04						
2.09	0.03	0.04						

C2 In(HfMg)_{0.5}Mo₃O₁₂

Table C2.1: In(HfMg)_{0.5}Mo₃O₁₂ Thermal Conductivity Data: B1 (as described in Chapter 9, Table 9.3); in order of data collection; where κ_m is the bulk thermal conductivity data as determined from the Klemen's model.³³²

T / K	$\kappa / \text{W m}^{-1} \text{K}^{-1}$	$\kappa_m / \text{W m}^{-1} \text{K}^{-1}$	T / K	$\kappa / \text{W m}^{-1} \text{K}^{-1}$	$\kappa_m / \text{W m}^{-1} \text{K}^{-1}$	T / K	$\kappa / \text{W m}^{-1} \text{K}^{-1}$	$\kappa_m / \text{W m}^{-1} \text{K}^{-1}$
300.79	0.51	0.77	71.00	0.40	0.60	2.08	0.06	0.08
297.50	0.50	0.76	66.89	0.40	0.60			
291.59	0.50	0.75	62.93	0.39	0.59			
285.74	0.50	0.75	59.11	0.39	0.59			
279.89	0.50	0.75	55.56	0.39	0.59			
274.05	0.49	0.74	52.22	0.39	0.58			
268.24	0.49	0.74	49.06	0.38	0.58			
262.43	0.49	0.74	46.06	0.38	0.58			
256.64	0.49	0.73	43.26	0.38	0.57			
250.86	0.48	0.73	40.69	0.38	0.57			
245.04	0.48	0.73	38.31	0.38	0.57			
239.23	0.48	0.72	36.08	0.38	0.57			
233.41	0.48	0.72	34.01	0.38	0.57			
227.60	0.48	0.72	32.09	0.38	0.57			
221.79	0.48	0.72	30.31	0.38	0.57			
215.99	0.47	0.71	28.66	0.38	0.57			
210.20	0.47	0.71	27.13	0.38	0.57			
204.40	0.47	0.70	25.70	0.38	0.57			
198.60	0.47	0.70	24.37	0.38	0.57			
192.79	0.46	0.70	23.13	0.38	0.57			
186.97	0.46	0.69	21.95	0.38	0.57			
181.16	0.46	0.69	20.85	0.38	0.57			
175.34	0.46	0.69	19.81	0.37	0.57			
169.54	0.45	0.69	18.81	0.37	0.57			
163.73	0.45	0.68	17.83	0.38	0.57			
157.94	0.45	0.68	16.87	0.37	0.56			
152.14	0.45	0.68	15.92	0.37	0.56			
146.32	0.45	0.67	14.98	0.36	0.55			
140.52	0.44	0.67	14.03	0.36	0.54			
134.71	0.44	0.66	13.08	0.35	0.54			
129.23	0.44	0.66	12.13	0.35	0.52			
124.06	0.44	0.66	11.18	0.34	0.51			
118.92	0.44	0.66	10.24	0.32	0.48			
113.77	0.43	0.65	9.31	0.31	0.47			
108.60	0.43	0.65	8.36	0.29	0.44			
103.44	0.42	0.64	7.42	0.27	0.41			
98.26	0.42	0.63	6.47	0.24	0.37			
93.35	0.42	0.63	5.50	0.22	0.33			
88.73	0.41	0.62	4.45	0.18	0.27			
84.07	0.41	0.62	3.43	0.13	0.20			
79.58	0.41	0.61	2.52	0.09	0.13			
75.30	0.40	0.61	2.10	0.06	0.09			

Table C2.2: In(HfMg)_{0.5}Mo₃O₁₂ Thermal Conductivity Data: B2 (as described in Chapter 9, Table 9.3); in order of data collection; where κ_m is the bulk thermal conductivity data as determined from the Klemen's model.³³²

T / K	$\kappa / \text{W m}^{-1} \text{K}^{-1}$	$\kappa_m / \text{W m}^{-1} \text{K}^{-1}$	T / K	$\kappa / \text{W m}^{-1} \text{K}^{-1}$	$\kappa_m / \text{W m}^{-1} \text{K}^{-1}$	T / K	$\kappa / \text{W m}^{-1} \text{K}^{-1}$	$\kappa_m / \text{W m}^{-1} \text{K}^{-1}$
300.08	0.55	1.07	89.63	0.42	0.82	8.98	0.31	0.61
297.36	0.53	1.02	85.56	0.42	0.81	7.21	0.28	0.54
291.53	0.52	1.01	81.60	0.42	0.80	6.32	0.26	0.49
285.72	0.52	0.99	77.63	0.41	0.80	5.43	0.23	0.45
279.89	0.51	0.99	73.79	0.41	0.79	4.40	0.19	0.37
274.36	0.51	0.99	70.10	0.41	0.78	3.32	0.14	0.27
269.20	0.51	0.98	66.56	0.40	0.78	2.34	0.09	0.17
264.02	0.50	0.97	63.20	0.40	0.78	2.15	0.07	0.13
258.88	0.50	0.97	59.96	0.40	0.77			
253.72	0.50	0.97	56.80	0.40	0.77			
248.58	0.50	0.96	53.80	0.39	0.76			
243.41	0.50	0.96	50.93	0.39	0.76			
238.24	0.50	0.96	48.25	0.39	0.75			
233.06	0.49	0.95	45.72	0.39	0.74			
227.89	0.49	0.95	43.29	0.39	0.74			
222.73	0.49	0.95	41.09	0.39	0.74			
217.58	0.49	0.94	38.98	0.38	0.74			
212.43	0.49	0.93	37.00	0.38	0.74			
207.28	0.48	0.93	35.15	0.38	0.74			
202.13	0.48	0.92	33.41	0.38	0.73			
196.99	0.48	0.92	31.79	0.38	0.73			
191.83	0.48	0.92	30.26	0.38	0.73			
186.67	0.47	0.92	28.82	0.38	0.74			
181.51	0.47	0.91	27.45	0.38	0.73			
176.35	0.47	0.91	26.18	0.38	0.74			
171.19	0.47	0.90	24.97	0.38	0.73			
166.03	0.47	0.90	23.83	0.38	0.73			
160.87	0.47	0.90	22.74	0.38	0.73			
155.71	0.46	0.89	21.68	0.38	0.73			
150.56	0.46	0.89	20.69	0.38	0.73			
145.41	0.46	0.88	19.73	0.38	0.73			
140.24	0.45	0.88	18.81	0.38	0.73			
135.06	0.45	0.87	17.91	0.38	0.73			
130.15	0.45	0.87	17.01	0.37	0.72			
125.50	0.45	0.86	16.10	0.37	0.72			
120.85	0.44	0.86	15.20	0.37	0.71			
116.20	0.44	0.85	14.31	0.36	0.70			
111.51	0.44	0.85	13.41	0.36	0.69			
106.85	0.44	0.84	12.52	0.35	0.68			
102.39	0.43	0.83	11.63	0.35	0.67			
98.12	0.43	0.83	10.75	0.34	0.65			
93.84	0.43	0.82	9.86	0.34	0.65			

Table C2.3: In(HfMg)_{0.5}Mo₃O₁₂ Thermal Conductivity Data: B3 (as described in Chapter 9, Table 9.3); in order of data collection; where κ_m is the bulk thermal conductivity data as determined from the Klemen's model.³³²

T / K	$\kappa / \text{W m}^{-1} \text{K}^{-1}$	$\kappa_m / \text{W m}^{-1} \text{K}^{-1}$	T / K	$\kappa / \text{W m}^{-1} \text{K}^{-1}$	$\kappa_m / \text{W m}^{-1} \text{K}^{-1}$	T / K	$\kappa / \text{W m}^{-1} \text{K}^{-1}$	$\kappa_m / \text{W m}^{-1} \text{K}^{-1}$
298.91	0.41	0.80	64.61	0.29	0.57	2.94	0.06	0.12
295.45	0.40	0.79	60.36	0.29	0.57	2.89	0.06	0.12
289.51	0.40	0.79	56.28	0.29	0.56	2.88	0.06	0.11
283.64	0.40	0.78	52.35	0.28	0.55	2.81	0.06	0.11
277.60	0.40	0.78	48.58	0.28	0.54	2.77	0.06	0.11
271.80	0.40	0.77	45.07	0.27	0.54	2.74	0.05	0.11
266.02	0.39	0.77	41.86	0.27	0.53	2.71	0.05	0.10
260.24	0.39	0.76	38.92	0.27	0.52	2.68	0.05	0.10
254.48	0.39	0.76	36.17	0.27	0.52	2.59	0.05	0.10
248.72	0.39	0.76	33.65	0.26	0.51	2.58	0.05	0.10
242.95	0.39	0.76	31.34	0.26	0.51	2.55	0.05	0.10
237.18	0.38	0.75	29.24	0.26	0.51	2.55	0.05	0.10
231.41	0.38	0.75	27.30	0.26	0.50	2.54	0.05	0.09
225.64	0.38	0.75	25.53	0.25	0.49	2.53	0.05	0.10
219.88	0.38	0.74	23.88	0.25	0.49	2.52	0.05	0.09
214.13	0.38	0.74	22.38	0.25	0.48	2.52	0.05	0.10
208.36	0.37	0.73	20.99	0.24	0.48	2.50	0.05	0.09
202.60	0.37	0.73	19.71	0.24	0.47	2.48	0.05	0.09
196.85	0.37	0.73	18.53	0.24	0.47	2.46	0.05	0.09
191.08	0.37	0.72	17.41	0.24	0.46	2.46	0.05	0.09
185.30	0.37	0.72	16.36	0.23	0.46	2.46	0.05	0.09
179.51	0.36	0.71	15.37	0.23	0.45	2.45	0.05	0.09
173.74	0.36	0.71	14.44	0.23	0.45	2.45	0.05	0.09
167.97	0.36	0.70	13.54	0.22	0.43	2.44	0.04	0.09
162.20	0.36	0.70	12.67	0.22	0.42	2.43	0.05	0.09
156.43	0.36	0.69	11.80	0.21	0.41	2.42	0.05	0.09
150.66	0.35	0.69	10.92	0.20	0.40	2.42	0.05	0.09
144.91	0.35	0.68	10.04	0.20	0.38	2.41	0.04	0.09
139.15	0.35	0.68	9.18	0.19	0.37	2.41	0.04	0.09
133.35	0.34	0.67	8.32	0.17	0.34	2.40	0.05	0.09
127.60	0.34	0.66	7.46	0.16	0.32	2.39	0.04	0.09
121.86	0.34	0.66	6.58	0.15	0.29	2.39	0.05	0.09
116.11	0.33	0.65	5.71	0.13	0.26	2.38	0.05	0.09
110.34	0.33	0.64	4.82	0.11	0.22	2.38	0.05	0.09
104.55	0.32	0.63	3.78	0.09	0.18	2.38	0.04	0.08
99.10	0.32	0.63	2.89	0.06	0.12	2.37	0.04	0.09
93.96	0.32	0.62	2.73	0.05	0.11	2.36	0.04	0.08
88.85	0.31	0.61	2.68	0.05	0.10	2.36	0.04	0.08
83.74	0.31	0.60	2.59	0.05	0.10	2.33	0.04	0.08
78.59	0.31	0.60	2.57	0.05	0.10	2.31	0.04	0.08
73.69	0.30	0.59	2.54	0.05	0.10	2.31	0.04	0.08
69.03	0.30	0.58	2.95	0.06	0.12	2.31	0.04	0.08

Table C2.3 continued: $\text{In}(\text{HfMg})_{0.5}\text{Mo}_3\text{O}_{12}$ Thermal Conductivity Data: B3 (as described in Chapter 9, Table 9.3); in order of data collection; where κ_m is the bulk thermal conductivity data as determined from the Klemen's model.³³²

T/K	$\kappa/\text{W m}^{-1}\text{K}^{-1}$	$\kappa_m/\text{W m}^{-1}\text{K}^{-1}$	T/K	$\kappa/\text{W m}^{-1}\text{K}^{-1}$	$\kappa_m/\text{W m}^{-1}\text{K}^{-1}$	T/K	$\kappa/\text{W m}^{-1}\text{K}^{-1}$	$\kappa_m/\text{W m}^{-1}\text{K}^{-1}$
2.30	0.04	0.08	2.11	0.04	0.07	1.99	0.03	0.06
2.29	0.04	0.08	2.10	0.04	0.07	1.99	0.03	0.06
2.29	0.04	0.08	2.10	0.04	0.07	1.99	0.03	0.06
2.29	0.04	0.08	2.10	0.04	0.07	1.99	0.03	0.06
2.28	0.04	0.08	2.10	0.04	0.07	1.99	0.03	0.06
2.27	0.04	0.08	2.10	0.04	0.07	1.99	0.03	0.06
2.27	0.04	0.08	2.09	0.04	0.07	1.99	0.03	0.06
2.26	0.04	0.08	2.09	0.04	0.07	1.99	0.03	0.06
2.25	0.04	0.08	2.09	0.03	0.07	1.99	0.03	0.06
2.25	0.04	0.08	2.09	0.04	0.07	1.99	0.03	0.06
2.24	0.04	0.08	2.09	0.04	0.07	1.98	0.03	0.06
2.24	0.04	0.08	2.08	0.04	0.07	1.98	0.04	0.07
2.24	0.04	0.08	2.08	0.04	0.07	1.98	0.03	0.07
2.23	0.04	0.08	2.07	0.03	0.07	1.97	0.03	0.07
2.23	0.04	0.08	2.06	0.03	0.07	1.97	0.03	0.07
2.23	0.04	0.08	2.06	0.03	0.07	1.97	0.03	0.07
2.23	0.04	0.08	2.05	0.03	0.07	1.97	0.03	0.07
2.22	0.04	0.08	2.05	0.03	0.07	1.99	0.03	0.06
2.21	0.04	0.07	2.05	0.03	0.07	1.99	0.03	0.06
2.20	0.04	0.07	2.05	0.03	0.07	1.99	0.03	0.06
2.19	0.04	0.07	2.05	0.03	0.07	1.99	0.03	0.06
2.19	0.04	0.07	2.05	0.03	0.07	1.99	0.03	0.06
2.19	0.04	0.07	2.04	0.03	0.07	1.99	0.03	0.06
2.19	0.04	0.07	2.04	0.03	0.07	1.99	0.03	0.06
2.18	0.04	0.07	2.04	0.03	0.07	1.99	0.03	0.06
2.18	0.04	0.07	2.04	0.03	0.07	1.99	0.03	0.06
2.18	0.04	0.07	2.04	0.03	0.07	1.99	0.03	0.06
2.18	0.04	0.07	2.04	0.03	0.07	1.99	0.03	0.06
2.18	0.04	0.07	2.03	0.04	0.07	1.98	0.03	0.06
2.18	0.04	0.07	2.03	0.04	0.07	1.98	0.04	0.07
2.18	0.04	0.07	2.03	0.04	0.07	1.98	0.03	0.07
2.18	0.04	0.07	2.02	0.04	0.07	1.97	0.03	0.07
2.16	0.04	0.07	2.02	0.04	0.07	1.97	0.03	0.07
2.16	0.04	0.07	2.02	0.03	0.06	1.97	0.03	0.07
2.15	0.04	0.07	2.01	0.03	0.06	1.97	0.03	0.07
2.15	0.04	0.07	2.01	0.03	0.06			
2.15	0.04	0.07	2.00	0.03	0.06			
2.14	0.04	0.07	2.00	0.03	0.06			
2.14	0.04	0.07	2.00	0.03	0.06			
2.14	0.04	0.07	2.00	0.03	0.06			
2.14	0.04	0.07	2.00	0.03	0.06			
2.13	0.04	0.07	2.00	0.03	0.06			
2.12	0.04	0.07	2.00	0.03	0.06			
2.11	0.04	0.07	2.00	0.03	0.06			

C3 In_{1.5}(HfMg)_{0.25}Mo₃O₁₂

Table C3.1: In_{1.5}(HfMg)_{0.25}Mo₃O₁₂ Thermal Conductivity Data: C1 (as described in Chapter 9, Table 9.3); in order of data collection; where κ_m is the bulk thermal conductivity data as determined from the Klemen's model.³³²

T / K	$\kappa / \text{W m}^{-1} \text{K}^{-1}$	$\kappa_m / \text{W m}^{-1} \text{K}^{-1}$	T / K	$\kappa / \text{W m}^{-1} \text{K}^{-1}$	$\kappa_m / \text{W m}^{-1} \text{K}^{-1}$	T / K	$\kappa / \text{W m}^{-1} \text{K}^{-1}$	$\kappa_m / \text{W m}^{-1} \text{K}^{-1}$
303.89	0.68	0.98	103.36	0.56	0.81	15.46	0.55	0.79
300.06	0.67	0.96	99.36	0.56	0.81	14.51	0.54	0.78
293.78	0.66	0.95	95.42	0.56	0.80	13.54	0.54	0.78
288.04	0.66	0.94	91.64	0.56	0.80	12.60	0.53	0.77
282.75	0.65	0.94	87.99	0.55	0.80	11.65	0.52	0.75
277.50	0.65	0.93	84.31	0.55	0.80	10.69	0.51	0.73
272.26	0.65	0.93	80.72	0.55	0.79	9.74	0.49	0.70
267.06	0.64	0.93	77.25	0.55	0.79	8.77	0.46	0.67
261.85	0.64	0.92	73.88	0.54	0.78	7.80	0.44	0.63
256.69	0.64	0.92	70.62	0.54	0.78	6.83	0.40	0.57
251.49	0.64	0.92	67.47	0.54	0.78	5.84	0.35	0.50
246.31	0.64	0.92	64.45	0.54	0.77	4.82	0.29	0.42
241.12	0.63	0.91	61.57	0.54	0.77	3.77	0.23	0.34
235.92	0.63	0.91	58.82	0.54	0.77	2.79	0.16	0.23
230.96	0.63	0.90	56.18	0.53	0.77	2.14	0.09	0.14
226.27	0.63	0.90	53.66	0.53	0.77	2.09	0.09	0.12
221.60	0.62	0.90	51.22	0.53	0.77			
216.93	0.62	0.90	48.91	0.53	0.77			
212.25	0.62	0.89	46.70	0.53	0.76			
207.58	0.62	0.89	44.58	0.53	0.76			
202.91	0.61	0.88	42.57	0.53	0.76			
198.23	0.61	0.88	40.68	0.53	0.77			
193.54	0.61	0.88	38.91	0.53	0.76			
188.86	0.61	0.87	37.23	0.53	0.77			
184.16	0.61	0.88	35.63	0.53	0.77			
179.49	0.61	0.87	34.10	0.53	0.77			
174.81	0.60	0.87	32.65	0.54	0.77			
170.12	0.60	0.87	31.28	0.54	0.77			
165.46	0.60	0.87	29.96	0.54	0.78			
160.79	0.60	0.86	28.69	0.54	0.78			
156.11	0.59	0.86	27.49	0.54	0.78			
151.42	0.59	0.85	26.34	0.54	0.78			
146.73	0.59	0.85	25.22	0.54	0.78			
142.02	0.59	0.85	24.16	0.55	0.79			
137.34	0.59	0.84	23.15	0.55	0.79			
132.85	0.59	0.84	22.16	0.55	0.79			
128.57	0.58	0.84	21.19	0.55	0.79			
124.30	0.58	0.84	20.22	0.55	0.79			
120.02	0.58	0.83	19.24	0.55	0.79			
115.74	0.57	0.83	18.30	0.55	0.79			
111.46	0.57	0.82	17.35	0.56	0.80			
107.32	0.57	0.82	16.41	0.55	0.79			

Table C3.2: $\text{In}_{1.5}(\text{HfMg})_{0.25}\text{Mo}_3\text{O}_{12}$ Thermal Conductivity Data: C (as described in Chapter 9, Table 9.3); in order of data collection; where κ_m is the bulk thermal conductivity data as determined from the Klemen's model.³³²

T / K	$\kappa / \text{W m}^{-1} \text{K}^{-1}$	$\kappa_m / \text{W m}^{-1} \text{K}^{-1}$	T / K	$\kappa / \text{W m}^{-1} \text{K}^{-1}$	$\kappa_m / \text{W m}^{-1} \text{K}^{-1}$	T / K	$\kappa / \text{W m}^{-1} \text{K}^{-1}$	$\kappa_m / \text{W m}^{-1} \text{K}^{-1}$
303.51	0.68	1.09	110.19	0.43	0.68	11.76	0.36	0.57
299.64	0.67	1.07	105.71	0.42	0.67	10.80	0.36	0.56
293.74	0.67	1.06	101.42	0.42	0.66	9.86	0.34	0.54
288.36	0.66	1.05	97.13	0.41	0.65	8.93	0.32	0.51
283.07	0.66	1.05	92.87	0.40	0.64	7.96	0.31	0.48
278.06	0.66	1.05	88.62	0.40	0.63	6.99	0.29	0.46
273.36	0.65	1.04	84.51	0.39	0.62	6.01	0.25	0.40
268.67	0.65	1.04	80.53	0.39	0.62	5.05	0.22	0.35
263.99	0.65	1.03	76.55	0.39	0.61	4.06	0.18	0.28
259.32	0.65	1.03	72.71	0.38	0.61	3.13	0.14	0.21
254.64	0.65	1.03	69.02	0.38	0.60	2.19	0.07	0.12
249.97	0.65	1.03	65.44	0.37	0.59	2.10	0.06	0.10
245.50	0.65	1.03	61.97	0.37	0.59			
241.23	0.65	1.03	58.60	0.37	0.58			
236.94	0.64	1.02	55.41	0.36	0.58			
232.67	0.63	1.01	52.38	0.36	0.57			
228.38	0.63	1.00	49.51	0.36	0.57			
224.10	0.62	0.99	46.78	0.36	0.57			
219.82	0.62	0.98	44.18	0.36	0.57			
215.55	0.61	0.97	41.78	0.36	0.57			
211.28	0.61	0.96	39.53	0.36	0.57			
207.02	0.60	0.95	37.42	0.36	0.57			
202.75	0.59	0.93	35.43	0.36	0.57			
198.49	0.58	0.93	33.58	0.36	0.57			
194.22	0.57	0.91	31.85	0.36	0.58			
189.74	0.57	0.90	30.24	0.36	0.57			
185.05	0.55	0.88	28.74	0.36	0.58			
180.38	0.55	0.87	27.33	0.36	0.58			
175.72	0.54	0.86	26.01	0.37	0.58			
171.03	0.53	0.84	24.75	0.37	0.58			
166.36	0.52	0.83	23.59	0.37	0.59			
161.70	0.51	0.81	22.46	0.37	0.59			
157.01	0.50	0.80	21.40	0.37	0.59			
152.32	0.50	0.79	20.39	0.37	0.59			
147.64	0.49	0.77	19.43	0.37	0.60			
142.96	0.48	0.76	18.46	0.37	0.59			
138.28	0.47	0.74	17.48	0.38	0.60			
133.61	0.46	0.74	16.53	0.38	0.60			
128.93	0.46	0.72	15.58	0.37	0.59			
124.25	0.45	0.71	14.63	0.37	0.59			
119.57	0.44	0.70	13.66	0.37	0.58			
114.86	0.44	0.69	12.71	0.36	0.57			

Table C3.3: $\text{In}_{1.5}(\text{HfMg})_{0.25}\text{Mo}_3\text{O}_{12}$ Thermal Conductivity Data: C3 (as described in Chapter 9, Table 9.3); in order of data collection; where κ_m is the bulk thermal conductivity data as determined from the Klemen's model.³³²

T / K	$\kappa / \text{W m}^{-1} \text{K}^{-1}$	$\kappa_m / \text{W m}^{-1} \text{K}^{-1}$	T / K	$\kappa / \text{W m}^{-1} \text{K}^{-1}$	$\kappa_m / \text{W m}^{-1} \text{K}^{-1}$	T / K	$\kappa / \text{W m}^{-1} \text{K}^{-1}$	$\kappa_m / \text{W m}^{-1} \text{K}^{-1}$
303.95	0.62	0.87	101.70	0.39	0.55	5.58	0.22	0.30
299.85	0.61	0.85	97.01	0.38	0.53	4.52	0.18	0.25
293.50	0.61	0.85	92.36	0.38	0.52	3.54	0.13	0.19
287.73	0.61	0.85	87.72	0.37	0.51	2.60	0.09	0.12
282.42	0.61	0.85	83.04	0.36	0.50	2.11	0.05	0.08
277.18	0.61	0.85	78.53	0.35	0.49	2.07	0.05	0.07
271.96	0.60	0.84	74.24	0.35	0.48			
266.78	0.60	0.84	69.94	0.34	0.48			
261.61	0.60	0.84	65.82	0.34	0.47			
256.43	0.60	0.84	61.85	0.33	0.46			
251.27	0.60	0.84	58.00	0.33	0.46			
246.34	0.60	0.84	54.43	0.33	0.45			
241.66	0.60	0.83	50.98	0.32	0.45			
236.99	0.59	0.83	47.61	0.32	0.45			
232.30	0.59	0.83	44.51	0.32	0.44			
227.62	0.59	0.83	41.65	0.32	0.44			
222.95	0.59	0.82	38.97	0.32	0.44			
218.29	0.59	0.83	36.52	0.32	0.44			
213.63	0.59	0.82	34.21	0.32	0.44			
208.97	0.59	0.82	32.07	0.32	0.45			
204.31	0.58	0.82	30.13	0.32	0.45			
199.64	0.58	0.81	28.34	0.32	0.45			
194.97	0.58	0.81	26.68	0.32	0.45			
190.31	0.58	0.81	25.15	0.33	0.45			
185.63	0.58	0.81	23.74	0.33	0.45			
180.96	0.58	0.81	22.43	0.33	0.46			
176.31	0.58	0.81	21.21	0.33	0.46			
171.65	0.58	0.81	20.07	0.33	0.46			
166.99	0.57	0.80	19.00	0.33	0.46			
162.34	0.57	0.80	17.97	0.33	0.46			
157.67	0.58	0.80	17.00	0.34	0.47			
153.14	0.51	0.71	16.05	0.34	0.47			
148.44	0.49	0.68	15.10	0.33	0.46			
143.74	0.48	0.67	14.15	0.33	0.46			
139.05	0.47	0.65	13.21	0.33	0.46			
134.38	0.46	0.64	12.26	0.32	0.45			
129.72	0.45	0.63	11.31	0.32	0.44			
125.01	0.44	0.61	10.37	0.31	0.43			
120.36	0.43	0.60	9.43	0.30	0.42			
115.72	0.42	0.58	8.48	0.29	0.40			
111.05	0.41	0.57	7.51	0.27	0.37			
106.38	0.40	0.56	6.55	0.24	0.34			

C4 In₂Mo₃O₁₂

Table C4.1: In₂Mo₃O₁₂ Thermal Conductivity Data: D1 (as described in Chapter 9, Table 9.3); in order of data collection; where κ_m is the bulk thermal conductivity data as determined from the Klemen's model.³³²

T / K	$\kappa / \text{W m}^{-1} \text{K}^{-1}$	$\kappa_m / \text{W m}^{-1} \text{K}^{-1}$	T / K	$\kappa / \text{W m}^{-1} \text{K}^{-1}$	$\kappa_m / \text{W m}^{-1} \text{K}^{-1}$	T / K	$\kappa / \text{W m}^{-1} \text{K}^{-1}$	$\kappa_m / \text{W m}^{-1} \text{K}^{-1}$
300.49	0.21	0.40	27.25	0.20	0.37			
295.60	0.20	0.39	28.58	0.19	0.37			
286.34	0.20	0.37	29.84	0.19	0.37			
276.36	0.19	0.36	31.05	0.19	0.37			
266.52	0.19	0.35	32.18	0.19	0.36			
256.82	0.18	0.35	33.17	0.19	0.36			
245.66	0.18	0.35						
233.00	0.18	0.34						
220.37	0.18	0.34						
207.76	0.17	0.33						
195.16	0.17	0.33						
182.53	0.17	0.33						
169.90	0.17	0.32						
157.26	0.17	0.32						
144.63	0.17	0.32						
132.00	0.17	0.32						
119.38	0.16	0.31						
106.74	0.16	0.31						
94.09	0.16	0.31						
81.48	0.16	0.31						
70.26	0.16	0.31						
60.58	0.16	0.31						
50.84	0.17	0.32						
42.06	0.17	0.32						
34.80	0.17	0.33						
28.60	0.18	0.34						
23.44	0.18	0.35						
19.06	0.19	0.35						
15.30	0.18	0.35						
12.22	0.17	0.33						
9.64	0.15	0.29						
7.46	0.13	0.25						
5.58	0.10	0.19						
4.14	0.07	0.13						
3.43	0.04	0.08						
10.57	0.21	0.40						
15.23	0.20	0.37						
18.37	0.20	0.37						
20.74	0.20	0.38						
22.70	0.20	0.38						
24.39	0.20	0.38						
25.87	0.20	0.37						

Table C4.2: In₂Mo₃O₁₂ Thermal Conductivity Data: D2 (as described in Chapter 9, Table 9.3); in order of data collection; where κ_m is the bulk thermal conductivity data as determined from the Klemen's model.³³²

T/K	$\kappa/W\ m^{-1}\ K^{-1}$	$\kappa_m/W\ m^{-1}\ K^{-1}$	T/K	$\kappa/W\ m^{-1}\ K^{-1}$	$\kappa_m/W\ m^{-1}\ K^{-1}$	T/K	$\kappa/W\ m^{-1}\ K^{-1}$	$\kappa_m/W\ m^{-1}\ K^{-1}$
298.96	0.45	0.88	32.45	0.46	0.89			
295.20	0.44	0.86	30.13	0.47	0.91			
288.31	0.44	0.86	28.03	0.48	0.93			
281.53	0.44	0.85	26.12	0.49	0.96			
274.83	0.43	0.84	24.40	0.50	0.97			
268.15	0.43	0.84	22.84	0.51	1.00			
261.51	0.43	0.83	21.43	0.52	1.01			
254.89	0.43	0.83	20.14	0.53	1.03			
248.28	0.42	0.83	18.96	0.53	1.03			
241.66	0.42	0.82	17.87	0.53	1.04			
234.44	0.41	0.81	16.84	0.54	1.05			
226.60	0.41	0.80	15.88	0.54	1.05			
218.78	0.40	0.79	14.93	0.54	1.06			
210.97	0.40	0.78	13.99	0.53	1.05			
203.16	0.39	0.77	13.07	0.52	1.03			
195.33	0.39	0.76	12.16	0.52	1.02			
187.49	0.38	0.75	11.24	0.50	0.99			
179.66	0.38	0.75	10.33	0.49	0.96			
171.82	0.38	0.74	9.43	0.46	0.91			
164.01	0.38	0.74	8.51	0.44	0.86			
156.17	0.37	0.73	7.60	0.40	0.79			
148.34	0.37	0.73	6.67	0.37	0.72			
140.52	0.37	0.72	5.74	0.32	0.63			
132.72	0.37	0.72	4.79	0.25	0.49			
124.89	0.37	0.72	3.82	0.19	0.37			
117.66	0.37	0.72	2.91	0.12	0.24			
111.28	0.36	0.71	2.35	0.08	0.15			
104.63	0.36	0.71	2.30	0.07	0.14			
97.99	0.36	0.71	2.24	0.07	0.13			
91.39	0.36	0.71	2.22	0.06	0.12			
84.83	0.36	0.71	2.20	0.06	0.12			
78.56	0.37	0.72	2.75	0.10	0.21			
72.72	0.37	0.73	2.73	0.10	0.19			
67.24	0.38	0.74						
62.06	0.38	0.74						
57.13	0.39	0.76						
52.64	0.39	0.77						
48.54	0.40	0.78						
44.74	0.41	0.80						
41.19	0.42	0.82						
37.95	0.43	0.85						
35.06	0.44	0.87						

Table C4.3: In₂Mo₃O₁₂ Thermal Conductivity Data: D3 (as described in Chapter 9, Table 9.3); in order of data collection; where κ_m is the bulk thermal conductivity data as determined from the Klemen's model.³³²

T / K	$\kappa / \text{W m}^{-1} \text{K}^{-1}$	$\kappa_m / \text{W m}^{-1} \text{K}^{-1}$	T / K	$\kappa / \text{W m}^{-1} \text{K}^{-1}$	$\kappa_m / \text{W m}^{-1} \text{K}^{-1}$	T / K	$\kappa / \text{W m}^{-1} \text{K}^{-1}$	$\kappa_m / \text{W m}^{-1} \text{K}^{-1}$
299.48	0.40	0.782	22.79	0.44	0.866			
295.54	0.39	0.763	21.01	0.45	0.874			
287.95	0.39	0.764	19.44	0.45	0.888			
279.92	0.39	0.757	18.02	0.46	0.896			
271.97	0.38	0.751	16.75	0.46	0.899			
264.10	0.38	0.743	15.57	0.46	0.901			
256.27	0.38	0.741	14.50	0.46	0.895			
248.46	0.38	0.735	13.50	0.45	0.887			
240.64	0.37	0.731	12.55	0.45	0.876			
232.83	0.37	0.721	11.62	0.44	0.856			
224.99	0.36	0.711	10.72	0.43	0.834			
217.18	0.36	0.702	9.80	0.40	0.792			
209.37	0.35	0.689	8.88	0.38	0.746			
201.57	0.35	0.680	7.96	0.35	0.690			
193.74	0.34	0.672	7.03	0.32	0.622			
185.93	0.34	0.664	5.16	0.23	0.453			
178.08	0.34	0.659	4.22	0.18	0.354			
170.25	0.33	0.652	5.94	0.28	0.550			
162.42	0.33	0.651	11.49	0.50	0.985			
154.60	0.33	0.650	15.36	0.47	0.928			
146.78	0.33	0.642	18.20	0.47	0.920			
138.96	0.33	0.636	20.46	0.46	0.909			
131.13	0.33	0.636	22.33	0.47	0.912			
123.30	0.32	0.634	23.97	0.46	0.900			
115.51	0.32	0.630	25.40	0.45	0.879			
107.67	0.32	0.628	26.68	0.45	0.871			
99.82	0.32	0.624	27.86	0.45	0.883			
91.99	0.32	0.624	28.95	0.43	0.850			
84.20	0.32	0.626	30.00	0.43	0.838			
76.95	0.32	0.635	31.00	0.42	0.827			
70.26	0.33	0.637	31.94	0.42	0.818			
64.05	0.33	0.649	32.83	0.42	0.817			
58.23	0.34	0.659	33.61	0.41	0.807			
52.75	0.34	0.674						
47.85	0.35	0.692						
43.38	0.36	0.710						
39.31	0.37	0.730						
35.68	0.39	0.754						
32.47	0.40	0.778						
29.59	0.41	0.800						
27.03	0.42	0.823						
24.77	0.43	0.841						

C5 Y₂Mo₃O₁₂

Table C5.1: Y₂Mo₃O₁₂ Thermal Conductivity Data: E1 (as described in Chapter 9, Table 9.3); in order of data collection; where κ_m is the bulk thermal conductivity data as determined from the Klemen's model.³³²

T/K	$\kappa / \text{W m}^{-1} \text{K}^{-1}$	$\kappa_m / \text{W m}^{-1} \text{K}^{-1}$	T/K	$\kappa / \text{W m}^{-1} \text{K}^{-1}$	$\kappa_m / \text{W m}^{-1} \text{K}^{-1}$	T/K	$\kappa / \text{W m}^{-1} \text{K}^{-1}$	$\kappa_m / \text{W m}^{-1} \text{K}^{-1}$
298.17	0.47	0.91	99.33	0.45	0.87	15.66	0.37	0.71
295.11	0.48	0.92	95.45	0.45	0.86	14.75	0.36	0.70
289.34	0.48	0.93	91.71	0.45	0.86	13.82	0.35	0.67
283.57	0.49	0.93	88.12	0.44	0.86	12.74	0.33	0.64
278.13	0.49	0.94	84.52	0.44	0.85	11.82	0.32	0.61
273.00	0.49	0.94	80.99	0.44	0.85	10.91	0.30	0.58
267.87	0.48	0.93	77.58	0.44	0.85	9.98	0.28	0.54
262.75	0.48	0.93	74.27	0.43	0.84	9.67	0.27	0.52
257.65	0.48	0.93	71.06	0.43	0.83	9.66	0.27	0.52
252.55	0.48	0.93	67.95	0.43	0.83	9.65	0.27	0.52
247.45	0.48	0.93	65.00	0.43	0.82			
242.32	0.48	0.93	62.19	0.43	0.82			
237.18	0.48	0.93	59.43	0.43	0.82			
232.03	0.48	0.92	56.74	0.42	0.82			
226.41	0.48	0.92	54.21	0.42	0.81			
221.29	0.48	0.92	51.81	0.42	0.81			
216.16	0.48	0.92	49.51	0.42	0.81			
211.04	0.48	0.92	47.31	0.42	0.80			
206.17	0.47	0.91	45.23	0.42	0.80			
201.55	0.47	0.91	43.27	0.42	0.80			
196.95	0.47	0.91	41.39	0.42	0.80			
192.34	0.47	0.91	39.61	0.42	0.80			
187.71	0.47	0.91	37.93	0.42	0.80			
183.08	0.47	0.91	36.33	0.41	0.80			
178.44	0.47	0.91	34.83	0.42	0.80			
173.80	0.47	0.91	33.38	0.42	0.81			
169.18	0.47	0.90	32.00	0.42	0.80			
164.55	0.47	0.90	30.70	0.42	0.80			
159.91	0.47	0.90	29.47	0.42	0.80			
155.29	0.47	0.90	28.29	0.42	0.80			
150.66	0.47	0.90	27.16	0.42	0.80			
146.05	0.47	0.90	26.06	0.42	0.80			
141.42	0.47	0.90	25.02	0.42	0.80			
136.79	0.46	0.89	24.02	0.41	0.79			
132.36	0.46	0.89	23.05	0.41	0.80			
128.15	0.46	0.90	22.11	0.41	0.79			
123.92	0.46	0.90	21.17	0.41	0.79			
119.70	0.46	0.89	20.23	0.41	0.79			
115.47	0.46	0.88	19.32	0.40	0.77			
111.23	0.46	0.88	18.40	0.39	0.76			
107.16	0.46	0.88	17.48	0.39	0.75			
103.26	0.45	0.87	16.58	0.38	0.73			

Table C5.2: $Y_2Mo_3O_{12}$ Thermal Conductivity Data: E 2 (as described in Chapter 9, Table 9.3); in order of data collection; where κ_m is the bulk thermal conductivity data as determined from the Klemen's model.³³²

T/K	$\kappa/W\ m^{-1}\ K^{-1}$	$\kappa_m/W\ m^{-1}\ K^{-1}$	T/K	$\kappa/W\ m^{-1}\ K^{-1}$	$\kappa_m/W\ m^{-1}\ K^{-1}$	T/K	$\kappa/W\ m^{-1}\ K^{-1}$	$\kappa_m/W\ m^{-1}\ K^{-1}$
299.99	0.34	0.60	2.21	0.01	0.02			
295.38	0.34	0.60						
287.07	0.34	0.61						
278.97	0.34	0.61						
270.99	0.33	0.60						
262.22	0.33	0.59						
252.58	0.33	0.59						
242.94	0.32	0.58						
233.30	0.32	0.57						
223.69	0.31	0.56						
214.09	0.30	0.54						
204.49	0.29	0.52						
194.89	0.29	0.51						
185.24	0.28	0.50						
175.65	0.27	0.48						
165.99	0.26	0.47						
156.34	0.26	0.47						
146.73	0.26	0.46						
137.09	0.25	0.45						
127.47	0.25	0.44						
117.83	0.24	0.43						
108.17	0.24	0.43						
98.51	0.23	0.42						
88.90	0.23	0.41						
79.25	0.22	0.40						
69.55	0.22	0.39						
59.84	0.21	0.38						
51.02	0.21	0.38						
43.11	0.21	0.37						
35.83	0.21	0.38						
29.61	0.21	0.38						
24.44	0.21	0.38						
20.04	0.21	0.38						
16.27	0.20	0.36						
13.18	0.18	0.32						
10.53	0.15	0.27						
8.27	0.12	0.21						
6.34	0.08	0.15						
4.72	0.05	0.10						
3.52	0.03	0.06						
2.53	0.02	0.03						
2.26	0.01	0.02						

Table C5.3: $Y_2Mo_3O_{12}$ Thermal Conductivity Data: E 3 (as described in Chapter 9, Table 9.3); in order of data collection; where κ_m is the bulk thermal conductivity data as determined from the Klemen's model.³³²

T/K	$\kappa/W\ m^{-1}\ K^{-1}$	$\kappa_m/W\ m^{-1}\ K^{-1}$	T/K	$\kappa/W\ m^{-1}\ K^{-1}$	$\kappa_m/W\ m^{-1}\ K^{-1}$	T/K	$\kappa/W\ m^{-1}\ K^{-1}$	$\kappa_m/W\ m^{-1}\ K^{-1}$
298.22	0.42	0.88	84.73	0.33	0.70	4.98	0.08	0.16
295.23	0.41	0.87	80.47	0.33	0.69	4.06	0.06	0.13
289.41	0.41	0.86	76.38	0.33	0.68	7.15	0.13	0.27
283.62	0.41	0.86	72.45	0.32	0.68	12.21	0.21	0.45
277.82	0.41	0.85	68.67	0.32	0.67	15.62	0.23	0.47
272.04	0.40	0.85	65.04	0.31	0.66	18.23	0.24	0.51
266.26	0.40	0.84	61.49	0.31	0.65	20.36	0.26	0.54
260.50	0.40	0.84	58.06	0.31	0.64	22.17	0.26	0.55
254.74	0.40	0.84	54.74	0.30	0.64	23.78	0.27	0.56
249.30	0.40	0.84	51.60	0.30	0.63	25.17	0.27	0.57
244.16	0.40	0.83	48.63	0.30	0.62	26.40	0.27	0.58
239.03	0.39	0.83	45.86	0.29	0.61	27.53	0.28	0.58
233.89	0.39	0.83	43.28	0.29	0.61	28.58	0.28	0.59
228.74	0.39	0.82	40.83	0.29	0.60	29.56	0.29	0.60
223.60	0.39	0.82	38.55	0.28	0.59	30.48	0.28	0.59
218.47	0.39	0.82	36.41	0.28	0.59	31.34	0.28	0.60
213.36	0.39	0.81	34.39	0.28	0.59	32.15	0.28	0.60
208.22	0.38	0.81	32.48	0.28	0.58	32.88	0.29	0.60
203.10	0.38	0.80	30.71	0.27	0.58	33.45	0.29	0.60
197.99	0.38	0.80	29.05	0.27	0.57	7.53	0.13	0.27
192.86	0.38	0.80	27.52	0.27	0.57	6.43	0.11	0.24
187.72	0.38	0.80	26.09	0.27	0.56	5.42	0.09	0.19
182.58	0.38	0.80	24.72	0.26	0.55	4.17	0.06	0.13
177.43	0.38	0.79	23.45	0.26	0.55	4.01	0.06	0.12
172.30	0.38	0.79	22.23	0.26	0.54	3.95	0.05	0.11
167.16	0.37	0.78	21.10	0.25	0.53	3.95	0.05	0.11
162.03	0.37	0.78	20.03	0.25	0.53	3.95	0.05	0.11
156.91	0.37	0.78	19.02	0.25	0.52	3.44	0.04	0.09
151.78	0.37	0.78	18.05	0.24	0.50	2.44	0.03	0.06
146.65	0.37	0.77	17.11	0.24	0.50	2.08	0.02	0.04
141.51	0.37	0.77	16.15	0.23	0.48	2.12	0.02	0.04
136.38	0.36	0.76	15.22	0.22	0.47	2.13	0.02	0.04
131.26	0.36	0.76	14.28	0.21	0.45			
126.14	0.36	0.75	13.36	0.21	0.43			
121.01	0.36	0.75	12.43	0.19	0.41			
116.12	0.36	0.75	11.51	0.18	0.39			
111.50	0.35	0.74	10.58	0.17	0.36			
106.86	0.35	0.74	9.68	0.16	0.33			
102.22	0.35	0.72	8.73	0.15	0.31			
97.58	0.34	0.72	7.79	0.13	0.27			
93.14	0.34	0.71	6.86	0.11	0.24			
88.94	0.34	0.71	5.91	0.10	0.20			

APPENDIX D - DSC

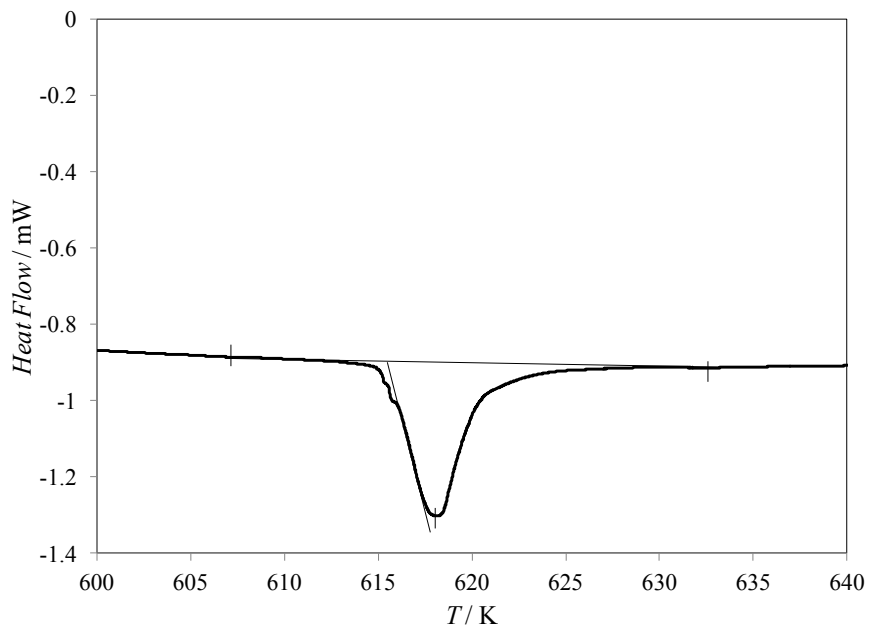


Figure D1.1: The DSC scan for $\text{In}_2\text{Mo}_3\text{O}_{12}$ at a heating rate of 5 K min^{-1} (exotherm up) shows the phase transition at an onset temperature of 615 K.

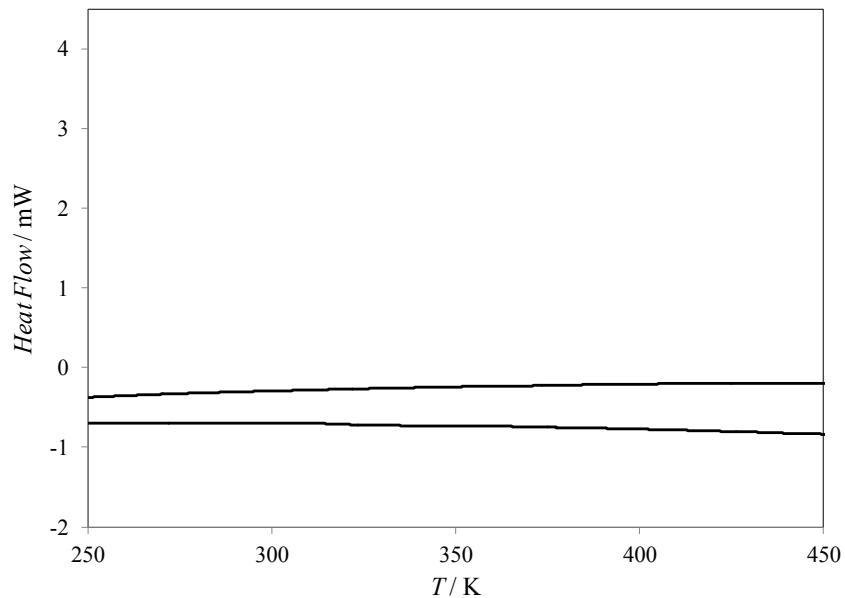


Figure D1.2: The DSC scan for a 98.275 mg sample of Sapphire at a heating rate of 10 K min^{-1} (exotherm up) shows a typical baseline from 250 K to 450 K on heating (top line) and cooling (bottom line).

APPENDIX E – X-RAY POWDER DIFFRACTION

E1 In(HfMg)_{0.5}Mo₃O₁₂

Table E1.1 Lattice parameters for In(HfMg)_{0.5}Mo₃O₁₂, on heating, as determined by Le Bail fitting.

$T / ^\circ\text{C}$	$a / \text{Å}$	$b / \text{Å}$	$c / \text{Å}$	$\beta / ^\circ$	$V / \text{Å}^3$	X^2
25	16.213(4)	9.5556(3)	18.880(2)	125.40886	2384.0(7)	2.14
50	16.217(0)	9.5605(0)	18.886(1)	125.40994	2386.5(3)	2.32
75	16.223(5)	9.5656(0)	18.896(4)	125.42087	2389.7(3)	2.43
100	16.232(8)	9.5725(1)	18.911(1)	125.43149	2393.0(8)	2.48
125	16.241(1)	9.5791(5)	18.928(0)	125.45454	2396.3(0)	2.72
150	16.245(3)	9.6075(9)	18.958(0)	125.40916	2411.6(3)	2.92
175	9.625(8)	13.2553(9)	9.52797)	-	1215.6(7)	3.92
200	9.626(3)	13.2574(0)	9.527(8)	-	1215.9(4)	3.57
225	9.625(6)	13.2589(7)	9.527(8)	-	1215.9(9)	3.36
250	9.624(7)	13.2605(5)	9.526(9)	-	1215.9(2)	3.20
275	9.623(4)	13.2623(6)	9.526(3)	-	1215.8(3)	3.25
300	9.622(5)	13.2647(4)	9.526(3)	-	1215.9(4)	3.21
325	9.620(8)	13.2662(0)	9.525(3)	-	1215.7(2)	3.08
350	9.619(4)	13.2677(8)	9.524(5)	-	1215.6(0)	3.06
375	9.618(6)	13.2696(7)	9.524(2)	-	1215.6(3)	3.22
400	9.617(4)	13.2709(3)	9.523(5)	-	1215.5(0)	3.09
425	9.616(4)	13.2727(3)	9.523(2)	-	1215.5(0)	3.02
450	9.615(8)	13.2747(2)	9.522(9)	-	1215.5(8)	3.07
475	9.614(9)	13.2766(5)	9.522(5)	-	1215.5(9)	3.11
500	9.614(0)	13.2780(9)	9.522(2)	-	1215.5(6)	3.14
525	9.613(3)	13.2796(8)	9.521(6)	-	1215.5(5)	3.08
550	9.612(1)	13.2811(6)	9.521(1)	-	1215.4(6)	3.05
575	9.610(8)	13.2823(1)	9.520(6)	-	1215.3(3)	2.80
600	9.609(9)	13.2842(3)	9.520(0)	-	1215.3(3)	3.25
625	9.608(5)	13.2849(2)	9.519(5)	-	1215.1(4)	2.89
650	9.607(9)	13.2871(2)	9.519(2)	-	1215.2(3)	2.97
675	9.606(8)	13.2886(1)	9.518(7)	-	1215.1(7)	3.03
700	9.605(3)	13.2887(6)	9.517(4)	-	1214.8(3)	2.48

Table E1.2 Lattice parameters for $\text{In}(\text{HfMg})_{0.5}\text{Mo}_3\text{O}_{12}$, on cooling, as determined by Le Bail fitting.

$T / ^\circ\text{C}$	$a / \text{Å}$	$b / \text{Å}$	$c / \text{Å}$	$\beta / ^\circ$	$V / \text{Å}^3$	χ^2
25	16.217(9)	9.5587(4)	18.883(6)	125.42(0)	2385.5(9)	2.57
50	16.222(2)	9.5625(7)	18.890(9)	125.42(5)	2387.9(9)	3.04
75	16.226(8)	9.5655(4)	18.899(9)	125.43(6)	2390.2(2)	3.19
100	16.234(2)	9.5709(3)	18.911(3)	125.44(7)	2393.7(5)	3.31
125	16.254(6)	9.5844(2)	18.938(3)	125.50(0)	2401.9(8)	5.19
150	16.215(4)	9.6130(8)	18.981(3)	125.29(3)	2415.0(1)	3.51
175	9.626(2)	13.2561(6)	9.528(8)	-	1215.9(3)	4.28
200	9.625(1)	13.2563(2)	9.527(8)	-	1215.6(9)	3.53
225	9.624(0)	13.2581(7)	9.527(1)	-	1215.6(2)	3.60
250	9.622(9)	13.2603(2)	9.526(7)	-	1215.6(3)	3.49
275	9.622(3)	13.2626(1)	9.526(6)	-	1215.7(6)	3.30
300	9.620(9)	13.2638(6)	9.525(6)	-	1215.5(7)	3.18
325	9.619(8)	13.2663(3)	9.525(2)	-	1215.6(0)	3.10
350	9.618(4)	13.2671(6)	9.524(3)	-	1215.3(8)	3.09
375	9.617(5)	13.2696(2)	9.524(0)	-	1215.4(6)	3.09
400	9.616(7)	13.2709(8)	9.523(3)	-	1215.3(8)	3.01
425	9.615(8)	13.2732(4)	9.523(0)	-	1215.4(5)	2.90
450	9.614(8)	13.2750(1)	9.522(6)	-	1215.4(3)	2.94
475	9.613(6)	13.2762(3)	9.521(7)	-	1215.2(7)	2.72
500	9.613(2)	13.2782(1)	9.521(6)	-	1215.3(9)	2.81
525	9.612(1)	13.2795(5)	9.521(1)	-	1215.3(2)	2.85
550	9.611(2)	13.2811(7)	9.520(8)	-	1215.3(0)	2.95
575	9.610(3)	13.2824(4)	9.520(3)	-	1215.2(5)	2.87
600	9.609(3)	13.2841(0)	9.519(6)	-	1215.1(8)	2.77
625	9.608(4)	13.2855(7)	9.519(4)	-	1215.1(9)	2.72
650	9.607(8)	13.2875(1)	9.519(3)	-	1215.2(7)	3.08
675	9.606(9)	13.2892(9)	9.518(8)	-	1215.2(6)	3.11
700	9.605(3)	13.2887(6)	9.517(4)	-	1214.8(3)	2.48

E2 In_{1.5}(HfMg)_{0.5}Mo₃O₁₂Table E2.1 Lattice parameters for In_{1.5}(HfMg)_{0.5}Mo₃O₁₂, on heating, as determined by Le Bail fitting.

<i>T</i> / °C	<i>a</i> / Å	<i>b</i> / Å	<i>c</i> / Å	<i>β</i> / °	<i>V</i> / Å ³	<i>X</i> ²
25	16.224(0)	9.5605(1)	18.875(3)	125.34(3)	2388.1(7)	1.82
50	16.227(6)	9.562(6)	18.882(0)	125.35(6)	2389.6(9)	1.68
75	16.230(4)	9.5646(9)	18.888(7)	125.36(3)	2391.2(7)	1.79
100	16.233(4)	9.5666(5)	18.896(3)	125.36(6)	2393.0(6)	1.87
125	16.239(0)	9.5701(9)	18.907(0)	125.37(3)	2395.9(2)	1.92
150	16.244(2)	9.5745(2)	18.915(6)	125.37(6)	2398.7(7)	2.25
175	16.252(4)	9.5790(6)	18.930(7)	125.40(3)	2402.2(3)	2.45
200	16.256(0)	9.5826(8)	18.939(9)	125.42(9)	2404.0(7)	3.04
225	16.266(0)	9.5889(1)	18.962(6)	125.48(4)	2408.3(8)	3.20
250	9.630(6)	13.2691(8)	9.533(0)		1218.2(3)	6.29
275	9.639(3)	13.2755(2)	9.538(5)		1220.6(0)	3.59
300	9.640(7)	13.2763(0)	9.539(6)		1221.0(0)	2.65
325	9.640(2)	13.2773(9)	9.539(9)		1221.0(9)	2.80
350	9.638(6)	13.2795(5)	9.539(2)		1220.9(8)	2.71
375	9.637(8)	13.2810(3)	9.538(4)		1220.9(1)	2.92
400	9.636(6)	13.2821(3)	9.537(2)		1220.7(1)	2.85
425	9.634(3)	13.2828(8)	9.536(3)		1220.3(7)	3.66
450	9.632(7)	13.2839(6)	9.535(4)		1220.1(5)	3.83
475	9.631(6)	13.2854(9)	9.534(9)		1220.0(8)	3.96
500	9.630(9)	13.2880(6)	9.534(5)		1220.1(9)	4.12
525	9.629(6)	13.2897(3)	9.534(1)		1220.1(3)	3.87
550	9.629(3)	13.2921(1)	9.533(6)		1220.2(3)	4.11
575	9.628(3)	13.2939(5)	9.533(4)		1220.2(6)	4.45
600	9.626(9)	13.2955(8)	9.532(4)		1220.1(1)	4.17
625	9.625(6)	13.2970(0)	9.532(0)		1220.0(1)	4.37
650	9.624(2)	13.2985(4)	9.531(5)		1219.9(2)	4.55
675	9.623(5)	13.3007(1)	9.531(1)		1219.9(7)	4.65
700	9.622(4)	13.3028(1)	9.530(4)		1219.9(3)	4.92


Table E2.2 Lattice parameters for $\text{In}_{1.5}(\text{HfMg})_{0.5}\text{Mo}_3\text{O}_{12}$, on cooling, as determined by Le Bail fitting.

$T / ^\circ\text{C}$	$a / \text{Å}$	$b / \text{Å}$	$c / \text{Å}$	$\beta / ^\circ$	$V / \text{Å}^3$	χ^2
25	16.223(6)	9.5614(5)	18.879(7)	125.35(8)	2388.4(7)	1.94
50	16.224(1)	9.5611(1)	18.881(9)	125.36(3)	2388.5(7)	1.97
75	16.226(4)	9.5619(7)	18.888(0)	125.36(9)	2389.7(4)	2.12
100	16.231(3)	9.5641(2)	18.896(8)	125.37(7)	2391.8(7)	2.17
125	16.236(0)	9.5669(2)	18.906(6)	125.38(0)	2394.4(1)	2.56
150	16.238(9)	9.5703(1)	18.912(8)	125.38(6)	2396.3(0)	3.11
175	16.248(8)	9.5761(7)	18.926(0)	125.42(5)	2399.7(2)	3.12
200	16.255(2)	9.5798(7)	18.939(5)	125.45(8)	2402.3(1)	3.62
225	16.270(8)	9.5911(2)	18.974(6)	125.51(0)	2410.3(8)	3.97
250	9.638(5)	13.2757(7)	9.538(9)		1220.5(9)	4.86
275	9.641(9)	13.2782(2)	9.540(3)		1221.4(2)	4.06
300	9.642(2)	13.2781(7)	9.540(7)		1221.5(1)	3.98
325	9.640(6)	13.2788(0)	9.540(1)		1221.2(8)	3.87
350	9.639(5)	13.2809(3)	9.539(5)		1221.2(6)	4.01
375	9.638(2)	13.2823(5)	9.538(3)		1221.0(8)	4.36
400	9.637(3)	13.2848(5)	9.537(8)		1221.1(2)	4.49
425	9.636(1)	13.2867(8)	9.537(1)		1221.0(6)	4.66
450	9.633(8)	13.2867(0)	9.536(1)		1220.6(4)	5.58
475	9.632(2)	13.2875(5)	9.534(8)		1220.3(4)	6.04
500	9.630(6)	13.2888(1)	9.534(2)		1220.1(8)	6.03
525	9.629(5)	13.2902(5)	9.533(4)		1220.0(6)	6.22
550	9.628(4)	13.2920(9)	9.532(9)		1220.0(3)	6.32
575	9.627(7)	13.2939(3)	9.532(3)		1220.0(4)	6.44
600	9.626(8)	13.2959(9)	9.532(1)		1220.0(8)	6.55
625	9.625(4)	13.2974(9)	9.531(4)		1219.9(6)	6.48
650	9.624(0)	13.2986(6)	9.530(9)		1219.8(2)	6.54
675	9.622(8)	13.3002(6)	9.530(4)		1219.7(5)	6.43
700	9.621(9)	13.3013(0)	9.529(8)		1219.6(7)	6.17

APPENDIX F – COPYRIGHT AGREEMENT LETTERS

PERMISSION FOR FIGURE 1.5 IN CHAPTER 1.



 **ACS Publications** High quality. High impact. **Title:** Negative Thermal Expansion and Phase Transitions in the ZrV₂-xPxO₇ Series

Author: V. Korthuis, N. Khosrovani, A. W. Sleight, N. Roberts, R. Dupree, and W. W. Jr. Warren

Publication: Chemistry of Materials

Publisher: American Chemical Society

Date: Feb 1, 1995

Copyright © 1995, American Chemical Society


PERMISSION/LICENSE IS GRANTED FOR YOUR ORDER AT NO CHARGE

This type of permission/license, instead of the standard Terms & Conditions, is sent to you because no fee is being charged for your order. Please note the following:

- Permission is granted for your request in both print and electronic formats, and translations.
- If figures and/or tables were requested, they may be adapted or used in part.
- Please print this page for your records and send a copy of it to your publisher/graduate school.
- Appropriate credit for the requested material should be given as follows: "Reprinted (adapted) with permission from (COMPLETE REFERENCE CITATION). Copyright (YEAR) American Chemical Society." Insert appropriate information in place of the capitalized words.
- One-time permission is granted only for the use specified in your request. No additional uses are granted (such as derivative works or other editions). For any other uses, please submit a new request.

PERMISSION FOR FIGURE 1.6 IN CHAPTER 1.



 **ACS Publications** Title: Negative Thermal Expansion in ZrW₂O₈ and HfW₂O₈
High quality. High impact.

Author: J. S. O. Evans et al.
Publication: Chemistry of Materials
Publisher: American Chemical Society
Date: Jan 1, 1996
Copyright © 1996, American Chemical Society

PERMISSION/LICENSE IS GRANTED FOR YOUR ORDER AT NO CHARGE

This type of permission/license, instead of the standard Terms & Conditions, is sent to you because no fee is being charged for your order. Please note the following:

- Permission is granted for your request in both print and electronic formats, and translations.
- If figures and/or tables were requested, they may be adapted or used in part.
- Please print this page for your records and send a copy of it to your publisher/graduate school.
- Appropriate credit for the requested material should be given as follows: "Reprinted (adapted) with permission from (COMPLETE REFERENCE CITATION). Copyright (YEAR) American Chemical Society." Insert appropriate information in place of the capitalized words.
- One-time permission is granted only for the use specified in your request. No additional uses are granted (such as derivative works or other editions). For any other uses, please submit a new request.

PERMISSION FOR FIGURE 1.7 IN CHAPTER 1.

License Details

This is a License Agreement between Kimberly J Miller ("You") and Elsevier ("Elsevier"). The license consists of your order details, the terms and conditions provided by Elsevier, and the payment terms and conditions.

License Number	3018180876524
License date	Oct 29, 2012
Licensed content publisher	Elsevier
Licensed content publication	Journal of Solid State Chemistry
Licensed content title	Polymorphism in yttrium molybdate Y ₂ Mo ₃ O ₁₂
Licensed content author	Stacy D. Gates, Cora Lind
Licensed content date	December 2007
Licensed content volume number	180
Licensed content issue number	12
Number of pages	5
Type of Use	reuse in a thesis/dissertation
Portion	figures/tables/illustrations
Number of figures/tables/illustrations	1
Format	both print and electronic
Are you the author of this Elsevier article?	No
Will you be translating?	No
Order reference number	None
Title of your thesis/dissertation	Towards Zero-Thermal Expansion Materials
Expected completion date	Oct 2012
Estimated size (number of pages)	250
Elsevier VAT number	GB 494 6272 12
Permissions price	0.00 USD
VAT/Local Sales Tax	0.0 USD / 0.0 GBP
Total	0.00 USD

PERMISSION FOR FIGURE 1.8 IN CHAPTER 1.



AMERICAN PHYSICAL SOCIETY

One Physics Ellipse, College Park, MD 20740 · <http://www.aps.org>

October 31, 2012

Kimberly J. Miller, B.Sc. M.Sc., Ph.D. Candidate
Department of Chemistry
Dalhousie University
Halifax NS, Canada

Ref # 21539

Thank you for your permission request dated October 29, 2012. We are pleased to grant you a non-exclusive, non-transferable permission, English rights, limited to **print and electronic format**, provided you meet the criteria outlined below. Permission is for a one-time use and does not include permission for future editions, updates, databases, translations, or any other matters. Permission must be sought for each additional use. This permission does not include the right to modify APS material.

Please print the required copyright credit line on the first page that the material appears: "Reprinted (abstract/excerpt/figure) with permission from [FULL REFERENCE CITATION] as follows: authors names, journal title, volume number, page number and year of publication. Copyright (YEAR) by the American Physical Society.

The following language must appear somewhere on the website: "Readers may view, browse, and/or download material for temporary copying purposes only, provided these uses are for noncommercial personal purposes. Except as provided by law, this material may not be further reproduced, distributed, transmitted, modified, adapted, performed, displayed, published, or sold in whole or part, without prior written permission from the American Physical Society."

Provide a hyperlink from the reprinted APS material (the hyperlink may be embedded in the copyright credit line). APS's link manager technology makes it convenient and easy to provide links to individual articles in APS journals. For information, see: <http://link.aps.org/>.

You must also obtain permission from at least one of the authors for each separate work, if you haven't done so already. The author's name and address can be found on the first page of the published Article.

Use of the APS material must not imply any endorsement by the American Physical Society.

Permission is granted for use of the following APS material only:

- Fig. 3, Phys. Rev. B 78, 054114 (2008)

Permission is limited to the single title specified of the publication as follows:

A thesis entitled, "Towards zero thermal expansion materials," to be published by Dalhousie University

If you have any questions, please refer to the Copyright FAQ at: <http://publish.aps.org/copyrightFAQ.html> or send an email to assocpub@aps.org.

Sincerely,

Melissa Overton
Publications Marketing Coordinator

PERMISSIONS FOR FIGURES 4.1, 4.2, 4.3, AND 4.4 IN CHAPTER 4.

License Details

This is a License Agreement between Kimberly J Miller ("You") and Springer ("Springer"). The license consists of your order details, the terms and conditions provided by Springer, and the payment terms and conditions.

License Number	3018200130982
License date	Oct 29, 2012
Licensed content publisher	Springer
Licensed content publication	Journal of Sol-Gel Science and Technology
Licensed content title	Rapid synthesis of the low thermal expansion phase of $\text{Al}_2\text{Mo}_3\text{O}_{12}$ via a sol-gel method using polyvinyl alcohol
Licensed content author	Monica Ari
Licensed content date	Jan 1, 2010
Volume number	58
Issue number	1
Type of Use	Thesis/Dissertation
Portion	Full text
Number of copies	4
Author of this Springer article	Yes and you are the sole author of the new work
Title of your thesis / dissertation	Towards Zero-Thermal Expansion Materials
Expected completion date	Oct 2012
Estimated size(pages)	250

PERMISSIONS FOR FIGURES 5.1, 5.2, 5.4, AND 5.5 IN CHAPTER 5 AND FIGURE 9.3 IN CHAPTER 9.



RightsLink®



ACS Publications
High quality. High impact.

Title: Correlation between AO6 Polyhedral Distortion and Negative Thermal Expansion in Orthorhombic Y₂Mo₃O₁₂ and Related Materials

Author: Bojan A. Marinkovic, Monica Ari, Roberto R. de Avillez, Fernando Rizzo, Fabio F. Ferreira, Kimberly J. Miller, Michel B. Johnson, and Mary Anne White

Publication: Chemistry of Materials

Publisher: American Chemical Society

Date: Jul 1, 2009

Copyright © 2009, American Chemical Society

PERMISSION/LICENSE IS GRANTED FOR YOUR ORDER AT NO CHARGE

This type of permission/license, instead of the standard Terms & Conditions, is sent to you because no fee is being charged for your order. Please note the following:

- Permission is granted for your request in both print and electronic formats, and translations.
- If figures and/or tables were requested, they may be adapted or used in part.
- Please print this page for your records and send a copy of it to your publisher/graduate school.
- Appropriate credit for the requested material should be given as follows: "Reprinted (adapted) with permission from (COMPLETE REFERENCE CITATION). Copyright (YEAR) American Chemical Society." Insert appropriate information in place of the capitalized words.
- One-time permission is granted only for the use specified in your request. No additional uses are granted (such as derivative works or other editions). For any other uses, please submit a new request.

PERMISSIONS FOR FIGURES 6.1, 6.2, 6.3, 6.4, 6.5, AND 6.6 IN CHAPTER 6 AND FIGURES 9.1, 9.7, AND 9.18 IN CHAPTER 9.

License Details

This is a License Agreement between Kimberly J Miller ("You") and Elsevier ("Elsevier"). The license consists of your order details, the terms and conditions provided by Elsevier, and the payment terms and conditions.

License Number	3018190785647
License date	Oct 29, 2012
Licensed content publisher	Elsevier
Licensed content publication	Solid State Communications
Licensed content title	Low-temperature investigations of the open-framework material HfMgMo ₃ O ₁₂
Licensed content author	Kimberly J. Miller, Michel B. Johnson, Mary Anne White, Bojan A. Marinkovic
Licensed content date	September 2012
Licensed content volume number	152
Licensed content issue number	18
Number of pages	5
Type of Use	reuse in a thesis/dissertation
Portion	full article
Format	both print and electronic
Are you the author of this Elsevier article?	Yes
Will you be translating?	No
Order reference number	None
Title of your thesis/dissertation	Towards Zero-Thermal Expansion Materials
Expected completion date	Oct 2012
Estimated size (number of pages)	250
Elsevier VAT number	GB 494 6272 12
Permissions price	0.00 USD
VAT/Local Sales Tax	0.0 USD / 0.0 GBP
Total	0.00 USD

REFERENCES

- (1) Evans, J. S. O.; Mary, T. A.; Sleight, A. W. *Physica B* **1998**, *241–243*, 311–316.
- (2) Sleight, A. W. *Curr. Opin. Solid State Mater. Sci.* **1998**, *3*, 128–131.
- (3) Sleight, A. W. *Annu. Rev. Mater. Sci.* **1998**, *28*, 29–43.
- (4) Barrera, G. D.; Bruno, J. A. O. Barron, T. H. K.; Allan, N. L. *J. Phys.: Condens. Matter* **2005**, *17*, R217–R252.
- (5) Grima, J. N.; Zammit, V.; Gatt, R. *Xjenza* **2006**, *11*, 17–29.
- (6) Miller, W.; Smith, C. W.; Mackenzie, D. S. Evans, K. E. *J. Mater. Sci.* **2009**, *44*, 5441–5451.
- (7) Takenaka, K. *Sci. Technol. Adv. Mater.* 2012, *13*, 013001:1-12.
- (8) Lind, C. *Materials* **2012**, *5*, 1125-1124.
- (9) Liang, E.-J. *Recent Pat. Mater. Sci.* **2010**, *3*, 106–128.
- (10) White, G. K. *Contemp. Phys.* **1993**, *34*, 193–204.
- (11) Swenson, C. A. *J. Phys. Chem. Ref. Data* **1983**, *12*, 179–182.
- (12) Holman, G. J. F.; ten Seldam, C. A. *J. Phys. Chem. Ref. Data* **1994**, *23*, 807–827.
- (13) Straumanis, M. E. *Monatsh. Chem.* **1971**, *102*, 1377–1386.
- (14) Krishnan, R. S. *Nature* **1944**, *154*, 486–487.
- (15) Buffington, R. M.; Latimer, W. M. *Coeff. Expans.* **1926**, *48*, 2 305–2319.
- (16) Röttger, K.; Endriss, A.; Ihringer, J. *Acta Crystallogr., Sect. B: Struct. Sci.* **1994**, *50*, 644–648.
- (17) LaPlaca, S.; Post, B. *Acta Crystallogr.* **1960**, *13*, 503–505.
- (18) White, M. A. *Physical Properties of Materials*; CRC Press: Boca Raton, FL, 2012.
- (19) Nye, J. F. *Physical Properties of Crystals, Their Representation by Tensors and Matrices*; Oxford University Press: New York, 1985.

-
- (20) Krupke, W. F.; Shinn, M. D.; Marion, J. E.; Caird, J. A.; Stokowski, S. E. *J. Opt. Soc. Am. B* **1986**, *3*, 102–114.
- (21) Evans, J. S. O. *J. Chem. Soc. Dalton Trans.* **1999**, 3317–3326.
- (22) Barron, T. H. K.; White, G. K. *Heat Capacity and Thermal Expansion at Low Temperatures*; Kluwer Academic/Plenum Publishers: New York, 1999.
- (23) Gatt, R.; Grima, J. N. *Phys. Status Solidi* **2008**, *2*, 236–238.
- (24) Grima, J. N.; Attard, D.; Gatt, R. *Science* **2011**, *331*, 687–688.
- (25) Pryde, A. K. A.; Hammonds, K. D.; Dove, M. T.; Heine, V.; Gale, J. D.; Warren, M. C. *J. Phys.: Condens. Matter* **1996**, *8*, 10973–10982.
- (26) Dove, M. T.; Trachenko, K. O.; Tucker, M. G.; Keen, D. A. *Rev. Mineral. Geochem.* **2000**, *39*, 1–33.
- (27) Dove, M. T.; Giddy, A. P.; Heine, V. *Trans. Am. Crystallogr. Assoc.* **1991**, *27*, 65–75.
- (28) Dove, M. T.; Gambhir, M.; Heine, V. *Phys. Chem. Miner.* **1999**, *26*, 344–353.
- (29) Dove, M. T.; Heine, V.; Hammonds, K. D. *Mineral. Mag.* **1995**, *59*, 629–639.
- (30) Hammonds, K. D.; Dove, M. T.; Giddy, A. P.; Heine, V.; Winkler, B. *Am. Mineral.* **1996**, *81*, 1057–1079.
- (31) Welche, P. R. L.; Heine, V.; Dove, M. T. *Phys. Chem. Miner.* **1998**, *26*, 63–77.
- (32) Evans, J. S. O.; David, W. I. F.; Sleight, A. W. *Acta Crystallogr., Sect. B: Struct. Sci.* **1999**, *55*, 333–340.
- (33) Heine, V.; Welche, P. R. L.; Dove, M. T. *J. Am. Ceram. Soc.* **1999**, *82*, 1793–1802.
- (34) Withers, R. L.; Tabira, Y.; Evans, J. S. O.; King, I. J.; Sleight, A. W. *J. Solid State Chem.* **2001**, *157*, 186–192.
- (35) Marinkovic, B. A.; Ari, M.; de Avillez, R. R.; Rizzo, F.; Ferreira, F. F.; Miller, K. J.; Johnson, M. B.; White, M. A. *Chem. Mater.* **2009**, *21*, 2886–2894.
- (36) Tao J. Z.; Sleight, A. W. *J. Solid State Chem.* **2003**, *173*, 442–448.

-
- (37) Hammonds, K. D.; Dove, M. T.; Giddy, A. P.; Heine, V. *Am. Mineral.* **1994**, *79*, 1207–1209.
- (38) Evans, J. S. O.; Mary, T. A.; Sleight, A. W. *J. Solid State Chem.* **1997**, *133*, 580–583.
- (39) Goodwin, A. L.; Kepert, C. J. *Phys. Rev. B* **2005**, *71*, 140301:1–4.
- (40) Lakes, R. *J. Mater. Sci. Lett.* **1996**, *15*, 475–477.
- (41) Jefferson, G.; Parthasarathy, T. A.; Kerans, R. J. *Int. J. Solids Struct.* **2009**, *46*, 2372–2387.
- (42) Berger, J.; Mercer, C.; McMeeking, R. M.; Evans A. G. *J. Am. Ceram. Soc.* **2011**, *94*, s42–s54.
- (43) Grima, J. N.; Ellul, B.; Attard, D.; Gatt, R.; Attard, M. *Compos. Sci. Technol.* **2010**, *70*, 2248–2252.
- (44) Lim, T.-C. *J. Mater. Sci.* **2012**, *47*, 368–373.
- (45) Chen, J.; Nittala, K.; Forrester, J. S.; Jones, J. L.; Deng, J.; Yu, R.; Xing, X. *J. Am. Chem. Soc.* **2011**, *133*, 11114–11117.
- (46) Azuma, M.; Chen, W.-t.; Seki, H.; Czapski, M.; Olga, S.; Oka, K.; Mizumaki, M.; Watanuki, T.; Ishimatsu, N.; Kawamura, N.; Ishiwata, S.; Tucker, M. G.; Shimakawa, Y.; Attfield, J. P. *Nat. Commun.* **2011**, *2*, 347:1–5.
- (47) Yamada, I.; Tsuchida, K.; Ohgushi, K.; Hayashi, N.; Kim, J.; Tsuji, N.; Takahashi, R.; Matsushita, M.; Nishiyama, N.; Inoue, T.; Irifune, T.; Kato, K.; Takata, M.; Takano, M. *Angew. Chem. Int. Ed.* **2011**, *50*, 6579–6582.
- (48) Takenaka, K.; Takagib, H. *Appl. Phys. Lett.* **2005**, *87*, 261902:1–3.
- (49) Takenaka, K.; Asano, K.; Misawa, M.; Takagi, H. *Appl. Phys. Lett.* **2008**, *92*, 011927:1–3.
- (50) Seyidov, M. Y.; Suleymanov, R. A. *J. Appl. Phys.* **2010**, *108*(6), 063540:1–6.
- (51) Qi, T. F.; Korneta, O. B.; Parkin, S.; De Long, L. E.; Schlottmann, P.; Cao, G. *Phys. Rev. Lett.* **2010**, *105*, 177203:1–4.
- (52) Qi, T. F.; Ge, M.; Korneta, O. B.; Parkin, S.; De Long, L. E.; Cao, G. *J. Sol. State Chem.* **2011**, *184*, 893–898.

-
- (53) Lupis, C. H. P. *Chemical Thermodynamics of Materials*; Elsevier Science Publishing Co., Inc.: New York, 1983.
- (54) Kitaigorodskii, A. I. *Molecular Crystals and Molecules*; Academic Press: New York, 1973.
- (55) Ott J. B.; Boerio-Goates, J. *Chemical Thermodynamics Vol. 1, Principles and Applications*; Academic Press: San Diego, 2000.
- (56) Dulong, P. L.; Petit, A. T. *Ann. Chim. Phys.* **1819**, *10*, 395-413.
- (57) Kennedy, C. A.; White, M. A. *Solid State Commun.* **2005**, *134*, 271–276.
- (58) Evans, J. S. O.; Mary, T. A.; Vogt, T.; Subramanian, M. A.; Sleight, A. W. *Chem. Mater.* **1996**, *8*, 2809–2823.
- (59) Degueldre, C.; Tissot, P.; Lartigue, H.; Pouchon, M. *Thermochim. Acta* **2003**, *403*, 267–273.
- (60) Patil, R. N.; Sabbarao, E. C. *J. Appl. Crystallogr.* **1969**, *2*, 281–288.
- (61) Mukherjee, B.; Boyle, A. J. F. *Phys. Status Solidi* **1967**, *22*, K131–K134.
- (62) Stoupin, S.; Shvyd'ko, Y. V. *Phys. Rev. B* **2011**, *83*, 104102:1–7.
- (63) Kittel, C. *Introduction to Solid State Physics*, 8th Ed.; John Wiley & Sons, Inc: New York, 2005.
- (64) Qui, L.; White, M. A. *J. Chem. Educ.* **2001**, *78*, 1076–1079.
- (65) Stevens, R.; Linford, J.; Woodfield, B. F.; Boerio-Goates, J.; Lind, C.; Wilkinson, A. P. *J. Chem. Thermodyn.* **2003**, *35*, 919–937.
- (66) Kennedy, C. A.; White, M. A.; Wilkinson, A. P.; Varga, T. *Phys. Rev. B* **2007**, *75*, 224302:1–9.
- (67) Yamamura, Y.; Nakajima, N.; Tsuji, T.; Isawa, Y.; Saito, K.; Sorai, M. *Solid State Commun.* **2002**, *121*, 213–217.
- (68) Furukawa, G. T.; Douglas, T. B.; McCoskey, R. E.; Ginnings, D. C. *J. Res. Natl. Bur. Stand.* **1956**, *57*, 67–82.

-
- (69) Murashov, V.; White, M. A. *Thermal Conductivity of Insulators and Glasses*. In *Thermal Conductivity: Theory, Properties, and Applications*; Tritt, T. M., Ed.; Kluwer Academic/Plenum Publishers: New York, 2004, 93–104.
- (70) Jakubinek, M. B.; Whitman, C. A.; White, M. A. *J. Therm. Anal. Calorim.* **2010**, *99*, 165–172.
- (71) Kennedy, C.A.; White, M.A.; Wilkinson, A.P.; Varga, T. *Appl. Phys. Lett.* **2007**, *90*, 151906:1-3.
- (72) Ernst, G.; Broholm, C.; Kowach, G. R.; Ramirez, A. P. *Nature* **1998**, *396*, 147–149.
- (73) David, W. I.; Evans, J. S. O.; Sleight, A. W. *Europhys. Lett.* **1999**, *46*, 661–666.
- (74) Yamamura, Y.; Ikeuchi, S.; Saito, K. *Chem. Mater.* **2009**, *21*, 3008–3016.
- (75) Mittal, R.; Chaplot, S. L. *Solid State Commun.* **2000**, *115*, 319–322.
- (76) Evans, J. S. O.; Mary, T. A. *Int. J. Inorg. Mater.* **2000**, *2*, 143–151.
- (77) Khosrovani, N.; Sleight, A. W.; Vogt, T. *J. Solid State Chem.* **1997**, *132*, 355–360.
- (78) Sleight, A. W.; Brixner, L. H. *J. Solid State Chem.* **1973**, *7*, 172–174.
- (79) Schneider, T.; Srinivasan, G.; Enz, C. P. *Phys. Rev. A* **1972**, *5*, 1528–1536.
- (80) Bull, I.; Lightfoot, P.; Villaescusa, L. A.; Bull, L. M.; Glover, R. K. B.; Evans, J. S. O.; Morris, R. E. *J. Am. Chem. Soc.* **2003**, *125*, 4342–4349.
- (81) Gindhart, A. M.; Lind, C.; Green, M. *J. Mater. Res.* **2008**, *23*, 210–213.
- (82) Evans, J. S. O.; Hu, Z.; Jorgensen, J. D.; Argyriou, D. N.; Short, S.; Sleight, A. W. *Science* **1997**, *275*, 61–65.
- (83) Jorgensen, J. D.; Hu, Z.; Teslic, S.; Argyriou, D. N.; Short, S.; Evans, J. S. O.; Sleight, A. W. *Phys. Rev. B* **1999**, *59*, 215–225.
- (84) Petzoldt, J.; Pannhorst, W. *J. Non-Cryst. Solids* **1991**, *129*, 191–198.
- (85) Pannhorst, W. *J. Non-Cryst. Solids* **1997**, *219*, 198–204.

-
- (86) Agostini, G.; Corvasce, F. G. Tire with Low Thermal Expansion Component. U.S. Patent 7,347,242, Mar 25, 2008.
- (87) Schlichter, S.; Herrmann, A. S. Apparatus at a Carding Machine having a Cylinder and Clothed and/or Unclothed Elements Located Opposite the Cylinder. U.S. Patent 7,694,393, Apr 13, 2010.
- (88) Dejneka, M. J.; Chapman, C. L.; Mixture, S. T. *J. Am. Ceram. Soc.* **2011**, *94*, 2249–2261.
- (89) Merkel, G. A. Optical Device with Negative Thermal Expansion Substrate and Uses Therefor. U.S. Patent 6,377,729, Apr 23, 2002.
- (90) Bookbinder, D. C.; Carberry, J. P.; Danielson, P. S.; DeMartino, S. E.; Hagy, H. E.; Wedding, B. M. Athermal Optical Waveguide Grating Device. U.S. Patent 6,603,900, Aug 5, 2003.
- (91) Matano, T.; Yoshihara, S. Substrate for Optical Communication Device, Method for Production thereof and Optical Communication Device Using the Same. U.S. Patent 7,106,941, Sep 12, 2006.
- (92) Pedersen, J. E.; Beukema, M.; Poulsen, C. V.; Eskildsen, L. E. Packaging of an Optical Fiber Laser. U.S. Patent 6,603,779, Aug. 5, 2003.
- (93) Jiang, T.; Wu, Z. Zero Insertion Force Sockets Using Negative Thermal Expansion Materials. U.S. Patent 6,264,486, July 24, 2001.
- (94) Suzuki, T.; Omote, A.; Kuwata, J. Zero Thermal Expansion Material and Practical Component Parts Making Use of the Same. U.S. Patent 6,844,283, Jan 18, 2005.
- (95) Hougham, G. G.; Chey, S. J.; Doyle, J. P.; Liu, X. H.; Jahnes, C. V.; Lauro, P. A.; LaBianca, N. C.; Rooks, M. J. Negative Thermal Expansion System (NTES) Device for TCE Compensation in Elastomer Composites and Conductive Elastomer Interconnects in Microelectronic Packaging. U.S. Patent 7,417,315, Aug 26, 2008.
- (96) Kohka, K. Negative Thermal Expansion Metal Electrically Connected to Motor Means for Microwave Oven. U.S. Patent 4,608,474, Aug 26, 1986.
- (97) McAvoy, G. J.; Lawlor, V. P.; Silverbrook, K. Thermal Bend Actuator Comprising Passive Element having Negative Thermal Expansion. U.S. Patent 7,735,970, Jun 15, 2010.

-
- (98) Jakubinek, M. B.; O'Neill, C.; Felix, C.; Price, R. B.; White, M. A. *Dent. Mater.* **2008**, *24*, 1468–1476.
- (99) Versluis, A.; Douglas, W. H.; Sakaguchi, R. L. *Dent. Mater.* **1996**, *12*, 290–294.
- (100) Boyd, R. N.; Colin, L.; Kaufman, E. G. Dental Filling Composition of a Coefficient of Thermal Expansion Approximating that of Natural Tooth Enamel. U.S. Patent 3,503,128, Mar 31, 1970.
- (101) Mary, T. A.; Evans, J. S. O.; Vogt, T.; Sleight, A. W. *Science* **1996**, *272*, 90–92.
- (102) Lewis, R. J., Sr., Ed. *Hawley's Condensed Chemical Dictionary*, 13th ed.; John Wiley & Sons: New York, 1997.
- (103) Ruml, V. *Tagungsband - Kammer Tech. Suhl* **1979**, *53*, 87-91.
- (104) Lind, C.; Gates, S. D; Pedoussaut; N. M.; Baiz, T. I. *Materials* **2010**, *3*, 2567–2587.
- (105) Tyagi, A. K.; Achary, S. N.; Mathews, M. D. *J. Alloys Compd.* **2002**, *339*, 207–210.
- (106) Korthuis, V.; Khosrovani, N.; Sleight, A. W.; Roberts, N.; Dupree, R.; Warren, W. W., Jr. *Chem. Mater.* **1995**, *7*, 412–417.
- (107) Hannink, R. H. J.; Kelly, P. M.; Muddle, B. C. *J. Am. Chem. Soc.* **2000**, *83*, 461–487.
- (108) De Buysser, K.; Van Driessche, I.; Vande Putte, B.; Vanhee, P.; Schaubroeck, J.; Hoste, S. *Inorg. Chem.* **2008**, *47*, 736–741.
- (109) Varga, T.; Wilkinson, A. P.; Lind, C.; Bassett, W. A.; Zha, C.-S. *Solid State Commun.* **2005**, *135*, 739–744.
- (110) Perottoni, C. A.; da Jornada, J. A. H. *Science* **1998**, *280*, 886–889.
- (111) Sikka, S. K. *J. Phys.: Condens. Matter* **2004**, *16*, S1033–S1039.
- (112) Miller, W.; Smith, C. W.; Dooling, P.; Burgess, A. N.; Evans, K. E. *Compos. Sci. Technol.* **2010**, *70*, 318–327.
- (113) Lommens, P.; De Meyer, C.; Bruneel, E.; De Buysser, K.; Van Driessche, I.; Hoste, S. *J. Eur. Ceram. Soc.* **2005**, *25*, 3605–3610.

-
- (114) Sumithra, S.; Umarji, A. M. *Mater. Res. Bull.* **2005**, *40*, 167–176.
- (115) Sumithra, S.; Umarji, A. M. *Solid State Sci.* **2006**, *8*, 1453–1458.
- (116) Watanabe, H.; Tani, J.; Kido, H.; Mizuuchi, K. *Mater. Sci. Eng., A* **2008**, *494*, 291–298.
- (117) Mittal, R.; Chaplot, S. L.; Schober, H.; Kolesnikov, A. I.; Loong, C.-K.; Lind, C.; Wilkinson, A. P. *Phys. Rev. B* **2004**, *70*, 214303:1–6.
- (118) Arora, A. K.; Yagi, T.; Miyajima, N.; Mary, T. A. *J. App. Phys.* **2005**, *97*, 013508:1–8.
- (119) Han, S. S.; Goddard, W. A., III. *J. Phys. Chem. C* **2007**, *111*, 15185–15191.
- (120) Chapman, K. W.; Chupas, P. J. *J. Am. Chem. Soc.* **2007**, *129*, 10090–10091.
- (121) Kingery, W. D.; Bowen, H. K.; Uhlmann, D. R. *Introduction to Ceramics*; John Wiley & Sons: New York, 1960.
- (122) Lind, C.; Coleman, M. R.; Kozy, L. C.; Sharma, G. R. *Phys. Status Solidi B* **2011**, *248*, 123–129.
- (123) Holliday, L.; Robinson, J. *J. Mater. Sci.* **1973**, *8*, 301–311.
- (124) Carter, C. B.; Norton, M. G. *Ceramic Materials Science and Engineering*; Springer: New York, 2007.
- (125) Graham, J.; Wadsley, A. D.; Weymouth, J. H.; Williams, L. S. *J. Am. Ceram. Soc.* **1959**, *42*, 570.
- (126) Nassau, K.; Levinstein, H. J.; Loiacono, G. M. *J. Phys. Chem. Solids* **1965**, *26*, 1805–1816.
- (127) Cundy, C. S.; Cox, P. A. *Chem. Rev.* **2003**, *103*, 663–701.
- (128) Ari, M.; Jardim, P. M.; Marinkovic, B.A.; Rizzo, F.; Ferreira, F. F. *J. Solid State Chem.* **2008**, *181*, 1472–1479.
- (129) Tkacová, K. *Mechanical Activation of Minerals*; Elsevier: New York, 1989.
- (130) Pourghahramani, P.; Forsberg, E. *Int. J. Miner. Process.* **2006**, *79*, 120–139.

-
- (131) Amade, R.; Heitjans, P.; Indris, S.; Finger, M.; Haeger, A.; Hesse, D. *J. Photochem. Photobiol., A* **2009**, *207*, 231–235.
- (132) Ari, M.; Miller, K. J.; Marinkovic, B. A.; Jardim, P. M.; de Avillez, R.; Rizzo F.; White M. A. *J. Sol-Gel Sci. Technol.* **2011**, *58*, 121–125.
- (133) Wu, M. M.; Cheng, Y. Z.; Peng, J.; Xiao, X. L.; Chen, D. F.; Kiyonagi, R.; Fieramosca, J. S.; Short, S.; Jorgensen, J.; Hu, Z. B. *Mater. Res. Bull.* **2007**, *42*, 2090–2098.
- (134) Wu, M. M.; Hu, Z. B.; Liu, Y. T. Chen, D. F. *Mater. Res. Bull.* **2009**, *44*, 1943–1947.
- (135) Sumithra, S.; Umarji, A. M. *Solid State Sci.* **2004**, *6*, 1313–1319.
- (136) Chang, L. L. Y.; Scroger, M. G.; Phillips, B. *J. Am. Ceram. Soc.* **1967**, *50*, 211–215.
- (137) Wilkinson, A. P.; Lind, C.; Pattanaik, S. *Chem. Mater.* **1999**, *11*, 101–108.
- (138) Kameswari, U.; Sleight, A. W.; Evans, J. S. O. *Int. J. Inorg. Mater.* **2000**, *2*, 333–337.
- (139) Lind, C.; Wilkinson, A. P. *J. Sol-Gel Sci. Technol.* **2002**, *25*, 51–56.
- (140) Gates, S. D.; Colin, J. A.; Lind, C. *J. Mater. Chem.* **2006**, *16*, 4214–4219.
- (141) Gates, S. D.; Lind, C. *J. Solid State Chem.* **2007**, *180*, 3510–3514.
- (142) Baiz, T. I.; Gindhart, A. M.; Kraemer, S. K.; Lind, C. *J. Sol-Gel Sci. Technol.* **2008**, *47*, 128–130.
- (143) De Buysser, K.; Smet, P. F.; Schoofs, B.; Bruneel, E.; Poelman, D.; Hoste, S.; Van Driessche, I. *J. Sol-Gel Sci. Technol.* **2007**, *43*, 347–353.
- (144) Zhang, H.; Zhang, Q.; Du, H.; Jia, Q. *Chem. Eng. Commun.* **2008**, *195*, 243–255.
- (145) Georgi, C.; Kern, H. *Ceram. Int.* **2009**, *35*, 755–762.
- (146) De Buysser, K.; Van Driessche, I.; Schaubroeck, J.; Hoste, S. *J. Sol-Gel Sci. Technol.* **2008**, *46*, 133–136.
- (147) Xu, G.-F.; Liu, Q.-Q.; Yang, J.; Sun, X.-J.; Cheng, X.-N. *Ceram. Int.* **2009**, *35*, 3131–3134.

-
- (148) Zhecheva, E.; Stoyanova, R.; Ivanova, S.; Nikolov, V. *Solid State Sci.* **2010**, *12*, 2010–2014.
- (149) Liu, Q.-Q.; Cheng, X.-N.; Yang, J.; Sun, X.-J. *J. Mater. Sci.* **2011**, *46*, 1253–1258.
- (150) Xing, X.; Xing, Q.; Yu, R.; Meng, J.; Chen, J.; Liu, G. *Physica B.* **2006**, *371*, 81–84.
- (151) Liu, Q.-Q.; Yang, J.; Sun, X.-J.; Cheng, X.-N.; Xu, G.-F.; Yan, X.-H. *J. Mater. Sci.* **2007**, *42*, 2528–2531.
- (152) Yang, J.; Liu, Q.; Sun, X.; Xu, G.; Cheng, X. *Ceram. Int.* **2009**, *35*, 441–445.
- (153) Sun, X.; Yang, J.; Liu, Q.; Cheng, X. *J. Alloys Compd.* **2009**, *481*, 668–672.
- (154) Chen, X.; Deng, X.; Ma, H.; Tao, J.; Zhao, X. *J. Solid State Chem.* **2011**, *184*, 1090–1095.
- (155) Liang, E. J.; Wang, S. H.; Wu, T. A.; Chao, M. J.; Yuan, B.; Zhang, W. F. *J. Raman Spectrosc.* **2007**, *38*, 1186–1192.
- (156) Liang, E. J.; Wu, T. A.; Yuan, B.; Chao, M. J.; Zhang, W. F. *J. Phys. D: Appl. Phys.* **2007**, *40*, 3219–3223.
- (157) Liang, E. J.; Wang, J. P.; Xu, E. M.; Du, Z. Y.; Chao, M. J. *J. Raman Spectrosc.* **2008**, *39*, 887–892.
- (158) Liang, E. J.; Huo, H. L.; Wang, Z.; Chao, M. J.; Wang, J. P. *Solid State Sci.* **2009**, *11*, 139–143.
- (159) Latka, L.; Goryachev, S. B.; Kozerski, S.; Pawlowski, L. *Materials*, **2010**, *3*, 3845–3866.
- (160) Poowancum, A.; Matsumaru, K.; Ishizaki, K. *J. Am. Ceram. Soc.* **2011**, *94*, 1354–1356.
- (161) Poowancum, A.; Matsumaru, K.; Juárez-Ramírez, I.; Torres-Martínez, L. M.; Fu, Z. Y.; Ishizaki, K. *Mater. Sci. Eng.* **2011**, *20*, 012010:1–7.
- (162) Xing, Q.; Xing, X.; Yu, R.; Du, L.; Meng, J.; Luo, J.; Wang, D.; Liu, G. *J. Cryst. Growth* **2005**, *283*, 208–214.

-
- (163) Kozy, L. C.; Tahir, M. N.; Lind, C.; Tremel, W. *J. Mater. Chem.* **2009**, *19*, 2760–2765.
- (164) Zhang, L.; Howe, J. Y.; Zhang, Y.; Fong, H. *Cryst. Growth Des.* **2009**, *9*, 667–670.
- (165) Noailles, L. D.; Peng, H.-h.; Starkovich, J.; Dunn, B. *Chem. Mater.* **2004**, *16*, 1252–1259.
- (166) Miller, W.; Smith, C. W.; Dooling, P.; Burgess, A. N.; Evans, K. E. *Phys. Status Solidi B* **2008**, *245*, 552–556.
- (167) Liu, Q.; Yang, J.; Cheng, X.; Liang, G.; Sun, X. *Ceram. Int.* **2012**, *38*, 541–545.
- (168) Wu, Y.; Liu, Q.; Wang, H. *J. Compos. Mater.* **2011**, *46*, 1453–1458.
- (169) Huang, R.-c.; Chen, Y.-q. *Appl. Math. Mech. (Engl. Transl.)* **2011**, *32*, 1377–1388.
- (170) Calvert, P.; Cima, M. *J. Am. Ceram. Soc.* **1990**, *73*, 575–579.
- (171) Mittemeijer, E. J. *Fundamentals of Materials Science*; Springer-Verlag: Berlin, 2010.
- (172) Dapiaggi, M.; Fitch, A. N. *J. Appl. Crystallogr.* **2009**, *42*, 253–258.
- (173) Rietveld, H. M. *J. Appl. Crystallogr.* **1969**, *2*, 65–71.
- (174) Brown, I. D.; Altermatt, D. *Acta Crystallogr., Sect. B: Struct. Sci.* **1985**, *41*, 244–247.
- (175) Makovicky, E.; Balić-Žunić, T. *Acta Crystallogr., Sect. B: Struct. Sci.* **1998**, *54*, 766–773.
- (176) Kalinko, A.; Kuzmin, A. *J. Non-Cryst. Solids* **2011**, *357*, 2595–2599.
- (177) Tucker, M. G.; Dove, M. T.; Keen, D. A. *J. Phys.: Condens. Matter* **2000**, *12*, L425–L430.
- (178) Chapman, K. W.; Chupas, P. J.; Kepert, C. J. *J. Am. Chem. Soc.* **2005**, *127*, 15630–15636.
- (179) Chapman K. W.; Chupas, P. J. *Chem. Mater.* **2009**, *21*, 425–431.

-
- (180) Billinge, S. J. L.; Dykhne, T.; Juhás, P.; Božin, E.; Taylor, R.; Florence, A. J.; Shankland, K. *CrystEngComm* **2010**, *12*, 1366–1368.
- (181) Young, C. A.; Goodwin, A. L. *J. Mater. Chem.* **2011**, *21*, 6464–6476.
- (182) James, J. D.; Spittle, J. A.; Brown, S. G. R.; Evans, R. W. *Meas. Sci. Technol.* **2001**, *12*, R1–R15.
- (183) Mary, T. A.; Sleight, A. W. *J. Mater. Res.* **1999**, *14*, 912–915.
- (184) Buessem, W. R. In *Mechanical Properties of Engineering Ceramics*; Kreigel, W. W., Palmour, H., III., Eds.; Interscience: New York, 1961.
- (185) Chen, X.; Tao, J.; Ma, H.; Zhao, X. *Acta Crystallogr., Sect. C: Cryst. Struct. Commun.* **2009**, *65*, i74–i76.
- (186) De Buysser, K.; Lommens, P.; de Meyer, C.; Bruneel, E.; Hoste, S.; van Driessche I. *Ceram.-Silik.* **2004**, *48*, 139–144.
- (187) Birkedal, H.; Krogh Andersen, A. M.; Arakcheeva, A.; Chapuis, G.; Norby, P.; Pattison, P. *Inorg. Chem.* **2006**, *45*, 4346–4351.
- (188) White, K. M.; Lee, P. L.; Chupas, P. J.; Chapman, K. W.; Payzant, E. A.; Jupe, A. C.; Bassett, W. A.; Zha, C.-S.; Wilkinson, A. P. *Chem. Mater.* **2008**, *20*, 3728–3734.
- (189) Marinkovic, B. A.; Jardim, P. M.; de Avillez, R. R.; Rizzo, F. *Solid State Sci.* **2005**, *7*, 1377–1383.
- (190) Liang, E.; Huo, H.; Wang, J.; Chao, M. *J. Phys. Chem. C* **2008**, *112*, 6577–6581.
- (191) Li, Z. Y.; Song, W. B.; Liang, E. J. *J. Phys. Chem. C* **2011**, *115*, 17806–17811.
- (192) Evans, J. S. O.; Mary, T. A.; Sleight, A. W. *J. Solid State Chem.* **1995**, *120*, 101–104.
- (193) Varga, T.; Moats, J. L.; Ushakov, S. V.; Navrotsky, A. *J. Mater. Res.* **2007**, *22*, 2512–2521.
- (194) Sivasubramanian, V.; Ravindran, T. R.; Nithya, R.; Arora, A. K. *J. Appl. Phys.* **2004**, *69*, 387–392.
- (195) Evans, J. S. O.; Mary, T. A.; Sleight, A. W. *J. Solid State Chem.* **1998**, *137*, 148–160.

-
- (196) Marinkovic, B. A.; Ari, M.; Jardim, P. M.; de Avillez, R. R.; Rizzo F.; Ferreira, F. F. *Thermochim. Acta* **2010**, 499, 48–53.
- (197) Forster, P. M.; Sleight, A. W. *Int. J. Inorg. Mater.* **1999**, 1, 123-127.
- (198) Baiz, T.I.; Heinrich, C.P.; Banek, N.A., Vivekens, B.L.; Lind, C. *J. Sol. State Chem.* **2012**, 187, 195-199.
- (199) Marinkovic, B. A.; Jardim, P. M.; Ari, M.; de Avillez, R. R.; Rizzo, F.; Ferreira, F. F. *Phys. Status Solidi B* **2008**, 245, 2514–2519.
- (200) Marinkovic, B.A. (Private Communication)
- (201) Ari, M.; Jardim, P.M.; Marinkovic, B. A.; Rizzo, F.; Ferreira, F. F. *J. Solid State Chem.* **2008**, 181, 1472-1479.
- (202) Wu, M.M.; Xiao, X.L.; Hu, z.B.; Liu, Y.T.; Chen, D.F. *Solid State Sci.* **2009**, 11, 325-329.
- (203) Suzuki, T.; Omote, A. *J. Am. Ceram. Soc.* **2004**, 87, 1365–1367.
- (204) Amos, T.G.; Yokochi, A.; Sleight, A.W. *J. Sol. State Chem.* **1998**, 141, 303–307.
- (205) Amos, T. G.; Sleight, A. W. *J. Sol. State Chem.* **2001**, 160, 230–238.
- (206) Matsuno, N.; Yoshimi, M.; Ohtake, S.; Akahane, T.; Tsuda, N. *J. Phys. Soc. Jpn.* **1978**, 45, 1542–1544.
- (207) Chatterji, T.; Hansen, T. C.; Brunelli, M.; Henry, P. F. *Appl. Phys. Lett.* **2009**, 94, 241902:1–3.
- (208) Taylor, D. *Trans. J. Br. Ceram. Soc.* **1985**, 84, 9–14.
- (209) Rodriguez, E. E.; Llobet, A.; Proffen, T.; Melot, B. C.; Seshadri, R.; Littlewood, P. B.; Cheetham, A. K. *J. Appl. Phys.* **2009**, 105, 114901:1–6.
- (210) Tao, J. Z.; Sleight, A. W. *J. Sol. State Chem.* **2003**, 173, 45–48.
- (211) Greve, B. K.; Martin, K. L.; Lee, P. L.; Chupas, P. J.; Chapman, K. W.; Wilkinson, A. P. *J. Am. Chem. Soc.* **2010**, 132, 15496–15498.

-
- (212) Li, C. W.; Tang, X.; Muñoz, J. A.; Keith, J. B.; Tracy, S. J.; Abernathy, D. L.; Fultz, B. *Phys. Rev. Lett.* **2011**, *107*, 195504:1–5.
- (213) Roy, R.; Agrawal, D. K.; McKinstry, H. A. *Annu. Rev. Mater. Sci.* **1989**, *19*, 59–81.
- (214) García-Moreno, O.; Fernández, A.; Khainakov, S.; Torrecillas, R. *Scr. Mater.* **2010**, *63*, 170–173.
- (215) Tiano, W.; Dapiaggi, M.; Artioli, G. *J. Appl. Crystallogr.* **2003**, *36*, 1461–1463.
- (216) White, G. K. *J. Phys. C: Solid State Phys.* **1978**, *11*, 2171–2174.
- (217) Schäfer, W.; Kirfel, A. *Appl. Phys. A: Mater. Sci. Process.* **2002**, *74*, S1010–S1012.
- (218) Couves, J. W.; Jones, R. H.; Parker, S. C.; Tschaufeser, P.; Catlow, C. R. A. *J. Phys.: Condens. Matter* **1993**, *5*, L329–L332.
- (219) Tschaufeser, P.; Parker, S. C. *J. Phys. Chem.* **1995**, *99*, 10609–10615.
- (220) Park, S. H.; Große Kuntze, R.-W.; Graetsch, H.; Gies, H. *Stud. Surf. Science Catal.* **1997**, *105*, 1989–1994.
- (221) Villaescusa, L. A.; Lightfoot, P.; Teat, S. J.; Morris, R. E. *J. Am. Chem. Soc.* **2001**, *123*, 5453–5459.
- (222) Colantuono, A.; Dal Vecchio, S.; Mascolo, G.; Pansini, M. *Thermochim. Acta* **1997**, *296*, 59–66.
- (223) Lightfoot, P.; Woodcock, D. A.; Maple, M. J.; Villaescusa, L. A.; Wright, P. A. *J. Mater. Chem.* **2001**, *11*, 212–216.
- (224) Woodcock, D. A.; Lightfoot, P.; Villaescusa, L. A.; Díaz-Cabañas, M.-J.; Camblor, M. A.; Engberg, D. *Chem. Mater.* **1999**, *11*, 2508–2514.
- (225) Woodcock, D. A.; Lightfoot, P.; Wright, P. A.; Villaescusa, L. A.; Díaz-Cabañas, M.-J.; Camblor, M. A. *J. Mater. Chem.* **1999**, *9*, 349–351.
- (226) Attfield, M. P.; Sleight, A. W. *Chem. Commun.* **1998**, 601–602.
- (227) Marinkovic, B. A.; Jardim, P. M.; Saavedra, A.; Lau, L. Y.; Baetz, C.; de Aveliz, R. R.; Rizzo, F. *Microporous Mesoporous Mater.* **2004**, *71*, 117–124.

-
- (228) Bhange, D. S.; Ramaswamy, V. *Mater. Res. Bull.* **2006**, *41*, 1392–1402.
- (229) Bhange, D. S.; Ramaswamy, V. *Microporous and Mesoporous Mater.* **2010**, *130*, 322–326.
- (230) Amri, M.; Walton, R. I. *Chem. Mater.* **2009**, *21*, 3380–3390.
- (231) Amri, M.; Clarkson, G. J.; Walton, R. I. *J. Phys. Chem. C* **2010**, *114*, 6726–6733.
- (232) Attfield, M. P.; Sleight, A. W. *Chem. Mater.* **1998**, *10*, 2013–2019.
- (233) Chen, J.; Xing, X.; Sun, C.; Hu, P.; Yu, R.; Wang, X.; Li, L. *J. Am. Chem. Soc.* **2008**, *130*, 1144–1145.
- (234) Chen, J.; Xing, X. R.; Liu, G. R.; Li, J. H.; Liu, Y. T. *Appl. Phys. Lett.* **2006**, *89*, 101914:1–3.
- (235) Hu, P.; Chen, J.; Deng, J.; Xing, X. *J. Am. Chem. Soc.* **2010**, *132*, 1925–1928.
- (236) Williams, D. J.; Partin, D. E.; Lincoln, F. J.; Kouvetakis, J.; O’Keeffe, M. *J. Solid State Chem.* **1997**, *134*, 164–169.
- (237) Hibble, S. J.; Chippindale, A. M.; Pohl, A. H.; Hannon, A. C. *Angew. Chem.* **2007**, *119*, 7246–7248.
- (238) Chapman, K. W.; Chupas, P. J.; Kepert, C. J. *J. Am. Chem. Soc.*, **2006**, *128*, 7009–7014.
- (239) Adak, S.; Daemen, L. L.; Hartl, M.; Williams, D.; Summerhill, J.; Nakotte, H. *J. Solid State Chem.* **2011**, *184*, 2854–2861.
- (240) Adak, S.; Daemen, L. L.; Nakotte, H. *J. Phys.: Conf. Ser.* **2010**, *251*, 012007:1–4.
- (241) Goodwin, A. L.; Calleja, M.; Conterio, M. J.; Dove, M. T.; Evans, J. S. O.; Keen, D. A.; Peters, L.; Tucker, M. G. *Science* **2008**, *319*, 794–797.
- (242) Bowmaker, G. A.; Kennedy, B. J.; Reid, J. C. *Inorg. Chem.* **1998**, *37*, 3968–3974.
- (243) Hibble, S. J.; Wood, G. B.; Bilbé, E. J.; Pohl, A. H.; Tucker, M. G.; Hannon, A. C.; Chippindale, A. M. *Z. Kristallogr.* **2010**, *225*, 457–462.
- (244) Chippindale, A. M.; Hibble, S. J. *J. Am. Chem. Soc.* **2009**, *131*, 12736–12744.

-
- (245) Goodwin, A. L.; Chapman, K. W.; Kepert, C. J. *J. Am. Chem. Soc.* **2005**, *127*, 17980–17981.
- (246) Kitazawa, T.; Nishikiori, S.-i.; Kuroda, R.; Iwamoto, T. *Chem. Lett.* **1988**, *17*, 1729–1732.
- (247) Kitazawa, T.; Nishikiori, S.-i.; Kuroda, R.; Iwamoto, T. *J. Chem. Soc., Dalton Trans.* **1994**, 1029–1036.
- (248) Phillips, A. E.; Goodwin, A. L.; Halder, G. J.; Southon, P. D.; Kepert, C. J. *Angew. Chem., Int. Ed.* **2008**, *47*, 1396–1399.
- (249) Phillips, A. E.; Halder, G. J.; Chapman, K. W.; Goodwin, A. L.; Kepert, C. J. *J. Am. Chem. Soc.* **2010**, *132*, 10–11.
- (250) Li, H.; Eddaoudi, M.; O’Keeffe, M.; Yaghi, O. M. *Nature* **1999**, *402*, 276–279.
- (251) Zhou, W.; Wu, H.; Yildirim, T.; Simpson, J. R.; Hight Walker, A. R. *Phys. Rev. B.* **2008**, *78*, 054114:1–5.
- (252) Wu, Y.; Kobayashi, A.; Halder, G. J.; Peterson, V. K.; Chapman, K. W.; Lock, N.; Southon, P. D.; Kepert, C. J. *Angew. Chem., Int. Ed.* **2008**, *47*, 8929–8932.
- (253) Dubbeldam, D.; Walton, K. S.; Ellis, D. E.; Snurr, R. Q. *Angew. Chem., Int. Ed.* **2007**, *46*, 4496–4499.
- (254) Huang, C. Y.; Agrawal, D. K.; McKinstry, H. A. *J. Mater. Sci.* **1995**, *30*, 3509–3514.
- (255) Woodcock, D. A.; Lightfoot, P.; Ritter, C. *Chem. Commun.* **1998**, 107–108.
- (256) Woodcock, D. A.; Lightfoot, P.; Smith, R. I. *Proc. Mater. Res. Soc. Symp.* **1999**, *547*, 191–196.
- (257) Kuru, Y.; Wohlschlögel, M.; Welzel, U.; Mittemeijer, E. J. *Appl. Phys. Lett.* **2007**, *90*, 243113:1–3.
- (258) Zheng, X. G.; Kubozono, H.; Yamada, H.; Kato, K.; Ishiwata, Y.; Xu, C. N. *Nat. Nanotechnol.* **2008**, *3*, 724–726.
- (259) Sun, Z. H.; Song, X. Y.; Yin, F. X.; Sun, L. X.; Yuan, X. K.; Liu, X. M. *J. Phys. D: Appl. Phys.* **2009**, *42*, 122004:1–5.

-
- (260) Li, W.-H.; Wu, S.Y.; Yang, C. C.; Lai, S. K.; Lee, K. C.; Huang, H. L.; Yang, H. D. *Phys. Rev. Lett.* **2002**, *89*, 135504:1–4.
- (261) Dantl, G. *Z. Phys.* **1962**, *166*, 115–118.
- (262) Das, D.; Jacobs, T.; Barbour, L. J. *Nat. Mater.* **2010**, *9*, 36–39.
- (263) Baughman, R. H. *J. Chem. Phys.* **1973**, *58*, 2976–2983.
- (264) Birkedal, H.; Schwarzenbach, D.; Pattison, P. *Angew. Chem., Int. Ed.* **2002**, *41*, 754–756.
- (265) Aleksandrovskii, A. N.; Esel'son, V. B.; Manzhelii, V. G.; Soldatov, A. V.; Sundqvist, B.; Udovidchenko, B. G. *Low Temp. Phys.* **1997**, *23*, 1256–1260.
- (266) Loktev, V. M. *Low Temp. Phys.* **1999**, *25*, 823–825.
- (267) Bao, W.; Miao, F.; Chen, Z.; Zhang, H.; Jang, W.; Dames, C.; Lau, C. N. *Nat. Nanotechnol.* **2009**, *4*, 562–566.
- (268) Kwon, Y.-K.; Berber, S.; Tománek, D. *Phys. Rev. Lett.* **2004**, *92*, 15901:1–4.
- (269) Jiang, J.-W.; Wang, J.-S.; Li, B. *Nanoscale* **2010**, *2*, 2864–2867.
- (270) Heberlein, D. C.; Adams, E. D. *Low Temp. Phys.* **1970**, *3*, 115–121.
- (271) Kofteros, M.; Rodriguez, S.; Tandon, V.; Murr, L. E. *Scr. Mater.* **2001**, *45*, 369–374.
- (272) Yan, X.; Cheng, X.; Xu, G.; Wang, C.; Sun, S.; Riedel, R. *Mat.-wiss. u. Werkstofftech.* **2008**, *39*, 649–653.
- (273) Wang, X.; Zhang, J.; Zhang, Y.; Zhang, J.; Lu, F.; Wang, X. *Rare Met.* **2010**, *29*, 371–375.
- (274) Tran, K. D.; Groshens, T. J.; Nelson, J. G. *Mater. Sci. Eng. A* **2001**, *303*, 234–240.
- (275) Wang, L. D.; Fei, W. D.; Yao, C. K. *Mater. Sci. Eng. A* **2002**, *336*, 110–116.
- (276) Ding, L.; Wang, C.; Na, Y.; Chu, L.; Yan, J. *Scr. Mater.* **2011**, *65*, 687–690.
- (277) Sun, L.; Kwon, P. *Mater. Sci. Eng. A* **2009**, *527*, 93–97.
- (278) Sun, L.; Sneller, A.; Kwon, P. *Compos. Sci. Technol.* **2008**, *68*, 3425–3430.

-
- (279) Yang, X.; Cheng, X.; Yan, X.; Yang, J.; Fu, T.; Qiu, J. *Compos. Sci. Technol.* **2007**, *67*, 1167–1171
- (280) Closmann, C.; Sleight, A. W.; Haygarth, J. C. *J. Solid State Chem.* **1998**, *139*, 424–426.
- (281) Evans, J. S. O.; Hanson, P. A.; Ibberson, R. M.; Duan, N.; Kameswari, U.; Sleight, A. W. *J. Am. Chem. Soc.* **2000**, *122*, 8694–8699.
- (282) Huang, L.; Xiao, Q.; Ma, H.; Li, G.; Liao, F.; Qi, C.; Zhao, X. *Eur. J. Inorg. Chem.* **2005**, 4521–4526.
- (283) De Meyer, C.; Bouree, F.; Evans, J. S. O.; De Buysser, K.; Bruneel, E.; Van Driessche, I.; Hoste, S. *J. Mater. Chem.* **2004**, *14*, 2988–2994.
- (284) Yamamura, Y.; Nakajima, N.; Tsuji, T.; Kijoma, A.; Kuroiwa, Y.; Sawada, A.; Aoyagi, S.; Kasatani, H. *Phys. Rev. B* **2004**, *70*, 104107:1–6.
- (285) Nakajima, N.; Yamamura, Y.; Tsuji, T. *Solid State Commun.* **2003**, *128*, 193–196.
- (286) Yamamura, Y.; Kato, M.; Tsuji, T. *Thermochim. Acta.* **2005**, *431*, 24–28.
- (287) Li, H.; Han, J.; Ma, H.; Huang, L.; Zhao, X. *J. Solid State Chem.* **2007**, *180*, 852–857.
- (288) Zhao, R.; Wang, X.; Tao, J.; Yang, X.; Ma, H.; Zhao, X. *J. Alloys Compd.* **2009**, *470*, 379–382.
- (289) Sivasubramanian, V.; Ravindran, T. R.; Kalavathi, S.; Arora, A. *J. Electroceram.* **2006**, *17*, 57–60.
- (290) Peng, J.; Wu, M. M.; Wang, H.; Hao, Y. M.; Hu, Z.; Yu, Z. X.; Chen, D. F.; Kiyonagi, R.; Fieramosca, J. S.; Short, S.; Jorgensen, J. *J. Alloys Compd.* **2008**, *453*, 49–54.
- (291) Peng, J.; Liu, X.; Guo, F.; Han, S.; Liu, Y.; Chen, D.; Zhao, X.; Hu, Z. *Trans. Nonferrous Met. Soc. China* **2009**, *19*, 1623–1627.
- (292) Peng, J.; Liu, X.; Guo, F.; Han, S.; Liu, Y.; Chen, D.; Hu, Z. *Int. J. Min. Met. Mater.* **2010**, *17*, 786–790.
- (293) Peng, J.; Wu, M. M.; Guo, F. L.; Han, S. B.; Liu, Y. T.; Chen, D. F.; Zhao, X. H.; Hu, Z. *J. Mater. Sci.* **2011**, *46*, 5160–5164.

-
- (294) Dugupta, N.; Sörge, E.; Butler, B.; Wen, T.-C.; Shetty, D.K.; Cambrea, L.R.; Harris, D.C. *J Mater. Sci.* **2012**, *47*, 6286.
- (295) Lu, C. H.; Saha, S. K. *J. Sol-Gel Sci. Technol.* **2001**, *20*, 27-34.
- (296) Archer, D. G.; Rudtsch, S. *J. Chem. Eng. Data* **2003**, *48*, 1157-1163.
- (297) NETZSCH DIL 402 C,
http://www.paralab.pt/client/documentos/portuguese/Netzsch/DIL/DIL402C_e_1106.pdf
- (298) Srikanth, V.; Subbarao, E.C.; Rao, G.V. *Ceram. Int.* **1992**, *18*, 251-261.
- (299) Le Bail, A.; Duroy, H.; Fourquet, J. L. *Mater. Res. Bull.* **1988**, *23*, 447-452.
- (300) Rietveld, H. M. *J. Appl. Crystallogr.* **1969**, *2*, 65-71.
- (301) Hunter, B. A.; Howard, C. J. *A Computer Program For Rietveld Analysis of X-ray and Neutron Powder Diffraction Patterns*, Australian Nuclear Science and Technology Organization, Lucas Heights Research Laboratories, 2000.
- (302) Ypma, T. J. *SIAM Rev.* **1995**, *37*, 531-551.
- (303) Davis, W. I. F. *J. Res. Natl. Inst. Stand. Technol.* **2004**, *109*, 107-123
- (304) Hunter, B. A. (n.d.), *High Quality Mass Unit-Cell refinement using Le Bail fitting and LHPM-Rietica*. Retrieved May 15, 2010, from <http://www.ccp14.ac.uk>.
- (305) *Physical Property Measurement System: Hardware and Options Manual*, Quantum Design, 2003.
- (306) Kennedy, C.A.; Stancescu, M.; Marriott, R.A.; White, M.A. *Cryogenics* **2007**, *47*, 107-112.
- (307) *Apiezon N: Cryogenic High Vacuum Grease - Specific Cryogenic Information*, Apiezon Products, M & I materials Ltd, August, 2005.
- (308) *Apiezon T: Medium Temperature Vacuum Grease*, Apiezon Products, M & I materials Ltd, August, 2005.
- (309) *Apiezon H: High Temperature Vacuum Grease*, Apiezon Products, M & I materials Ltd, August, 2005.

-
- (310) Sumithra S.; Waghmare, U. V.; Umarji, A. M. *Phys. Rev. B* **2007**, *76*, 024307:1-5.
- (311) Yanase, I.; Miyagi, M.; Kobayashi, H. *J. Eur. Ceram. Soc.* **2009**, *29*, 3129-3134.
- (312) Saha, S. K.; Pathak, A.; Pramanik, P. *J. Mater. Sci. Lett.* **1995**, *14*, 35-37.
- (313) Pramanik, P. *Bull. Mater. Sci.* **1996**, *19*, 957-961.
- (314) Sun, Y. K.; Oh, I. H. *Ind. Eng. Chem. Res.* **1996**, *35*, 4296-4300.
- (315) Hunyek, A.; Sirisathitkul, C.; Harding, P. *Adv. Mat. Res.* **2010**, *93-94*, 659-663.
- (316) Allred, A. L.; Rochow, E. G. *J. Inorg. Nucl. Chem.* **1958**, *5*, 264-268.
- (317) Li, K.; Xue, D. J. *J. Phys. Chem. A* **2006**, *110*, 11332-11337.
- (318) Köhler, J.; Imanaka, N.; Adachi, G. *Chem. Mater.* **1998**, *10*, 3790-3812.
- (319) Artioli, G.; Dapiaggi, M.; Fornasini, P.; Sanson, A.; Rocca, F.; Merli, M. *J. Phys. Chem. Solids* **2006**, *67*, 1918-1922.
- (320) Smith, T F.; White, G. K. *J. Phys. C: Solid State Phys.* **1975**, *8*, 2031-2042.
- (321) Liang, E. J.; Liang, Y.; Zhao, Y.; Liu, J.; Jian, Y. *J. Phys. Chem. A* **2008**, *112*, 12582-12587.
- (322) Shannon, R.D.; *Acta Cryst.* 1976, *A32*, 751-767.
- (323) Miller, K. J.; Johnson, M. B.; White, M. A.; Marinkovic, B. A. *Solid State Commun.* **2012**, *152*, 1748-1752.
- (324) Romao, C.P.; Miller, K.J.; Whitman, C.A.; White, M.A.; Marinkovic B.A. *in press in Comprehensive Inorganic Chemistry 2*, K. Poeppelemeier, Ed..
- (325) Tokoro, H.; Nakagawa, K.; Imoto, K.; Hakoe, F.; Ohkoshi, S. –I. *Chem. Mater.* **2012**, *24*, 1324-1330.
- (326) Gavrichev, K. S.; Gorbunov, V. E.; Golushina, L. N.; Nikiforova, G. E.; Totrova, G. A.; Shaplygin, I. S. *Zhurnal Fizicheskoi Khimii* **1993**, *67*, 1731-1733.
- (327) Boerio-Goates, J. (private communication).
- (328) Cordfunke, E.H.P.; Westrum, E.F. *J. Phys. Chem. Solids* **1992**, *53*, 361-365.
- (329) Todd, S.S. *J. Am. Chem. Soc.* **1953**, *75*, 3035-3036.

-
- (330) Westrum Jr., E.F.; Justice, B.H.; Sommers, J.A.; Johnson, D.A. *J. Therm. Anal. Calorim.* **1999**, *57*, 659-667.
- (331) Drymiotis, F.R.; Ledbetter, H.; Betts, J.B.; Kimura, T.; Lashley, J.C.; Migliori, A.; Ramirez, A.P.; Kowach, G.R.; Van Duijn, J. *Phys. Rev. Lett.* **2004**, *93*, 025502:1-4.
- (332) Klemens, P.G. *High Temp. - High Pressure* **1991**, *23*, 241-248.
- (333) Bryan, C.; Whitman, C.A.; Johnson, M.B.; Murray, P.; Bourque, A.; Dąbkowska, H.A.; Gaulin, B.D.; White, M.A. *Phys. Rev. B* **2012**, *86*, 054303:1-7.
- (334) Cahill, D.G.; Pohl, R.O. *Ann. Rev. Phys. Chem.* **1988**, *39*, 93-121.
- (335) Chen, G. *Int. J. Therm. Sci.* **2000**, *39*, 471-480.
- (336) Johnson, M.B.; James, D.D.; Bourque, A.; Dąbkowska, H.A.; Gaulin, B.D.; White, M.A. *J solid state Chem.* **2009**, *182*, 725-729.